University of Glasgow | Experimental Particle Physics

Searches for Doubly Charmed Baryons at LHCb

Murdo Traill

Experimental Particle Physics

School of Physics and Astronomy

University of Glasgow

Submitted in the fulfillment of the requirements for the degree of Doctor of Philosophy

July 2019

Abstract

The results of two separate searches for the doubly-charmed Ξ_{cc}^{++} particle through the $\Xi_{cc}^{++} \to \Lambda_c^+ K^- \pi^+ \pi^+$ and $\Xi_{cc}^{++} \to D^+ p K^- \pi^+$ decay modes are presented in this thesis. Both analyses examine proton-proton collision data collected by the LHCb detector at the European Laboratory for Particle Physics.

The $\Xi_{cc}^{++} \to \Lambda_c^+ K^- \pi^+ \pi^+$ analysis resulted in the first-ever observation of a doubly-charmed baryon, namely the Ξ_{cc}^{++} state. Using data recorded in 2016 at LHCb, the mass of the Ξ_{cc}^{++} state was measured to be

$$m(\Xi_{cc}^{++}) = 3621.40 \pm 0.72\,(\text{stat}) \pm 0.27\,(\text{syst}) \pm 0.14\,(\Lambda_c^+)\,\text{MeV}/c^2,$$

where the first and second uncertainties are statistical and systematic, respectively, and the last uncertainty is due to the limited knowledge on the mass of the Λ_c^+ baryon. The signal was determined to be compatible with a weak decay.

The second Ξ_{cc}^{++} analysis did not yield any evidence of the $\Xi_{cc}^{++} \to D^+ p K^- \pi^+$ decay within the data recorded in 2016 so, instead, the following branching fraction ratio upper limit is set

$$\frac{\mathcal{B}(\Xi_{cc}^{++} \to D^+ p K^- \pi^+)}{\mathcal{B}(\Xi_{cc}^{++} \to \Lambda_c^+ K^- \pi^+ \pi^+)} < 1.7\,(2.1) \times 10^{-2}$$

at the 90% (95%) confidence level and at the measured mass of the Ξ_{cc}^{++} particle from the $\Xi_{cc}^{++} \to \Lambda_c^+ K^- \pi^+ \pi^+$ analysis. No signal is observed in the mass range $3300-3800\,\text{MeV}/c^2$.

Additionally, a new multivariate-based trigger line was developed for reconstructing $\Xi_c^+ \to p K^- \pi^+$ decays at LHCb. The new trigger makes use of the Bonsai Boosted Decision Tree method and is designed with searches for doubly-charmed particles in mind. This trigger gives a 36% increase in the signal yield of potential Ξ_c^+ particles compared to an original trigger line that was designed for the similar purposes.

Aside from searches for doubly-charmed baryons, a short study is conducted into the calibration of the Ring Imaging Cherenkov (RICH) subdetectors at the LHCb detector. A method was successfully developed to obtain high momentum tracks without any knowledge of the magnetic field, which will be used in the future to test the hypothesis that the magnetic field is causing discrepancies seen between data and simulation for the RICH-1 Cherenkov angle resolution.

Acknowledgments

If someone had told me in the distant past that one day I would contribute to the discovery of a subatomic particle, I would never have believed them. It has been an amazing journey, filled with occasional lows but mostly brilliant highs, that has brought this about, and certainly a journey I would not have finished without the help from many others along the way. I would like to acknowledge these people now who have got me through to the completion of my research and this thesis.

First and foremost, a huge thank you to my excellent supervisors Paul Soler and Lars Eklund for guiding me through the difficult but extremely rewarding world of academia and for giving me the opportunity to undertake this PhD adventure in the first place. The help and advice you have both given me over the last few years has been nothing short of incredible so I owe you both a great deal of gratitude. It has been a pleasure working with you both and I hope we will stay in touch.

A special mention then has to go to Patrick Spradlin, who really introduced me to doubly-charmed-baryon research and who helped answer many of my trivial questions, especially in the early days of my studies. I have always admired your passion and integrity for research Patrick and I certainly would not have completed this PhD without your immense knowledge of charm physics that you bestowed on me, so thank you.

I would also like to take the time to recognise some of the other members of the LHCb collaboration, whom I worked with. To Ao Xu, thank you for your very insightful and helpful discussions during our time together. Your work rate and commitment is something to be commended and you certainly pushed me to new levels just to keep pace with you. To Jibo, Mat, Yanxi and Zhenwei, thanks for the time and effort you have given me over the years to help me understand some of the more complex parts of my analyses; I really appreciated it. My thanks also to all at the Charm Working Group for providing a stimulating and productive environment in which to work. To my fellow simulation liaisons; Kevin and Tommasso, many thanks for all their work in helping process the countless number of MC requests. A fews beers at R1 were always richly deserved after those days. Thanks to Antonis, Mike and Silvia of the RICH team for giving me the chance to make a meaningful contribution to the operations of RICH sub-detectors during data taking and then particularly Chris Jones for your patience and assistance during my software studies. An additional thank you must go to Silvia

Gambetta for giving me the opportunity to visit the LHCb cavern on my last day on LTA to cap a great 18 months living and working in France and Switzerland.

At CERN, I was fortunate to make some great friends, particularly through skiing; those trips away, carving down some of the best slopes in Europe, with all of you were some of the most fun days of my life. A particular heartfelt thank you to all those who came along for the 2018 LTA Ski Trip that I organised to Val Thorens, making it such a fun week; Team Jäger will never die even though my liver likely did that week. Also a big thank you to Alan, Shane and the CERN running club for some much needed accompanied runs that always helped me relax after work. Of course, a thanks are in order for Ladam and the Brozsons; David, Fenton, Jenny and Rob for the memories of that amazing month we spent navigating America after the Fermilab summer school. I am still not sure how we survived that trip.

Back at Glasgow, I would also like to thank all the members of the particle physics group for treating me so nicely from day one. It has been a pleasure working and socialising with you all. A special shout to Cameron Dean for all his help over the years, especially for his gift of the Cameron Dean Coffee Machine; there can be no doubt that the writing of this thesis would not have been completed without the lovely nectar that it provided. I want to say the very best of luck to all the current LHCb students; David, Dana, George and Lauren, for the rest of their PhD studies. I particularly look forward to hearing about the progress made by Dana as she carries the doubly-charmed flag forward for Glasgow; I have my fingers crossed her hard work will lead to some exciting results.

Finally, I would like to show my appreciation for Lisa and my family for their never-ever ending support. To Lisa, I really cannot thank you enough. You were always around to listen to me and help me out with any troubles that came my way, and this is despite my “12 month” stay in Geneva. You will forever remain the best discovery from my PhD studies. To Ron, Sarah and not forgetting Freddie, whose presence may have actually delayed the write up of this thesis, thank you for always believing in me; this was the impression I got from the questions asking me when I was getting a real job anyway. Lastly, and most importantly, I want to thank my parents; my mum, Elaine, without her love (and bottomless fridge), I would not be where I am today. She has given me every opportunity in life, which I am eternally grateful for; and, finally, my late father Andrew, who would jokingly, yet proudly, call me Einstein, I wish you were around to see me complete this journey. This thesis is dedicated to my parents.

Declaration

The research results presented in this thesis are the product of my own work. Appropriate references are provided when the results of third parties are mentioned. The research presented here was not submitted for another degree in any other department or university.

– Murdo Traill

Preface

This thesis documents the work carried out by the PhD candidate, within the LHCb collaboration, in primarily searching for doubly-charmed baryons using the proton-proton collision data collected by the LHCb detector in 2016. The thesis also details the candidate's design of a new multivariate-based trigger line, now in use at LHCb, as well as a feasibility study involving the RICH sub-detectors.

Chapter 1 reviews the theory behind the properties and decays of doubly-charmed baryons. This chapter includes a review of the current best theory of particle physics, the Standard Model, then an overview of the quark model and flavour physics and, in particular, a discussion on the weak decays of hadrons. The chapter concludes with a detailed description of the theoretical and experimental status of doubly-charmed baryons prior to the research mentioned in this thesis. The PhD candidate did not contribute to any of the work discussed in this chapter.

Chapter 2 describes the design and operations of the Large Hadron Collider beauty (LHCb) detector. The systems that make LHCb an excellent laboratory to search for doubly-charmed baryons are described in detail. The chapter ends with a brief description of the data processing work-flow at LHCb and an explanation of how data is simulated at LHCb. The PhD candidate did not contribute to the construction or design of the LHCb detector, which was built before they joined the collaboration, but they did contribute to the operation of the detector in 2017 and 2018. This chapter is included because this detector records the data that are used in the analyses described in this thesis. The chapter is based on information from the LHCb design and performance papers.

Chapter 3 presents a study carried out by the PhD candidate to measure the angular resolution of Cherenkov radiation, light that is given off by particles crossing through the RICH sub-detectors, when no magnetic field is present. The Cherenkov angle resolution of RICH-1 is known to be different in data and simulation; one possible reason for this is explored in this chapter. The PhD candidate performed the study by adapting the software primarily written by Dr Chris Jones from the University of Cambridge.

Chapter 4 describes an analysis of $\Xi_{cc}^{++} \to \Lambda_c^+ K^- \pi^+ \pi^+$ decays reconstructed from data recorded at LHCb. The research was conducted by the PhD candidate in partnership with colleagues from the University of Glasgow (Prof. Paul Soler and Dr Patrick Spradlin), the Laboratoire de l'Accélérateur Linéaire (Dr Yanxi Zhang) and Tsinghua University

(Mr Ao Xu and Prof. Zhenwei Yang). The chapter gives a full account of the selection of the data that the PhD candidate, alongside Mr Ao Xu, performed, as well as the background studies checked by the candidate for this decay mode. Only a summary of the studies related to the mass measurement is given, since the PhD candidate did not contribute significantly in this area, with the majority of this work carried out by Dr Yanxi Zhang. The work ultimately led to the first-ever discovery of a doubly-charmed baryon, namely the Ξ_{cc}^{++} state, accompanied by a measurement of its invariant mass.

Chapter 5 presents the main contribution by the PhD candidate to this thesis. The chapter describes a first-ever search for $\Xi_{cc}^{++} \to D^+ p K^- \pi^+$ decays at LHCb. The layout of the chapter follows similarly to Chapter 4 but with more details given on the background and mass measurement studies to reflect the greater contribution by the PhD candidate. Ultimately, no signal is found in this search channel. Therefore, the chapter proceeds to explain the way in which an upper limit can be set on the ratio of the branching fractions between the $\Xi_{cc}^{++} \to \Lambda_c^+ K^- \pi^+ \pi^+$ and $\Xi_{cc}^{++} \to D^+ p K^- \pi^+$ decay modes, before it discloses the value of this limit. All the work detailed in this chapter was carried out and implemented by the PhD candidate in consultation with Prof. Lars Eklund, Prof. Paul Soler and Dr Patrick Spradlin, all of the University of Glasgow.

Chapter 6 is dedicated to the design of a new trigger line that was developed by the PhD candidate for reconstructing $\Xi_c^+ \to p K^- \pi^+$ decays. The design, testing and performance of this trigger line are described in this chapter. In keeping with the main goal of this thesis, the new trigger line is made to be sensitive to searches of doubly-charmed baryons. The trigger line was deployed for data taking in July 2018 and the initial results showed a significant increase in the signal yield of Ξ_c^+ particles. The work presented in this chapter is solely carried out by the PhD candidate with guidance from Prof. Jibo He and Dr Patrick Spradlin.

Chapter 7 summarises the results of all the candidate's work and states the experimental status of doubly-charmed baryons at the time this thesis was completed. The author's subjective outlook on this type of research is also imparted to the reader.

Contents

Abstract **I**

Acknowledgments **II**

Declaration **IV**

Preface **V**

Contents **VII**

List of Figures **XI**

List of Tables **XV**

1 Introduction and Theory **1**

1.1 The Standard Model . . . 2

1.1.1 The Elementary Particles . . . 2

1.1.2 SM Mathematical Formalism . . . 6

1.2 Quarks and Hadron Spectroscopy . . . 8

1.2.1 The Quark Model . . . 9

1.2.2 Quantum Chromodynamics . . . 12

1.2.3 QCD Methods . . . 14

1.3 Hadronic Weak Decays . . . 16

1.3.1 Quark Mixing . . . 16

1.3.2 The CKM Matrix . . . 18

1.3.3 Electroweak Quark Sector . . . 19

1.4 Doubly Charmed Baryons . . . 21

1.4.1 Theoretical Properties . . . 21

1.4.2 Search Modes . . . 24

1.4.3 Past Experimental Searches . . . 26

1.5 Chapter Summary . . . 28

2 The LHCb Detector **29**

2.1 The Large Hadron Collider . . . 29

2.2 The LHCb Detector . . . 32

2.3 Tracking . . . 34
2.3.1 Vertex Locator . . . 36
2.3.2 Tracking Detectors . . . 39
2.3.3 Spectrometer Magnet . . . 42
2.4 Particle Identification . . . 44
2.4.1 Ring Imaging Cherenkov Detectors . . . 44
2.4.2 Calorimeter System . . . 48
2.4.3 Muon System . . . 51
2.5 Triggering at LHCb . . . 53
2.5.1 Level-0 Trigger . . . 54
2.5.2 High Level Trigger . . . 55
2.6 Offline Processing of Data . . . 57
2.7 Simulation of Data . . . 58
2.8 Chapter Summary . . . 59

3 RICH Magnetic Field Studies 60
3.1 Introduction . . . 60
3.1.1 Hybrid Photon Detectors . . . 61
3.1.2 Magnetic Distortion Correction System . . . 62
3.2 Cherenkov Angle Resolution . . . 64
3.3 Magnet-Off Studies . . . 66
3.4 Results and Discussion . . . 67
3.5 Chapter Summary . . . 70

4 Observation of $\Xi_{cc}^{++} \to \Lambda_c^+ K^- \pi^+ \pi^+$ 72
4.1 Analysis Strategy . . . 73
4.2 Data Samples . . . 74
4.2.1 LHCb Data . . . 74
4.2.2 Simulation . . . 75
4.3 Candidate Selection . . . 75
4.3.1 Overview . . . 75
4.3.2 Trigger Selection . . . 77
4.3.3 MC Sample Setup . . . 79
4.3.4 Offline Processing and Preselection . . . 81
4.3.5 Multivariate Selection . . . 82
4.3.6 Rejection of Specific Backgrounds . . . 90
4.4 Background Studies . . . 94
4.4.1 Λ_c^+ Background . . . 95
4.4.2 Multiple Candidates . . . 95

4.4.3 Misidentified Background . . . 97
4.5 Mass Measurement Studies . . . 100
4.5.1 Mass Models . . . 100
4.5.2 Systematic Uncertainties . . . 103
4.6 Results . . . 105
4.6.1 Mass Distributions . . . 105
4.6.2 Resonant Structures . . . 110
4.6.3 Lifetime Checks . . . 110
4.6.4 Conclusion and Discussion . . . 112
4.7 Chapter Summary . . . 113

5 Searches for $\Xi_{cc}^{++} \to D^+ p K^- \pi^+$ 115
5.1 Analysis Strategy . . . 116
5.2 Data Samples . . . 118
5.2.1 LHCb Data . . . 118
5.2.2 Simulation . . . 118
5.3 Candidate Selection . . . 119
5.3.1 Overview . . . 120
5.3.2 Trigger Selection . . . 122
5.3.3 MC Sample Setup . . . 125
5.3.4 Offline Processing and Preselection . . . 126
5.3.5 Multivariate Selection . . . 127
5.3.6 Rejection of Specific Backgrounds . . . 134
5.4 Background Studies . . . 139
5.4.1 D^+ Background . . . 140
5.4.2 Sub-decay Structures . . . 142
5.4.3 Multiple Candidates . . . 143
5.4.4 Misidentified Background . . . 145
5.5 Mass Measurement Studies . . . 149
5.5.1 Mass Models . . . 149
5.5.2 Momentum Scaling Calibration . . . 152
5.5.3 Bias of the D^+ Mass . . . 153
5.5.4 Bias of the Ξ_{cc}^{++} Mass . . . 154
5.5.5 Uncertainty on the D^+ Mass . . . 154
5.5.6 Final State Radiation . . . 155
5.5.7 Stability with respect to MVA Selection . . . 157
5.6 Mass Distributions . . . 159
5.7 Ratio of Branching Fractions . . . 162

5.7.1 Normalisation Yield . . . 163
5.7.2 Signal Remodelling . . . 163
5.7.3 Efficiencies . . . 165
5.7.4 Systematic Uncertainties . . . 167
5.7.5 Upper Limits . . . 171
5.7.6 Summary of Branching Fraction Ratio Measurement . . . 172
5.7.7 Conclusion and Discussion . . . 173
5.8 Chapter Summary . . . 174

6 Charm Baryon Trigger Studies 175
6.1 Introduction and Motivation . . . 175
6.2 Technicalities . . . 176
6.2.1 Turbo Streams . . . 176
6.2.2 Bonsai Boosted Decision Tree . . . 177
6.3 Trigger Development . . . 178
6.3.1 Data Samples . . . 179
6.3.2 Preselection . . . 180
6.3.3 Multivariate Selection . . . 180
6.3.4 Optimisation and Performance . . . 183
6.4 Mass Distributions . . . 187
6.5 Conclusion and Discussion . . . 189
6.6 Chapter Summary . . . 189

7 Conclusion 190
7.1 Summary . . . 190
7.2 Outlook . . . 192

Appendix A Biases from Turbo Processing 194

Appendix B $\Xi_{cc}^{++} \to \Lambda_c^+ K^- \pi^+ \pi^+$ Run I Analysis 198
B.1 Data and MC Samples . . . 198
B.2 Selection . . . 198

Appendix C PID Calibrations with PIDCalib 205

Appendix D Efficiencies in Phase Space 207

Bibliography 211

List of Figures

1.1 $SU(4)$ baryons . . . 11
1.2 Feynman diagrams and rules for QCD interactions . . . 15
1.3 Baryon masses from Lattice QCD . . . 17
1.4 Quark lifetime diagrams of doubly-charmed baryons . . . 22
1.5 Feynman diagrams of cc di-quark production in hadronic collisions . . . 23
1.6 Feynman diagrams for $\Xi_{cc}^{++} \to \Lambda_c^+ K^- \pi^+ \pi^+$ . . . 26
1.7 Feynman diagrams for $\Xi_{cc}^{++} \to D^+ p K^- \pi^+$ . . . 26
1.8 SELEX search results for the Ξ_{cc}^+ baryon . . . 27
1.9 LHCb search results for the Ξ_{cc}^+ baryon . . . 28

2.1 CERN accelerator complex . . . 31
2.2 $b\bar{b}$ angular production at LHCb . . . 32
2.3 Geometry of the LHCb detector . . . 33
2.4 Instantaneous luminosity versus time . . . 35
2.5 Integrated luminosity for data-taking years at LHCb . . . 35
2.6 VELO layout and support system . . . 37
2.7 VELO modules and sensors . . . 38
2.8 Micro-strips on VELO module . . . 38
2.9 Performance of the VELO subdetector . . . 39
2.10 Tracking system . . . 40
2.11 Tracker Turicensis . . . 41
2.12 Inner Tracker . . . 42
2.13 Schematic of the magnet . . . 43
2.14 Cherenkov angle versus momentum . . . 45
2.15 Schematic of the RICH subdetectors . . . 46
2.16 RICH event display example . . . 47
2.17 Kaon identification efficiency versus momentum . . . 48
2.18 Calorimeters segmentation . . . 50
2.19 Illustration of HCAL module . . . 50
2.20 Side view of muon system . . . 52
2.21 Muon identification and misidentification rates . . . 54
2.22 Overview of LHCb trigger system . . . 56
2.23 LHCb data flow in Run II . . . 58

3.1 Schematic of a Hybrid Photon Detector . . . 62

3.2 Photograph of the Magnetic Distortion Calibration System 63
3.3 Illustration of a Cherenkov radiation cone 64
3.4 Cherenkov angle resolution distributions in a non-zero magnetic field . . 65
3.5 Cherenkov angle resolution distributions from data 68
3.6 Cherenkov angle resolution distributions from simulation 70

4.1 Topology of $\Xi_{cc}^{++} \to \Lambda_c^+ K^- \pi^+ \pi^+$ 76
4.2 Signal and background correlation matrices 85
4.3 Distributions of training variables used in multivariate 86
4.4 Signal-background retention rate curve 87
4.5 Normalised response output from multivariate classifiers 88
4.6 Punzi figure of merit versus multivariate response 89
4.7 Dependency of multivariate selection on mass 90
4.8 Dependency of Punzi figure of merit on lifetime 91
4.9 Distribution of opening angles between same-charged tracks 92
4.10 Invariant-mass distribution of clone candidates 93
4.11 Invariant-mass distribution of duplicate candidates 94
4.12 Invariant-mass distribution of Λ_c^+ candidates 96
4.13 Invariant-mass distributions of Ξ_{cc}^{++} candidates in set Λ_c^+ mass regions . . 96
4.14 Invariant-mass distributions of multiple Ξ_{cc}^{++} candidate events 98
4.15 Invariant-mass distributions of reflection background 99
4.16 Invariant-mass distributions of Ξ_{cc}^{++} candidates within reflection regions . 99
4.17 Invariant-mass distributions of Ξ_{cc}^{++} candidates versus PID requirements 100
4.18 Invariant-mass distribution of signal in simulation with fit 102
4.19 Invariant-mass distributions of combinatorial background with fit 103
4.20 Comparison of invariant-mass distributions in data and control modes . . 106
4.21 Invariant-mass distribution of signal found in 2016 data 107
4.22 Relationship between invariant mass of Ξ_{cc}^{++} and Λ_c^+ candidates 107
4.23 Invariant-mass distributions of Ξ_{cc}^{++} candidates in 2012 data sets with fit 108
4.24 Possible resonance structures in 2016 data 111
4.25 Invariant-mass distributions following tighter decay-time requirements . . 111
4.26 Decay-time distributions of Ξ_{cc}^{++} candidates in data and simulation . . . 112

5.1 Invariant-mass distributions of charm decays from LHCb trigger 116
5.2 Comparison of p_T spectrum in data and simulation 119
5.3 Topology of $\Xi_{cc}^{++} \to D^+ p K^- \pi^+$ 121
5.4 Invariant-mass distribution of D^+ candidates from Turbo 125

5.5 Invariant-mass distribution of different category events in simulation . . . 126
5.6 Invariant-mass distribution of Ξ_{cc}^{++} candidates in mass sidebands 128
5.7 Distributions of training variables used in multivariate 130
5.8 Signal and background correlation matrices 131
5.9 Signal-background retention rate curves 132
5.10 Punzi figure of merit and multivariate-response distributions 133
5.11 Dependency of multivariate selection on mass 134
5.12 Dependency of Punzi figure of merit on PID requirements 135
5.13 Distribution of opening angles between same-charged tracks 137
5.14 Invariant-mass distribution of clone candidates 137
5.15 Ghost-probability distributions of final-state tracks 138
5.16 Invariant-mass distribution of duplicate candidates 139
5.17 Invariant-mass distributions of D^+ candidates 141
5.18 Invariant-mass distribution of Ξ_{cc}^{++} candidates in set D^+ mass regions . . 141
5.19 Invariant-mass distribution of partial decay products in WSP data 143
5.20 Invariant-mass distribution of partial decay products in WSM data . . . 144
5.21 Invariant-mass distribution of resonance regions in WSP data 145
5.22 Invariant-mass distribution of resonance regions in WSM data 146
5.23 Invariant-mass distributions of multiple Ξ_{cc}^{++} candidates events 146
5.24 Invariant-mass distributions of reflection backgrounds 147
5.25 Invariant-mass distributions of Ξ_{cc}^{++} candidates within reflection regions . 148
5.26 Invariant-mass distributions of Ξ_{cc}^{++} candidates versus PID requirements 148
5.27 Invariant-mass distribution of signal in simulation with fit 150
5.28 Invariant-mass distributions of combinatorial background with fit 152
5.29 Change in mass after momentum scaling correction 153
5.30 Bias of the measured mass as a function of lifetime 155
5.31 Change in the Ξ_{cc}^{++} mass versus the change in D^+ mass 156
5.32 Effects of final-state radiation on measured Ξ_{cc}^{++} mass 157
5.33 Change in the Ξ_{cc}^{++} mass as function of the multivariate selection 158
5.34 Invariant-mass distribution of D^+ candidates in data 159
5.35 Comparison of invariant-mass distributions in data and control modes . . 160
5.36 Invariant-mass distribution of Ξ_{cc}^{++} candidates in data 161
5.37 Local p-value from $\Xi_{cc}^{++} \to D^+ pK^-\pi^+$ mass distribution 161
5.38 Normalisation yield in $\Xi_{cc}^{++} \to \Lambda_c^+ K^-\pi^+\pi^+$ channel 164
5.39 Comparison p_T distributions of $\Xi_{cc}^{++} \to D^+ pK^-\pi^+$ data and simulation . 164
5.40 p_T correction factors for simulated events 165

5.41 Confidence level scores versus assumed ratio of branching fractions 172

6.1 A comparison of the different Turbo streams at LHCb 177
6.2 Comparison of training variables in signal and background 184
6.3 Discretised training variables used to train multivariate classifier 185
6.4 Correlation matrices for training variables in signal and background . . . 185
6.5 Response distribution for multivariate in $\Xi_c^+ \to pK^-\pi^+$ trigger 186
6.6 Performance of cut-based and multivariate-based $\Xi_c^+ \to pK^-\pi^+$ trigger . 188

A.1 Overview of momentum-scaling-correction factors 195
A.2 Λ_c^+ mass-biasing effects due to Turbo requirements 196
A.3 Momentum-scaling-correction factors after lifetime corrections 197

B.1 Signal and background correlation matrices in Run I data samples 201
B.2 Signal-background retention rate curves in Run I data samples 202
B.3 Response curves from multivariate classifier with tight preselection 202
B.4 Response curves from multivariate classifier with loose preselection 203
B.5 Punzi figure of merit versus multivariate response 204

C.1 Two-dimensional binning distributions for PIDCalib 206

D.1 Invariant-mass combinations in $\Xi_{cc}^{++} \to D^+pK^-\pi^+$ data and simulation . 208
D.2 Invariant-mass combinations in $\Xi_{cc}^{++} \to \Lambda_c^+K^-\pi^+\pi^+$ data and simulation 209
D.3 The ratio of efficiencies for potential resonances in simulation 210

List of Tables

1.1 The leptons of the Standard Model . . . 3
1.2 The quarks of the Standard Model . . . 4
1.3 The bosons of the Standard Model . . . 6
1.4 Properties of doubly-charmed baryons . . . 24
1.5 Promising search modes of doubly-charmed baryons . . . 25

3.1 Cherenkov angle resolution values from simulation . . . 69

4.1 HLT1 trigger requirements for Ξ_{cc}^{++} searches . . . 78
4.2 HLT2 trigger requirements for $\Xi_{cc}^{++} \to \Lambda_c^+ K^- \pi^+ \pi^+$ . . . 80
4.3 Preselection requirements for $\Xi_{cc}^{++} \to \Lambda_c^+ K^- \pi^+ \pi^+$ . . . 82
4.4 Multivariate training variables for $\Xi_{cc}^{++} \to \Lambda_c^+ K^- \pi^+ \pi^+$ . . . 84
4.5 Optimised requirement for different multivariate classifiers . . . 89
4.6 Mass model parameter value from fit to simulation . . . 103
4.7 Systematic uncertainties related to mass measurement . . . 109

5.1 HLT2 trigger requirements for $\Xi_{cc}^{++} \to D^+ p K^- \pi^+$ . . . 124
5.2 Preselection requirements for $\Xi_{cc}^{++} \to D^+ p K^- \pi^+$ . . . 127
5.3 Multivariate training variables for $\Xi_{cc}^{++} \to D^+ p K^- \pi^+$ . . . 131
5.4 Optimised requirement for different multivariate classifiers . . . 133
5.5 Mass model parameter value from fit to simulation . . . 151
5.6 Systematic uncertainties related to mass measurement . . . 158
5.7 Analysis efficiencies for selecting Ξ_{cc}^{++} decays . . . 168
5.8 Uncertainties associated to single-event-sensitivity parameter . . . 170

6.1 Selection criteria of cut-based $\Xi_c^+ \to p K^- \pi^+$ trigger . . . 181
6.2 Selection criteria of multivariate $\Xi_c^+ \to p K^- \pi^+$ trigger . . . 181
6.3 Sources of signal $\Xi_c^+ \to p K^- \pi^+$ decays for BBDT training . . . 182
6.4 Sources of Ξ_c^+ baryons for trigger training . . . 182
6.5 Binning schemes of the discretised training variables in Ξ_c^+ trigger . . . 183
6.6 Rates and efficiencies of different $\Xi_c^+ \to p K^- \pi^+$ trigger configurations . . . 187
6.7 Signal qualities of Ξ_c^+ candidates from $\Xi_c^+ \to p K^- \pi^+$ triggers . . . 187

B.1 Stripping requirements for $\Xi_{cc}^{++} \to \Lambda_c^+ K^- \pi^+ \pi^+$ . . . 200
B.2 Optimised requirement for different multivariate classifiers in Run I . . . 204

C.1 Binning scheme for PID calibration . . . 205

Chapter 1

Introduction and Theory

> "We are driven by the usual insatiable curiosity of the scientist, and our work is a delightful game."
>
> – Murray Gell-Mann, inventor of the Quark Model

The research encapsulated in this thesis was motivated by the mystery of the undiscovered and the profound sense that something must exist, it just needs to be found. Similarly to the famous Higgs boson that eluded physicists for decades, the group of particles known as doubly-charmed baryons had for so long been predicted, yet, were unconfirmed experimentally. Apart from being unique systems for studying the strong interaction, the very same force that holds protons and hence you, me and the paper this thesis is printed on, together, doubly-charmed baryons should and need to exist; human curiosity alone should motivate a search for them.

If one were to look for such creatures of the particle world, there can be no better hunting ground than that of the LHCb detector, the topic of Chapter 2 of this thesis. With its outstanding vertex reconstruction, supreme particle identification capabilities and excellent mass resolution, the data sets recorded and provided by this machine are primed for searches of doubly-charmed baryons. To this end, a series of searches is carried out for one specific doubly-charmed baryon using some of the largest data sets available at the time from the LHCb detector.

Before the complete details of these analyses are presented in Chapters 4 and 5, the relevant theoretical literature on doubly-charmed baryons is reviewed and the history of past searches for these types of particles is also discussed. To achieve this, firstly, the highly successful Standard Model, which underpins all of modern particle physics, is introduced to the reader in Section 1.1, before the chapter builds up to explain the origin of doubly-charmed baryons in Section 1.2 and the fundamentals of their decay in Section 1.3. The chapter concludes with an overview of the predicted properties and experimental status of doubly-charmed baryon, as it was before any of the work discussed in this thesis had started, in Section 1.4.

1.1 The Standard Model

Particle physics is a study of the most basic building blocks of nature, the so-called elementary particles that exist down at the unimaginably smallest scales, around 10^{-19} m according to some recent measurements [1]. These subatomic particles and their interactions with each other fundamentally shape the universe that is observed today. When this field of research began, there was just a handful of particles, the first being J.J Thompson's electron discovered in 1887. Since then, the advancement of cosmic ray science and, more importantly, the introduction of particle accelerators has unveiled numerous more particles and phenomena that soon made it apparent that not all particles are elementary.

To bring clarity to the situation, a rigorous mathematical framework was developed in the later half of the 20^{th} century. This theoretical construction has come to be known as the Standard Model (SM) of particle physics and it is arguably one of the most successful theories in science [2]. Indeed, almost all results in particle physics to date have agreed with SM predictions to an unprecedented accuracy; however, it is not without its limitations and discrepancies with experiment. In this section, the particles and interactions described by the SM are outlined, while the formalism of the SM is also reviewed.

1.1.1 The Elementary Particles

Today, physicists know that the world is fundamentally made up of seventeen particles that come in three forms referred to as quarks, leptons and bosons. A somewhat concise overview of all the elementary particles is presented in this section in order to give the reader just a general sense of their properties and functions.

The first feature of elementary particles to know about is that they are generally characterised by quantum numbers. These are attributes that include the perhaps more familiar property of electric charge, as well as the more abstract quantity 'spin', best described as the intrinsic angular momentum of a particle. Elementary particles are grouped by physicists into two broad categories due to this spin quantity. They either reside in the family of fermions that have half-integer spin or with bosons that have whole-integer spin. Unlike bosons, fermions obey the Pauli exclusion principle [3], which states that no two identical fermions can be in the same quantum state. This important physical law has far reaching implications in terms of what fermions and bosons represent and do in nature. The last important point to note at this stage, is that all fundamental particles have a corresponding anti-particle that has the same mass but opposite quantum numbers. Anti-particles will not be discussed in great detail in this thesis as they are treated equally to particles in the studies of doubly-charmed baryons.

Lepton	Generation	Mass (MeV/c^2)	Electric Charge	e No.	μ No.	τ No.
Electron, e	I	0.511	-1	$+1$	0	0
Electron neutrino, ν_{e}		$< 2 \times 10^{-6}$	0	$+1$	0	0
Muon, μ	II	105.66	-1	0	$+1$	0
Muon neutrino, ν_{μ}		< 0.9	0	0	$+1$	0
Tau, τ	III	1776.86 ± 0.12	-1	0	0	$+1$
Tau neutrino, ν_{τ}		< 18.2	0	0	0	$+1$

Table 1.1: Lepton content of the Standard Model with all the values taken from the Particle Data Group [1]. The spin of all leptons is equal to $\frac{1}{2}$. The e, μ and τ numbers denote the flavour quantum numbers.

Fermions

Fermions form the basis of all visible matter in the universe, which, on a side note, actually only accounts for around 5% of the mass in the entire universe [4].[1] Fermions themselves can be divided into two subgroups called quarks and leptons. Both quarks and leptons happen to come in sets of threes, referred to as a generation, where each member of a generation is identical apart from in mass. The reason for this almost cloning-like effect of quarks and leptons in generations is however not understood.

Focusing now on the lepton family, each generation has a charged and neutral particle. They are the well known electron (e) and the heavier muon (μ) and tau (τ) leptons, all of which have a negative electric charge of -1. Their neutral and near massless counterparts are referred to as the electron neutrino (ν_{e}), muon neutrino (ν_{μ}) and tau neutrino (ν_{τ}). The ν_{τ} neutrino was only discovered as recently as 2000 by the DONUT collaboration [5]. As an added point of interest, there exists the possibility that neutrinos are themselves their own anti-particle, existing as Majorana fermions [6], but this hypothesis has not been proven experimentally. Beyond spin and electric charge, leptons also carry a 'flavour' quantum number that is associated to the generation in which they exist. Lepton flavour is found to be conserved in all interactions except in neutrino oscillations, the very phenomenon that led to the discovery that neutrinos have mass [7]. Nevertheless, all calculations in the SM are performed assuming neutrinos are massless. This approximation is sensible given that the set upper limits on the masses of neutrinos are much smaller than the masses of other SM particles. A summary of the masses and previously discussed quantum numbers of the leptons is given in Table 1.1.

The rest of the fermion family is made up of the whimsically named quarks. Similarly to the way in which leptons manifest, there are two quarks in each generation, one with an

[1] Around 95% of the universe is thought to be comprised of dark matter and dark energy, the composition and existence of which is unexplained by the Standard Model [4].

Quark	Generation	Mass (MeV/c^2)	Electric Charge	I_3	C	S	T	B
Up, u	I	$2.2^{+0.5}_{-0.4}$	$+\frac{2}{3}$	$+\frac{1}{2}$	0	0	0	0
Down, d		$4.7^{+0.5}_{-0.3}$	$-\frac{1}{3}$	$-\frac{1}{2}$	0	0	0	0
Charm, c	II	$(1.28^{+0.03}_{-0.04}) \times 10^3$	$+\frac{2}{3}$	0	+1	0	0	0
Strange, s		95^{+9}_{-3}	$-\frac{1}{3}$	0	0	−1	0	0
Top, t	III	$(173.0 \pm 0.4) \times 10^3$	$+\frac{2}{3}$	0	0	0	+1	0
Bottom, b		$(4.18^{+0.04}_{-0.03}) \times 10^3$	$-\frac{1}{3}$	0	0	0	0	−1

Table 1.2: Quark content of the Standard Model with all the values taken from the Particle Data Group [1]. The spin of all quarks is equal to $\frac{1}{2}$ and each quark carries either red, green or blue colour charge. The I_3, C, S, T and B quantities denote the flavour quantum numbers.

electric charge of $+2/3$, while the other has an electric charge of $-1/3$. Quarks also carry the property of 'flavour' just like leptons. The positive electrically-charged quarks are known as the up (u), charm (c) and top (t) flavoured quarks and the negative electrically-charged quarks are called the down (d), strange (s) and bottom (b) flavoured quarks. Note that the b and t quarks are sometimes referred to as beauty and truth, respectively, by the more imaginative scientist. These flavour types are embodied by flavour quantum numbers. For historic reasons, the flavour quantum number for the u and d quarks is called isospin (I), while the I_3 quantity denotes the z component of the quark isospin. The remaining quantum numbers are rather amusingly called charm (C), strangeness (S), topness (T) and bottomness (B). The flavour numbers are not strictly conserved by quarks, which makes the quark sector particularly interesting to study; more about this in Section 1.3.

The notable difference between quarks and leptons is that quarks carry a property known as 'colour' that comes in three forms, imaginatively coined red, green or blue, then anti-red, anti-green or anti-blue, for their anti-particle equivalent. Due to a process known as colour-confinement [8], states with non-neutral colour cannot exist freely as individual objects. This is to be discussed thoroughly in Section 1.2, where the protagonists of this thesis, the doubly-charmed baryons, will be introduced. A summary of the masses and the previously discussed quantum numbers of the quarks is given in Table 1.2.

Bosons

Quarks and leptons interact with one another via the four fundamental forces of nature, namely: electromagnetism, the nuclear strong force, the nuclear weak force and gravity. The latter, gravity, is many orders of magnitude weaker than the other forces, so can be safely ignored at the energy scales used in SM calculations, which is convenient given the inability of the SM to explain gravity anyway.

However, electromagnetism and the two nuclear forces are described within the SM by the second main family of elementary particles, the integer spin bosons. According to the SM, the forces of nature are actually the result of fermions transferring momentum between each other through the exchange of bosons. Electrically charged particles, which include all the fermions, apart from the three neutrinos, interact with the electromagnetic force that is mediated by the light-bearing photon (γ). Since photons do not possess rest mass or charge, they do not readily interact with other photons [9] nor will they decay to other elementary particles. This gives the electromagnetic force its infinite working range, so much that its effects are felt on an every-day basis at the macroscopic scale.

The lesser-known nuclear weak force is responsible for the beta decay of radioactive particles, among other phenomena. This fundamental force is mediated by the electromagnetically charged $W^{\pm}$ bosons and also a neutral Z^0 boson, all of which are relatively large in mass compared to most other SM particles. Consequently, this force of nature only operates on a very short range of order 10^{-18} m [1] so, not surprisingly, its effects are not particularly felt at the energy and lengths scales that humans perceive. Furthermore, the $W^{\pm}$ and Z^0 bosons only interact with fermions that conform to specific conditions; the charged weak bosons only couple to left-handed particles, while the neutral weak boson interacts with both left and right-handed particles.[2]

Last but certainly not least, there exists the nuclear strong force which, as hinted by its name, is the most powerful of all the four fundamental forces. The nuclear strong force is mediated by bosons called gluons (g) that only interact with elementary particles that carry colour charge. Hence, gluons couple with all flavours of quarks but not with the leptons. Despite the gluon being massless, the range of the strong force is not infinite, like for the electromagnetic force, as the gluons themselves also carry colour charge. Thus, gluons can self-interact [8], which effectively limits the range of the strong force down to the scale of 10^{-15} m [1], by no coincidence the same size as the atomic nucleus, which the nuclear strong force is tasked with 'gluing' together. Recall that colour confinement means that quarks cannot exist freely as non-colour-neutral objects, and gluons are no different; they exist in nature as one of only eight possible colour-neutral states.

This leads to the last piece of the fundamental particle jigsaw, the aforementioned Higgs boson (H^0). The existence of a Higgs boson was born out of the need to explain the non-zero masses of the $W^{\pm}$ and Z^0 bosons, which were expected to be massless in the earliest formulations of the SM. To solve this problem, a scalar field was theorised to exist, where the the Higgs boson is the quantisation of this scalar field. Elementary particles would then interact with this field, causing the symmetry between the $W^{\pm}$

[2]If the spin of a particle is aligned with its momentum, the particle is referred to as right-handed, whereas if the two quantities are anti-parallel, the particle is referred to as left-handed. All points in between can be described as a superposition of left and right-handed.

Boson	Mass (GeV/c^2)	Electric Charge	Spin	I_3
Photon, γ	0	0	1	0
$W^{\pm}$	80.379 ± 0.012	±1	1	±1
Z^0	91.1876 ± 0.0021	0	1	0
Gluon, g	0	0	1	0
Higgs, H^0	125.18 ± 0.16	0	0	0

Table 1.3: Boson content of the Standard Model with all the values taken from the Particle Data Group [1]. The colour charge of the gluons can be one of eight possible colour-neutral combinations, whereas photons do not posses colour charge.

and Z^0 bosons to break, which in turn would give all SM particles their mass [10–12]. The massless nature of the gluon and photon is then eloquently explained by their non-interaction with the Higgs field. This incredibly crucial particle to the workings of the SM was found in 2012 by the ATLAS [13] and CMS collaborations [14] and completed the discovery of all elementary particles in the SM. The $W^{\pm}$ and Z^0 bosons were identified a few decades before the Higgs by the UA1 and UA2 experiments [15–17]. The discussed properties of all SM bosons are listed in Table 1.3.

1.1.2 SM Mathematical Formalism

The Standard Model is best described as a Quantum Field Theory [8] that obeys gauge symmetries, which gives the model its extraordinary predictive power. A very brief summary of these mathematical concepts is presented in this section.

Quantum Field Theory (QFT) is the combination of three pillars of physics: special relativity, classical field theory and quantum mechanics. In this framework, the elementary particles of Section 1.1.1 are represented as quanta of fields. Field in this case means a set of numbers assigned to a point in space and time and then quanta are the excited states of these fields. Symmetries, as mentioned above, then refers to a property of fields, where the physics and observables that the field describe, remain unchanged after applying a mathematical operation to all the fields in space and time. In this case, the term gauge then just means 'measure', such that a field with a gauge symmetry can be 're-measured' from different baselines without any properties of the system changing.

Standard Model bosons, which govern the fundamental forces of nature, can now be viewed as representations of a gauge group − a mathematical group of gauge symmetries. Gauge groups control the way in which gauge bosons exchange quantum numbers and, therefore, how they ultimately interact with other elementary particles. The gauge group chosen to describe each fundamental force is based on the results of experimental observation and is not self-contained within the Standard Model itself. It so happens that the

Special Unitary group of order n, $SU(n)$, describes an interaction with $(n^2 - 1)$ gauge bosons in the Standard Model. A mentioned before, the nuclear strong force is mediated by eight distinct gluon states and as such can be described by the $SU(3)$ group. Furthermore, the nuclear weak force governed by the W^+, W^- and Z^0 bosons, can be described by the $SU(2)$ group. As for electromagnetism with only one gauge boson, the photon, it is described well by the Unitary group, $U(1)$. The overall gauge theory of the Standard Model is thus described by $SU(3) \times SU(2) \times U(1)$. One of the great achievements underlining the SM was the realisation that the electromagnetic and nuclear weak force may be unified as one force, the electroweak force [18, 19].

Concentrating now more on the field theory side of QFT, the interactions between fundamental particles are described by interaction terms in the Lagrangian involving their corresponding fields. The Lagrangian, L, describes the dynamics of any general system. In classical mechanics it is defined as

$$L = T - V, \tag{1.1}$$

where the T and V terms are the total kinetic and potential energies of the system, respectively. The dynamics of the particles in the Standard Model can also be described in terms of Lagrangians. However, because elementary particles are treated as mathematical fields it is simpler to consider the Lagrangian field density, $\mathcal{L}$, instead, which is related to L by integration over the three spatial components of the system

$$L = \int \mathcal{L} d^3\vec{x}. \tag{1.2}$$

The dynamics of an elementary particle can then be calculated from substituting the Lagrangian density term $\mathcal{L}$ into the Euler−Lagrange equation

$$\frac{\partial \mathcal{L}}{\partial \psi} = \partial_\mu \left(\frac{\partial \mathcal{L}}{\partial(\partial_\mu \psi)} \right) = 0, \tag{1.3}$$

where ψ is the field representing the elementary particle and ∂_μ is the covariant derivative with the index μ running over all space-time coordinates. The Euler−Lagrange equation is a result of the principle of least action, which in the quantum world loosely means a particle will chose a path through time and space that minimises the action, $\mathcal{S}$, defined as

$$\mathcal{S} = \int \mathcal{L}(\psi, \partial_\mu \psi) d^\mu x. \tag{1.4}$$

This is conceptually important to remember for Section 1.2.3 when possible solutions to one type of quantum field theory are discussed.

A useful property of Lagrangians is that the dynamics of a system can be conveniently calculated from the summation of them when they describe the individual components of that total system. Hence, the total Lagrangian of the Standard Model can be simply expressed as

$$\mathcal{L}_{\text{SM}} = \mathcal{L}_{\text{Fermion Kinetic}} + \mathcal{L}_{\text{Boson Kinetic}} + \mathcal{L}_{\text{Higgs}} + \mathcal{L}_{\text{Yukawa}}, \tag{1.5}$$

where the kinetic terms of the fermions and bosons, $\mathcal{L}_{\text{Fermion Kinetic}}$ and $\mathcal{L}_{\text{Boson Kinetic}}$, respectively, have been separated out. The $\mathcal{L}_{\text{Yukawa}}$ term will be described in more detail in Section 1.3.3 but it is related to the masses of the fermions, while $\mathcal{L}_{\text{Higgs}}$ contains the interaction terms that give rise to the masses of gauge bosons.

The exact form of each $\mathcal{L}$ term in Equation 1.5 depends on the spin of the particle that it describes. For example, a non-interacting spin-half fermion with invariant mass, m, is represented by a Dirac spinor field, ψ, and its Lagrangian is given by

$$\mathcal{L} = \overline{\psi}\big(i\gamma^{\mu}\partial_{\mu} - m\big)\psi, \tag{1.6}$$

where γ^{μ} are the Dirac gamma matrices and $\overline{\psi}$ is a shorthand, used throughout this chapter, for the matrix multiplication of the object with γ^0, so $\psi^{\dagger}\gamma^0$ in this case. Contrarily, a non-interacting spin-one boson is represented by a vector field, A, and is described by the following Lagrangian

$$\mathcal{L} = -\frac{1}{4}F_{\mu\nu}F^{\mu\nu}, \tag{1.7}$$

where $F_{\mu\nu}$ is the strength of the vector field A, defined as $F_{\mu\nu} \equiv \partial_{\mu}A_{\nu} - \partial_{\nu}A_{\mu}$. For instance, A can represent the photon field and if Equation 1.7 is substituted into Equation 1.3, then Maxwell's equations of electromagnetism fall out. Since the Higgs boson is a scalar however, see Table 1.3, it cannot be described by the Lagrangian stated in Equation 1.7.

1.2 Quarks and Hadron Spectroscopy

The plethora of new particles observed at high-energy particle accelerator experiments were not understood overnight. It took the effort of several physicists over many years to arrive at the neat categorisation of elementary particles that was described in the last section. It was a particularly laborious task trying to make sense of the quark sector where colour-confinement meant quarks never existed freely.

This section firstly explains the origin of the quark model and the properties of objects resulting from combinations of quarks, of which are now known as hadrons. The

theory of the nuclear strong force, the fundamental interaction that binds hadrons together, is also described as a prelude to the phenomenology of doubly-charmed baryons that is discussed in Section 1.4.

1.2.1 The Quark Model

By the middle of the 20th century, a new paradigm was needed to explain the never-ending arrival of new particles that were being found in experiments. The first step towards a clearer picture was the introduction of the particle property known as strangeness (S), which was previously mentioned in Section 1.1.1. This concept was independently proposed by Gell-Mann [20] and Nishijima [21], both in 1953, to explain the 'strange' long-lived nature of new states that was not in keeping with their large mass. The idea eventually led to Gell-Mann's Eightfold Way [22], a classification method described by the $SU(3)$ mathematical group. In this scheme, particles that were known to interact with a then theorised form of the nuclear strong force (required to keep the atomic nucleus from splitting) were divided into subgroups by mass and then by spin. When the strangeness of these two groups of particles were plotted against their electric charge, patterns representing an octet and a decuplet appeared, see Figure 1.1. This hinted at an underlying symmetry of the strong interaction. Although, it soon became apparent that $SU(3)$ symmetry is actually only an approximate symmetry; the reason, unknown at the time, was that the different masses of these particles and their weak interactions were breaking the symmetry.

However, one major success of the Eightfold Way was the prediction of a particle with $S = -3$ that appeared in Gell-Mann's decuplet representation but which had not been experimentally found. In 1964, this predicted state, the Ω^- particle, was discovered at the Brookhaven Laboratory with a measured mass in alignment with that predicted by the Eightfold Way [23]. This ultimately made Gell-Man suspect that the true mathematical group describing these particles had a fundamental triplet representation, which would correspond to the real elementary particles. These came to be known as the low-mass u, d and s flavoured quarks.

The discovery of the Ω^- particle also introduced a problem however, because on first viewing, it appeared to violate the Pauli exclusion principle with its three identical s quarks. This was resolved, shortly after the Ω^- discovery, by the introduction of colour charge [24] that allowed each s quark to exhibit a unique quantum state. With the later discoveries of the heavier quarks: the c quark in 1974 detailed in the revolutionary J/ψ papers [25, 26]; the b quark in 1978 through the Υ resonance [27]; and, finally, the t quark in 1995 via its decay that was observed at the CDF [28] and D$\emptyset$ detectors [29], the quark model of particle physics became universally accepted. The first direct evidence

for a quark came from deep inelastic experiments at SLAC in 1968 [30, 31], before this quarks were considered merely mathematical abstractions.

Baryons

Fast forward to present day and the quark model is well established; colour confinement dictates that quarks bind together, or 'hadronise', to form colour-neutral hadrons and that there are two commonly accepted configurations of hadrons. Firstly, a quark, q, and an anti-quark, $\bar{q}$, can combine to form a $q\bar{q}$ state whereby the colour charges are equal and opposite; this system is referred to as a 'meson'. Secondly, three quarks may form a qqq state that collectively contains all the different colour charges and is thus said to be 'colourless' in the same way visible light is white from the combination of the red, green and blue wavelengths; this object is termed a 'baryon'. Note that the top quark, due to its relatively large mass (see Table 1.2), decays through the weak force before it is allowed to hadronise. The top quark is therefore never the constituent of any bound hadron.

The four lightest quarks (u, d, s and c) can be represented by the $SU(4)$ symmetry group. However, it should be pointed out that this symmetry is not a perfect one since the c quark is so much heavier than the other lightest quarks. By expressing the $SU(4)$ group as a tensor product and a direct sum of its bases

$$4 \otimes 4 \otimes 4 = 20 \oplus 20'_1 \oplus 20'_2 \oplus \bar{4}, \tag{1.8}$$

the configurations of the baryons can be seen to form three separate twentyplet patterns as well as one quartet. The baryons are split into these different twentyplet representations based on their spin-parity assignment, J^P, where J denotes the total angular momentum of the baryon, which is the angular momentum, l, of the quark-bound system plus the total spin, s, of each individual quark, while the P represents the parity quantum number that reflects the spatial coordinates of a particle. Depending on the orientation of the quark spins, the ground-state baryons, ones with no orbital angular momentum, either have a spin-parity assignment of $J^P = {}^1/_2^+$ ($\uparrow\downarrow\uparrow$) or $J^P = {}^3/_2^+$ ($\uparrow\uparrow\uparrow$), which are, respectively, the 20-plet and $20'_1$-plet shown in Figure 1.1. Gell-Mann's octet and decuplet of his Eightfold Way classification scheme form the bottom layers of these two twentyplets. In the bottom layer of the 20-plet diagram, the more familiar nucleons of the atom, the proton, $p(uud)$, and the neutron, $n(udd)$, with a spin-parity assignment of $J^P = {}^1/_2^+$ are shown. Note that they have no constituent charm quarks however. At this point in the chapter, the sought-after doubly-charmed baryons can now be properly defined. They are baryons composed of two charm quarks in combination with an additional third lighter quark and are represented by the Ξ_{cc} and Ω_{cc} states pictured in the $SU(4)$ twentyplets of Figure 1.1.

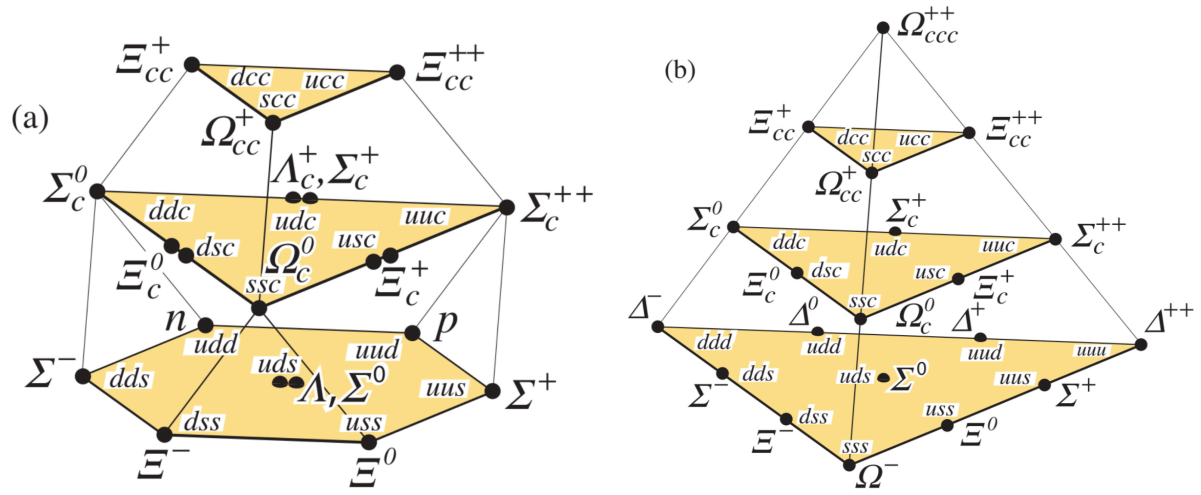

Figure 1.1: (a) The 20-plet corresponding to the $J^P = {}^1/_2^+$ baryons and (b) the $20'_1$-plet corresponding to the $J^P = {}^3/_2^+$ baryons, all corresponding to the $SU(4)$ representation of the four lightest quarks. The charm quantum number, C, of each state in the twentyplets increase from bottom to the top layer. The plots were reproduced from [1].

Apart from the baryon configurations mentioned previously, resonances of all baryons are also possible when the ground states, the states with the lowest energy levels, become orbitally or radially excited ($l > 0$), thus leading to various spin-parity combinations. Resonances, with larger masses than their ground state counterparts, then typically decay via the nuclear strong force, which results in their characteristically short lifetimes.

From the experimental side, many of the charmed mesons predicted by the quark model, as well as their excitations, have been observed. In fact, the LHCb experiment has recently observed a new excited charmed-beauty meson $B_c^+(\bar{b}c)$ [32]. However, the spectra of charmed baryons are not as well understood. All the ground states with charm quantum number $C = 0$ or $C = 1$ have been discovered [1]. Yet, many states, such as the triply-charmed baryons, remain undiscovered. As for doubly-charmed baryons, none had been unambiguously observed prior to the start of the research in this thesis. They are extensively discussed in Section 1.4, so will not be commented on further here.

Exotic Hadrons

Nowadays, the story of hadrons does not appear to end with mesons and baryons. Lets revisit the Pauli exclusion principle, where an equivalent but more mathematically rigorous definition of this law would be that the wave-function for a fermion state must be antisymmetric under the exchange of two quarks of equal mass. This means the quark model, as originally set out by Gell-Mann [33] and Zweig [34], does not in fact rule out the possibility of tetraquark, $q\bar{q}q\bar{q}$, and pentaquark, $qqqq\bar{q}$, states, and it seems nature agrees. Evidence for these types of hadrons has become common place in recent years. It kicked off with the discovery of the $X(3872)$ particle by the Belle experiment in 2003 [35] and has

since seen a wealth of viable exotic candidates, tetraquarks in particular, being identified in experiment [36–39]. Most recently, the LHCb collaboration announced the discovery of three new charmonium-pentaquarks, the $P_c(4312)^+$, $P_c(4440)^+$ and $P_c(4457)^+$ states, through the studies of $\Lambda_b^0 \to J/\psi p K^-$ decays [40, 41]. On the other hand, a frustrating feature of many exotic hadron observations is that they are seen by only one experiment or only through one decay mode. There also lies great uncertainty in the mass models used to predict these unconventional hadrons. More data will be required from high-energy physics experiments in the future to accurately measure the masses and quantum numbers of these unknown states such that their true nature can be ascertained.

1.2.2 Quantum Chromodynamics

The underlying theory that describes the nuclear strong force in the Standard Model is called Quantum Chromodynamics (QCD). As discussed in Section 1.1.1, the nuclear strong force is mediated by the spin-one massless coloured gluons that interact with the colour-charged quarks. Additionally, recall from Section 1.1.2, that the nuclear strong force can be described by a $SU(3)$ symmetry and, as a consequence, there are eight types of gluons. Now lets explore QCD in more detail.

The theory of QCD not only describes quarks and gluons but also the interactions between them. In terms of the dynamics within the QCD framework, a quark may emit or absorb a gluon, as well as vice versa, and any two gluons may directly interact, all of which can lead to the exchange of momentum and colour. This means a gluon and quark in isolation are still described by the Lagrangians given in Equations 1.6 and 1.7, respectively, but the full QCD Lagrangian has additional terms to account for the interactions between these elementary particles, which also maintain the gauge symmetry of the Lagrangian. The QCD Lagrangian is mostly simply defined as

$$\mathcal{L}_{\text{QCD}} = \overline{\psi}\big(i\gamma^\mu D_\mu - m\big)\psi - \frac{1}{4}G^a_{\mu\nu}G^{\mu\nu}_a, \tag{1.9}$$

where $G^{\mu\nu}_a$ is a tensor denoting the gluonic field strength, now replacing $F_{\mu\nu}$ in Equation 1.7 and D_μ is the gauge covariant derivative, replacing ∂_μ in Equation 1.6. The subscript a in the $G^{\mu\nu}_a$ tensor runs from $1-8$ to represent the different possible gluon states. Analysing the gauge covariant derivative D_μ further, it is defined as

$$D_\mu = \partial_\mu + i\, g_s t_a G^a_\mu, \tag{1.10}$$

where g_s is the effective colour charge, which determines the strength of interaction between the colour-charged particles, t_a are the generators of the $SU(3)$ group and G^a_μ represents the field of the gluon. Furthermore, the gluonic field strength tensor $G^a_{\mu\nu}$ can

be expanded as

$$G^a_{\mu\nu} = \partial_\mu G^a_\nu - \partial_\nu G^a_\mu + g_s f^{abc} G^b_\mu G^c_\nu, \tag{1.11}$$

where f^{abc} are the structure coefficients of the $SU(3)$ group and the '$g_s f^{abc} G^b_\mu G^c_\nu$' term generates the gluon self-interactions. This term leads to the special properties of QCD that make it unique from other quantum-gauge theories, and which are discussed next.

Furthermore, following the examination of QCD, the picture of baryons as bound systems of only three quarks should also be slightly refined. A baryon should be viewed as a system of three valence quarks within a 'sea' of virtual quarks and gluons that are allowed to exist within the permitted dynamics of QCD.[3]

Asymptotic Freedom

Quantum field theories are typified by the theme that nothing is truly constant. This is because all quantities that are held fixed within the theory actually depend upon the wavelength of the tool being used to measure them; even the number of particles is not conserved in a quantum field theory. Instead, these quantities are renormalised by processes involving virtual-particles. As a result, somewhat paradoxically, the coupling constants (*e.g.* for Quantum Chromodynamics, the g_s term in Equation 1.11) depend on the energy scale at which one observes them.

In 1973, Gross, Politzer and Wilczek discovered that the strength of the nuclear strong interaction, characterised by the strong coupling constant, α_s, becomes logarithmically weaker as the energy, E, at which the hadron is probed at increases, such that

$$\alpha_s(E) \simeq \frac{g_s}{\ln\left(\frac{E}{\Lambda_{\mathrm{QCD}}}\right)}, \tag{1.12}$$

where Λ_{QCD} is the QCD scale parameter [42, 43]. This extraordinary phenomenon is known as asymptotic freedom and it means that at the very highest energy scales, the quarks and gluons behave as a free non-interacting particles. Asymptotic freedom can be qualitatively understood as the result of a battle between quark-antiquark pairs screening and reducing the effective colour charge measured and the colour-anticolour constituent gluons 'antiscreening' and enhancing the effective charge.

Conversely, the strong coupling α_s also increases with decreasing energy. This trend is expected to be responsible for the principle of colour confinement, whereby quarks and gluons cannot be separated from their parent hadron without producing new hadrons. Colour confinement is hitherto an empirical fact but has not been mathematically proven.

[3] A virtual particle is a transient quantum fluctuation that exhibits some of the characteristics of an ordinary particle, while having its existence limited by the Heisenberg uncertainty principle.

Although QCD seemingly does not allow quarks and gluons to be free, it was expected a signature of their existence could come in the form of narrow-cone-like shapes of hadrons or 'jets' being produced when an original hadron system becomes fragmented during an energetic collision. The gluon was discovered in this manner following the observation of three-jet events at DESY in 1979 by the TASSO experiment at the PETRA collider [44].

1.2.3 QCD Methods

The Lagrangian of Quantum Chromodynamics, as expressed in Equation 1.9, cannot be solved using first principles of mathematics. Despite this disappointing fact, many clever techniques have been developed by physicists over the years to allow for quantitative and qualitative predictions on observables (mass, lifetime *etc.*) of hadrons, with results in heavy-flavour hadron spectroscopy testing and refining these models all the time. Some of the more broadly used QCD techniques are discussed next.

Perturbation Theory

One common way to solve problems in Quantum Field Theory is using perturbation theory. The general idea of perturbation theory is that one starts with a simple system for which a mathematical solution is known and then a 'perturbing' term is added that represents a weak disturbance to the system. In the context of QFT, this effectively means making an approximation of the Lagrangian by expressing it as a perturbative expansion in terms of the coupling constants of the interaction. Alternatively, this method can be interpreted as only considering the most probable path integrals of an elementary particle travelling and interacting between two points in space and time. After the perturbative expansion, each term can be visually represented by a schematic known as a Feynman diagram, which themselves can be thought of as a notation for a mathematical expression. Once all Feynman diagrams are drawn for a process, to the appropriate order in the pertubative expansion, then the diagrams are translated into calculable mathematics using the Feynman rules. Some examples of these Feynman rules and their corresponding Feynman diagrams that are used in perturbative QCD are shown in Figure 1.2.

For QCD, this approach only works at high energies when asymptotic freedom can be exploited; otherwise the strong coupling constant α_s is not small but approximately equal to one and thus the theory is no longer renormalisable. Predictions from pertubative QCD are possible but generally the uncertainties lie at around the 10% level [45–47].

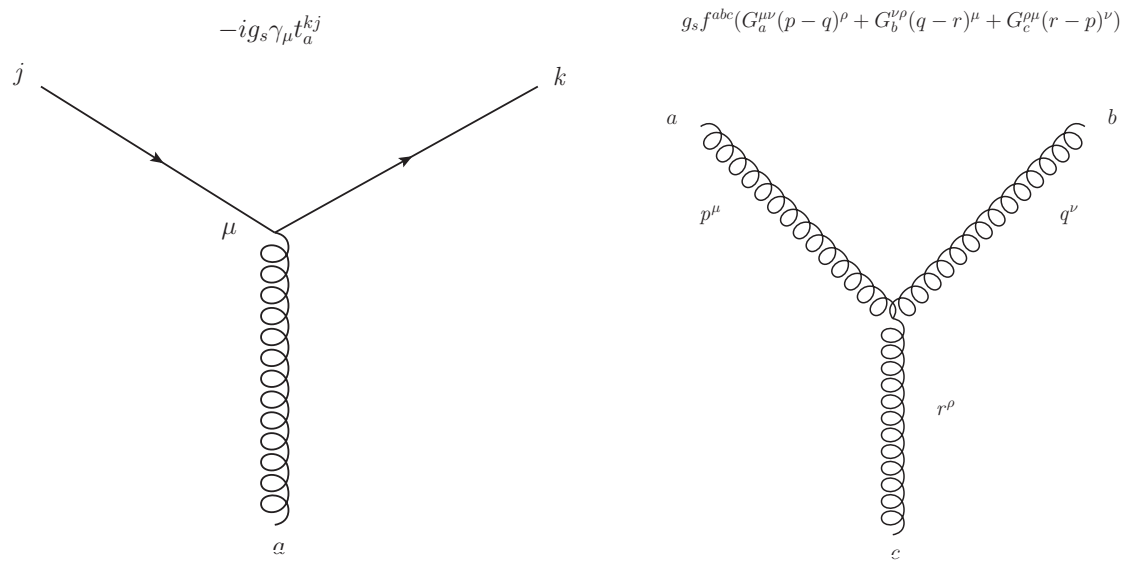

Figure 1.2: Feynman diagrams (below) and corresponding Feynman rules (above) for parts of interactions allowed within Quantum Chromodynamics: (left) quark-gluon-quark vertex showing an emission of a gluon with colour structure a and (right) three-gluon vertex where the gluons have colour structure a, b and c and the gluon momenta are taken to be incoming.

Lattice QCD

Many theoretical physicists use a numerical method technique called Lattice QCD [48] when perturbative methods cannot be used. Lattice techniques involve simulating fundamental particle interactions on a patch of discretised space-time, *i.e.* a lattice, using sophisticated supercomputers. Each point on the lattice has a value assigned to it, which signifies the probability of the presence of other quarks and gluons as well as the strength of the nuclear strong force. In this setup, all path integrals are calculated automatically in the simulation; there is no need to work out the most probable paths of the particles like in perturbation theory. However, similarly to perturbation theory it is also a method of approximation; space-time is most definitely not discrete. Hence, the simulations are also generally performed with different lattice spacings with the trends then examined to extrapolate the results to a zero lattice spacing representing a continuous space-time.

While Lattice QCD is a time-consuming and resource-intensive approach, uncertainties in lattice simulations can in many cases be a lot smaller than in perturbative QCD, at about the 1% level [49]. The method has proven to be greatly effective in understanding how quarks and gluons bind together to form baryons and mesons, particularly for the latter [50–52]. The masses of baryons containing at least one c or b quark, as calculated by Brown *el al.* [51] when using Lattice QCD techniques, are shown in Figure 1.3, where the fine agreement between the results of Lattice QCD and experiment can be seen.

Heavy Quark Effective Theory

In recent years, Heavy Quark Effective Theory (HQET) [53] has emerged as a very useful tool for handling QCD calculations. This technique involves performing an expansion in terms of the inverse powers of the quark masses, combined with terms in the Lagrangian that are not dependent on the mass of a heavy quark. This effective approach is only appropriate when quarks are much heavier than the QCD scale, Λ_{QCD}, which is at around 200 MeV. In fact, the world-average value of α_s at the energy scale corresponding to the rest mass of the Z^0 boson has been determined to be $\alpha_s(M_{Z^0}) = 0.1184 \pm 0.0007$ [54]. As can be determined from Equation 1.12, the QCD scale loosely marks the boundary between where QCD is strongly coupled ($E \ll \Lambda_{\mathrm{QCD}}$) and then the regime where it is asymptotically weaker ($E \gg \Lambda_{\mathrm{QCD}}$) and as such when perturbative expansion is useful. This essentially rules out using HQET to perform calculations on hadrons composed of the lightest u, d and s quarks, as the name might have suggested.

HQET has however proven adept at predicting the mass and lifetime of mesons and baryons containing the heavier b quark, with HQET results showing good agreement with experiment [55,56]. Since doubly-charmed baryons contain two heavy charms quarks, they become very interesting systems to test HQET. The two charm quarks can be treated as a single static di-quark object in this theory with the lighter up-type quark 'orbiting' around it. Ultimately, the agreement of HQET predictions with the result of experiment in the doubly-charmed baryon sector will help tune it as a QCD method.

1.3 Hadronic Weak Decays

The mathematical formalism that was described in Section 1.1.2 only accounted for the interactions of one generation of quark and leptons under the $SU(3) \times SU(2) \times U(1)$ symmetry group. The discovery of additional generations of fermions brought added complexities that had to be incorporated within the Standard Model.

This section is dedicated to explaining the different ways in which quark flavours interact before the section proceeds to explain the impact of this on the weak decays of hadrons that includes the aforementioned doubly-charmed baryons.

1.3.1 Quark Mixing

Around the same time as the quark model was developing, weak decays of hadrons were shown not to conserve the property of Strangeness. Recall that Strangeness is a reflection of the number of valence s quarks in a hadron. Evidence of strangeness-violating decays meant that quarks had to be transmuting into different flavours of quarks.

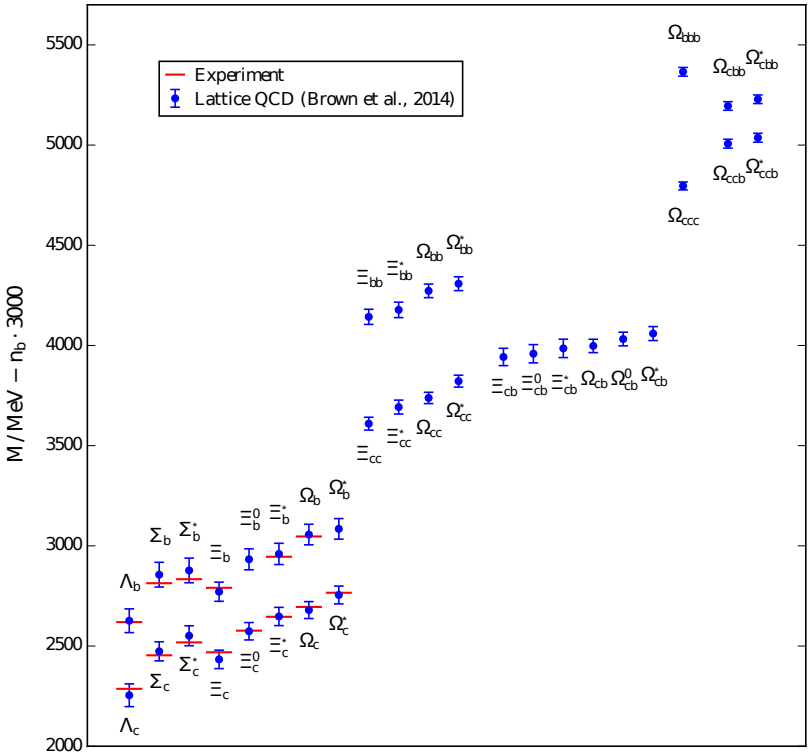

Figure 1.3: A summary of heavy-flavour baryon masses from Lattice QCD calculations. The term n_b stands for the number of bottom quarks in the hadron. The masses of baryons containing n_b bottom quarks have been offset by $-3n_b$ to allow their masses to be shown alongside the lighter charmed baryons. This plot was reproduced from [51].

The first possible explanation for this phenomenon came from Italian physicist Cabibbo in 1963, who postulated that the states in which quarks propagate freely are different to the states in which they interact with the mediators of weak nuclear force, *i.e.* the $W^{\pm}$ and Z^0 bosons. In quantum-field-theory terminology, this would imply that the mass and flavour eigenstates of the quark fields are in fact different.

At a time when only the three lightest quarks had been discovered, Cabibbo proposed that the flavour eigenstate of the down quark, denoted d′, can be represented as a rotation of mass eigenstates of the down and strange quark fields such that

$$\mathrm{d}' = \mathrm{d}\cos\theta_\mathrm{c} + \mathrm{s}\sin\theta_\mathrm{c}, \tag{1.13}$$

where θ_c is the rotation angle and d and s are the mass eigenstates. Under this formalism in the Standard Model, the flavour of a quark could readily change without its electric charge altering. Around the same time, Flavour Changing Neutral Currents (FCNC), whereby a quark could change flavour without changing electrical charge, were shown to be highly suppressed because decays such as $K_\mathrm{L} \to \mu^+\mu^-$ had not been observed in experiment. The reason for this suppression was resolved by the discovery of the charm quark and the Glashow-Illiopoulis-Maiani mechansim (GIM) [57], which demonstrated

that this fourth quark would almost perfectly cancel first-order FCNC contributions in the SM. Now extending Equation 1.13 to account for the charm quark and the extra mixing contributions it brings, the flavour eigenstates s′ and d′ of the strange and down quarks, respectively, can be expressed in matrix notation as

$$\begin{pmatrix} \mathrm{d}' \\ \mathrm{s}' \end{pmatrix} = \begin{pmatrix} \cos\theta_\mathrm{c} & \sin\theta_\mathrm{c} \\ -\sin\theta_\mathrm{c} & \cos\theta_\mathrm{c} \end{pmatrix} \begin{pmatrix} \mathrm{d} \\ \mathrm{s} \end{pmatrix} \equiv \mathrm{V}_c \begin{pmatrix} \mathrm{d} \\ \mathrm{s} \end{pmatrix}, \tag{1.14}$$

where the θ_c parameter, within the 2×2 mixing matrix, $\mathrm{V_c}$, is named the Cabibbo angle and it controls the level of mixing between the quarks in the first and second generations.

1.3.2 The CKM Matrix

In 1964, the symmetry described by the combined Charge conjugation and Parity (CP) operations was shown to be broken in the weak decays of certain neutral hadrons by Cronin and Fitch [58].[4] These findings were incompatible with there being only two generations of quarks because at the time it was known that the minimum dimensionality of any quark-mixing matrix that permits CP-violation in weak interactions should be three.

Therefore, in 1973, before neither the bottom nor top quark were discovered, the quark-mixing matrix of the Standard Model was extended by Kobayashi and Maskawa to account for an expected three generations of quarks [59, 60]. They related the nuclear weak interaction eigenstates of quarks to their mass eigenstates as follows

$$\begin{pmatrix} \mathrm{d}' \\ \mathrm{s}' \\ \mathrm{b}' \end{pmatrix} = \begin{pmatrix} V_{ud} & V_{us} & V_{ub} \\ V_{cd} & V_{cs} & V_{cb} \\ V_{td} & V_{ts} & V_{tb} \end{pmatrix} \begin{pmatrix} \mathrm{d} \\ \mathrm{s} \\ \mathrm{b} \end{pmatrix} \equiv \mathrm{V_{CKM}} \begin{pmatrix} \mathrm{d} \\ \mathrm{s} \\ \mathrm{b} \end{pmatrix}, \tag{1.15}$$

where the $|V_\mathrm{ij}|^2$ terms give the probability of quark with flavour j decaying to a quark with flavour i and the 3×3 matrix, $\mathrm{V_{CKM}}$, is known as the Cabibbo-Kobayashi-Maskawa (CKM) quark-mixing matrix. Note that the $\mathrm{V_{CKM}}$ matrix is set up in Equation 1.15 to describe the interactions of the down-type quarks (d, s and b) but the same mathematical structure holds for the up-type quarks (u, c and t) as well.

Similarly to the one mixing angle θ_c that parametrises the $\mathrm{V_c}$ matrix in Equation 1.14, three mixing angles plus one complex phase can describe the $\mathrm{V_{CKM}}$ matrix as

$$\mathrm{V_{CKM}} = \begin{pmatrix} c_{12}c_{13} & s_{12}c_{13} & s_{13}e^{-i\delta} \\ -s_{12}c_{23} - c_{12}s_{23}s_{13}e^{i\delta} & c_{12}c_{23} - s_{12}s_{23}s_{13}e^{i\delta} & s_{23}c_{13} \\ s_{12}s_{23} - c_{12}c_{23}s_{13}e^{i\delta} & -c_{12}c_{23} - s_{12}s_{23}s_{13}e^{i\delta} & c_{23}c_{13} \end{pmatrix}, \tag{1.16}$$

[4] Charge conjugation reverses the sign of all the internal quantum numbers (*i.e.* changes a particle into its antiparticle) except from spin, which depends on the coordinate system being used.

where $\theta_{12} = \theta_c$, $c_{\mathrm{ij}} \equiv \cos\theta_{\mathrm{ij}}$ and $s_{\mathrm{ij}} \equiv \sin\theta_{\mathrm{ij}}$ are the angles controlling the level of quark mixing between the generations i and j and the δ parameter is the additional complex phase that cannot be removed by simple phase transformations of the quark fields, unlike in the case of the $\mathrm{V_c}$ matrix. The value of these parameters are not dictated by theory but are measured by experiment; the current world-average values are $\theta_{12} = (13.04 \pm 0.05)^\circ$, $\theta_{13} = (0.201 \pm 0.011)^\circ$, $\theta_{23} = (2.38 \pm 0.06)^\circ$and $\delta = (1.20 \pm 0.08)\,\mathrm{rad}$ [1].

Since the behaviour of quarks is determined by the $\mathrm{V_{CKM}}$ matrix but that of anti-quarks is governed by the hermitian conjugate of the $\mathrm{V_{CKM}}$ matrix, then it is the non-zero δ phase that leads to the quarks and anti-quarks behaving differently under the nuclear weak interaction. The consequences of CP-violation in the transitions of quarks between generations is one main topic of flavour physics that is explored by research groups such as the LHCb collaboration. Currently, the measured level of CP-violation in the quark sector is not large enough to explain the observed imbalance of matter and anti-matter in the universe.

1.3.3 Electroweak Quark Sector

Following the early ideas by Cabibbo and the subsequent work by Kobayashi and Maskawa, the idea of quark mixing between generations was firmly cemented into the Standard Model framework. Revisiting the $\mathcal{L}_{\mathrm{Yukuwa}}$ term in the Standard Model Lagrangian as expressed in Equation 1.5, and ignoring the leptons, this term can be expanded as

$$\mathcal{L}_{\mathrm{Yukawa}} = -[Y_d]_{ij}\overline{d}^T_{Li}\Phi d_{Rj} - [Y_u]_{ij}\overline{u}^T_{Li}\epsilon_{ij}\Phi^* u_{Rj} + \mathrm{h.c}, \tag{1.17}$$

where: the i and j indices are summed over the different generations of quarks; u_L (u_R) and d_L (d_R) are the left (right)-handed quarks; Y_u (Y_d) is the Yukawa coupling for the up (down)-type quarks, expressed as a three dimensional square matrix in flavour space; Φ is the Higgs field; ϵ is an antisymmetric tensor; and lastly the h.c term stands for the hermitian conjugate such that anti-quark contributions are included.

The Yukawa couplings for each generation can be chosen to reproduce the measured masses of the quarks. As the interactions of the quarks in one generation are the same as those in any other generation, the fermion kinetic Lagrangian term, $\mathcal{L}_{\mathrm{Fermion\,Kinetic}}$, in Equation 1.5 should also be invariant under unitary rotations between the generations. Thus, the flavour eigenstates can be rotated to give the mass eigenstates, which then correspond to the diagonalised Yukawa matrices. For three generations of quarks, the diagonalised Yukawa matrices result in the $\mathrm{V_{CKM}}$ matrix discussed in Section 1.3.2.

Solving the Yukawa Lagrangian, using perturbation theory and utilising the appropriate Feynman rules, the interaction term to first-order in the perturbative expansion,

for the coupling of up-type and down-type quarks to the W^- boson can be expressed as

$$-\frac{g_{\mathrm{w}}}{2\sqrt{2}}\begin{pmatrix}\overline{u} & \overline{c} & \overline{t}\end{pmatrix}\gamma^{\mu}(1-\gamma^{5})\mathrm{V_{CKM}}\begin{pmatrix}d\\ s\\ b\end{pmatrix}W^{-}+\mathrm{h.c}, \tag{1.18}$$

where: $\mathrm{V_{CKM}}$ is the CKM mixing matrix from Equation 1.15; g_{w} is the coupling constant of the weak interaction; γ^{μ} are the gamma matrices; and $\gamma^5 \equiv i\gamma^0\gamma^1\gamma^2\gamma^3\gamma^4$. Expression 1.18 shows that the quarks can undergo an interaction with the electroweak force and be transformed into different flavours of quarks in different generations, where the amplitude of these interactions is governed by the magnitude of the elements within the $\mathrm{V_{CKM}}$ matrix, exactly as was conveyed in Section 1.3.2. The world-average experimental value for the magnitude of the V_{ij} elements [1] are as follows

$$|\mathrm{V_{CKM}}| = \begin{pmatrix}0.97420 \pm 0.00021 & 0.2243 \pm 0.0005 & 0.00394 \pm 0.00036\\ 0.218 \pm 0.004 & 0.977 \pm 0.017 & 0.0422 \pm 0.0080\\ 0.0081 \pm 0.0005 & 0.0394 \pm 0.0023 & 1.019 \pm 0.025\end{pmatrix}, \tag{1.19}$$

which clearly shows there is a hierarchy for the weak decays of quarks. The transitions occurring with the same generation have a large probability of occurring and so are said to be 'Cabibbo favoured', while the transitions matching to the off-diagonal elements in the $\mathrm{V_{CKM}}$ matrix are said to be 'Cabibbo suppressed'. For instance, the following hadronic weak decays of the singly-charmed D^+ hadron; $D^+ \to K^-\pi^+\pi^+$ and $D^+ \to K^-K^+\pi^+$, occur by a charm quark emitting a W^+ boson and transforming into a strange quark and a down quark, respectively. One would expect a higher rate of the former decay given the values of the V_{cs} and V_{cd} elements and indeed this is reflected in the rates of these two decay modes [1]

$$\mathcal{B}(D^+ \to K^-\pi^+\pi^+) = (8.98 \pm 0.28) \times 10^{-2} \tag{1.20}$$

$$\mathcal{B}(D^+ \to K^-K^+\pi^+) = (9.51 \pm 0.34) \times 10^{-3} \tag{1.21}$$

where the branching fraction, $\mathcal{B}$, indicates the fraction of particles which decay by the mode specified with respect to the total number of particles which decay. Depending on the structure of a decay there can be multiple Cabibbo-suppressed or Cabibbo-favoured transitions in a single decay. This was an important consideration when determining the appropriate search modes of doubly-charmed baryons. The properties and decay modes of the doubly-charmed baryons are discussed in the next section.

1.4 Doubly Charmed Baryons

Doubly-charmed baryons (DCBs) are baryons composed of two heavy charm quarks in combination with another valence quark and they are firmly predicted by a quark model that has to date predicted over a hundred baryon states discovered in experiment.

Searches for DCBs are important because DCBs provide a unique system for testing different methods used in chromodynamics, particularly non-perturbative techniques. While baryons composed of the lighter up, down and strange quarks suffer from the classical three-body problem of dynamics, DCBs are much easier to model. They can be described in calculations as a single static and heavy cc diquark structure with a lighter quark orbiting. This type of simplification facilitates many theoretical approaches, particularly in Heavy Quark Effective Theory as was discussed in Section 1.2.3. Improvements in QCD techniques would in turn help aid progress in understanding exotic hadrons such as the tetraquark and pentaquark candidates of Section 1.2.1.

This section will describe the expected properties of doubly-charmed baryons based on recent theoretical work that has then also motivated the strategies of the search analyses described in Chapter 4 and Chapter 5 of this thesis. Equally, this section will discuss the variety of searches for doubly-charmed baryons performed by different research groups, prior to any of the analyses detailed in this thesis had begun.

1.4.1 Theoretical Properties

Under the $SU(4)$ formalism of baryons discussed in Section 1.2.1, there should exist three doubly-charmed baryon with a spin-parity assignment of $J^P = {}^1/_2^+$ and three with a spin-parity assignment of $J^P = {}^3/_2^+$ [61]. These baryons would correspond to a ccd (Ξ_{cc}^+) state, a ccu (Ξ_{cc}^{++}) state and a ccs (Ω_{cc}^+) state. With the same total number of u and d valence quarks, the Ξ_{cc}^+ and Ξ_{cc}^{++} states would form a doublet with isospin, $I = {}^1/_2$, with $SU(2)$ symmetry, while the Ω_{cc}^+ state would form a singlet with zero isospin.

Various QCD methods have been used to predict the masses of the DCBs with spin-parity $J^P = {}^1/_2^+$. This includes, but is not limited to, adaptations of the quantum chromodynamics methods discussed in Section 1.2.3. Most techniques agree that the Ξ_{cc} isospin partners should have a mass between $3500-3800\,\mathrm{MeV}/c^2$ [62–77]. Additionally, the masses of the Ξ_{cc}^+ and Ξ_{cc}^{++} baryons are expected to be very similar because of the isospin symmetry between the up and down quarks [78–80]. On the other hand, the Ω_{cc}^+ state is expected to be $100\,\mathrm{MeV}/c^2$ heavier than the Ξ_{cc} baryons as it contains the more massive strange quark [62–77]. One fairly precise prediction is from a lattice calculation that expects the mass of the spin-1/2 Ξ_{cc} states to be $(3606 \pm 11 \pm 8)\,\mathrm{MeV}/c^2$ [77], where the first uncertainty is statistical and the second is systematic due to the tuning of the

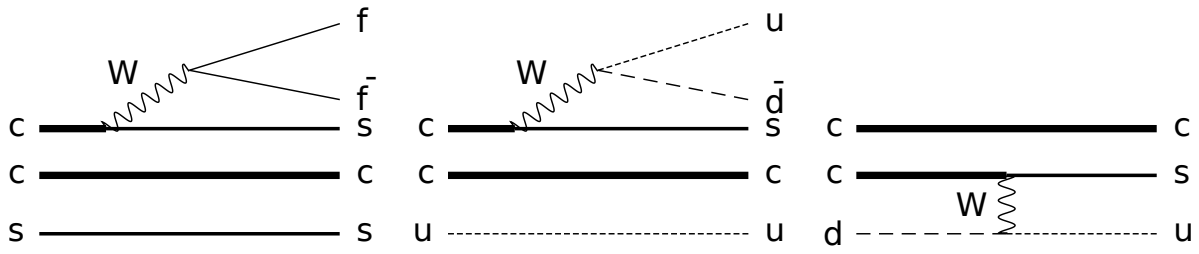

Figure 1.4: Quark diagrams of general decay of different doubly-charmed baryons where the form of the weak decay is (left) W^- external emission in a semi-leptonic decay, (middle) W^- external emission to a quark-antiquark final state and (right) W exchange. The diagrams were reproduced from [88].

charm quark masses. The masses of spin-3/2 DCBs are expected to be 50–100 MeV/c^2 larger than their spin-1/2 counterparts.

QCD methods can also be used to calculate the lifetime of a particle. The probability that a quasi-stable particle will decay is governed by the rules of Relativistic Quantum Field Theory. As such, the decay rate, Γ, of a particle is given by the sum squared of the amplitudes (terms from each Feynman diagram contribution) of all possible ways in which the particle can decay. The decay rate then gives the probability that the particle decays in a unit of time with the lifetime of a particle given as $\tau = 1/\Gamma$. The decay rate Γ also contributes to the width of any signal peak in the distribution of mass measurements of a particle due to the Heisenberg's Uncertainty principle. When it comes to the lifetimes of the spin-1/2 DCBs, there is a large spread in their predicted values. For instance, the predicted lifetime of the Ξ_{cc}^+ baryon spans the range 50−250 fs, while the Ξ_{cc}^{++} baryon is expected to be three to four times longer lived with a predicted lifetime between 200−1050 fs [81–86]. The predicted larger lifetime of the Ξ_{cc}^{++} baryon over the Ξ_{cc}^+ baryon can be qualitatively explained by the destructive Pauli interference [87] of its charm-quark decay products and its valence up quark in the initial state acting as a spectator, whereas the lifetime of the Ξ_{cc}^+ baryon should be shortened due to an additional contribution from W-exchange between the charm and down quarks. A combination of these effects, leads to following generally well accepted hierarchy of lifetimes; $\tau(\Xi_{cc}^{++}) > \tau(\Omega_{cc}^+) \gg \tau(\Xi_{cc}^+)$, for the spin-1/2 DCBs. Quark diagrams illustrating the exchange and spectator contributions for the Ξ_{cc}^+, Ξ_{cc}^{++} and Ω_{cc}^+ baryons are shown in Figure 1.4.

The cross section, a measure of the rate of production, of a DCB can also be predicted using QCD techniques. The typical approach is to compute the production of two $c\bar{c}$ pairs using pertubative QCD, then the formation of the cc di-quark formed from these $c\bar{c}$ pairs can be treated non-pertubatively along with the hadronization process that binds the cc di-quark to a light quark to create a DCB. However, the predicted cross-sections are generally associated with sizeable uncertainties since charm quarks have large non-perturbative contributions. The data sets used in the research described in this thesis

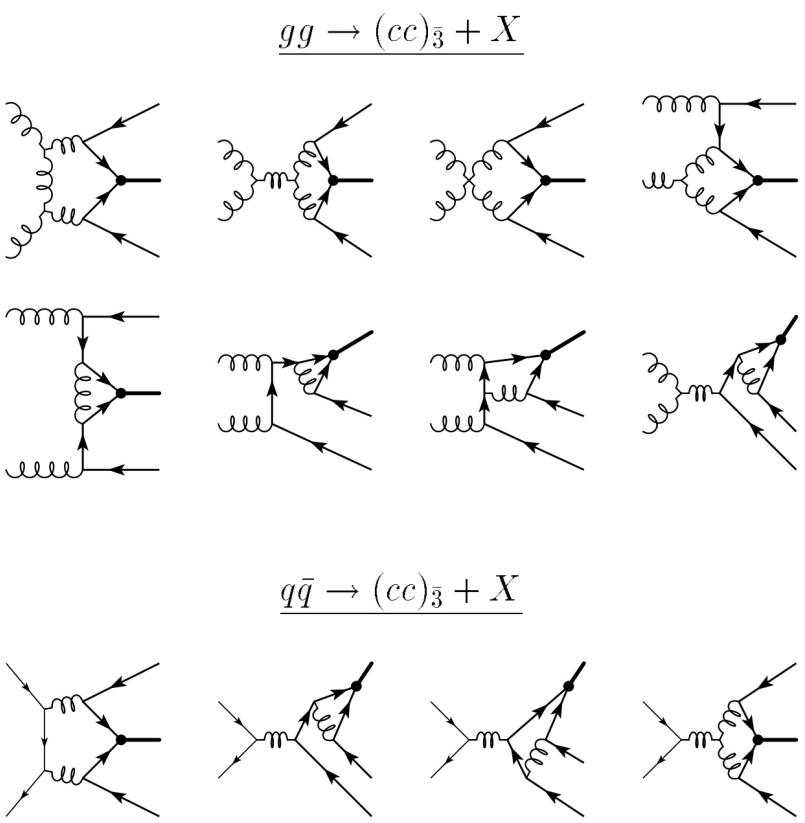

Figure 1.5: Feynman diagrams for the production of a cc-diquark from (top) gluon-gluon and (bottom) quark-antiquark interactions. The initial (final) state quarks are denoted by the thin (bold) lines and the gluons are depict as the helical lines. The figure was reproduced from [89].

correspond to information from proton-proton collisions. Now most theoretical calculations for the production cross section of the Ξ_{cc} baryons in proton-proton collisions at $\sqrt{s} = 14\,\text{TeV}$ are between $60-1800\,\text{nb}$ [89, 90], while the Ω_{cc}^{+} cross section is expected to be a factor of three smaller due to the fragmentation fractions of u, d and s quarks in proton-proton collisions [91–94]. Examples of possible production mechanisms that can lead to the formation of DCBs in hadronic collisions are shown in Figure 1.5. It is interesting to note that some theorists suggest searching for DCBs in heavy-ion collisions, since the cross sections of DCBs might be enhanced by a few orders of magnitude when quark gluon plasma is produced [95–97]. Experimentally, cc quark production from proton-proton collisions is found to be dominated by double-parton scattering according to the double-heavy production measurements performed by the LHCb collaboration [98]. Double-parton scattering (DPS) is when two independent hard scattering processes occur in two independent collisions that each produces a $c\bar{c}$ pair. Yet, there is no experimental evidence to suggest that DPS is the dominant mechanism for DCB production or whether it is suppressed in the hadronization process such that single-parton scattering leads.

From theoretical expectations, it was clear that the spin-1/2 Ξ_{cc}^{++} state was the DCB

State	Valence quarks	Mass (MeV/c^2)	Lifetime (fs)	I (J^P)
Ξ_{cc}^{+}	ccd	3500–3800	50–250	$\frac{1}{2}$ ($\frac{1}{2}^+$)
Ξ_{cc}^{++}	ccu	3500–3800	200–1050	$\frac{1}{2}$ ($\frac{1}{2}^+$)
Ω_{cc}^{+}	ccs	3600–3900	200–500	0 ($\frac{1}{2}^+$)

Table 1.4: Properties of the $SU(4)$ doubly-charmed baryons with $J^P = {}^1/_2^+$. The values are taken from a variety of different sources [62–77, 81–86, 91–94].

with the most promise for discovery, given the combination of its relatively long lifetime and its high production cross section, compared to the other two states. All the properties of the spin-1/2 $SU(4)$ DCBs that were discussed above are summarised in Table 1.4.

1.4.2 Search Modes

Like most hadrons, doubly-charmed baryons are quasi-stable systems and will decay to more stable particles, typically charged kaons ($K^{\pm}$), protons (p) and charged pions ($\pi^{\pm}$), which can be detected by high-energy physics detectors to infer their existence. The lowest lying doubly-charmed baryons with $J^P = {}^1/_2^+$ can only decay via the nuclear weak interaction and as such they should be conveniently displaced for their production point; this is one of the key signatures of signal in the search analyses of Chapters 4 and 5. However, their hadronic weak decays usually lead to multiple detectable particles in the final state.[5] This can negatively impact the ability of the detector to reconstruct the full decay. Then in the case of doubly-charmed baryons with $J^P = {}^3/_2^+$, these will decay almost instantaneously to their $J^P = {}^1/_2^+$ state, either electromagnetically or via the strong nuclear force, emitting a photon in the former case and pions in the latter. Hence, searches for these doubly-charmed baryons will be difficult due to the challenge of reconstructing even more tracks. Any signal will also have a broad decay width making it challenging to disentangle from background.

In hadronic multi-body decays, intermediate and strongly-decaying particles can be produced, such that the final state is topologically similar were the decay to proceed in a non-resonant fashion. In recent years, research into doubly-charmed-baryon decays has focused on cases where the baryon weakly decays to two such intermediate particles [99]. Within this line of research, the $\Xi_{cc}^{++} \to \Lambda_c^+ K^- \pi^+ \pi^+$ decay mode was predicted to be the most promising for discovery with its branching fraction expected to reach as high as 10% if the Ξ_{cc}^{++} baryon decays predominately via the Σ_c^{++} and $\bar{K}^{*0}$ resonances [99]. The first-order, or 'tree-level', amplitude of the inclusive $\Xi_{cc}^{++} \to \Lambda_c^+ K^- \pi^+ \pi^+$ decay, where

[5] Semi-leptonic decays of doubly-charmed baryons are not pursued in any search analysis in this thesis since the LHCb detector is not optimised for detecting neutrinos.

State	Decay mode	Branching fraction
Ξ_{cc}^{++}	$\Sigma_c^{++}\bar{K}^{*0}$	1.0
	pD^{*+}	0.04
	pD^{+}	0.0008
Ξ_{cc}^{+}	$\Lambda_c^{+}\bar{K}^{*0}$	$(\mathcal{R}_\tau/0.3)\times 0.22$
	$\Sigma_c^{++}K^{-}$	$(\mathcal{R}_\tau/0.3)\times 0.01$
	$\Xi_c^{+}\rho^{0}$	$(\mathcal{R}_\tau/0.3)\times 0.04$
	$\Lambda^{0}D^{+}$	$(\mathcal{R}_\tau/0.3)\times 0.004$
	pD^{0}	$(\mathcal{R}_\tau/0.3)\times 0.001$

Table 1.5: Promising pseudo-two-body search modes of the Ξ_{cc}^{++} and Ξ_{cc}^{++} baryons. The branching fractions are relative to the $\Sigma_c^{++}\bar{K}^{*0}$ mode, which is defined to be 1.0 and is expected to reach the 10% level. $\mathcal{R}_\tau$ denotes the ratio of lifetimes between the Ξ_{cc}^{++} and Ξ_{cc}^{++} states, assumed to be ∼0.3. This table was adapted from [99].

its decay products are uniform across the entire phase space, is shown in the left plot of Figure 1.6, while its pseudo-two-body $\Xi_{cc}^{++}\to(\Sigma_c^{++}\to\Lambda_c^{+}\pi^{+})(\bar{K}^{*0}\to K^{-}\pi^{+})$ decay, is shown in the right plot of Figure 1.6. The branching fractions for other pseudo-two-body decays of the Ξ_{cc}^{+} and Ξ_{cc}^{++} states, relative to the $\Xi_{cc}^{++}\to\Sigma_c^{++}\bar{K}^{*0}$ decay mode, are listed in Table 1.5. Note that the values quoted in Table 1.5 also depend on the ratio between the assumed lifetimes of the Ξ_{cc}^{+} and Ξ_{cc}^{++} states, $\mathcal{R}_\tau$. In this case $\mathcal{R}_\tau$ is assumed to be approximately 0.3. The $\Xi_{cc}^{++}\to\Lambda_c^{+}K^{-}\pi^{+}\pi^{+}$ decay mode will be the focus of the analysis described in Chapter 4.

Another decay mode that is not listed in Table 1.5 but which could also proceed in a pseudo-two-body manner, is that of the $\Xi_{cc}^{++}\to D^{+}pK^{-}\pi^{+}$ decay. For example, it may decay via an excited Σ^{+*} baryon, with a mass greater than $1572\,\mathrm{MeV}/c^2$, that then decays to a $pK^{-}\pi^{+}$ final state. The properties of Σ^{+*} baryons are however not well known [1] and so the pseudo-two-body nature of the $\Xi_{cc}^{++}\to\Sigma^{+*}(\to pK^{-}\pi^{+})D^{+}(\to K^{-}\pi^{+}\pi^{+})$ decay, cannot be assured.[6] The tree-level amplitude of the inclusive $\Xi_{cc}^{++}\to D^{+}pK^{-}\pi^{+}$ decay with a uniform phase-space distribution of its decay products is shown on the left of Figure 1.7, while its pseudo-two-body decay that was discussed above is shown on the right of Figure 1.7 for comparison. Unlike in the $\Xi_{cc}^{++}\to\Lambda_c^{+}K^{-}\pi^{+}\pi^{+}$ decay mode, the $\Xi_{cc}^{++}\to D^{+}pK^{-}\pi^{+}$ decay is expected to be dominated by complex Bow-tie and colour-commensurate Feynman diagrams [100,101] that are not easy to be studied in theoretical models. The $\Xi_{cc}^{++}\to D^{+}pK^{-}\pi^{+}$ decay mode will be the main subject of Chapter 5.

Finally, by comparing the leading-order Feynman diagrams shown in Figure 1.6 and Figure 1.7, it can be seen that the same V_{CKM} elements are needed to describe the decays.

[6] Other pathways available to the $\Xi_{cc}^{++}\to D^{+}pK^{-}\pi^{+}$ decay to act as a pseudo-two-body decay could involve intermediate $\Xi_c^{+*}(3302)$ or $\Sigma^{++*}(2808)$ resonances but these states have not been observed [1].

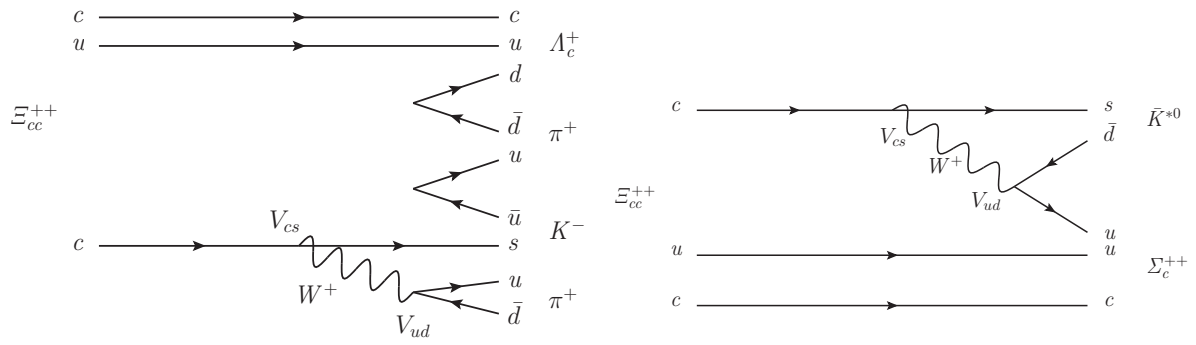

Figure 1.6: Feynman diagram contributing to (left) the inclusive $\Xi_{cc}^{++} \to \Lambda_c^+ K^- \pi^+ \pi^+$ decay and (right) the pseudo-two-body $\Xi_{cc}^{++} \to \Sigma_c^{++} K^{*0}$ decay.

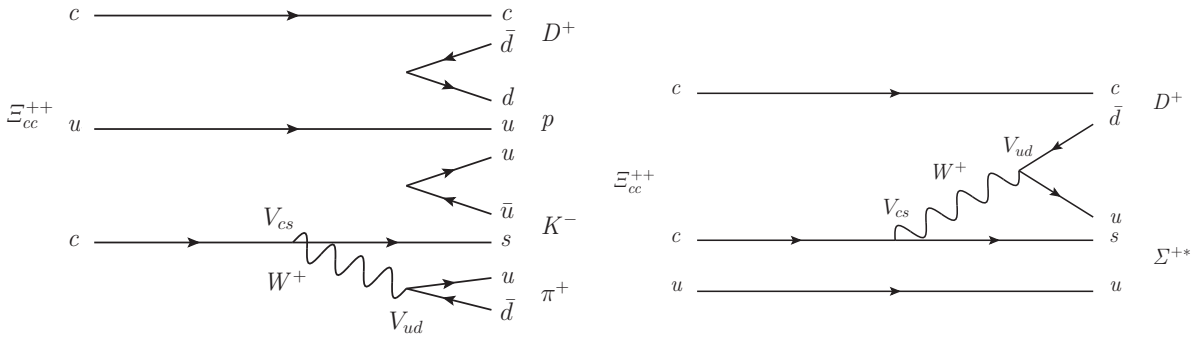

Figure 1.7: Feynman diagram contributing to (left) the inclusive $\Xi_{cc}^{++} \to D^+ p K^- \pi^+$ decay and (right) the pseudo-two-body $\Xi_{cc}^{++} \to D^+ \Sigma^{+*}$ decay.

Hence, the branching fractions of the $\Xi_{cc}^{++} \to \Lambda_c^+ K^- \pi^+ \pi^+$ and $\Xi_{cc}^{++} \to D^+ p K^- \pi^+$ decay modes would be expected to be similar, for the reasons explained in Section 1.3.3, if intermediate resonances and phase space factors are ignored.

1.4.3 Past Experimental Searches

Doubly-charmed baryons have been searched for in the past by various research groups that specialise in heavy flavour physics, most famously by the SELEX collaboration [102] at the Fermi National Accelerator Laboratory in the United States.

In 2002, SELEX reported signals of the Ξ_{cc}^+ baryon through the $\Xi_{cc}^+ \to \Lambda_c^+ K^- \pi^+$ decay mode in data resulting from a beam, containing a mixture of p, Σ^- and π^- hadrons, colliding with fixed foil targets [103]. SELEX followed this up by claiming an observation of the same state via the $\Xi_{cc}^+ \to D^+ p K^-$ decay mode in 2004 [104]. The peaks reported by the SELEX group are shown in the plots in Figure 1.8. The reported state had a combined average mass of $(3519 \pm 2)\,\mathrm{MeV}/c^2$ from both these analyses, which is consistent with the expected mass of a doubly-charmed baryon as discussed in Section 1.4.1. However, the lifetime was found to be compatible with zero within the experimental resolution and

less than 33 fs at the 90% Confidence Level (CL). This lifetime result was certainly not in keeping with theoretical expectations for a weakly decaying Ξ_{cc}^{+} state, see Table 1.4. Furthermore, SELEX estimated that 20% of their Λ_c^+ (udc) yield originated directly from decays of Ξ_{cc}^{+} baryons but it is expected that the production of doubly-charmed baryons is suppressed by several orders of magnitude with respect to singly-charmed baryons [91].

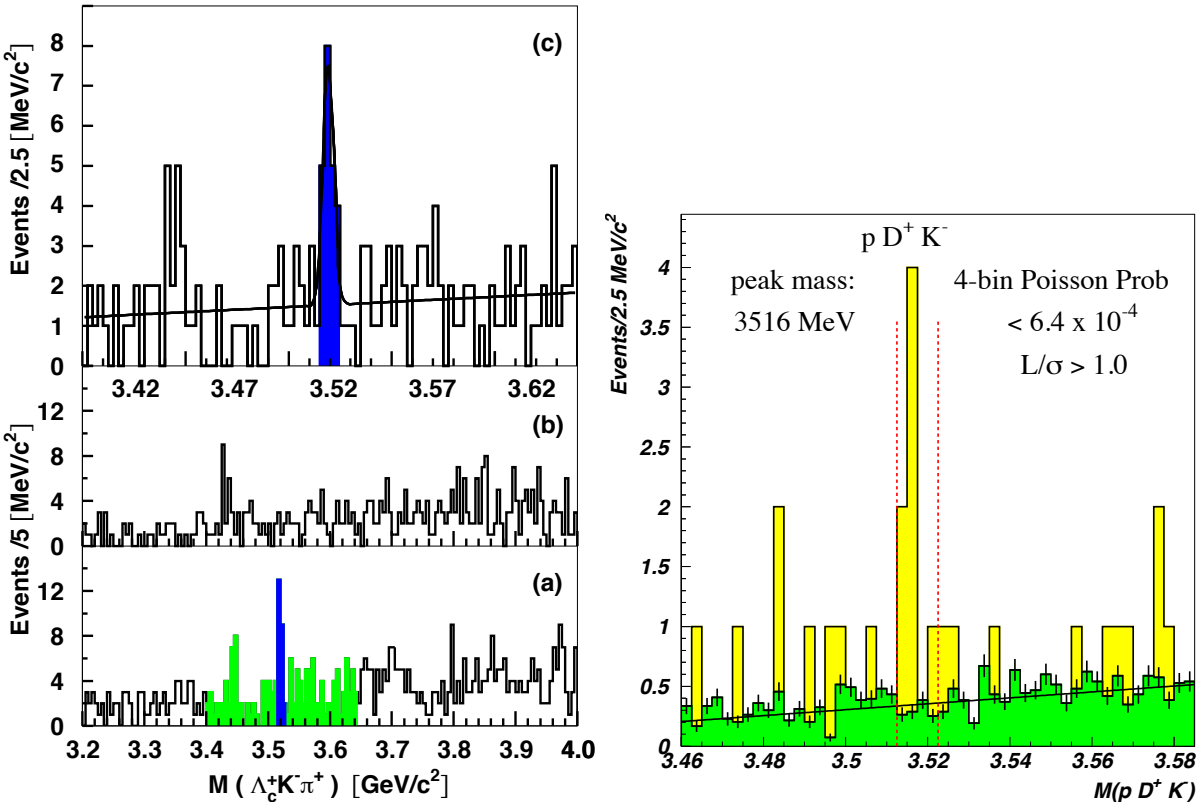

Figure 1.8: Results from the SELEX collaboration showing a peaking structure around 3.5 GeV/c^2 in their $\Lambda_c^+ K^-\pi^+$ (left) and D^+pK^- (right) data mass spectra [103, 104].

Searches for the same state reported by the SELEX group were carried out between 2003 and 2006 in different production environments at the FOCUS [105], BaBar [106] and Belle experiments [107] but all these groups failed to find such a particle. Most recently in 2013, the LHCb collaboration searched for the Ξ_{cc}^{+} state through the $\Xi_{cc}^{+} \to \Lambda_c^+ K^-\pi^+$ decay using proton-proton collision data [108]. The LHCb collaboration found no significant signal in the mass range 3300−3800 MeV/c^2, as is evident from the left-hand plot of Figure 1.9. Instead, LHCb set upper limits at the 95% CL on the following ratio

$$\mathcal{R} = \frac{\sigma(\Xi_{cc}^{+}) \times \mathcal{B}(\Xi_{cc}^{+} \to \Lambda_c^+ K^-\pi^+)}{\sigma(\Lambda_c^+)}, \tag{1.22}$$

where σ and $\mathcal{B}$ denote production cross section and branching fraction quantities, respectively. The value of the upper limit on $\mathcal{R}$ as a function of the mass and lifetime of the Ξ_{cc}^{+} baryon is shown in the right-hand plot of Figure 1.9. LHCb found the upper limit

on this ratio $\mathcal{R}$ to be in the 10^{-4} to 10^{-2} range, with the value being dependent on the lifetime of the Ξ_{cc}^{+} baryon. The value reported by SELEX for the same ratio is not covered by this range.

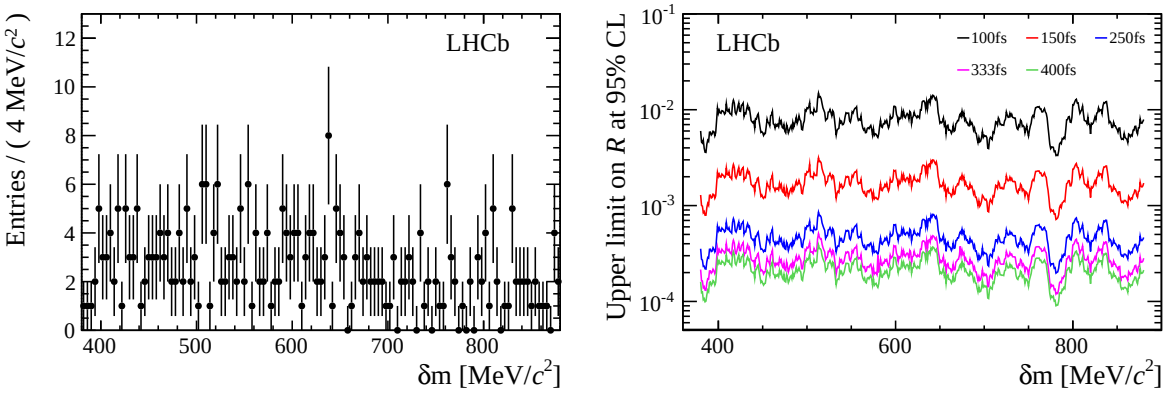

Figure 1.9: Results for the search of the $\Xi_{cc}^{+} \to \Lambda_c^{+} K^{-}\pi^{+}$ decay by the LHCb collaboration [108]. (Left) The $\delta(m)$ distribution for Ξ_{cc}^{+} candidates, where $\delta(m)$ is a mass difference variable defined as $m(\Lambda_c^{+} K^{-}\pi^{+}) - m(\Lambda_c^{+}) - m(K^{-}) - m(\pi^{+})$. (Right) The upper limit ratio of $\sigma(\Xi_{cc}^{+}) \times \mathcal{B}(\Xi_{cc}^{+} \to \Lambda_c^{+} K^{-}\pi^{+})$ relative to $\sigma(\Lambda_c^{+})$ under different $\delta(m)$ and lifetime, τ, hypotheses where σ and $\mathcal{B}$ denotes cross section and branching fraction.

Therefore, these results from the LHCb collaboration are not consistent with those reported by SELEX group. However, the production environments at these experiments are vastly different so it is not impossible that the hyperon beams could enhance the production cross section of Ξ_{cc}^{+} baryons. These inconsistent results remain a longstanding puzzle in the Ξ_{cc} sector. LHCb concluded that future searches for doubly-charmed baryons will benefit from larger data samples and improved trigger conditions at their facilities.

1.5 Chapter Summary

This chapter began by explaining the motivation for the research presented in this thesis. This is that doubly-charmed baryons are potentially very helpful for furthering the understanding of the nuclear strong force and so there should be an incentive to discover these types of particles. The chapter then introduces the Standard Model, the current framework that is used to explain all phenomena in particle physics. The relevant concepts within the Standard Model are then systematically introduced, with each idea building on the last, such that ultimately the fundamental properties of doubly-charmed baryons can be explained. The promising search modes of the doubly-charmed baryons are then discussed before the chapter concludes on a historical note, with a brief overview of the previous attempts to find doubly-charmed baryons.

Chapter 2

The LHCb Detector

> "Despite my resistance to hyperbole, the Large Hadron Collider belongs to a world that can only be described with superlatives."
>
> – Lisa Randall, author of 'Knocking on Heaven's Door'

The LHCb detector is a high-energy physics experiment at the Large Hadron Collider in Geneva, Switzerland. LHCb was originally designed to perform precision heavy-flavour physics measurements but it now encompasses a much wider physics research programme, which includes searches for doubly-charmed baryons.

In this chapter, the LHC accelerator complex, which delivers pp collisions to the LHCb detector, is discussed in Section 2.1. The LHCb detector and its subsystems are described in detail in Section 2.2 through to Section 2.4. An overview of the LHCb trigger system is then presented in Section 2.5 before the chapter concludes with a description of how data is processed and also simulated at LHCb in Section 2.6 and Section 2.7, respectively.

2.1 The Large Hadron Collider

The Large Hadron Collider (LHC) [109] is a particle accelerator situated at the European Laboratory for Particle Physics (CERN) [110] on the French-Swiss border. The collider is housed in a tunnel approximately 27 km in circumference and roughly 100 m underground. The tunnel was constructed between 1983 to 1988 to originally host the Large Electron-Positron (LEP) collider [111] prior to the start of the LHC project. Ultimately, the LHC was designed to help test the Standard Model (SM) to its limits by discovering new phenomena that the SM could not explain.

The LHC first started taking data with protons in September 2008 when a connection between a dipole and quadrapole magnet suffered a catastrophic structural failure. This caused a chain reaction, which quenched several magnets along the accelerator and caused substantial damage. The fault was found in one of the flexible connectors, which initiated

an extensive repair campaign in the LHC. The damage meant operations did not resume until March 2010, which marked the start of the first prolonged period of data taking at the LHC, referred to as Run I. Run I operations concluded in December 2012 for scheduled further repairs to the LHC and its enclosed experiments. The second period of data taking, Run II, started in June 2015 and finished in December 2018. As of the end of Run II, the LHC was still the most powerful particle accelerator in the world based on its capacity to accelerate protons to a centre-of-mass energy, $\sqrt{s}$, of 14 TeV. The value of $\sqrt{s}$ is a measure of the invariant mass of the two colliding protons and indicative of the energy available to create new particles in a single proton-proton (pp) collision.[1] After a two-year-long shutdown period for extensive upgrades, the LHC will restart again in 2021 for the Run III operational period.

The LHC is not a standalone machine but is connected to a chain of accelerators at CERN as depicted in Figure 2.1. Before reaching the LHC, the protons pass through each of these older accelerators, gaining energy as they do. The protons originate from a hydrogen gas source that is ionised by an electric field to leave a surplus of protons. These protons are then accelerated by the LINear ACcelerator 2 (LINAC 2) to an energy of 50 MeV using radio frequency (RF) technology. After which the protons are injected into the Proton Synchrotron Booster (PSB), a system of four superimposed synchrotron rings, by a kicker magnet in pulses every 100 ms. This injection procedure eventually effects the arrangement and spacing of the protons that circulate the LHC. The protons are placed in bunches, groups of up to 1×10^{11} protons, which are separated relative to one another. In Run I the intervals between proton bunches colliding inside the LHC was 50 ns and in Run II it was 25 ns. The protons then exit the PSB at an energy of 1.4 GeV and continue into the Proton Synchrotron (PS), where they are accelerated to 24 GeV, then the Super Proton Synchrotron (SPS), where they reach an energy of 450 GeV. At this stage the protons are injected from the SPS into the LHC where they are divided into two beams traveling in opposite directions. This marks the beginning of a physics 'Fill'; a continuous block of time in which the LHC receives proton bunches from SPS before ending with the proton beams being directed out of the LHC. Superconducting dipole magnets keep the proton bunches bending on a circular trajectory around the LHC while its ultrahigh vacuum (better than 10^{-8} mbar) minimises beam degradation. The proton bunches are kept focused by quadrupole magnets cooled to 1.9 K by super-fluid liquid helium. A total of 16 superconducting RF cavities accelerate the proton beams from the injection energy of 450 GeV to the desired $\sqrt{s}$ ready for collisions to take place. A more comprehensive overview of the LHC design can be found in reference [112].

[1] LHC ran at $\sqrt{s} = 7 - 8$ TeV for Run I and $\sqrt{s} = 13$ TeV for Run II but is expected to operate at the design $\sqrt{s} = 14$ TeV in future operational periods.

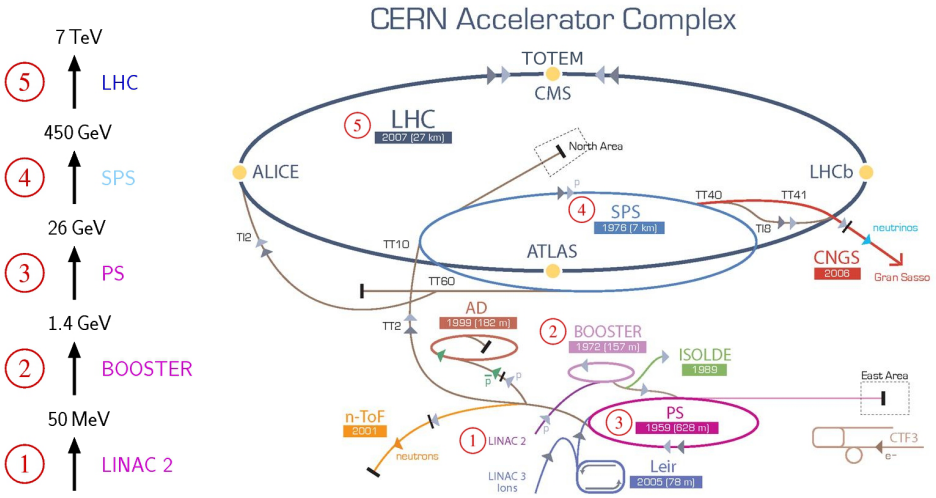

Figure 2.1: The layout of the CERN complex, showing each accelerator connected to the LHC and their corresponding energies. The figure was reproduced from [113].

Along the LHC accelerator there are four locations where the beams are brought together to allow the proton bunches to collide and produce new particles. The beams are forced to collide at an angle of a few mrad so they do not interact with each other via electromagnetic forces outside the designated collision region. Four large scale physics detectors then sit at these beam crossing points to measure the properties of the resulting collisions. The detectors are stored in large cavern spaces deep underground. The Compact Muon Solenoid (CMS) [114] and A Toroidal LHC ApparatuS (ATLAS) [115] are general purpose barrel shaped detectors designed to measure all detectable products from the collisions of protons. ATLAS and CMS jointly discovered the Higgs boson [13, 14], the particle that the LHC accelerator was mainly built to find, in 2012. Their research goals now include precision Higgs, electroweak and top physics and searches of physics unexplainable within the current SM framework, but which could be explained by theories such as supersymmetry. A Lead Ion Collision Experiment (ALICE) [116] is designed to examine collisions of lead nuclei, which circulate the LHC rather than protons during special operational periods. ALICE is studying the exotic state of matter known as quark-gluon plasma that exists at unimaginably high temperatures. The last of the four main LHC experiments is the LHC beauty (LHCb) experiment, which is focused on heavy-flavour physics. The data examined in this thesis were recorded by LHCb and so this detector is discussed in greater detail, than the other LHC detectors, in the subsequent sections.

There are three further experiments on the LHC accelerator, which are not situated at a pp interaction point. They are; the TOTEM [117] experiment, designed to measure the total pp cross section, the LHCf [118] experiment, aiming to measure the production cross sections of neutral particles; and finally, the Monopole and Exotics Detector at the LHC (MoEDAL) [119], focused on searches for evidence of magnetic monopoles.

2.2 The LHCb Detector

The LHCb experiment [120] is a single-arm forward detector designed to observe hadrons containing the relatively heavy charm (c) and bottom (b) quarks. The LHCb collaboration focuses on making precise measurements of the properties of these particles, which includes, but is not limited to, the violation of Charge-Parity (CP) symmetry conservation and studies of rarer decay modes.

Heavy quark production at the LHC is dominated by gluon-gluon fusion and quark-antiquark annihilation processes due to the up-up-down (uud) valence quark structure of the colliding protons. The kinetic energy of the partons (quarks and gluons) inside the protons at the time of collision are much larger than the relatively low masses of the c and b quarks. As such these hard scattering processes ultimately lead to the production of $c\bar{c}$ and $b\bar{b}$ quark pairs whose polar angles, relative to the LHC beam pipe, are very small and correlated. These kinematic effects result in approximately 27% of all hadrons [121], formed from these $b\bar{b}$ pairs, being produced in cone-like distributions collinear to the original proton beams, as shown in Figure 2.2. The distribution of these b-hadrons motivated the unique design of the LHCb detector, which unlike other LHC experiments, was built in only one direction along the LHC beam line such that the pp interaction point is not in the centre of the detector. This had the advantage of freeing up more space in the cavern to construct larger subdetector systems with easier access to route services (*e.g.* cables and cooling) and reduced the amount of material in the detector acceptance, which helped the LHCb collaboration save on financial costs.

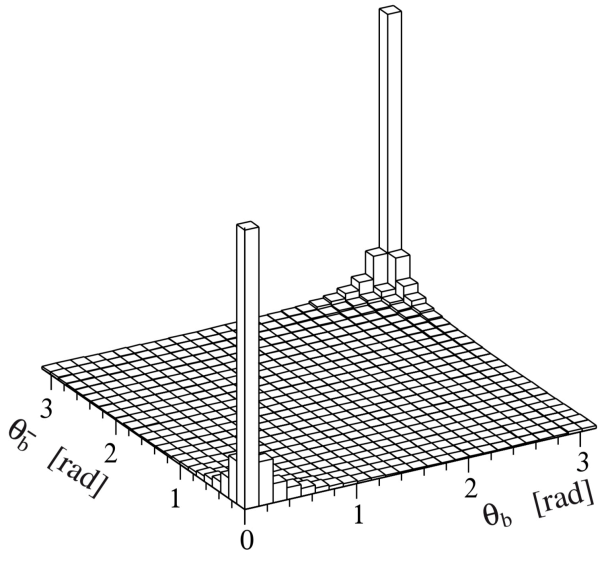

Figure 2.2: The angular production distribution of $b\bar{b}$ quark-antiquark pairs from simulated pp collisions, at $\sqrt{s} = 14\,\text{TeV}$, reproduced from [122].

A vertical cross-section of the LHCb detector, with respect to its global coordinate system, is shown in Figure 2.3. A right-handed coordinate system is chosen, such that the z-axis is defined to positive in the same direction as the clockwise circulating proton travelling in the LHC. The y-axis is perpendicular to the z-axis in the vertical plane with the positive direction chosen to be upwards, and then the x-axis is in the horizontal, with the positive direction pointing into the centre of the LHC ring. The pp interactions take place at $(x, y, z) = (0, 0, 0)$ surrounded by the VErtex LOcator (VELO) subdetector, which provides the first tracking points of any new particles created in the collisions. Particles travelling within the acceptance of LHCb then traverse the first of two Ring-Imaging CHerenkov (RICH) subdetectors, which contribute towards particle identification at LHCb, before passing through the Tracker Turicensis (TT). The particles then reach a powerful magnet, which bends the trajectories of charged particles and allows their momenta to be determined, after which they traverse three further tracking stations (T1-T3) and a second RICH system. Lastly, they pass through the calorimetry systems (ECAL and HCAL) and the muon chambers (M1-M5), if they penetrate through the detector far enough. These subdetectors help identify photons, electrons, charged hadrons and muons. The total angular coverage of LHCb ranges from 10 mrad to 300 (250) mrad in the horizontal (vertical) plane.

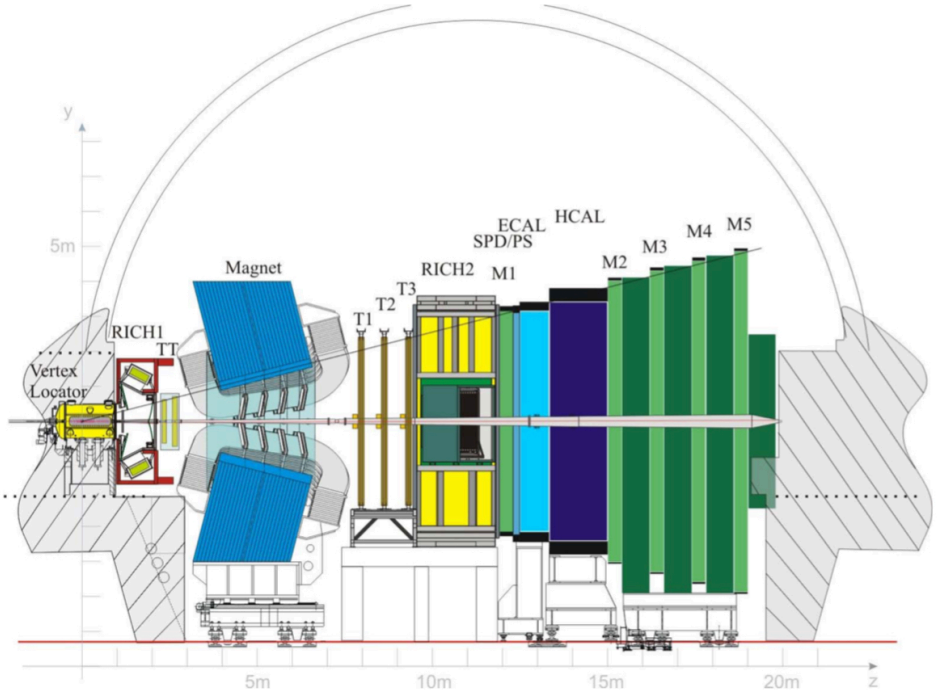

Figure 2.3: An illustration of the LHCb detector as seen in the y–z reference plane with all the subdetectors shown. The illustration was reproduced from [120].

Analyses performed at LHCb need to reliably measure the points in space where heavy-flavoured hadrons decay into more stable particles. This generally works more

efficiently when the number of pp collisions producing tracks within the LHCb acceptance is relatively low. This is known as pile-up; the average pile-up in Run II was 1.6 tracks per bunch crossing. Pile-up is connected to the luminosity, $\mathcal{L}$, of a particle accelerator, which is defined as the number of particle bunch crossings per unit area per unit time. The maximum $\mathcal{L}$ delivered by the LHC accelerator to ATLAS and CMS during Run II resulted in $\mathcal{O}(50)$ interactions per bunch crossing. LHCb cannot perform well in these nominal LHC conditions. To overcome this, the $\mathcal{L}$ delivered to LHCb is reduced by a factor of 10–50 compared to the $\mathcal{L}$ reaching the general purpose detectors. This is achieved by continually altering the overlap of the colliding beams in the transverse (y–z) direction during a physics Fill. This yields a roughly constant instantaneous $\mathcal{L}$ within a range of 5%. Degradation of the proton beams as they circulate the imperfect vacuum of the LHC is however inevitable. This means once the beams are fully overlapping, stable conditions can no longer be maintained. The nominal time-scale of a physics Fill at LHCb is thus around 15 hours, see Figure 2.4. Each Fill is composed of approximately one hour 'Runs'. LHCb Runs are a partition of the collected data in the form of manageable chunks based on time. Like Fills at LHCb, Runs are assigned serial numbers. A comparison plot of the instantaneous luminosity delivered to ATLAS, CMS and LHCb is shown in Figure 2.4.

A total integrated luminosity of $3\,\text{fb}^{-1}$ of data was recorded from a centre-of-mass energy of 7 TeV (2011) and 8 TeV (2012) during Run I. Between 2015 and 2018, $7.1\,\text{fb}^{-1}$ of data was recorded at a higher centre-of-mass energy of 13 TeV where the production cross sections of $b\bar{b}$ and $c\bar{c}$ quark pairs is two times larger than at 7 TeV [123]. Around $7(1) \times 10^{12}$ $c\bar{c}$ ($b\bar{b}$) quark pairs are produced each year in Run-II pp collisions [123]. The recorded total integrated luminosity for LHCb by the end of data taking in Run II totalled around 9.1 fb^{-1} of data, making it the largest data set specific for heavy-flavour physics ever gathered. The breakdown of the recorded integrated luminosity at LHCb from each year of data taking is shown in Figure 2.5.

Data recorded in both Run I and Run II were used in the analysis work presented in this thesis. The searches for a doubly charmed baryon, described in Chapters 4 and 5, uses data from 2012, 2015 and 2016. The RICH calibration studies detailed in Chapter 3 uses 2016 data, while the trigger studies presented in Chapter 6 were carried out on 2016 data and were verified using 2018 data. The main components of the LHCb detector are detailed in Sections 2.3−2.5. Collectively, these systems were essential in recording and processing the data used in the analyses presented in this thesis.

2.3 Tracking

The path of any particle created in a pp collision at LHCb, which is stable on the time-scale of the detector and is within its acceptance, is tracked by a combination of a vertex locator,

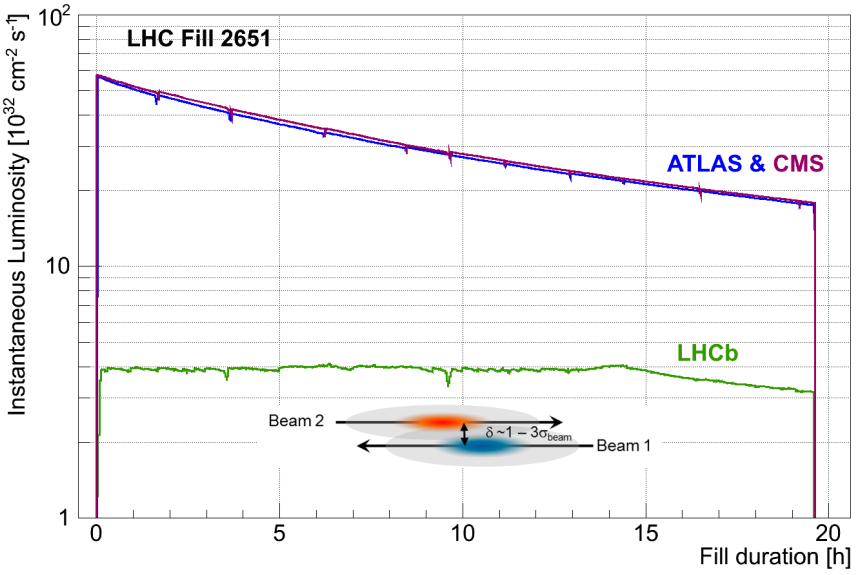

Figure 2.4: A plot of instantaneous luminosity versus time, in hours, at the ATLAS (blue), CMS (purple) and LHCb (green) *pp* interaction points, during LHC Fill 2651. The plot was reproduced from [124].

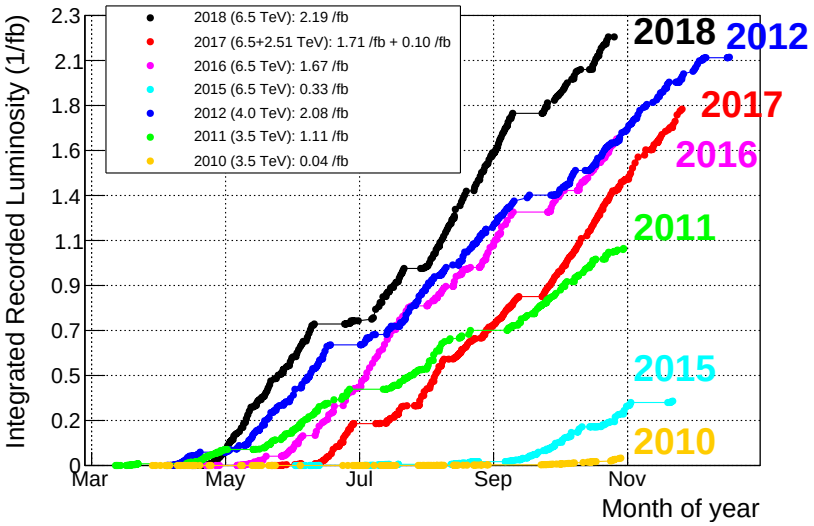

Figure 2.5: The integrated luminosity from *pp* collisions recorded at LHCb during different data-taking years up to the end of Run II. The plot was reproduced from [125].

a series of tracking stations and a dipole magnet. Each particle leaves behind different signatures in all or some of these sub-detectors with the magnet's field causing certain tracks to bend if they originate from electrically charged particles. Then through use of a Kalman Filter process [126], these detector hits are iteratively group together to determine the likely trajectory of many particle as possible. Each track is also given a χ^2 per degree of freedom (χ^2_{vtx}/ndf) to determine the quality of the reconstructed track. The

combined tracking system must be able to reconstruct the trajectory of particles and their associated points of decay with high spatial resolution, such that the momenta of tracks can be determined to great accuracy. With the knowledge of these track trajectories and points of decays at hand, full decay chains of particles of interest can be assembled and decay topologies understood. This makes the tracking system fundamental to all physics analyses at LHCb.

2.3.1 Vertex Locator

The VELO [121], an abbreviation for VErtex LOcator, is a silicon micro-strip detector capable of precise tracking near the LHCb pp interaction point. The VELO gathers information from electronic hits in its micro-strips to reconstruct the trajectories of particles. Primarily, the VELO is used to distinguish between locations where pp interactions occur in bunch crossings, known as the Primary Vertices (PVs), and points in space were long-lived hadrons decay, which are referred to as Displaced Vertices (DVs). The number of PVs from a single bunch crossing is kept relatively low at LHCb through the process of luminosity leveling. The active region of the VELO is large enough to reconstruct the majority of heavy-flavoured hadrons, which typically travel a few mm to a few cm from a PV. Combining the momentum measurements made by the downstream tracking stations with knowledge of the positions of the PVs and DVs in an event, then the time before a particle decays, its decay time, can be determined by LHCb. An event is defined as the complete detector readout for a proton bunch crossing.

Due to the short Flight Distance (FD) of the particles of interest to LHCb and their close proximity to the beam line, it is important that the VELO is situated as close to the pp collisions as possible to minimise the extrapolation distance between the first hit of a reconstructed track and the interaction point. However, if the VELO is too close to the beam line then it will incur radiation damage. For this reason, the VELO is constructed as two structures with the ability to separate from one another. During the beam injection from the SPS to the LHC, the VELO is retracted to 29 mm away from the beam into two composite halves, one either side of the LHC beam pipe. When the beams are declared stable during a physics fill, the halves are carefully brought together by a mechanical system that leaves the halves overlapping slightly such that the pp interaction point is fully enclosed. At this point the VELO is centred around the beam-line and is ready for data taking. When fully closed, the VELO has a a 7 mm aperture in the centre to enable the proton beams to pass through without interacting with and damaging the silicon-strips. The closest active region of the micro-strips then begins 8.2 mm from the beam line. At these close proximities, the VELO material is still inside the radius nominally covered by the LHC pipe. Therefore, to maintain a good vacuum within the beam pipe,

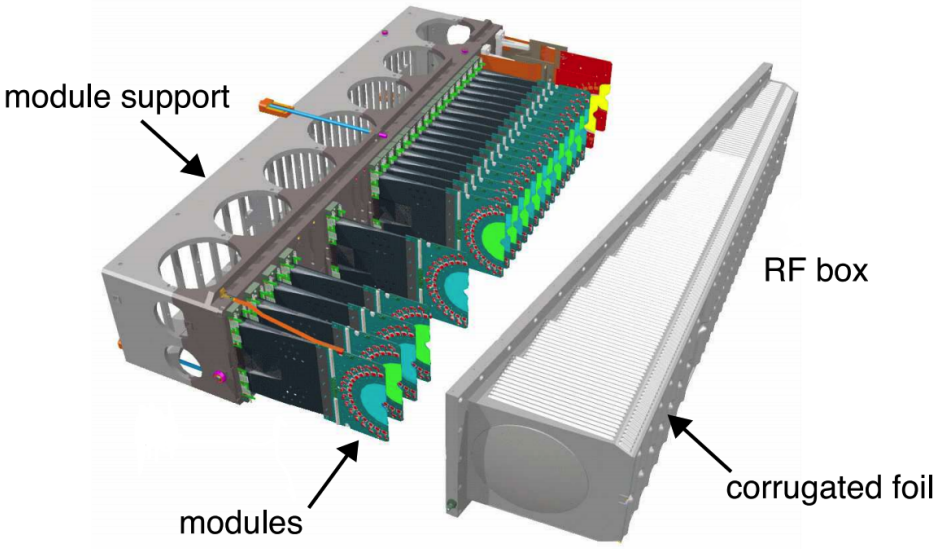

Figure 2.6: One half of the fully assembled VELO subdetector showing the individual modules and their support system with the RF-box removed, reproduced from [120].

to shield against electromagnetic activity from the beams and to provide a continuous path for the mirror currents of the beam through the VELO, the micro-strip detectors are mounted within a structure covered by aluminium foil, known as the Radio Frequency box (RF-box). On the side of the RF-box that is facing the beam, the foil is slighter thinner at only 300 μm to minimise the amount of material the tracks see but is still thick enough to separate the RF-box from the beam vacuum. As a result, a vacuum pressure of approximately 10^{-7} mbar is achieved inside the VELO. Figure 2.6 shows the layout of one half of the VELO once the RF-box is opened up.

The VELO halves both contain twenty-one identical detector modules positioned along the beam line in each half. The temperature of the modules are maintained below zero degrees by a bi-phase cooling system. Each module contains two semi-circular shaped senors composed of 300 μm thick silicon wafer with implanted aluminium micro-strips. The sensors measure the radial coordinate, R, and the azimuthal angle coordinate, ϕ, of the tracks of particles passing the VELO. The z-coordinate is determined from what module along the beam line registered the hit. As shown in Figure 2.7, the VELO modules are packed more closely together near the interaction region; this is to give an improved PV resolution. Each time the VELO is closed the alignment of the R sensor is required to have an accuracy smaller than 100 μm relative to the other half of the detector. In Run II, the alignment is checked at the end of every Fill, while in Run I the alignment was updated a few times during the year. A schematic of the R and ϕ sensors is shown in Figure 2.8 for one VELO module. The pitch − the distance between the sensor strips − increases further from the beam line, starting at around 40 μm and going up to roughly 100 μm. In total, each sensor has 2,048 readout channels.

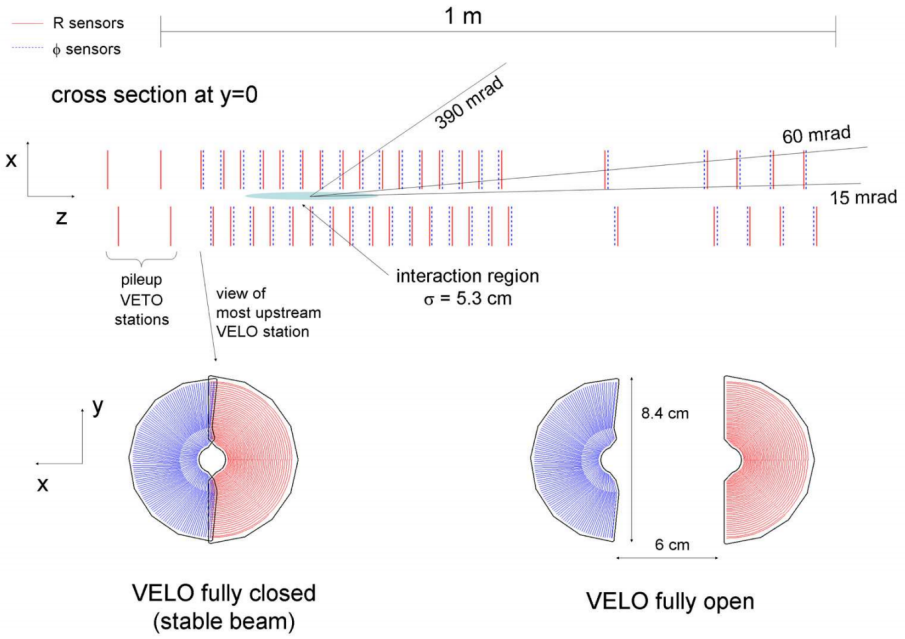

Figure 2.7: An overview of the layout of the VELO modules with the R sensors (red) and ϕ sensors (blue) also shown, reproduced from [120].

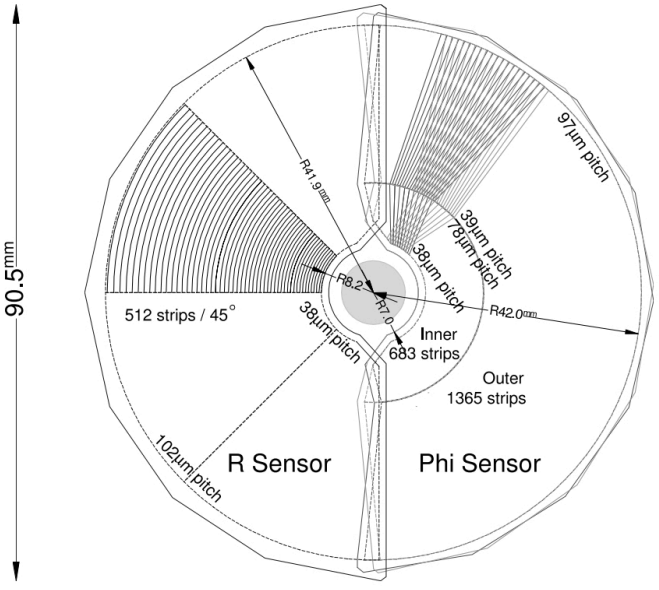

Figure 2.8: The layout of the silicon micro-strips on the R and ϕ sensors of a singular VELO module, reproduced from [120].

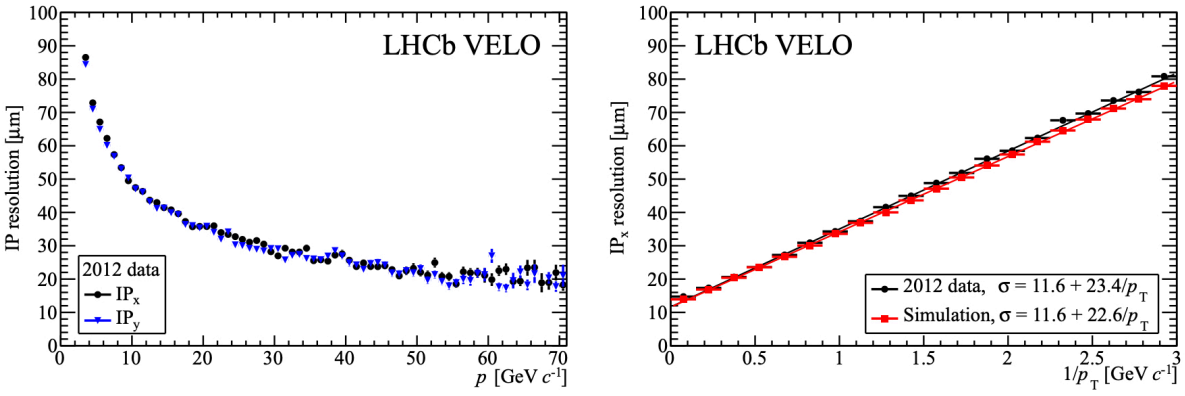

Figure 2.9: (Left) The IP resolution, in μm, as a function of the momentum of a track, in GeV/c. (Right) The IP$_x$ resolution, in μm, as a function of the inverse of the momentum of a track, in GeV/c, for 2012 data (black) and simulated pp events (red). Both plots were reproduced from [121].

The VELO can also determine the Impact Parameter (IP) of track. The IP quantity is the distance of closest approach with respect to a reconstructed PV. The increase in pitch ensures that the measurements along the track contribute to the precision of the IP value approximately equally. An associated quantity of the IP variable, the χ^2_{IP} of a track, helps determine the likely PV from which a particle originated. The χ^2_{IP} is defined as the difference in χ^2 of a given PV reconstructed with and without the considered track. Decays of heavy-flavoured hadrons generally have larger FD and IP values than the decays of light hadrons at LHCb. This makes the FD and IP quantities particularly useful for separating these two different classes of decays in an event. The performance of the VELO can be quantified by its excellent IP resolution, which was found to be less than 35 μm for particles with transverse momentum (p_{T}) greater than 1 GeV/c for 2012 data [121]. The same data set showed that for a typical pp event, the vertex resolution was between 10 and 20 μm. This accuracy means LHCb is more precise at locating vertex objects than any other LHC experiment thanks to the VELO. In the left plot of Figure 2.9, the IP resolution in the x and y directions are given as a function of the momentum of a track. The right plot of Figure 2.9 shows the dependency of the IP resolution projected in the x-axis, on the inverse of a track's transverse momentum.

2.3.2 Tracking Detectors

Assisting the VELO subdetector in tracking particles through LHCb are a further four planar detectors; the Tracker Turicensis (TT) and three tracking stations (T1-T3) [127]. The high levels of radiation close to the beam line means the TT and the inner regions of T1-T3 are built of radiation-hard silicon strips. They are thus collectively known as the Silicon Trackers (ST). The ST have a high granularity to keep hit occupancy at a

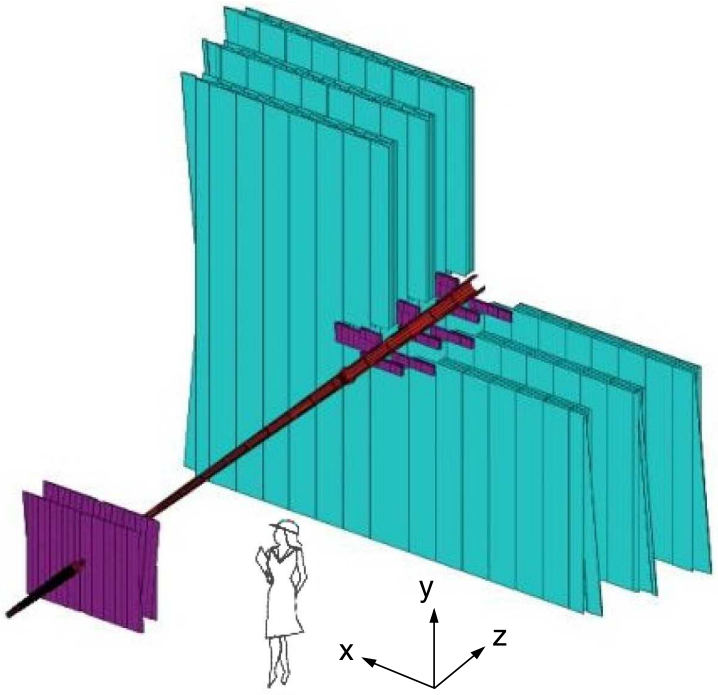

Figure 2.10: A perspective view of the tracking system with the ST (purple) and the OT (blue) shown, reproduced from [120].

low enough level to allow for effective track reconstruction. The outer regions of T1-T3, relative to the beam line, are referred to as the Outer Tracker (OT) [127]. The OT is situated in a region of the detector that is subject to a lower number of particles per unit area compared to the ST. The lower particle flux means the OT is set up as a drift-time detector with cost-effective gas filled straw tubes. Despite their different locations and constructions, the ST and OT ultimately both serve the same purpose - to measure the trajectories of charged particles such that their momenta can be measured. The illustration in Figure 2.10 gives an overall perspective of the layout of the tracking detectors at LHCb.

The TT has a length of 1.5 m and a width of 1.3 m to cover the full acceptance of the LHCb detector. It is composed of four layers of 500 μm thick p^+-on-n silicon micro-strip sensors with a pitch of approximately 200 μm. The first (TTa) and last layer (TTb) of the TT have their sensors oriented vertically while the middle two sensors are oriented at $\pm$ 5° from the horizontal in opposing directions. The angled orientation of the layers of the TT is shown in Figure 2.11. The reason for this arrangement is that it maximises the resolution in the x-direction, which is the direction responsible for the momentum resolution; the resolution in the y-direction is only needed for pattern recognition and is less critical. This angled orientation of the layers leads to an excellent single-hit spatial resolution of 50 μm [127]. The detection layers are separated by approximately 30 cm in the z-axis and each TT sensor carries 512 readout strips.

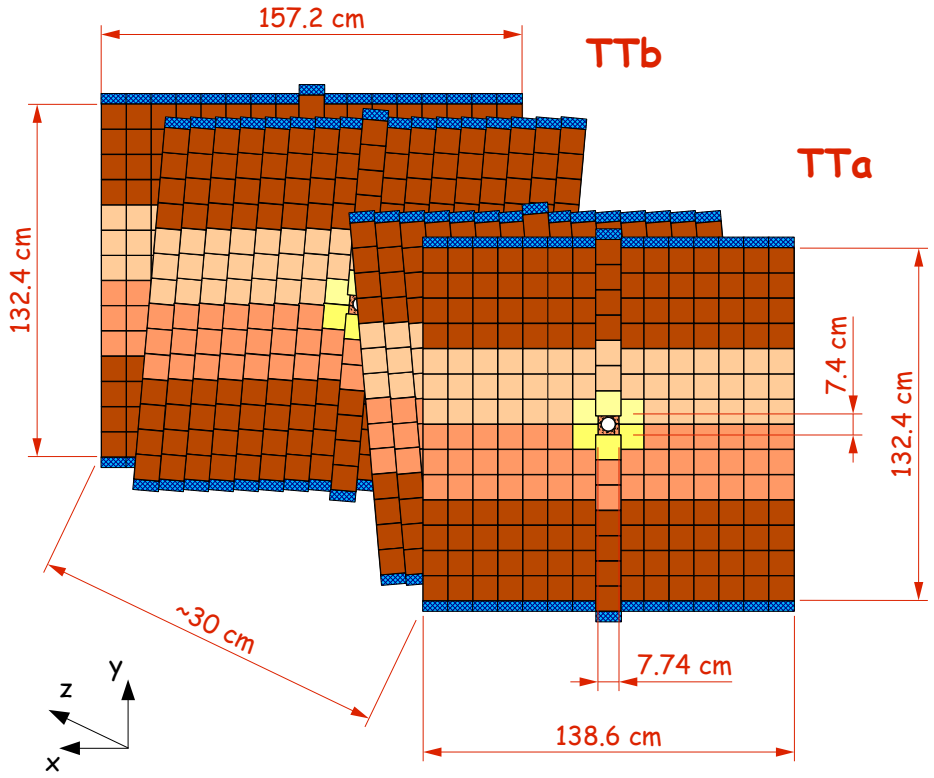

Figure 2.11: The layout and dimensions of the four detection layers of the Tracker Turicensis subdetector. The illustration was reproduced from [128].

The inner regions of the T1-T3 tracking stations are designed similarly to the TT, with a stereo-angle rotation in the alignment of its layers. The layers are arranged in a cross-shape, measuring 1.2 m wide and 0.4 m high, as shown in Figure 2.12. A greater horizontal coverage than vertical one is required to account for the bending of particles from the field of the dipole magnet. The silicon strips have a pitch of around 193 μm and a spatial resolution of approximately 50 μm. The remainder of the T1-T3 stations, consists of an array of straw tube modules. These OT modules consist of two layers of drift tube with an internal diameter of 4.9 mm. The tubes are filled with a mixture of argon (70%) and CO_2 (30%) gases, which become ionised following the passing of charged particles through them. This induced ionisation of the gas releases electrons that are attracted towards a carbon-doped cathode where the signal is deposited. A gold-plated anode wire is located at the centre of the tubes and the outer layer of the tube walls are made from aluminium. The drift time of the electrons travelling to the centre of the tubes is measured with respect to the crossing signal of the inducing track. The gas mixture is specifically chosen such that a low drift time of around 50 ns and a spatial resolution of 200 μm are achieved. By combining knowledge of the drift time and drift velocity from

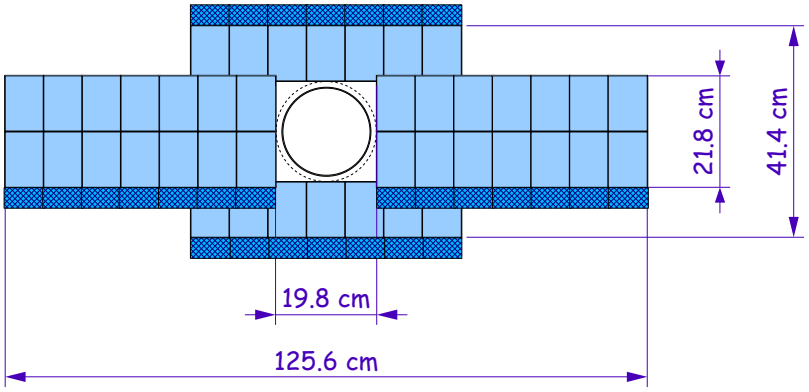

Figure 2.12: The layout of the inner regions of the T1-T3 showing the array of straw tube modules. The illustration was reproduced from [128].

each passing charged particle, the position of the track through the subdetector can be determined. Overall, the OT consists of 55,000 individual straw tubes.

The performance of the tracking system at LHCb was evaluated during Run I [127]. The track hit efficiency of the ST was measured using a pure sample of $J/\psi \to \mu^+\mu^-$ decays. The muon tracks must pass some basic kinematic requirements and need to have a momentum greater than 10 GeV/c to reduce multiple scattering. The hit efficiency is defined as the ratio of the number of hits found against the number of hits expected, for a given sector of the tracking system. For the TT, this efficiency was measured to be greater than 99.7% (99.8%) in 2011 (2012) data. Similarly, T1-T3 also had a very high hit efficiency of 99.8% (99.9%) according to 2011 (2012) data. The performance of the tracking system can also be evaluated in terms of its hit resolution. The resolution is determined using data from the unbiased residuals of the measured hit position and the extrapolated track position when the hit is removed from the fit. The hit resolution of the TT is measured to be 52.6 (53.4) μm in 2011 (2012) data and for the inner region of the T1-T3 tracker, it was found to be 50.3 (54.9) μm in 2011 (2012) data.

2.3.3 Spectrometer Magnet

The LHCb tracking system exploits a dipole magnet to bend the tracks of charged particles. The curvature of the tracks and precision knowledge of the magnet's field at all points allows the particle's momentum to be determined. Thanks to the magnet and the rest of the tracking system, the relative uncertainty on the momentum resolution varies from 0.5% at low momentum to 1.0% at 200 GeV/c [127], leading to an excellent mass resolution of around 10 MeV/c^2.

The magnet is situated immediately after the TT as shown in Figure 2.3. The centre of the magnet is 5.3 mm from the pp interaction point, along the z-axis. It is composed

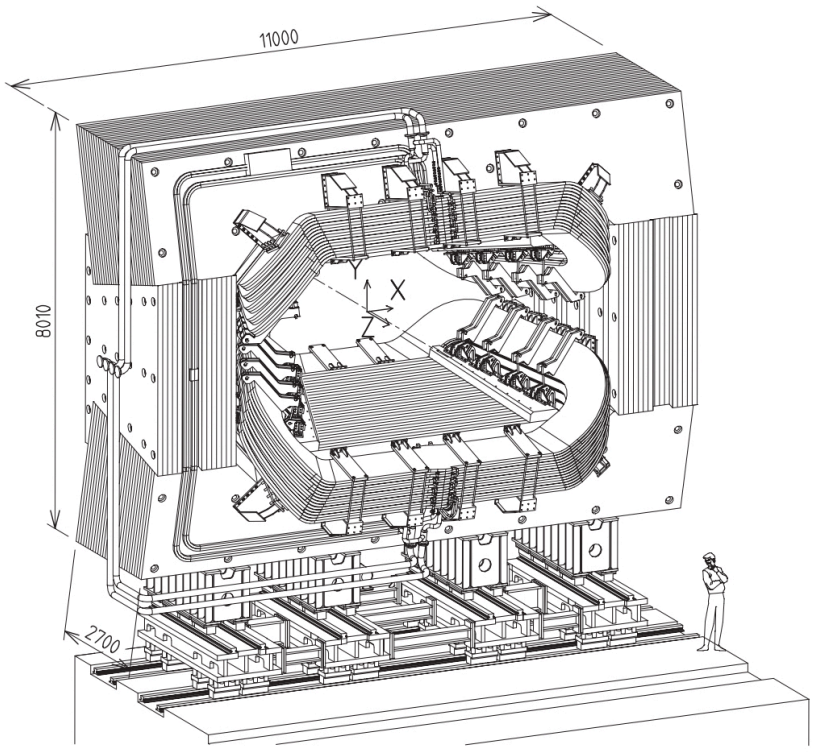

Figure 2.13: A perspective view of the magnet with dimensions given in units of mm and the electrical connections and water cooling system also shown. The figure was reproduced from [120].

of a 1,500 ton iron yoke and two conical saddle shaped coils located above and below the beam line. The coils are made of aluminum and weigh in at around 27 tonnes. A schematic diagram of the magnet, showing its design, is given in Figure 2.13. This is a warm magnet capable of producing an integrated magnetic field strength of approximately 4 Tm between the interaction point and the tracking stations, with the principal field component directed along the y-axis.

A precise knowledge of the magnetic field is required to ensure a good momentum resolution can be achieved. This is particularly important for the LHCb detector, since its tracking stations are fairly spaced apart compared to other high energy physics experiments. The integrated field was measured using an array of Hall probes and is found to give a very high relative precision of 4×10^{-4} across the measured volume. Data is collected at LHCb for both 'MagUp' (field pointing in $+y$ direction) and 'MagDown' (field pointing in $-y$ direction) configurations for an approximately equal amount of time during data taking to cancel out potential asymmetry effects caused by the magnetic field. For instance, the performance of the drift tubes in the OT are very sensitive to the direction of the magnetic field. This detector effect could be misinterpreted as signs of CP-violation if not treated correctly. However, the polarity of the magnet is only flipped a few times per year of data taking so not to damage the magnet.

2.4 Particle Identification

The importance of precise tracking of particles for analyses at LHCb is highlighted in Section 2.3. However, without the ability to identify the type of tracks created in a pp collision, the LHCb detector could not separate decays of heavy-flavoured hadrons from other decays present in an event. A combination of two Cherenkov radiation detectors, a calorimeter system and a set of muon chambers allows LHCb to determine what tracks pass through the detector to an outstanding level of accuracy. For the analyses present in this thesis, where a variety of different track species are present in the decays of interest, this proficiency in identifying tracks is particularly important.

2.4.1 Ring Imaging Cherenkov Detectors

Two Ring Imaging CHerenkov detectors (RICH-1 and RICH-2) contribute towards efficient particle identification (PID) at LHCb. PID refers to the determination of the species of a track reconstructed in the detector, namely; electrons (e), muons (μ), pions (π), kaons (K) and protons (p) in the case of the RICH subdetectors. The RICH systems offer the best means of identifying charged hadrons at LHCb but the calorimeter and muon systems provide complimentary information, which further enhance PID capabilities of LHCb. Information from RICH-1 and RICH-2 ultimately help reduce the chances of wrongly misidentifying decays as ones of interest in any particular analysis.

The RICH subdetectors exploit the phenomenon of Cherenkov radiation to extract PID information. This situation occurs when a charged particle traveling through a dielectric material emits a cone of coherent light if its velocity is greater than the phase velocity of light in the dielectric. The opening angle, θ_c, of this light cone is dependent on the particle's velocity according to

$$\cos\theta_c = \frac{1}{n\beta}, \tag{2.1}$$

where n is the refractive index of the dielectric material that the particle passes through and β is the ratio of the particle's velocity to the speed of light in a vacuum, v/c. The value of θ_c is relative to the inducing particle's trajectory. By making use of some basic relativistic kinematics, Equation 2.1 can be rearranged in terms of the mass, m, and momentum, p, of the particle inducing the Cherenkov radiation as

$$\cos\theta_c = \frac{1}{n}\sqrt{1+\left(\frac{mc}{p}\right)^2}. \tag{2.2}$$

In essence, this means that if the momentum, p, of the particle can be measured, along with the Cherenkov angle, θ_c, of its emitted light cone, then the rest mass, m, of the particle can be inferred. At high enough momentum however ($p \gg mc$), all track types give the same value for θ_c, equal to $1/n$, see Equation 2.1, and the particles become indistinguishable from each other; these tracks are said to be saturated. Figure 2.14 shows the dependence of θ_c on the momentum of a particle for different species of particles. All track types are shown to be saturated above 20 GeV/c. An analysis utilising saturated tracks is presented in Chapter 3 where the effect of saturation is discussed in more detail.

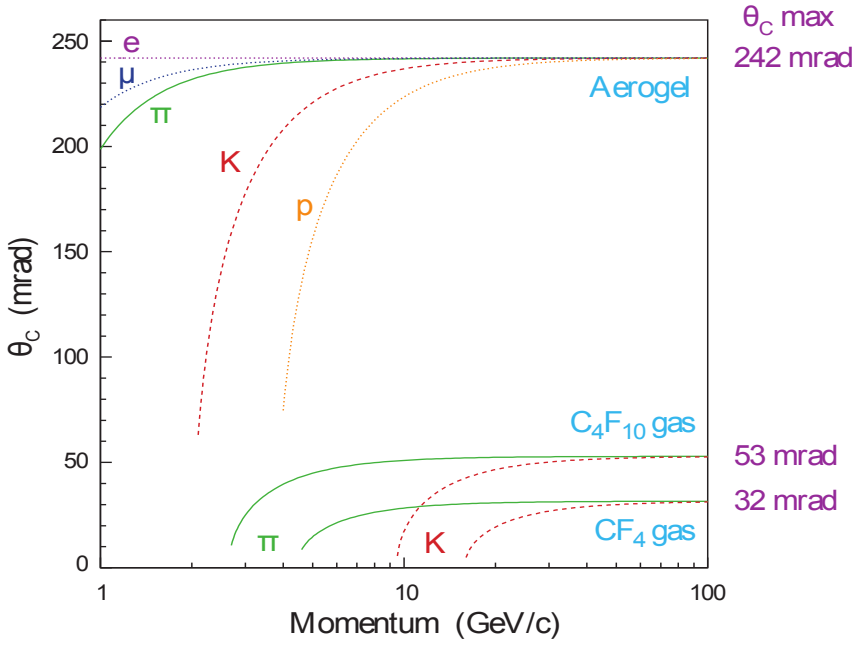

Figure 2.14: The Cherenkov angle, θ_c, in mrad, of photons produced in the RICH subdetectors by electrons (purple), kaons (red), pions (green) and protons (orange) as a function of particle momentum, in GeV/c. The plot was reproduced from [120].

RICH-1 [129] is located between the VELO and the TT. It covers the full angular acceptance of the LHCb, 25 mrad to 300 (250) mrad in the horizontal (vertical) plane and is designed to perform PID for tracks with momentum between 1 and 60 GeV/c. RICH-1 is divided into two halves set above and below the beam pipe, which are referred to as the 'Up' and 'Down' sections. RICH-2 [130] is positioned between the magnet and the T3 tracking plane. It provides PID for higher momentum tracks which are between 15 to 100 GeV/c. Since high momentum tracks are not swept out to wide angles by the magnetic field, they predominantly stay close to the beam line. Therefore, RICH-2 covers a smaller angular region of 15 mrad to 100 (120) mrad in the vertical (horizontal) plane. RICH-2 is also similarly divided into two sections, named 'A' and 'C', and in the horizontal in this case. Section A is closer to the centre of the LHC ring with Section C further away. Figure 2.15 shows the layout of RICH-1 and RICH-2 in the vertical and horizontal planes, respectively.

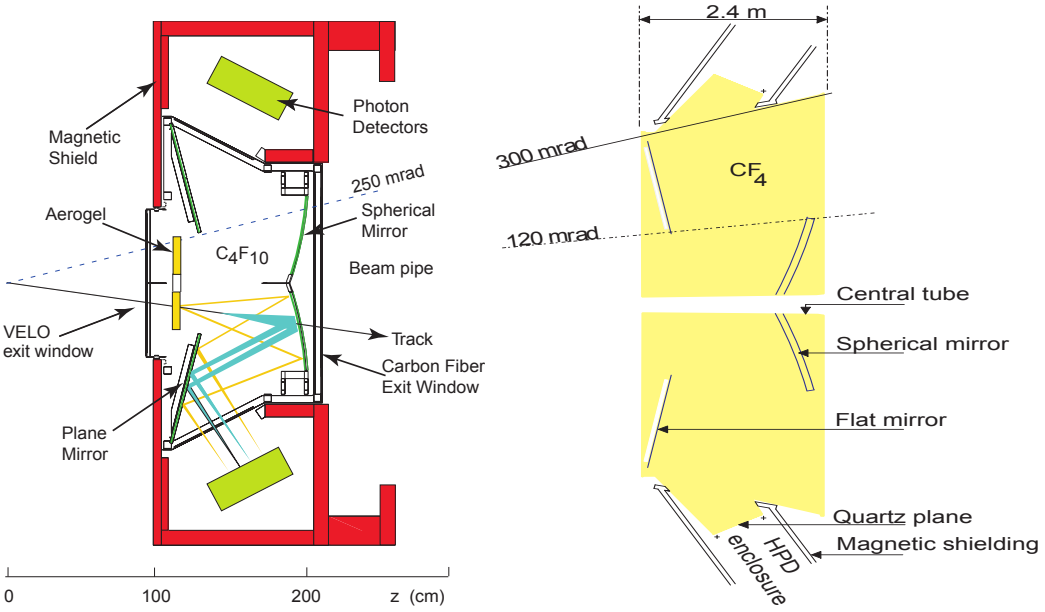

Figure 2.15: Schematic of the RICH-1 (left) and RICH-2 (right) subdetectors at LHCb. Both diagrams were reproduced from [120].

The dielectric materials within the RICH systems are known as the radiators. They determine the momentum range in which the RICH systems are sensitive. There were two radiators present in RICH-1 during Run I; C_4F_{10} gas ($n \simeq 1.0014$) and an aerogel block ($n \simeq 1.03$). The aerogel block was removed before the start of data taking in Run II, due to worse than expected performance caused by the block. RICH-2 contained a CF_4 gas radiator ($n \simeq 1.0005$) in both Run I and Run II. In order for the RICH systems to be able to detect the emitted Cherenkov light from each particle, the light is reflected out of the detector's acceptance by a series of flat and spherical mirrors towards Hybrid Photon Detectors (HPDs). The mirrors are very precisely aligned and monitored for movement at the end of each physics Fill in Run II. The emitted light cones are ultimately seen as ring structures when projected onto these HPDs. Images of Cherenkov rings from a nominal pp event at LHCb are shown in Figure 2.16. The candidate's preliminary study into the effects of the magnetic field on the θ_c resolution in RICH-1 necessitates a thorough discussion of the workings of the HPDs. As such, all the technical details about the HPDs, used in RICH-1 and RICH-2, are given in Chapter 3.

Every track object with an associated momentum measurement from the tracking system and travelling through the RICH subdetectors, has its expected θ_c angle calculated under five different mass hypotheses (e, K, μ, π and p) according to Equation 2.2. The radius of the photon ring corresponding to this expected value of θ_c is then compared to a fit of the detector responses simultaneously [132]. A few examples of the fits to different Cherenkov rings can also be seen in Figure 2.16. Under each mass hypothesis the log-likelihood of the RICH detector response fit compared to the expected photon ring

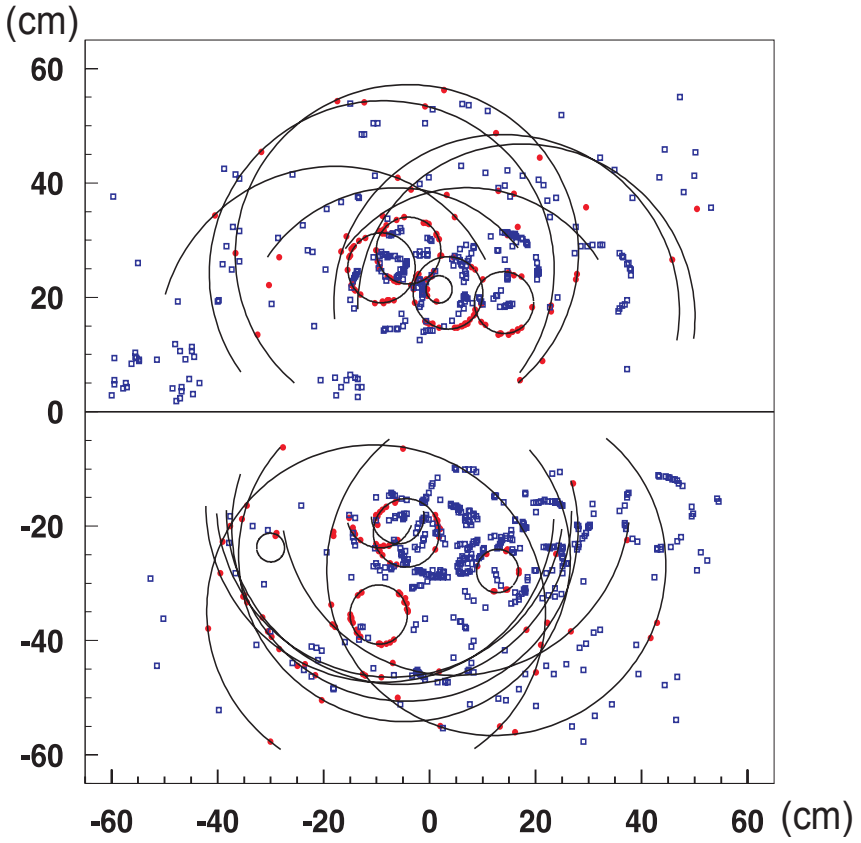

Figure 2.16: An example event display showing Cherenkov rings formed from hits in the HPDs in the Up (top plot) and Down (bottom plot) sections of RICH-1. The rings that have not been fitted have no associated track. The figure was reproduced from [131].

radius is calculated. However, instead of computing the absolute log-likelihood values, the RICH PID software calculates the difference in log-likelihood (DLL) between the pion hypothesis and each of the four remaining mass hypotheses, x, where $x \in \mathrm{e}, K, \mu, p$, such that $\mathrm{DLL}_x \equiv \mathrm{DLL}_x - \mathrm{DLL}_\pi$. The choice of pions as the reference hypothesis is somewhat arbitrary and based on the fact they are the most abundantly produced particle at LHCb.

This DLL procedure does carry a certain rate of misidentification however; tracks can be wrongly assigned a track type which does not reflect their true identity. To investigate the rate at which this occurs, the RICH particle identification performance is studied using data containing large samples of genuine pion, kaon and proton tracks. These data control samples are selected independent of any RICH information by using kinematic criteria alone. Pion and kaon tracks are taken from $D^{*+} \to D^0(K^-\pi^+)\pi^+$ decays with proton tracks coming from $\Lambda^0 \to p\pi^-$ decays. The kaon identification and kaon-pion misidentification efficiencies for 2011 data, across different values of track momentum, are shown in Figure 2.17. A loose ($\mathrm{DLL}_{K\pi} > 0$) and a tight ($\mathrm{DLL}_{K\pi} > 5$) DLL requirement are also separately applied to the data shown in the results in Figure 2.17. The correct PID rate decreases at higher momentum, since tracks near saturation and the value of θ_c then tends towards the same value for each mass hypothesis. Overall the PID performance

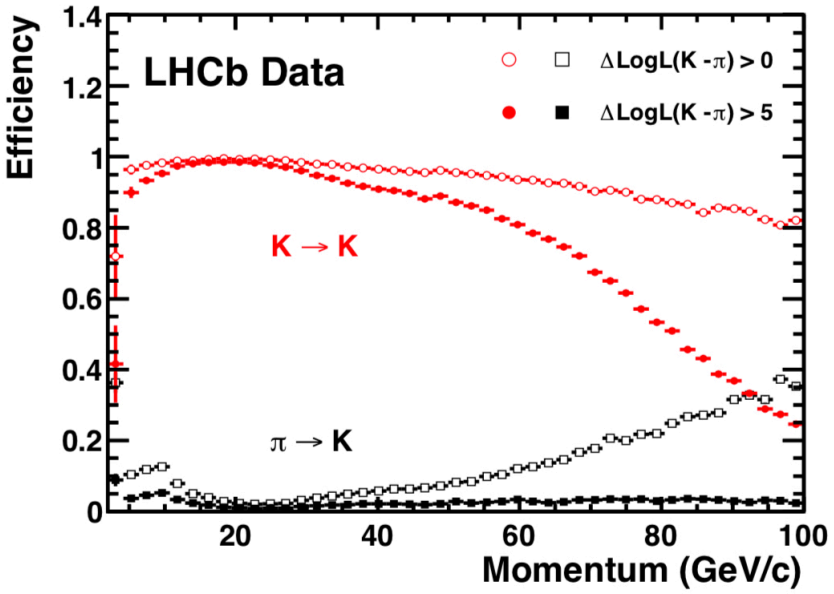

Figure 2.17: Kaon identification efficiency (red) and kaon-pion misidentification rate (black) as a function of track momentum, in GeV/c, from 2011 data. The plot was reproduced from [133].

is shown to be excellent however, with a greater than 90% correct PID rate and a less than 10% mis-ID rate for the kaon across a wide momentum range [133]. The rate of identification and misidentification was also found to be uncorrelated. Similar studies are conducted for the pion and proton (mis)identification performances and efficiencies of greater (less) than 90% (10%) are also found for these hadrons.

Despite the excellent performance of the RICH systems, making requirements on the equivalent PID variables in simulation are generally not recommend by the LHCb collaboration since MC cannot accurately simulate the run-time conditions of the RICH detectors. For instance, the refractive index n of the radiators are dependent on the pressure and temperature inside the RICHes. This varies throughout the annual operational period but in simulation the refractive index is set as a constant value, roughly the average expected value throughout the year. Hence, there is usually some non-negligible difference between PID discriminants for data and simulation.

2.4.2 Calorimeter System

Electron and hadron candidates can also be identified by a calorimeter system at LHCb. This system consists of scintillating-pads, pre-shower detectors, a hadronic calorimeter and an electromagnetic calorimeter. Collectively, these subdetectors provide a means of identifying electrons, hadrons and photons in a pp event. They also allow particles with high transverse energy to be identified; such energetic particles usually originate from decays of heavy-flavoured particles.

The Electromagnetic CALorimeter (ECAL) and the Hadronic CALorimeter (HCAL) are both situated between the first and second muon tracking stations, as shown in Figure 2.3. The ECAL is used to record the position and energy of particles that interact primarily via the electromagnetic interaction (electrons and photons) while the HCAL serves the equivalent purpose but for hadrons, which interact via the strong force. The HCAL is particularly important for identifying neutral hadrons, since they are not picked up by the tracking stations or identified by the RICH systems. In order to distinguish electrons from hadrons, the ECAL is preceded by a Scintillator Pad Detector (SPD), which identifies charged hadrons and allows neutral ones to be rejected, then a Pre-Shower (PS) detector, which detects electromagnetic showers, and thus identifies electrons only. The information recorded by the calorimeters is particularly important in the hardware stage of LHCb's trigger; this is discussed more in Section 2.5.1. In general, all four components of the calorimeter system operate similarly; particles are stopped in flight by metallic materials, which absorb all the energy of incident particles and then produce cascade showers of secondary particles which generate light in the scintillation pads. The photons released by these scintillating pads are then read out by wavelength-shifting (WLS) fibres.

The calorimeter's design accounts for the difference in particle flux at various parts of the system during a nominal pp event. The granularity of the SPS, PS, ECAL and HCAL modules varies radially from the beam line to ensure a low particle occupancy across all modules. The segmentation of the modules is shown in Figure 2.18. The SPD, PS and ECAL are each split into three sections and the HCAL is divided into two parts. The SPD and PS use multi-anode photo-multiplier tubes (MaPMTs) to read out all photons from 64 different WLS fibres. The MaPMTs allow each WLS fibre to be read out individually, giving a finer granularity to the sensors. The SPD and PS are very similar in design. They both consist of a 15 mm thick lead plates, sandwiched in between two scintillator pads. The SPD determines whether the incident particle is charged or not, then the PS determines whether the particle has created an electromagnetic shower in the lead converter. This effectively allows charged and neutral electromagnetic objects to be differentiated. The active area of the SPD is 7.6 m wide and 6.2 m tall whereas the PS is around 0.5% larger than that.

The ECAL and HCAL modules are equally very similar in design, both contain alternating layers of absorbing and scintillating materials, but they do have some important differences. The ECAL modules are comprised of a 2 mm lead layer to induce electromagnetic showers, followed by 4 mm of scintillator material to capture the shower produced in the lead. On the other hand, the HCAL modules use 1 cm thick iron as the absorber material instead of lead and have 3 mm thick scintillators. The total depth of the ECAL is 42 cm, which corresponds to 25 radiation lengths, to ensure that all the energy from incident photons and electrons is captured. The HCAL is 5.6 λ_{int} deep in the direction of

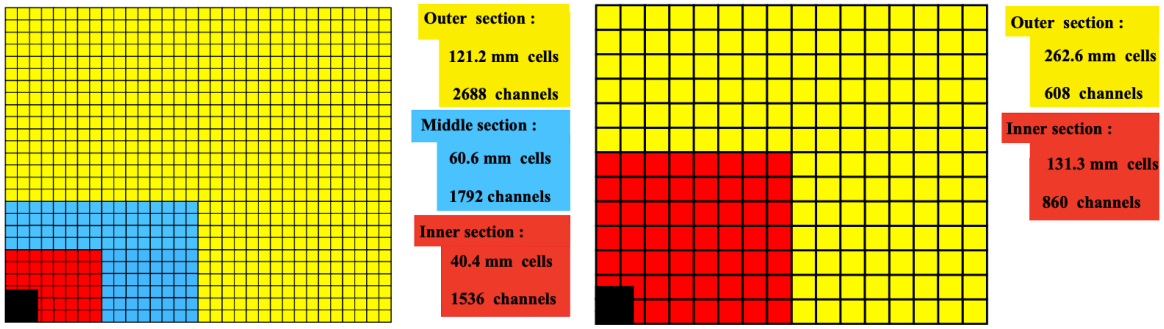

Figure 2.18: Diagram showing the segmentation design for each of the SPD, PS and ECAL (left) and the HCAL (right). The position of the beam pipe is shown in black. The figure was reproduced from [120].

the beam. The λ_{int} parameter is the material's hadronic interaction length, which gives the average distance that hadrons travels between nuclear interactions. The orientation of the scintillators and absorber plates in the ECAL and HCAL modules are also different. The HCAL modules are aligned parallel to the z-axis while the ECAL ones are perpendicular to the z-axis. Both the ECAL and HCAL use individual photo-multiplier tubes (PMTs) to read out the signal from their WLS fibres. The fibres are grouped in bundles to give an even coarser granularity than in the SPS and PS. The layout of an HCAL module, showing its absorbers and scintillators, is given in Figure 2.19.

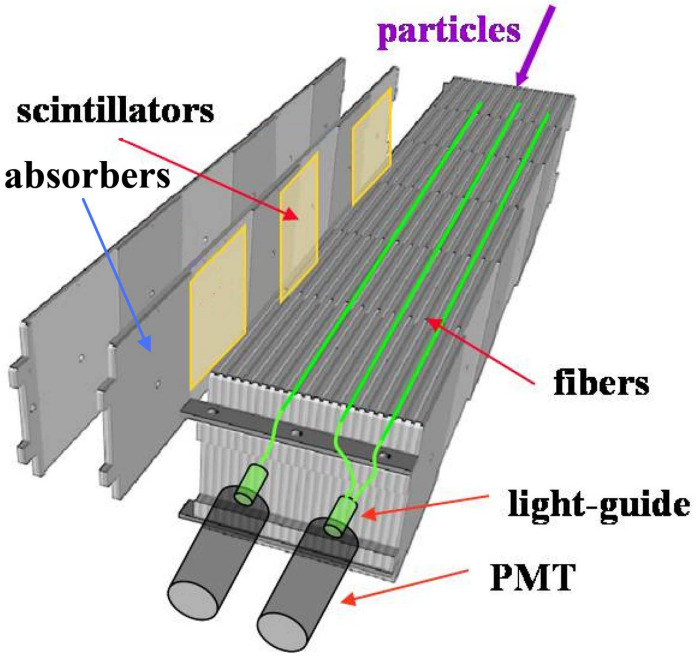

Figure 2.19: The layout of an HCAL module showing the scintillators, absorbers, PMTs and WLS fibres. The illustration was reproduced from [120].

The full performance of the calorimeters is determined from analyses performed

throughout Run I. An array of light emitting diodes (LEDs) are used to monitor the response of the PMTs in both the ECAL and HCAL during different data-taking periods. Good agreement was found between the response of the calorimeters to the light produced by the LEDs and from real signal from particles created in *pp* collisions. The reconstruction and PID performance of the calorimeter system was also carefully measured using $J/\psi \to e^+e^-$ decays from 2011 data. The samples were selected using calorimeter information only. The average electron identification efficiency is found to be $(91.9 \pm 1.3)\%$ while the misidentification rate is only $(4.54 \pm 0.02)\%$ [124]. The inclusion of information from the RICH system is found to increase the electron identification efficiency as well. The reconstruction efficiency of high-energy photons in the ECAL is determined using fits to the invariant mass distribution of selected $B^0 \to K^{*0}(K^+\pi^-)\gamma$ candidates from data; the mass resolution is found to be $93\,\text{MeV}/c^2$ [124]. Using the same sample of B^0 mesons, and a sample of neutral pions, both with similar requirements applied, the average photon identification efficiency is measured to be 95%. This is based on the ability of an Artificial Neural Network (ANN) classifier to select photons within the sample. The ANN manages to reject 45% of the misidentified pion candidates incorrectly reconstructed as photons. Finally, the energy resolution achieved in the ECAL is measured to be $\frac{8\%}{\sqrt{E}} \bigoplus 0.8\%$ while for HCAL it is $\frac{69\%}{\sqrt{E}} \bigoplus 9\%$, where E refers to the energy of the particles in units of GeV [120].

2.4.3 Muon System

The muon system at LHCb is designed to measure the position and energy of tracks left by muons [134]. Due to the comparatively large mass of muons, they emit far less energy through the process of Bremsstrahlung radiation compared to the other particles. Muons then typically penetrate the full length of the detector and thus this system is placed furthest from the *pp* interaction point. Efficient muon tracking is important for many reasons at LHCb; for example, muons are used to help search for rare decays of $B_s \to \mu^+\mu^-$, a channel particularly sensitive to new physics; they also aid in the study of neutral-meson mixing because the charge of muon tracks in a meson decay can infer the flavour of the meson at production. This process is known as 'tagging' at LHCb.

The muon system consists of five rectangular stations (M1-M5) with M1 in front of the SPS/PS and M2-M5 behind the HCAL, as shown in Figure 2.3. The position of the M1 station before the calorimeter is specifically chosen to enhance the momentum measurement of a muon track, which is useful for muon-specific triggers. This is discussed in more detail in Section 2.5. Placed between each muon station are 80 cm thick iron absorbers, which are used to ensure only high momentum muons, above 6 GeV, reach the final M5 station. The surface area of each station also increases further along the

z-axis to ensure an angular acceptance between 20 (16) mrad and 306 (258) mrad in the horizontal, (vertical) plane, respectively. A side-view of all five muon chambers is presented in Figure 2.20. The M1-M3 muon stations are primarily used for tracking and momentum measurements so they have relatively fine granularity along the x-axis to give good spatial resolution. Instead M4-M5 are much coarser as they are intended for accurate PID. For the same reason as the calorimeters, the muon stations are segmented in a particular design to account for varying regions of particle flux across the muon system. As shown in Figure 2.20, the stations are also divided into four separate regions, R1, R2, R3 and R4, based on distance from the beam line. The granularity of each of these regions is such that they all have roughly the same occupancy during a pp event.

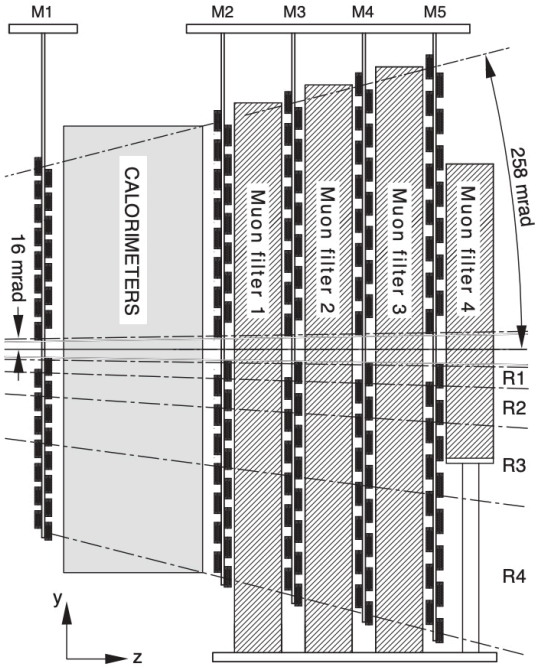

Figure 2.20: A view of the different five muon stations, M1-M5, at LHCb as seen in the y-z plane. The figure was reproduced from [120].

Apart from the inner region of M1, all the sensors in the muon stations use multi-wire proportional chambers (MWPCs). They are composed of two cathode plates spaced 5 mm apart and kept at a potential of 2.5−2.8 kV. A gas mixture containing CO_2 (55%), Ar (40%), and CF_4 (5%) is placed in the gap between the cathodes. A gold-plated tungsten wire, 30 μm in diameter, collects and reads out the electrons produced from ionised gas with a drift-time resolution of 5 ns achieved. Over a thousand MWPCs are used in total across all five chambers. The M1 station is much closer to the interaction point than M2-M5, and as such experiences a much greater particle flux. Therefore, the innermost region of M1, also known as R1, consists of 12 radiation-hard Gas Electron Multiplier (GEM) chambers instead of MWPCs. Each GEM chamber is constructed of sensors with a cathode and anode outer layer with three interceding GEM foils positioned

in between. These foils are surrounded by an inert gas with a composition similar to that found in the MWPCs; CO_2 (15%), Ar (45%), and CF_4 (40%). With the use of this gas, the resulting drift-time resolution of the GEMs is 3 ns.

The performance of the muon system was evaluated using 2011 data using pure samples of tracks selected on kinematic requirements only. The muon identification efficiency and mis-identification rates were based on muon tracks from $J/\psi \to \mu^+\mu^-$ decays, proton tracks from $\Lambda^0 \to p\pi^-$ decays, and kaon and pion tracks both taken from tagged $D^{*+} \to D^0(K^-\pi^+)\pi^+$ decays. The muon selection (mis)identification efficiencies as a function of momentum, are shown in Figure 2.21. Additional PID requirements are also applied to the data samples used in the plots in Figure 2.21. The PID variables used here are not based on the DLL values computed by the RICH systems, as discussed in Section 2.4.1, but instead are Boolean-type variables, which classify a track as either a muon or not a muon. This decision is based on the matching of hits on the muon chambers to the extrapolation of its track. This process is dependent on the p_{T} of the track and thus also the number of muon stations the track passes. Based on the muon sample, the average muon identification efficiency is an excellent 98%. The misidentification rates are also all less than 1% at high p_{T}, based on the kaon, pion and proton samples [135].

2.5 Triggering at LHCb

The LHC operates with a pp bunch crossing rate of 40 MHz. From these bunch crossings around 25% contain decays of heavy-flavoured hadrons that are of interest to LHCb. Beauty and charm hadrons for example are produced inside the detector acceptance at rates exceeding 50 kHz and 1 MHz, respectively. To record each of these interesting interactions would sum to an overwhelming amount of data; too much for the detector to process and for the storage systems to record. The role of the trigger is to reduce the data down to a manageable storage rate using simple selection criteria. LHCb has a flexible and efficient trigger system in place to achieve this reduction. It is organised in three levels [136]; an initial hardware trigger followed by a two-stage high-level trigger based in software. The hardware trigger runs synchronously with the frequency of the pp collisions during a physics Fill at LHC. The overall trigger system operates in a consecutive manner whereby the first software trigger only processes events that pass the hardware trigger and likewise for the second software trigger with respect to the first software trigger. Only events passing all three stages of the trigger are sent to permanent storage where this data is processed further for use in offline physics analyses.

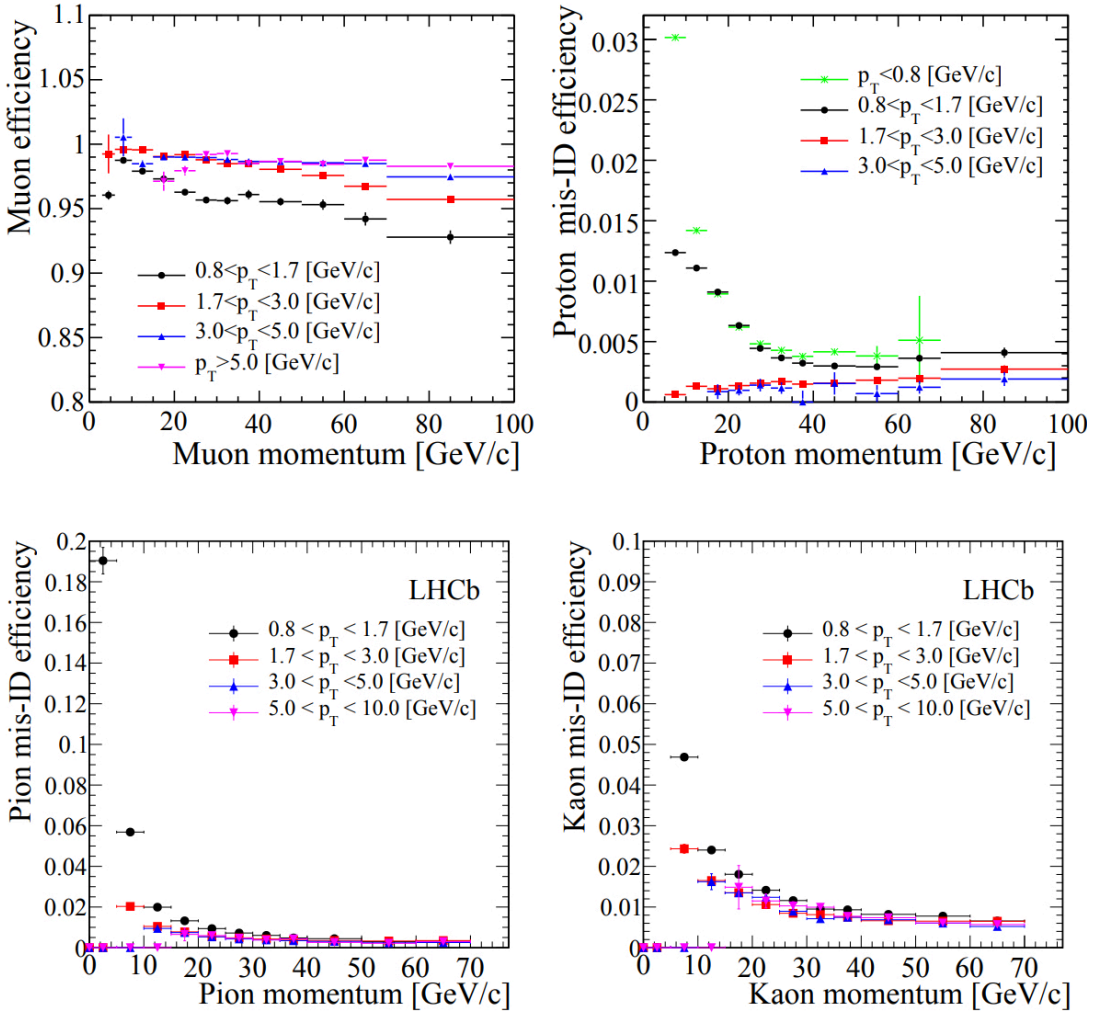

Figure 2.21: The muon selection efficiency versus muon momentum (top left), the muon-proton misidentification rate versus proton momentum (top right), the muon-pion misidentification rate versus pion momentum (bottom left) and the muon-kaon misidentification rate versus kaon momentum (bottom right) are shown. The momentum is measured in units of GeV/c for all plots and each was reproduced from [124].

2.5.1 Level-0 Trigger

The Level-0 (L0) hardware trigger is required to reduce the retention rate of data down from 40 MHz to 1 MHz after which the software triggers can then apply a more thorough event selection to the remaining data. This essentially means the L0 trigger removes 97% of the inelastic pp interactions at LHCb. It decides what events to retain based on information gathered from a combination of the VELO, calorimeter and muon systems. The L0 trigger only retains events containing tracks that have large transverse energy, E_{T}. The measurement of E_{T} is based on the hadron, electron and photon clusters in the calorimeters. Additionally, L0 only keeps events with pairs of high p_{T} muons, since high E_{T} and p_{T} tracks indicate the likely presence of heavy-flavoured hadrons in an event. Furthermore, the L0 trigger vetoes events that have a large number of tracks, since large

track multiplicities worsen reconstruction capabilities at LHCb. All this type of event information is sent to the front-end electronics of a custom built decision unit (L0DU). The L0DU then takes the decision whether to keep the event or not, around 6 μs after the associated pp collision took place.

2.5.2 High Level Trigger

The first-stage High Level Trigger (HLT1) receives information on the entire detector from events passing the L0 trigger. HLT1 is implemented in the C++ computing language within the software package Moore [137]. The software is run on the event filter farm, which is located in the LHCb cavern and is comprised of thousands of computing nodes. Using simple and fast reconstruction algorithms, HLT1 identifies tracks from charged particles passing the VELO and tracking stations to confirm the decisions made by L0. It matches the clusters in the calorimeters or hits in the muon stations to these reconstructed tracks, or identifies clusters as from photons and neutral hadrons if there is no associated tracks. HLT1 reduces the retention rate of events to approximately 30 kHz (110 kHz) during Run I (II). The remaining events are fed to the second-stage software trigger.

The second-stage High Level Trigger (HLT2) performs an event reconstruction based on all detector information available from the surviving events. With this full reconstruction capability, the HLT2 trigger looks for specific decays of heavy-flavoured hadrons, applying many and different selection algorithms to do so. These algorithms are based in the software package DaVinci [138], also written in the C++ computing language. The algorithms make use of a variety of selection criteria including requirements on PID (only in Run II) and the aforementioned FD and IP variables of a decay. HLT2 also has access to kinematic and topological information of a decay, such as the invariant mass of the reconstructed heavy-flavour hadron and its direction with respect to a PV of an event. The decays that HLT2 select are formed by combining sets of tracks under the assumption that they are the decay products, or 'daughters', of a single heavy-flavoured hadron, referred to as the 'mother' particle. The decays can also be of an 'explicit' nature where a mother particle is fully reconstructed or the decay can be selected in the more general 'inclusive' sense whereby a partial reconstruction of the mother particle is performed. The final decision of HLT2 is formed from a logical OR of these exclusive and inclusive selections; the events then just need to be accepted by one of these selection algorithms to pass HLT2. During Run I (II), events accepted by HLT2 are sent to permanent storage with an output rate of roughly 5 kHz (12.5 kHz). A flow diagram showing the processing path of data through the trigger system at LHCb during Run II is shown in Figure 2.22.

The performance of the trigger is important for any analysis at LHCb in which a detailed understanding of selection efficiencies are required, for instance in cross section

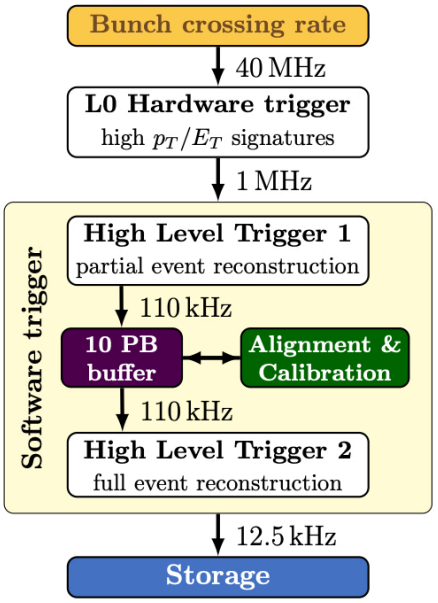

Figure 2.22: An overview of the LHCb trigger system in Run II showing the processing of events. The figure was reproduced from [139].

and branching fraction measurements. However, calculating the absolute efficiency of the entire trigger's selection of a decay mode is problematic as it is difficult to determine exactly what object in the event got triggered to allow the event to pass. To make the situation slightly more clearer, trigger requirements are made on individual physics objects such as reconstructed particles or decay modes rather than the event as a collective. Particles, reconstructed from tracks, are classified into different trigger categories based on these trigger decisions. A physics object is said to be 'Triggered On Signal' (TOS) if it is sufficient to trigger the event while it is referred to as 'Trigger Independently of Signal' (TIS) if something else in the event could have triggered the event. Events can be both TOS and TIS simultaneously, and are designated as TIS and TOS with respect to each trigger line in the L0 and HLT1. The choice whether an event object is TIS, TOS or both is ultimately done by a software tool within DaVinci, which compares the hits that created the event object in the trigger against the hits used in the offline reconstruction. The use of TIS and TOS is particularly important for the work discussed in Chapter 6. In that analysis, the classification of events as TIS with respect to a set of L0 lines conveniently allows some systematic uncertainties to cancel out.

The trigger setup described above is accurate for Run I but in Run II, HLT2 lines also had the option of using 'Turbo' processing. Turbo is handled by the software package Tesla [140], which takes candidates selected by HLT2 and saves them straight to disk where they can be accessed by analysts; there is no need for the offline reconstruction. Turbo allows more interesting events to be saved offline since Turbo event sizes are smaller in memory; this helps overcome the higher rate of interesting events being

produced in pp collisions following the increase in $\sqrt{s}$ in Run II. Turbo processing is only made possible because online reconstruction in Run II incorporates near-real-time alignment and calibration of the detector. This means the trigger reconstruction and offline reconstruction are consistent and of the same high-quality.

The design of the HLT2 is what makes the trigger system at LHCb so dynamic and flexible. New selection algorithms or 'lines' can be easily added into the HLT2 software during periods when no data is being taken. A new inclusive HLT2 Turbo trigger line for doubly-charmed-baryon searches was developed by the candidate. This line was merged into Moore in time for the start of 2018 data taking and will be discussed in Chapter 6.

2.6 Offline Processing of Data

Data selected by the trigger system is written to durable tape storage devices offline. A series of software applications then further processes and formats this raw data to get it ready for physics analyses. The Brunel package [141] performs a rigorous reconstruction on the triggered data in the same way as is done in HLT2, but now without the same tight time constraints. Brunel runs over the raw hits and clusters, recorded by the detector, to form vertex and track objects. It also assigns PID scores to each track using information from the RICH, calorimeter and muon systems, as described in Section 2.4. This results in a significant improvement for the resolutions of measurable parameters compared to their equivalent in Moore. However, this process take a long time, around 2 s per event and also results in output data sets much larger in memory than before. Therefore, data from stable running periods are reconstructed in single sessions at times when stable versions of the reconstruction algorithms and detector alignment information exist. To save on disk space, the same software used in HLT2 is implemented in the DaVinci package and performs a selection on the data output from Brunel to look for certain decay modes of particles. This process is known as 'Stripping' and is done to provide relevant and useful subsets of the full data to the end users who analyse the data for specific studies. DaVinci works by combing track and vertex objects, created by Brunel, under different hypotheses to determine if they originated directly from the decay of a single mother particle, or if they can be reconstructed as several daughter particles. DaVinci can also be re-run locally by a user, rather than done centrally, to change the requirements of a selection and, or, to add more useful variables to data sets. The data processing flow at LHCb in Run II is pictorially shown in Figure 2.23. The candidate's analysis work on searches for a doubly charmed baryon, presented in Chapters 4 and 5, makes use of Turbo data rather than Stripped data.

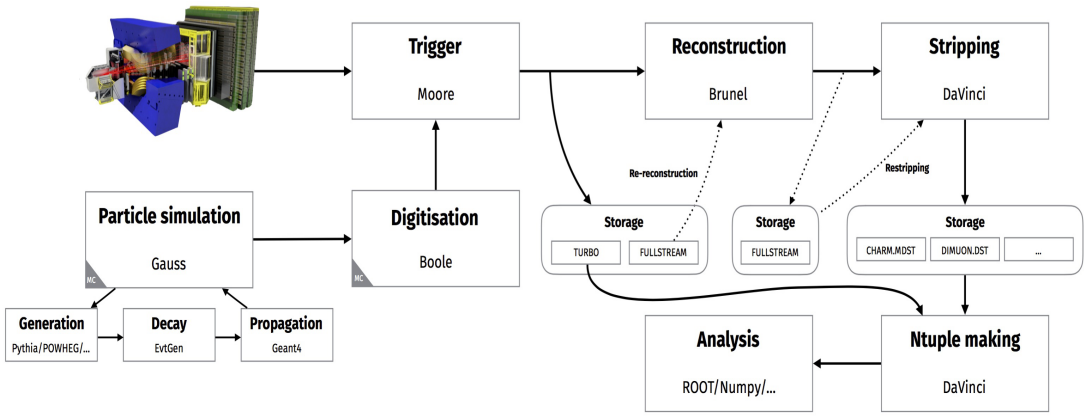

Figure 2.23: The data processing flow at LHCb in Run II with the software applications used at each stage shown. The figure was reproduced from the LHCb [142].

2.7 Simulation of Data

Understanding the final states of high energy particle collisions at the LHC is a very challenging task. Typically hundreds of particles are produced in every event and in most processes of interest the momenta can range over many orders of magnitude. The relevant decay amplitudes are too difficult to compute beyond the first few orders of perturbation theory and in the case of QCD processes, they involve the intrinsically non-perturbative and unsolved problem of confinement. However, the hard process of the collision in which heavy objects are created, or a large momentum transfer occurs, can be handled more effectively by computer simulation using Monte Carlo (MC) techniques. The large and variable dimensions of the phase space of the decay products at high-energy physics experiments make MC the appropriate integration method of choice; its accuracy improves inversely as the square root of the number of integration points and this is irrespective of the dimension used in the integration [143].

The LHCb collaboration, uses the Pythia [144] Monte Carlo generator, within the framework of the Gauss package [145], to simulate most of processes of interest to them. However, other special generators are sometimes used for particular types of decays. Of particular importance to the work described in thesis is the Genxicc generator [146], which is used to generate doubly-charmed baryons.[2] The decays of unstable particles produced by Pythia are then controlled by the EvtGen package [149]. Final-state radiation, which accompanies the hard scattering process, is generated by the Photos package [150]. The interactions of the particles with the LHCb detector material, such as the scattering and deposition of energy, is then simulated with the Geant4 toolkit [151]. Finally, the simulated hits made in the virtual LHCb detector are converted to signals

[2]The Herwig [147] and Sherpa [148] packages are other examples of MC generators which are sometimes used to simulate the *pp* interaction.

that mimic the real detector by the BOOLE application [152]. Simulated data is then processed and formatted in the same way as data from real pp collisions using BRUNEL and DAVINCI.

The accurate simulation of pp collisions and detector processes by MC generators is essential to almost all physics analyses performed at LHCb. Among other uses, simulation is needed to devise an optimum procedure for selecting events of interest in data, to calculate efficiencies that come with the selection of data, to evaluate systematic uncertainties that comes with subjective treatment of data and to understand the detector responses to pp collisions.

2.8 Chapter Summary

This chapter first described the layout and operations of the LHC accelerator complex. The design of the LHCb detector, one of the main experiments on the LHC, was then discussed in detail. Each subdetector comprising LHCb was examined, starting with the tracking system, then the particle identification system before concluding with details on how the trigger selects events. Information on the design of each subdetector was given and an evaluation of their individual and collective performances were highlighted by referring to past studies conducted by the LHCb collaboration. The different stages of data processing, in order for physics analyses to be performed, is then mentioned and finally, a brief description of the way in which LHCb simulates pp collisions and their subsequent interplay with a virtual LHCb detector was discussed. In summary, LHCb is an excellent and unique experiment for acquiring data to perform world-class heavy-flavoured physics analyses.

Chapter 3

RICH Magnetic Field Studies

"If you thought that science was certain – well, that is just an error on your part."

– Richard Feynman, renowned developer of Quantum Field Theory

Like the majority of analyses performed at LHCb, searches for doubly-charmed baryons would not be possible if it were not for the detector's ability to accurately identify final-state particles. The responsibility of particle identification at LHCb is partially attributed to the RICH systems, which have unrivalled efficiency among all the LHC subdetectors at identifying hadrons. Yet, despite their excellent performance, not every detail about them is fully understood. In particular, the Cherenkov angle resolution of the RICH-1 subdetector is slightly worse than the expected value obtained from simulation [133].

This short chapter describes a preliminary study into the effect of the field of the LHCb magnet on the Cherenkov angle resolution. Section 3.1 first gives the reader more information on the RICH systems than what was disclosed in Chapter 2; specifically, on the optical detectors that are used to record the Cherenkov signal and on the technical details of a system that is used to correct for image distortions caused by the magnetic field. The discrepancy in the performance of RICH-1 with data and simulation is described in Section 3.2. The software challenges that were needed to be overcome so that the Cherenkov angle resolution may be measured without knowledge of the magnetic field is presented in Section 3.3. Finally, the outcome of this work is discussed in Section 3.4.

3.1 Introduction

The design, purpose and performance of the Ring Imaging CHerenkov (RICH) subdetectors was covered in Section 2.4.1, while their layouts are shown in Figure 2.15, but it is perhaps worth reiterating the main points here. There are two RICH systems within the LHCb detector that measure Cherenkov light from tracks covering different momentum ranges. The RICH systems exploit the phenomenon known as Cherenkov radiation to identify the type of track that passed through their gas radiators. The Cherenkov

radiation is reflected towards optical sensors using a combination of flat and spherical mirrors. Furthermore, all tracks with momentum greater than approximately 25 GeV/c give the same Cherenkov radiation angle and are said to be saturated, see Figure 2.14. The type of optical sensors that are used in the RICH systems and their susceptibility to a magnetic field are discussed next.

3.1.1 Hybrid Photon Detectors

The RICH systems use Hybrid Photon Detectors (HPDs) to detect the Cherenkov photons emitted by electrically charged particles. The HPDs were designed in collaboration with industry to create a product with excellent timing resolution and a large active coverage area to ensure the number of recorded Cherenkov photons is maximised [153].

The HPDs consist of a vacuum tube with a 8 mm thick spherical quartz entrance window that has a radius of curvature of 55 mm. The inner surface of this optical window is coated with a multi-alkali photocathode. When Cherenkov photons hit the photocathode, electrons are produced. The quantum efficiency − the ratio between the number of Cherenkov photons to that of the photoelectrons − varies depending on the wavelength of the incident photon but is around 30% [133]. The HPDs are designed to be sensitive to Cherenkov radiation with a wavelength between 200−600 nm. The resulting photoelectrons are then subject to an approximate 15 kV high voltage that accelerates them towards a reverse-biased silicon detector at the end of the tube. There are 1,042 pixel elements on the silicon detector and each is $500 \times 500\,\mu\text{m}^2$ in size. In total, RICH-1 has 196 HPDs, while RICH-2 has 288 HPDs. A schematic of an individual HPD is shown in Figure 3.1, with a possible trajectory of a photoelectron also indicated. The location of the HPDs in RICH-1 and RICH-2, relative to each RICH system, is shown in Figure 2.15.

In general, the performance of HPDs is known to be affected by an external magnetic field. This is the case because a magnetic field will influence the trajectories of the photoelectrons within the vacuum of a HPD and as such will change the read out position of the photoelectrons on the silicon detector. Depending on the orientation of the magnetic field to the HPD plane, the distortion to the true photoelectron trajectory may be extreme and it can even entirely compromise the photon-position resolution. Therefore, HPDs are normally designed to work efficiently up to only 1.5 mT axial fields. In the case of the HPDs in the RICH systems at LHCb, all are affected by the fringe magnetic field of the spectrometer magnet. However, the effect is much more pronounced for the HPDs in the RICH-1 subdetector since it is located immediately before the magnet, as can be seen from Figure 2.3. To reduce the strength of the magnetic field, each HPD is surrounded by a nickel-iron mu-metal shield. Even with this added protection, measurements made while the magnetic field is full strength indicate that non-uniform fields with strength up

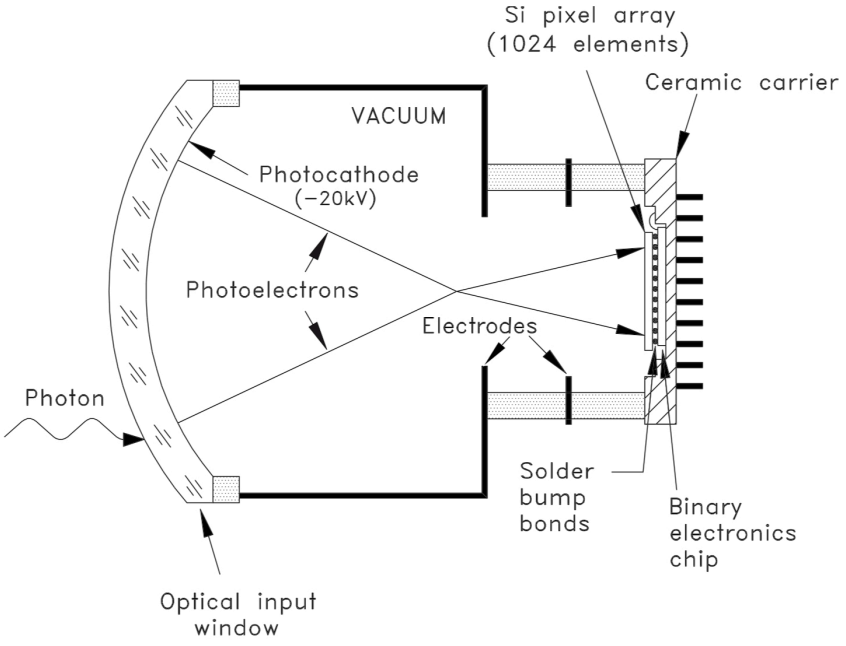

Figure 3.1: A schematic of a Hybrid Photon Detector (HPD) as used in the RICH subdetectors at LHCb. The figure was reproduced [120].

to 2.4 (0.6) mT penetrate the HPDs of RICH-1(2). These fields will cause distortions to the Cherenkov signal in a manner that is impossible to predict a priori. The system that accounts for the effects of this stray field in RICH-1 is discussed next, whereas a similar system that performs the equivalent operation for RICH-2 [154] will not be reviewed as the details are not as important to the study laid out in this chapter.

3.1.2 Magnetic Distortion Correction System

As discussed previously, inferring the point at which a Cherenkov photon was incident on the optical input window is non-trivial because of the influence of the magnetic field. Thus, correction factors need to be applied to every HPD in the radial and axial directions during the reconstruction of data. On top of the distortions caused by the magnetic field, variations in the high voltage supply and geometry of the quartz window can also lead to biases in the Cherenkov image. The correction factors for all these effects are handled by the Magnetic Distortion Calibration System (MDCS) of the RICH-1 subdetector [155].

The MDCS of RICH-1 is comprised of two identical light-projection systems, one for each HPD enclosure in the Up and Down sides, see Figure 2.15. Each system is composed of green light-emitting diodes (LEDs) mounted on a carbon-fibre support that spans the width of the boxes housing the HPDs. A picture of the MDCS hardware in RICH-1 is shown in Figure 3.2. To produce more accurate results, the spots created by these light bars are smaller in size compared to the silicon pixels at the end of the HPD tubes.

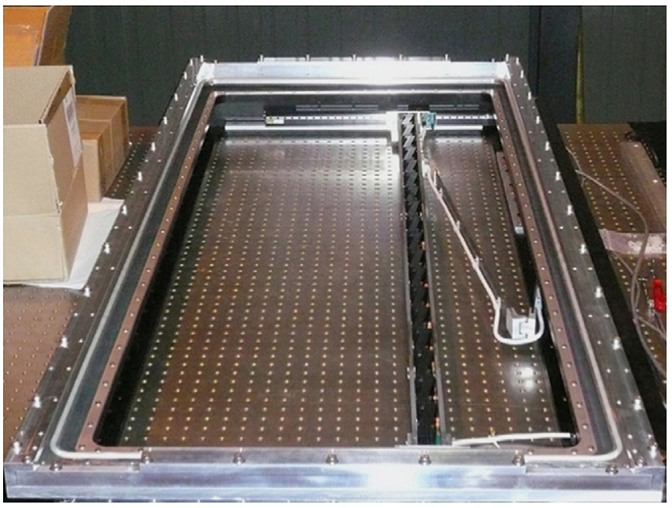

Figure 3.2: A photograph of the Magnetic Distortion Calibration System in RICH-1 prior to its installation in the subdetector. The light bar is shown a third of the way along its full extended range. The figure was reproduced from [155].

Special data-taking Runs are performed once per operational year to scan the HPDs using the MDCS such that the distortion for a given magnetic field configuration can be mapped. During these MDCS scans, the light bars are moved interactively around in two dimensions by the RICH-1 global control system and are made to illuminate each column of HPDs for around 5 seconds. The LEDs shine a known pattern of photons onto the photocathodes of each HPD. Typically, this sparse pattern means an HPD is illuminated by a single LED at each step of the scan such that a pixel hit can be easily associated to an LED position. In this way, the MDCS can monitor how the hit pattern on the silicon pixels is modified by a non-zero magnetic field. The data recorded during these scans can then inversely map the distorted pixel hit to its real position on the entrance window.

The transformation of the position of the hit pixels on the silicon array to that of the corresponding light spot at the exterior of the HPD window involves both radial and axial components. Thanks to the iron shielding, the magnetic field is predominately parallel to the tube axis of the HPDs in RICH-1, while the transverse field is negligible in strength so can be safely assumed to be radially symmetric around the tube axis. Thus, this transformation can be parameterised as follows

$$R_B = k_1 R_A + k_2 R_A^2 + k_3 R_A^3 \tag{3.1}$$

$$\phi_B = \phi_A + c_0 + c_1 R_A + c_2 R_A^2 + c_3 R_A^3, \tag{3.2}$$

where (R_A, ϕ_A) are the radial and axial coordinates of a point on the silicon pixel sensor, (R_B, ϕ_B) are similarly the coordinates of a point on the outer surface of the quartz window. The k_i and c_i parameters are extracted by the MDCS. They are deduced by minimising the distance between the position of the selected pixel hits, suitably transformed with

Equations 3.1 and 3.2, and the coordinate grid that is defined by the geometry of the light bar and the logic of its movement. These calibration parameters are used by the BRUNEL software package [141] that reconstructs the trajectory of the tracks through the magnet and the RICH systems.

3.2 Cherenkov Angle Resolution

Along with its particle identification efficiency, the performance of the RICH subdetectors can also be quantified by its the Cherenkov resolution angle. The Cherenkov angle is the polar angle, in spherical coordinates, of the emitted cone of Cherenkov radiation emitted from the RICH radiator material when it rapidly depolarises, as can be seen in Figure 3.3. However, for performance purposes, the more important quantity to determine is that of the difference between the measured and expected Cherenkov angle defined as

$$\Delta\theta_c = \theta_c - \theta_{\text{exp}}, \tag{3.3}$$

where θ_c is the measured angle between a charged particle's track, taken at the half-way point of the radiator, and the photon candidate observed as a HPD hit and θ_{exp} is the expected Cherenkov angle for the charged particle calculated from the track's momentum using Equation 2.2. The candidate photons for each track are determined by combining the photon emission point with the measured hit positions of the photons.[1] The trajectory of the Cherenkov photons through the RICH optical system is determined from simulation, taking into account knowledge of the mirror and HPD alignment.

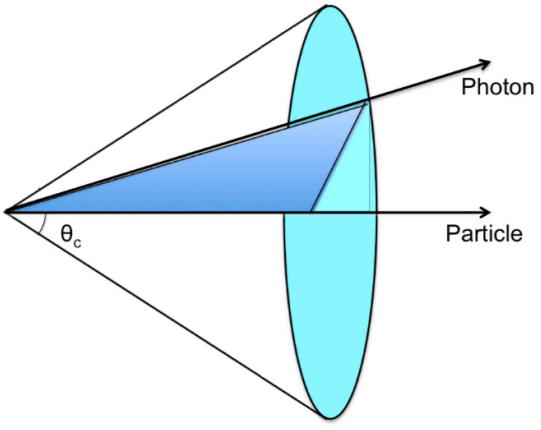

Figure 3.3: Illustration of a Cherenkov radiation cone with the Cherenkov angle θ_c indicated relative to the emission point. The figure was reproduced from [156].

[1]The true emission point of Cherenkov radiation is unknown so the midpoint of the track's path through the radiator is chosen as default. The uncertainty in the reconstructed Cherenkov angle due to the emission point is made by design to be smaller than the other sources of finite angular resolution.

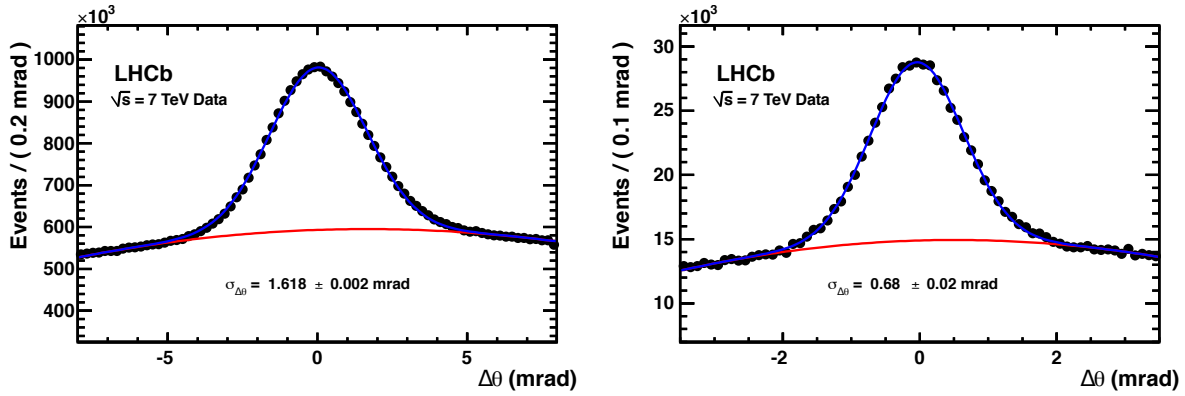

Figure 3.4: Cherenkov angle resolution distribution for RICH-1 and RICH-2 using high momentum tracks from Run I data at LHCb. The background is described by a second-order polynomial (red) while the signal is represented by a Gaussian function. The total fit (blue) is overlaid. The figure was reproduced from [133].

The construction of Equation 3.3 exploits the fact that Cherenkov photons correctly assigned to a charged particle track will ideally form a $\Delta\theta_c$ distribution that is Gaussian with a mean close to zero and a width that is equal to Cherenkov angle resolution. Additionally, backgrounds that arise from HPD hits being assigned to incorrect tracks, form a smooth and non-peaking distribution underneath the Cherenkov signal. A typical example of the Cherenkov angle distributions for particles passing through RICH-1 and RICH-2 are shown in Figure 3.4. The fit overlaid is the combined model of a Gaussian function for the signal peak and a second-order polynomial for the background. From these fits, the Cherenkov angle resolution is determined to be (1.618 ± 0.002) mrad for RICH-1 and (0.68 ± 0.02) mrad for RICH-2. The resolution of RICH-2 is in excellent agreement with the expected value of (0.68 ± 0.01) mrad from simulation [133]. However, the resolution of RICH-1 is worse by 6.5% compared with its expected value of (1.52 ± 0.02) mrad [133].

This Cherenkov angle resolution discrepancy in RICH-1 is hitherto not understood; mirror alignment is likely not the issue since it is actually RICH-2 that has the more complex optical system and the performance of RICH-2 agrees very well with simulation. The obvious reason for this trend would be the calibration of the HPDs due to incorrect applied magnetic field corrections. Recall that RICH-1 is subject to stray fields that are four times stronger than in RICH-2, as was discussed in Section 3.1.2. Since the Cherenkov angle contributes to the accuracy of particle identification, see Equation 2.2, then almost all physics analyses at LHCb would benefit if the cause for this discrepancy could be isolated and resolved.

3.3 Magnet-Off Studies

Studies performed by the LHCb collaboration have shown that the Magnetic Distortion Correction System improves the Cherenkov angle resolution. Without the corrections that this system applies to data, the per-photon resolution of the Cherenkov angle is found to be significantly worse in RICH-1 [133]. This does not mean the applied corrections are perfect however. For one, this approach assumes that the stray magnetic field configuration in the HPDs stays constant throughout the year, which is likely a safe assumption based on records kept by the LHCb collaboration, but there is always a possibility the dipole itself becomes magnetised through the process of magnetic hysteresis.

Strategies

Therefore, in an attempt to rule out the MDCS as the cause of this diminished resolution in RICH-1, the candidate took on the challenge of extracting the Cherenkov angle resolution from data recorded at the LHCb detector when no magnetic field was present.

The data used for this study when no magnetic field was present, hereon in referred to as 'MagOff' data, was recorded by the LHCb detector at the start of the 2016 data-taking period (Runs 173103−173111) when all subdetectors were performing calibrations before the official start of *pp* data taking in Run II. Data recorded around a similar time (Runs 179092−179101) but under the influence of a non-zero magnetic field, now called 'MagOn' data, was also examined to cross check all results.

Without a magnetic field to bend the trajectories of charged particles, there is no momentum information available in the MagOff data set and so the expected Cherenkov angle cannot be evaluated using Equation 2.2. Two seemingly feasible solutions to this problem were determined to be:

1. To select muon or pion tracks (identified by M1-M5 or HCAL) that are saturated in RICH-2 and then measure their Cherenkov angle in RICH-1;

2. To measure the Cherenkov angle of all tracks in RICH-2 and then calculate the momentum of the track by inverting Equation 2.2 and assuming a mass of a muon.

However, it was expected to be quite difficult to measure the single-track Cherenkov angle resolution in RICH-2 in both these approaches because of larger background contributions. Without the magnetic field, particles would not be focussed into the detector systems and would only spread out naturally, inversely proportional to the square of the distance to the beam axis. Additionally, muons are scarce in nominal collisions since they must result from secondary decays of heavier hadrons. Since the MagOff data was recorded when the instantaneous luminosity was lower than normal, the total number of muons is expected to be particularly low.

Methodology

For either strategy to work, the 'nominal' configuration of Brunel, defined to be the version used during official *pp* collisions when a non-zero magnetic field is present, is extensively altered to assume an expected momentum value for all tracks. A momentum value of 25 GeV/c, corresponding to the saturation point for muon tracks in RICH-1, is thus hard coded into the Brunel software for local testing. However, the direction of each track is kept the same, as if it was calculated by Brunel in the nominal case. Only 'long' tracks − tracks that have associated hits in each of the VELO, TT and T1-T3 tracking stations − are considered in this analysis as they have the best tracking resolution. Several requirements on the quality of the data are also removed within the Brunel to allow the software to successfully reconstruct this type of data. This altered version of Brunel is referred to as 'hacked' Brunel for the rest of the chapter.

MC events simulated with the Gauss [145], Boole [152] and Moore [137] applications, see Section 2.7, along with the hacked version of Brunel, are also studied to understand the results of MagOff data with Brunel in this setup. The MC samples used in this study are not full Pythia production samples. Instead, a single signal particle is generated in Gauss whose kinematics can be configured to follow different distributions. This means the characteristics of the event can be better controlled. Note that the efficiencies resulting from these samples are usually too good compared to the full simulation since the detector occupancy is much lower. However, these MC samples are still appropriate for the studies of the Cherenkov angle resolution. Furthermore, the MDCS parameters are inherently used in the generation of these MC samples so inversely mapping the silicon pixel hits to the corresponding hit on the quartz window will be exact unlike in real data.

3.4 Results and Discussion

In the end, the hacked version of Brunel created by the PhD candidate was able to reconstruct Cherenkov angle information without direct knowledge of a track's momentum. However, preliminary results show no clear Gaussian-shaped Cherenkov signal centered around the zero value in MagOff conditions. Instead, the Cherenkov angle distribution for candidate photons of long tracks from charged particles is flat in shape.

A comparison of the Cherenkov angle distribution from MagOn and MagOff data, with no offline RICH DLL requirements applied, is shown in Figure 3.5. The MagOn data reconstructed with nominal Brunel shows the expected Cherenkov angle distribution with a mean of zero and a resolution in keeping with performance expectations. On the other hand, both MagOn and MagOff data processed with hacked Brunel do not

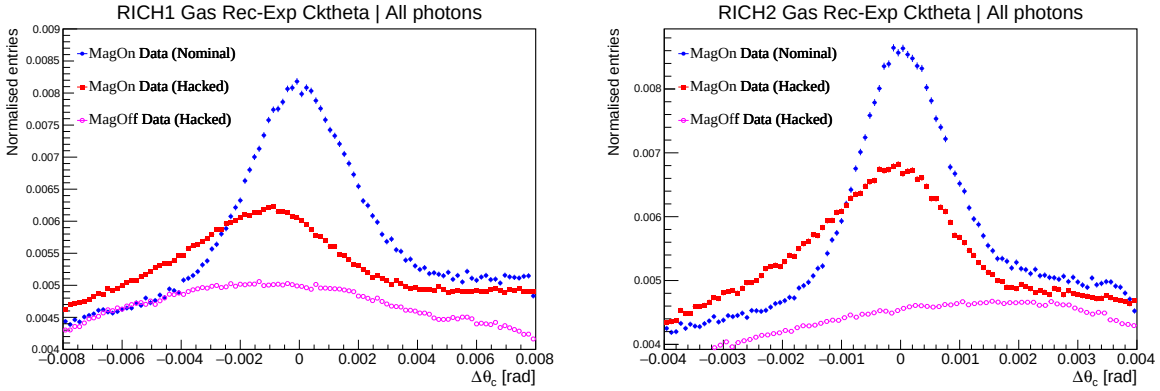

Figure 3.5: Cherenkov angle distribution of long tracks passing through the (left) RICH-1 and (right) RICH-2 subdetectors for MagOn data processed with nominal Brunel (blue), for MagOn data processed with hacked Brunel (red) and for MagOff data processed with hacked Brunel (magenta).

show a peak centered at zero. In the case of the MagOn data, reconstructed with hacked Brunel, the signal peak is skewed from the zero value, while the MagOff data interpreted with hacked Brunel gives a completely smooth distribution. Speculatively, this flat distribution was considered to be a result of a negligible number of saturated tracks with momentum around 25 GeV/c in the MagOff data sample.

To understand and control the situation better, six individual simulated samples are generated, each with 25,000 events, to monitor the Cherenkov angle resolution resulting from different types of event situations. Muon tracks are generated with various kinematic distributions, while pion, proton and kaon tracks are additionally generated in one sample. Some of the simulated samples result from very simple production setups, while others are more similar to a true pp event at LHC with multiple tracks of different species present. The production configurations of the generated samples are as follows:

1. $p = 25$ GeV/c; $\theta \in 30{-}50$ mrad; 1 $\mu^{+/-}$ track per event;
2. $p \in 20{-}30$ GeV/c; $\theta \in 30{-}50$ mrad; 1 $\mu^{+/-}$ track per event;
3. $p \in 10{-}100$ GeV/c; $\theta \in 30{-}50$ mrad; 1 $\mu^{+/-}$ track per event;
4. $p \in 20{-}30$ GeV/c; $\theta \in 10{-}100$ mrad; 1 $\mu^{+/-}$ track per event;
5. $p \in 20{-}30$ GeV/c; $\theta \in 30{-}50$ mrad; 1$-$10 $\mu^{+/-}$ tracks per event;
6. $p \in 10{-}100$ GeV/c; $\theta \in 10{-}100$ mrad; 1$-$10 μ, π, p or K tracks per event,

where θ in this case refers to the production polar angle of the charged track at the pp interaction point and p is the momentum with which the track is generated. The results from reconstructing these simulated events with hacked Brunel are shown in

Simulation scenario	MagOn		MagOff	
	RICH-1 (mrad)	RICH-2 (mrad)	RICH-1 (mrad)	RICH-2 (mrad)
1	1.624 ± 0.004	0.653 ± 0.002	1.629 ± 0.004	1.368 ± 0.023
2	1.622 ± 0.004	0.654 ± 0.002	1.634 ± 0.004	1.328 ± 0.022
3	1.622 ± 0.004	0.642 ± 0.002	1.641 ± 0.005	1.376 ± 0.027
4	1.605 ± 0.004	0.643 ± 0.002	1.614 ± 0.004	1.279 ± 0.025
5	1.627 ± 0.002	0.654 ± 0.001	1.641 ± 0.004	1.315 ± 0.019
6	1.601 ± 0.002	0.618 ± 0.001	1.621 ± 0.002	1.291 ± 0.016

Table 3.1: Cherenkov angle resolution value from a fit to MagOff and MagOn simulated events that reflect a variety of different event compositions. The simulation scenarios are described in the main text.

Table 3.1. Recall that hacked Brunel assumes a 25 GeV/c momentum value for all tracks. It appears that the Cherenkov resolution in RICH-1 is only marginally different between MagOn and MagOff data, whereas for RICH-2, the MagOff case returns a resolution that is hugely worse compared to MagOn data. The closeness in value of the assumed momentum value, hard coded into Brunel, to that of the actual momentum of the track appears to have negligible influence on the resolution achieved. Both strategies of measuring the Cherenkov angle resolution in RICH-1 are dependent on reliable RICH-2 information, which does not appear to have been obtained using hacked Brunel on MagOff data. The distribution of the Cherenkov angle resulting from tracks in the second simulated sample is shown in Figure 3.6 with a Gaussian plus second-order polynomial fit overlaid. The background contribution in RICH-2 in the MagOff situation can be seen to be significantly greater than for MagOn data since the occupancy will be larger.

On closer inspection of the simulated data, the track resolution primarily in the y direction for RICH-2 is found to be significantly worse for MagOff data compared to MagOn data, causing this factor two worse Cherenkov angle resolution in RICH-2. The concern is that the current information stored in the software database to describe the alignment and calibration of all subdetectors under zero magnetic field conditions is not reasonable. For instance, the position of the electronic hits in the gas straw tubes of the Outer Trackers (OT) is expected not to be quite identical in magnet-off conditions to that of the magnet-on situation. The OT expects a curve drift path of the electrons towards the anode, which is not created under the magnet-off conditions. These uncertainties over the validity of the tracking alignment stalled any further progress of this study. This problem will need to be resolved in the future if the Cherenkov angle resolution is to be measured using data recorded under zero magnetic field conditions.

Focusing on the positives however, the hacked version of Brunel developed during this study is able to reconstruct Cherenkov angle information without being fed an

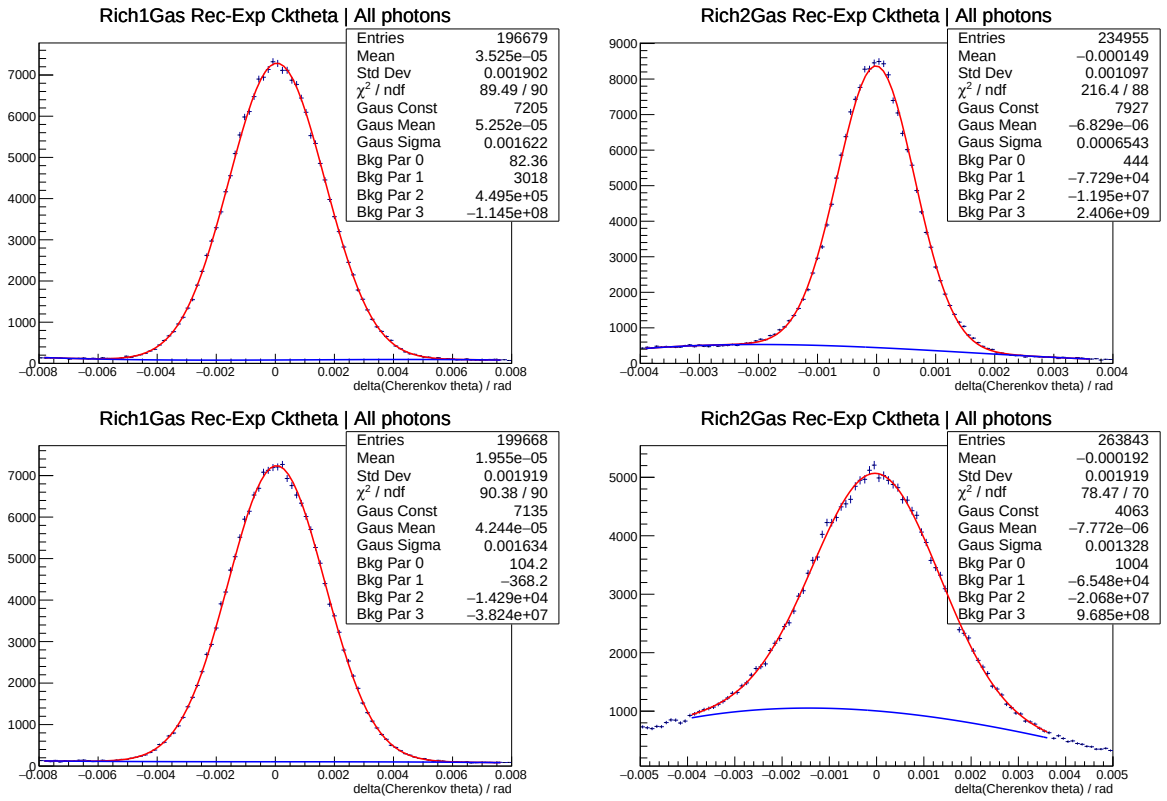

Figure 3.6: Cherenkov angle resolution distributions from simulation in (left) RICH-1 and (right) RICH-2 under (top) MagOn and (bottom) MagOff conditions for single muon track events where the muon has a momentum between $20-30\,\mathrm{GeV}/c$. The results of the (red) signal fit using a Gaussian function and the (blue) background fit using second-order polynomial are shown overlaid.

expected momentum value of a track. Once the caveat of the tracking issue is resolved, this configuration of Brunel will be useful for studies without magnetic field, for example when momentum information biases a result. One possible application could be in a 'tracking-less' momentum measurement of long-lived particles. In summary, the Magnetic Distortion Correction System cannot be for certain identified as the source of the diminished Cherenkov angle resolution in the RICH-1 subdetector but a by-product of this study was the creation of a preliminary version of Brunel that potentially has many applications to physics analyses at LHCb.

3.5 Chapter Summary

This chapter first presented a recap of the purpose and technicalities of the Ring Imaging CHerenkov (RICH) systems at the LHCb detector. The Hybrid Photon Detectors that record the Cherenkov radiation within the RICH systems are then discussed in detail as well as the Magnetic Distortion Correction system that is deployed during data reconstruction to correct any biases from a variety of source including the stray magnetic field

of the spectrometer dipole. The performance of the RICH subdetectors in terms of the Cherenkov angle resolution is then discussed with the degraded resolution of RICH-1, compared to expectations, highlighted. The strategy and methodology for attempting to measure the Cherenkov angle resolution without direct knowledge of the momentum of tracks is then outlined. Finally, the preliminary results of the analysis are disclosed with a discussion on the use and future of this work also mentioned.

Chapter 4

Observation of $\Xi_{cc}^{++} \to \Lambda_c^+ K^- \pi^+ \pi^+$

> "We have to remember that what we observe is not nature itself but nature exposed to our method of questioning."
>
> – Werner Heisenberg, key pioneer of Quantum Mechanics

In this chapter, a first-ever search for $\Xi_{cc}^{++} \to \Lambda_c^+(\to pK^-\pi^+)K^-\pi^+\pi^+$ decays at the LHCb detector is presented. The analysis was carried out by the candidate at the beginning of their PhD studies in collaboration with the Laboratoire de l'Accélérateur Linéaire (LAL) in Orsay, France and Tsinghua University in Beijing, China. The candidate led the design of the event selection and contributed to the background determination and the mass fits. The aim of this analysis was to discover the doubly-charmed Ξ_{cc}^{++} baryon and measure its mass. This was to be achieved by observing the Ξ_{cc}^{++} baryon decaying weakly to a singly-charmed Λ_c^+ baryon, a K^- meson and two π^+ mesons, with the Λ_c^+ baryon then decaying to a proton and a further K^- meson and π^+ meson. The charge-conjugate decay is also included in the search, as is the case for any decay detailed in this chapter. With two heavy constituent charm quarks, the Ξ_{cc}^{++} baryon provides a unique system for testing techniques describing the strong interaction.

Following the unsuccessful search by the LHCb collaboration to observe the singly-charged Ξ_{cc}^{+} (ccd) baryon through the $\Xi_{cc}^{+} \to \Lambda_c^+ K^-\pi^+$ decay mode in Run I [108], focus at LHCb changed to searching for the Ξ_{cc}^{++} (ccu) baryon within its larger data sets. This was motivated by the expected longer lifetime of the Ξ_{cc}^{++} state over its isospin parter [74]. If Ξ_{cc}^{++} baryons travel far from the pp interaction point then it is expected that combinatorial backgrounds may be more easily removed during the selection of data. As discussed in Section 1.4.2 the Cabibbo-favoured $\Xi_{cc}^{++} \to \Lambda_c^+ K^-\pi^+\pi^+$ decay mode was identified as the most promising decay mode for discovering the Ξ_{cc}^{++} baryon, with an expected branching fraction of near 10% [99].

This analysis uses two statistically independent samples of pp collision data collected by the LHCb experiment; one corresponding to an integrated luminosity of around $1.7\,\text{fb}^{-1}$ collected at a centre-of-mass energy of 13 TeV in 2016 and the other matching to

approximately 2.1 fb^{-1} collected at 8 TeV and recorded in 2012. The 2016 data sample serves as the main data set for this analysis with the 2012 acting as a cross-check sample. All aspects of the $\Xi_{cc}^{++} \to \Lambda_c^+ K^- \pi^+ \pi^+$ analysis are outlined in this chapter from the background studies to the results of the final mass measurement but particular detail is given to the event selection, the area the candidate was most active in. The work discussed in this chapter was published in Reference [157].

4.1 Analysis Strategy

At the time of conducting the $\Xi_{cc}^{++} \to \Lambda_c^+ K^- \pi^+ \pi^+$ analysis, the Ξ_{cc}^{++} baryon had never been observed and its mass and lifetime were unknown. Therefore, the analysis is performed without any definite assumption of these basic particle properties. All data are investigated if they pass an event selection process that requires the reconstructed Ξ_{cc}^{++} and Λ_c^+ baryons to reside in well-defined mass regions. Data not passing the event selection are not included in the final fit to the $\Lambda_c^+ K^- \pi^+ \pi^+$ mass spectrum. To avoid any potential biases, all aspects of the analysis procedure are determined before data in the right-sign (RS) $\Xi_{cc}^{++} \to \Lambda_c^+ K^- \pi^+ \pi^+$ decay mode, the mode that may contain the real signal, are examined within the mass search regions of the analysis. Instead, the analysis is developed around a simulated sample of RS decays, a data set consisting of non-physical $\Xi_{cc}^{++} \to \Lambda_c^+ K^- \pi^- \pi^+$ decays, which contains a wrong-signed (WS) combination of final-state particles and a data set containing doubly-Cabibbo-suppressed (DCS) $\Xi_{cc}^{++} \to \Lambda_c^+ K^+ \pi^- \pi^+$ decays. The Λ_c^+ baryon is reconstructed in the $pK^-\pi^+$ final state in both the WS and DCS data sets.

Simulated RS decays are generated with the properties of the Ξ_{cc}^{++} baryon set to commonly predicted values from theory. For most studies, the mass of the Ξ_{cc}^{++} baryon in simulation is set to a singular value. However, the impact of the Ξ_{cc}^{++} mass on any outcomes of the analysis is investigated by altering the mass value set in simulation and then studying the resulting changes to different kinematic distributions. The simulated Ξ_{cc}^{++} baryons are generated with a default lifetime but other lifetimes are studied throughout the analysis by weighting its decay time distribution to mimic other desired lifetime hypotheses. The daughter tracks of the Ξ_{cc}^{++} baryon are distributed according to a model that is uniform in phase space, while the Λ_c^+ decay is generated with a four-component pseudo-resonance model based on the best knowledge of the $\Lambda_c^+ \to pK^-\pi^+$ decay at the time. The p_T spectrum of the Ξ_{cc}^{++} baryon is taken from a dedicated doubly-heavy-flavour MC event generator.

The main data sets used in this analysis contain decays that are reconstructed at the trigger level using Turbo processing. The trigger requirements are already relatively tight to reduce the bandwidth. On top of the trigger, requirements are imposed on the

data, which retain almost all signal MC events but reduce the size of the offline data sets. A multivariate selection is then used to fully exploit the difference between signal and background events and to yield a significant level of potential signals. The multivariate selection is trained on a simulated RS sample and the WS control mode.

Once the event selection, background determination and mass measurement studies are complete, the RS data are scrutinised and the signal significance is calculated. A contingency plan is devised for every potential measure of signal significance before the examination of RS data. A limit on the product of the production cross section of the Ξ_{cc}^{++} baryon and the $\Xi_{cc}^{++} \to \Lambda_c^+ K^- \pi^+ \pi^+$ branching fraction against the production cross section of Λ_c^+ baryons originating from their PV is set rather than a mass measurement if any signal observed is not statistically greater than five standard deviations over the background contribution.

4.2 Data Samples

In this section, the data samples that are collected and simulated by LHCb for use in the $\Xi_{cc}^{++} \to \Lambda_c^+ K^- \pi^+ \pi^+$ search analysis are discussed in detail.

4.2.1 LHCb Data

The main data set used in this analysis was recorded by the LHCb detector at $\sqrt{s} = 13\,\text{TeV}$ throughout 2016 under very similar beam, detector and trigger conditions. Approximately equal sizes of MagUp ($792\,\text{pb}^{-1}$) and MagDown ($826\,\text{pb}^{-1}$) data are used. Exclusive trigger lines are designed to reconstruct the RS, WS and DCS data sets. The selection requirements of these Turbo lines are discussed in detail in Section 4.3.

Data recorded in 2012 is also analysed independently of the 2016 data as a means of cross-checking the results obtained with the 2016 sample. Since Turbo processing was not available in Run I, the 2012 data is a Stripped sample. Despite data also being collected in 2011 and 2015, these data sets are not studied. For 2011 data, only around 70% of the data is usable since a dedicated $\Xi_{cc}^{++} \to \Lambda_c^+ K^- \pi^+ \pi^+$ HLT2 line was not available for the first $0.35\,\text{fb}^{-1}$ of the data collected that year. In the case of 2015 data, the integrated luminosity totals to a comparatively small amount as shown in Figure 2.5. There was also no available simulated $\Xi_{cc}^{++} \to \Lambda_c^+ K^- \pi^+ \pi^+$ samples with 2015 data-taking conditions at the time this analysis was performed.

4.2.2 Simulation

The GENXICC generator [158] is used to simulate the production of the Ξ_{cc}^{++} signals at LHCb.[1] To achieve this, GENXICC is interfaced with the PYTHIA package with a specific LHCb configuration [159]. The generator uses a single-parton-scattering model to produce the Ξ_{cc}^{++} baryons via gluon-gluon fusion, gluon-charm collisions and charm-charm collisions within the framework of non-relativistic Quantum Chromodynamics. The Ξ_{cc}^{++} baryon's mass is set to $3597.98\,\text{MeV}/c^2$ while its lifetime is set to 333 fs.

The Ξ_{cc}^{++} baryons then decay according to the `PHSP` EVTGEN model [149], which populates the decay products uniformly across the entire available phase space. The simulation of the intermediate $\Lambda_c^+ \to pK^-\pi^+$ decay includes contributions from strongly decaying resonances; 17.8% proceed via $\Lambda_c^+ \to \Delta^{++}(p\pi^+)K^-$, 16.1% by$\Lambda_c^+ \to pK^*(K^-\pi^+)$ and 8.1% go through $\Lambda_c^+ \to \Lambda(1520)(pK^-)\pi^+$ decays. All these resonant decays are governed by the `VSS` EVTGEN model [149]. The remaining Λ_c^+ baryons decay according to the PHSP model. Around two million simulated $\Xi_{cc}^{++} \to \Lambda_c^+ K^-\pi^+\pi^+$ events are produced for both MagUp and MagDown magnet conditions for this analysis. Selection requirements that are specifically applied to the simulated $\Xi_{cc}^{++} \to \Lambda_c^+ K^-\pi^+\pi^+$ sample are discussed in Section 4.3.3.

4.3 Candidate Selection

In this section, the selection of potential $\Xi_{cc}^{++} \to \Lambda_c^+ K^-\pi^+\pi^+$ decays (candidates) from a subset set of pp collision data recorded in 2016, is discussed in detail. This includes the selection requirements in the online data processing (L0, HLT1 and Turbo HLT2 lines) as well as the offline selections that were designed by the PhD candidate, with the help of others. The details of the requirements imposed on 2012 data are outlined in Appendix B.

4.3.1 Overview

A typical LHCb event contains on average a 100 reconstructed tracks, mostly from pions. Therefore, to potentially select out any $\Xi_{cc}^{++} \to \Lambda_c^+ K^-\pi^+\pi^+$ decays from the other activity in the event, selection criteria needs to be devised that exploits the characteristic topology of heavy-flavoured-hadron decays and their kinematics. As already mentioned in Chapter 2, the daughter tracks of heavy hadrons tend to have larger p_T, compared to generic tracks from light-quark background, because of the higher masses of heavy hadrons. Hence, a common theme throughout the selection process is only to accept

[1] The authors of GENXICC also created the BCVEGPY generator [146] which simulates the production of doubly-heavy B_c^+ mesons. The BCVEGPY p_T spectrum is in very good agreement with data at LHCb, which suggests the Ξ_{cc}^{++} p_T spectrum provided by GENXICC should also be reasonable.

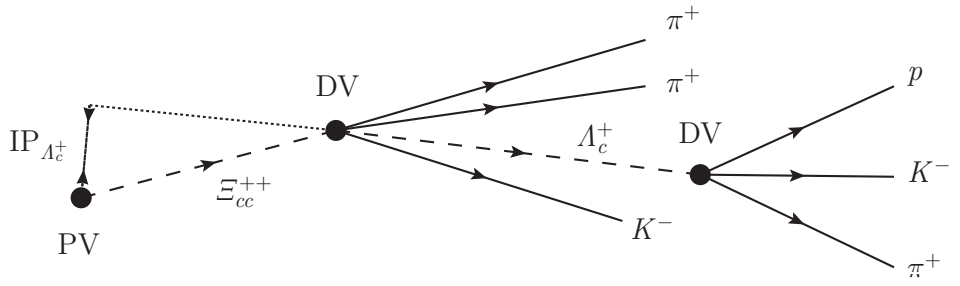

Figure 4.1: The topology of the $\Xi_{cc}^{++} \to \Lambda_c^+(\to pK^-\pi^+)K^-\pi^+\pi^+$ decay.

events that contain tracks with large p_T. Equally, the daughter tracks of the Ξ_{cc}^{++} candidates will have a large IP with respect to their associated PV. This is in contrast with the Ξ_{cc}^{++} candidate itself that will have a small IP. Therefore, IP-related variables are also very useful discriminants for picking out $\Xi_{cc}^{++} \to \Lambda_c^+ K^-\pi^+\pi^+$ candidates. Furthermore, since the daughter tracks of the Ξ_{cc}^{++} decay will be significantly displaced from the event's associated PV (due to the relatively long Λ_c^+ lifetime and the expected non-zero lifetime of the Ξ_{cc}^{++} baryon) then FD variables are also advantageous. By definition, the Ξ_{cc}^{++} candidates must originate from its best associated PV. The best associated one is the PV that best fits the flight direction of the reconstructed Ξ_{cc}^{++} candidate. Therefore, by requiring that the DIRection Angle (DIRA) − the angle between the momentum vector of the Ξ_{cc}^{++} candidate and the line joining the PV and DV of the Ξ_{cc}^{++} candidate − is close to zero, then more sensible $\Xi_{cc}^{++} \to \Lambda_c^+ K^-\pi^+\pi^+$ candidates are retained for further studies. A combination of all the variables mentioned above is expected to help isolate $\Xi_{cc}^{++} \to \Lambda_c^+ K^-\pi^+\pi^+$ decays from the rest of the activity in an event. A pictorial diagram of the $\Xi_{cc}^{++} \to \Lambda_c^+(\to pK^-\pi^+)K^-\pi^+\pi^+$ decay is shown in Figure 4.1, where the IP of the Λ_c^+ candidate with respect to the PV of the event is also highlighted.

This philosophy of how to pick out $\Xi_{cc}^{++} \to \Lambda_c^+ K^-\pi^+\pi^+$ decays is utilised in four distinct stages of a candidate selection procedure. The general outline is:

- Tracks are reconstructed, selected and combined in to signal candidates centrally through the trigger (Section 4.3.2);
- A rectangular cut-based preselection is applied (Section 4.3.4);
- A mulitvariate selection is used on the remaining events (Section 4.3.5);
- A specialised selection removes candidates arising from cloning of tracks and track-exchanges (Section 4.3.6).

The design of the candidate selection is based on information from the following decay chains:

RS: $\Xi_{cc}^{++} \to \Lambda_c^+ (\to pK^-\pi^+)\, K^-\pi^+\pi^+$;

WSP: $\Xi_{cc}^{++} \to \Lambda_c^+ (\to pK^-\pi^+)\, K^-\pi^-\pi^+$;

WSM: $\Xi_{cc}^{++} \to \Lambda_c^+ (\to pK^-\pi^+)\, K^+\pi^-\pi^+$.

These data samples are used to measure and optimise the performance of the selection prior to examination of RS data. The kinematic distributions in the WS and DCS data sets are expected to be the same as that of the combinatorial background in the $\Xi_{cc}^{++} \to \Lambda_c^+ K^- \pi^+ \pi^+$ channel. The signal events are represented by signal MC and the background primarily by WS data. For both signal and background events, the Ξ_{cc}^{++} candidates are required to pass the full trigger requirements and offline selections. They also must have an associated Λ_c^+ candidate with a reconstructed mass between $[2270, 2306]\,\mathrm{MeV}/c^2$ approximately $\pm 3\sigma$ around the known Λ_c^+ baryon mass ($2286\,\mathrm{MeV}/c^2$ [1]). The reconstructed invariant mass of the Ξ_{cc}^{++} candidates must also be in the range $[3300, 3800]\,\mathrm{MeV}/c^2$ in order to be considered. RS data within these mass regions are not examined prior to the finalisation of the candidate selection.

To improve the mass resolution, the following mass estimator is used in the analysis

$$m(\Lambda_c^+ K^-\pi^+\pi^+) \equiv M(\Lambda_c^+ K^-\pi^+\pi^+) - M([pK^-\pi^+]_{\Lambda_c^+}) + M_{\mathrm{PDG}}(\Lambda_c^+), \tag{4.1}$$

where $M(\Lambda_c^+ K^-\pi^+\pi^+)$ is the measured invariant mass of the Ξ_{cc}^{++} candidate, $M([pK^-\pi^+]_{\Lambda_c^+})$ is the measured invariant mass of the $pK^-\pi^+$ combination corresponding to the intermediate Λ_c^+ candidate and $M_{\mathrm{PDG}}(\Lambda_c^+)$ is the known mass of the Λ_c^+ baryon. By using the definition of mass in Equation 4.1, a mild correlation between decay time and invariant mass is reduced and the mass resolution is improved. This effect is explained in more detail in Appendix A. The final mass measurement is made by fitting the distribution of this $m(\Lambda_c^+ K^-\pi^+\pi^+)$ mass estimator in RS data. Analogous mass variables are used for the WS and DCS samples when discussing the studies of background in Section 4.4.

4.3.2 Trigger Selection

Firstly, the Ξ_{cc}^{++} candidates must pass any L0 trigger line active during the 2016 data-taking period. This requirement is not strict but serves to maximise the number of events passing the selection for the fit to the final $m(\Lambda_c^+ K^-\pi^+\pi^+)$ mass spectrum. The efficiency of this L0 requirement is also difficult to evaluate but is equally not required when only a mass measurement is sought; a precise understanding of efficiencies is not necessary, as long as the requirement does not bias the mass distribution.

However, events do have to pass specific algorithms in the HLT1 trigger. The Ξ_{cc}^{++} and Λ_c^+ candidates both have to be TOS (see Section 2.5.2) with respect to the

Table 4.1: HLT1 trigger requirements for selecting RS, WS and DCS decays.

Trigger line	Selections
`Hlt1TrackMVA`	$p > 5\,\text{GeV}/c$, $\chi^2/\text{ndf} < 2.5$, $P(\text{ghost}) < 0.2$, $\{p_\text{T} > 1\,\text{GeV}/c$, $\log\chi^2_\text{IP} > (\frac{1}{(p_\text{T}-1)^2} + \frac{1.1\times(25-p_\text{T})}{25} + \log(7.4)\}$ or $\{p_\text{T} > 25\,\text{GeV}/c$, $\chi^2_\text{IP} > 7.4\}$, MatrixNet > 0.95
`Hlt1TwoTrackMVA`	Tracks: $p > 5\,\text{GeV}/c$, $\chi^2/\text{ndf} < 2.5$, $P(\text{ghost}) < 0.2$; Tracks: $p_\text{T} > 0.6\,\text{GeV}/c$, $\chi^2_\text{IP} > 4$; Vertex: $\chi^2_\text{vtx} < 10$, $M(\pi\pi) > 1\,\text{GeV}/c^2$; MatrixNet > 0.95

`Hlt1TrackMVA` line, which selects tracks with large χ^2_IP, p_T and momentum or the Ξ_{cc}^{++} and Λ_c^+ candidates both have to be TOS with respect to the `Hlt1TwoTrackMVA` line, which selects two tracks with reasonably large χ^2_IP and p_T and requires the two tracks to form a good vertex with a large invariant mass. Both trigger lines also try to eliminate ghost tracks by applying a selection requirement on the ghost probability factor, $P(\text{ghost})$.[2] The HLT1 requirements are found to introduce a lifetime biasing effect whereby Ξ_{cc}^{++} candidates with longer decay times are favoured over ones with shorter decay times. Finally, candidates are required to pass a `MatrixNet` classifier algorithm [139] within the software trigger, which has been trained on p_T and vertex χ^2_vtx information prior to data taking to recognise signal. The selection criteria of these two HLT1 lines are detailed in Table 4.1

After the L0 and HLT1 selections, events in this analysis are subject to the requirements of specific HLT2 lines that have Turbo processing enabled. The RS, WS and DCS data sets each separately come from dedicated Turbo lines that were developed before the start of the Run II. These Turbo lines were not developed by the candidate but by others in the LHCb collaboration. The three lines for RS, WS and DCS are identical apart from the charge combination required of the final-state particles. A full quantitative overview of the requirements in these trigger lines are given in Table 4.2, while the more important requirements are summarised as follows:

- $\Lambda_c^+ \to pK^-\pi^+$ candidates are reconstructed from three charged tracks that pass appropriate hadron DLL PID requirements, as well as quality requirements to reject low momentum tracks. The proton track must have momentum greater than $10\,\text{GeV}/c$ (to allow for discrimination between kaons and protons in RICH-1) and requirements are made on final-state track combinations; at least one of the three tracks must have $p_\text{T} > 1\,\text{GeV}/c$ and $\chi^2_\text{IP} > 16$ and at least two of them must have

[2] A ghost is a track that has been classified as having likely not been produced by a real particle. Ghosts are recognised by pattern recognition algorithms at LHCb [160].

$p_T > 400\,\text{MeV}/c$ and $\chi^2_{IP} > 9$. The Λ_c^+ candidate must have a good vertex fit quality and must point back to its associated PV such that its DIRA value is small. The DV of the Λ_c^+ candidate must be significantly displaced from its PV and only Λ_c^+ candidates whose mass is within $\pm 75\,\text{MeV}/c^2$ of the known Λ_c^+ mass are retained.

- $\Xi_{cc}^{++} \to \Lambda_c^+ K^- \pi^+ \pi^+$ candidates are reconstructed from the Λ_c^+ candidates plus three tracks that pass appropriate hadron DLL PID and momentum requirements. The vector sum of the p_T of the three tracks is required to be greater than $2\,\text{GeV}/c$. The three tracks and the Λ_c^+ candidate are required to form a vertex and each pairwise combination of the four tracks is required to have a Distance Of Closest Approach (DOCA) of less than 10 mm. The DV of the Λ_c^+ candidate must be 10 mm further along the z-axis from the decay vertex of the Ξ_{cc}^{++} candidate. The Ξ_{cc}^{+} candidates are also not explicitly required to be displaced from the PV, nor are IP requirements imposed on its daughters, so that the selection is sensitive to short-lived Ξ_{cc}^{++} candidates.

The trigger configuration in Run I was very different to Run II; for example, the Turbo HLT2 triggers were not available. Therefore, the online processing of the 2012 data proceeds very differently. The Λ_c^+ candidates in 2012 data are required to be TOS with respect to an inclusive HLT2 line and also need to be selected by an exclusive Ξ_{cc}^{++} Stripping line. More details on the trigger and Stripping requirements used in the 2012 data selection are given in Appendix B.

4.3.3 MC Sample Setup

As discussed in Section 2.4.1, PID discriminants are poorly modelled in simulation at LHCb for a variety of reasons. Therefore, the DLL PID requirements that are part of the selection criteria of the Turbo trigger lines, see Table 4.2, are not directly applied to the MC samples, which are used to optimise the offline selection. Instead their effect is emulated through a software package called `PIDCalib` [161] that is produced and maintained by LHCb. The details of this procedure are fully described in Appendix C. All other selection criteria in the HLT2 trigger lines are directly imposed on MC events.

In addition to the trigger requirements, selections are applied to the MC sample during its generation phase to ensure the simulated $\Xi_{cc}^{++} \to \Lambda_c^+ K^- \pi^+ \pi^+$ decays are produced within the geometric acceptance of the LHCb detector and so that computing resources are not wasted generating events that will be ultimately rejected by the trigger and selection anyway. A software tool within the Gauss package forces all charged particles to be produced with a polar angle that is between 10 mrad to 400 mrad relative to the z-axis. The tool also forces all Ξ_{cc}^{++} signals to have p_T greater than $3\,\text{GeV}/c$. This tool

Table 4.2: HLT2 trigger requirements for selecting RS, WS and DCS decays in the $\Xi_{cc}^{++} \to \Lambda_c^+ K^- \pi^+ \pi^+$ analysis. The requirements and limits remained fixed throughout the 2016 data-taking period.

Candidate	Variable	Requirement
Daughters of Λ_c^+	Track quality	$\chi^2/\text{ndf} < 3$
	Momentum	$p > 1\,\text{GeV}/c$
	Transverse momentum	$p_\text{T} > 200\,\text{MeV}/c$
	Arithmetic sum of daughter p_T	$> 3\,\text{GeV}/c$
	Impact parameter significance	$\chi^2_\text{IP} > 6$
	Proton momentum	$> 10\,\text{GeV}/c$
	Proton PID	$\text{DLL}_{p\pi} > 5$ & $\text{DLL}_{pK} > 0$
	Kaon PID	$\text{DLL}_{K\pi} > 5$
	Pion PID	$\text{DLL}_{K\pi} < 5$
	Maximum p_T	$> 1\,\text{GeV}/c$
	Second maximum p_T	$> 400\,\text{MeV}/c$
	Maximum χ^2_IP	> 16
	Second maximum χ^2_IP	> 9
Λ_c^+ mother	Vertex quality	$\chi^2_\text{vtx}/\text{ndf} < 10$
	Cosine of DIRA	> 0.99995
	Decay time	$\tau > 0.15\,\text{ps}$
	Mass	$[2200, 2350]\,\text{MeV}/c^2$
Daughters of Ξ_{cc}^{++}	Track quality	$\chi^2/\text{ndf} < 3$
	Transverse momentum	$p_\text{T} > 500\,\text{MeV}/c$
	Momentum	$p > 1\,\text{GeV}/c$
	Kaon PID	$\text{DLL}_{K\pi} > 10$
	Pion PID	$\text{DLL}_{K\pi} < 0$
Ξ_{cc}^{++} mother	Vector sum of daughter p_T	$> 2\,\text{GeV}/c$
	Vertex quality	$\chi^2_\text{vtx}/\text{ndf} < 60$
	DV of Λ_c^+ w.r.t. Ξ_{cc}^{++}	$(z_{\Lambda_c^+} - z_{\Xi_{cc}^{++}}) > 0.01\,\text{mm}$
	Distance of closest approach	$\text{DOCA} < 10\,\text{mm}$
	Mass	$[3100, 4000]\,\text{MeV}/c^2$

allows different transverse momentum thresholds to be assigned. The PhD candidate chose a p_T limit based on studies with other MC samples; examining the p_T distribution of Ξ_{cc}^{++} candidates from simulation retained after the trigger selection. Thus, the lower limit of $3\,\text{GeV}/c$ was chosen in order to retain a higher number of MC events to which to optimise the offline selection with.

The reconstructed objects (tracks, calorimeter clusters *etc.*) created in the simulation are also matched to the same generated objects produced by GAUSS. This process of association is referred to as 'truth-matching' and for this analysis, truth-matching requires all reconstructed tracks in the MC sample to belong to the correct particle type and to be associated to the correct particle decay.

4.3.4 Offline Processing and Preselection

The RS data directly from the output of Turbo will still contain a large number of uninteresting background decays, despite the relatively tight requirements of the trigger. To overcome this, a set of simple sequential rectangular cut-based requirements or 'preselections', are used to remove obvious background events. These preselections are applied to data before the data is more intensively scrutinized in the next stage of the selection to fully exploit differences between signal and background decays.

Before the preselections are devised, the remaining events that passed the trigger are further processed offline using the `DecayTreeFitter` (DTF) tool [162] within the DAVINCI software. This tool simultaneously fits the entire chain of a respective decay using momenta and vertex position information, such that all tracks have valid kinematic distributions and the mass resolution is improved. This works oppositely to the reconstruction algorithms deployed in Turbo and Stripping, which begin with the daughter tracks of a decay and work backwards to form the mother particle. With DTF, various constraints on particle masses and, or, vertex positions are possible. The implementation of the DTF tool used in this analysis forces all Ξ_{cc}^{++} candidates to originate from their best associated PV. No mass constraints are used with the DTF tool when designing this event selection. Studies discussing any of the reconstructed mass terms in Equation 4.1, here in after, have the Ξ_{cc}^{++} candidates refitted with the DTF tool, unless stated otherwise. At the same time that DTF refits the Ξ_{cc}^{++} decays, it also applies a momentum scaling calibration [163] to data such that the measured momentum of tracks is corrected for possible biases. Biases can occur for several reasons during data taking such as from a non-perfect alignment of the tracking system or the uncertainty on the magnetic field. For the Run II data, the momentum scaling is calibrated using large samples of detached J/ψ mesons in $J/\psi \to \mu^+\mu^-$ decays and reconstructed Stripped $B^+ \to J/\psi K^+$ decays [164, 165].

Table 4.3: The preselection requirements that are applied to data offline.

Particle	Requirement
All tracks	$2 \leq p \leq 150\,\text{GeV}/c$ $1.5 \leq \eta \leq 5.0$ `ProbNNghost` < 0.9
Proton	`ProbNNp` > 0.1
Kaons	`ProbNNk` > 0.1
Pions	`ProbNNpi` > 0.1
Ξ_{cc}^{++} candidate	$\log(\chi^2_{\text{IP}}) < 4$ $\chi^2_{\text{vtx}}/\text{ndf} < 10$ $p_{\text{T}} > 4\,\text{GeV}/c$ $\chi^2_{\text{vtx}} < 80$ (with DTF refit)

The requirements of the preselection are chosen based on data extracted from the WS Turbo line and on the MC events passing the same requirements as WS data plus the generator-level and truth-matching requirements, discussed in Section 4.3.3. Using the WS data to represent background and the MC events as signal decays, various requirements and limits on different quantities of the $\Xi_{cc}^{++} \to \Lambda_c^+ K^- \pi^+ \pi^+$ decays are investigated to find the combination that retains almost entirely all signal while removing a non-negligible amount of background. The final preselection requirements are listed in Table 4.3. The selection criteria include loose PID requirements for all final-state particles, topological cuts and requirements to ensure few ghost tracks pass the preselection. The PID variables used here are not the RICH DLL discriminants but are PID variables called `ProbNN` that combine information for the whole PID system at LHCb[3]. Requirements are imposed on the momentum and pseudorapidity, η, of final-state tracks such that data set is compatible with `PIDCalib`. Additionally, the Ξ_{cc}^{++} candidates are required to originate from their best associated PV and to have a good vertex from the initial fit and the refit performed by the `DTF` tool.

4.3.5 Multivariate Selection

The second stage of the offline selection relies on sophisticated multivariate analysis techniques to reduce one particular source of background called combinatorial background. This arises when unrelated tracks from different processes are incorrectly combined to form decays during the reconstruction process performed by Brunel. This typically

[3]ProbNN are PID scores calculated by neural networks from likelihood ratios. The ProbNN algorithm at LHCb considers all mass hypotheses for a track, unlike the DLL discriminants that only take the difference in likelihoods between two hypotheses.

occurs in all heavy-flavoured decays when their daughter tracks are not significantly separated from the several other tracks also produced near the PV. Other sources of background are studied in Section 4.4 following the application of the candidate selection.

Overview

Multivariate (MVA) selections offer a better means of discriminating between different processes in a system than the simple rectangular-cut based requirements that were used in the preselection. They collate information from multiple input variables that describe a system well to form a single variable called a multivariate. This multivariate then possesses more discriminating power alone than the original input variables when a selection is placed upon it. In the context of this analysis, MVA classifying algorithms are used to examine multiple features of a $\Xi_{cc}^{++} \to \Lambda_c^+ K^- \pi^+ \pi^+$ decay, establishing correlations and patterns between these features to determine the probability of a Ξ_{cc}^{++} candidate belonging to a certain type of event; in this case, signal or background. The software package, 'A Toolkit for Multivariate Analysis' (TMVA) [166], integrated with ROOT [167], provides the environment for the processing and application of the multivariate classification techniques needed in this stage of the selection. In TMVA, a single response variable is returned for each Ξ_{cc}^{++} candidate to reflect its likely event classification.

Training and Testing

In order for the TMVA algorithms to classify an event as signal or background, they must first be trained on samples of known composition, so they can learn to recognise the key features of both different types of decay. This is an example of supervised learning, to which all multivariate methods in TMVA respond. Using a select set of input training variables, the TMVA algorithms can then establish if a Ξ_{cc}^{++} candidate in RS data corresponds to a real signal. Several classifiers, trained using various different sets of input variables, are trialled to find the most suitable method for this analysis.

Simulated MC events train the classifiers to recognise signal while the WS (DCS) data is used as the default (cross-check) sample for training the classifier to learn about background. The WS and DCS samples have the preselections, which are detailed in Table 4.3, applied to them, as does the MC sample but the PID `ProbNN` requirements in this case are applied by weighting the MC sample according to information from `PIDCalib`. In order to increase the number of signal MC events, the L0 trigger requirements are not applied to either the signal or background sample. Only 5% of the WS sample is used in the background training, because of the large size of its data set, while the remaining 95% is used to optimise the final requirement imposed on the MVA response. Following the standard TMVA approach, both the signal and background samples are randomly

Table 4.4: The final ten variables used to train the multivariate classifier. In all cases 'log' denotes the natural logarithmic of the quantity.

Training variables
1) $\log(\chi^2_{\rm IP})$ of Ξ_{cc}^{++} to its PV
2) $\cos^{-1}$(DIRA) of Ξ_{cc}^{++} to its PV
3) $\log(\text{FD}\,\chi^2)$ of Ξ_{cc}^{++} from its PV
4) $\chi^2_{\rm vtx}$/ndf of the Λ_c^+ vertex fit
5) $\chi^2_{\rm vtx}$/ndf of the Ξ_{cc}^{++} vertex fit (no DTF refit)
6) $\chi^2_{\rm vtx}$/ndf of the Ξ_{cc}^{++} vertex fit (DTF refit with Ξ_{cc}^{++} PV constraint)
7) Smallest $\log(\chi^2_{\rm IP})$ among the daughters (Λ_c^+, K^-, π^+ and π^+) of the Ξ_{cc}^{++}
8) Scalar $p_{\rm T}$ sum of the daughters (Λ_c^+, K^-, π^+ and π^+) of the Ξ_{cc}^{++}
9) Smallest $p_{\rm T}$ among the daughters (Λ_c^+, K^-, π^+ and π^+) of the Ξ_{cc}^{++}
10) Smallest $p_{\rm T}$ among the final daughters of the Λ_c^+

split into two disjoint subsamples; one for training the classifiers and the other to test that the classifier has not been over-trained.[4]

The input variables for the MVA training are chosen based on their ability to discriminate between signal and background but effort is made not to use variables which are highly correlated. Given the limited number of signal MC events, the approach is to minimise the number of variables used to reduce the risk of over-training. Several variables are considered but only ten variables are used in the final multivariate selection. The final training variables used are listed in Table 4.4 and the level of correlation among each variable is shown in Figure 4.2. The distributions of each of the training variables in the signal and background sample are shown in Figure 4.3. As a reminder from Section 2.3.1, the $\chi^2_{\rm IP}$ is defined as the difference in χ^2 of a given PV reconstructed with and without track under consideration. The flight distance (FD) χ^2 is defined as the χ^2 of the hypothesis that the decay vertex of a candidate coincides with its primary vertex.

The choice of which MVA classifier to use for this analysis was narrowed down after examining the signal efficiency versus background rejection power for different classifiers using the final ten training variables. The aim is to select a classifier which retains the highest proportion of signal while rejecting as much background as possible. Several algorithms are considered but different Boosted Decision Tree (BDT) and Multi-Layer Perceptron (MLP) classifiers are found to give the best performance.[5] The background

[4]Over-training refers to cases when the training is too specific to a particular data set meaning that the classifier cannot be reliably applied to other samples on which it was not trained.

[5]BDTG is a BDT classifier with Gradient Boosting and the MLPBNN is a feed-forward MLP that uses the BFGS method [168] for training rather than a backward-propagation method.

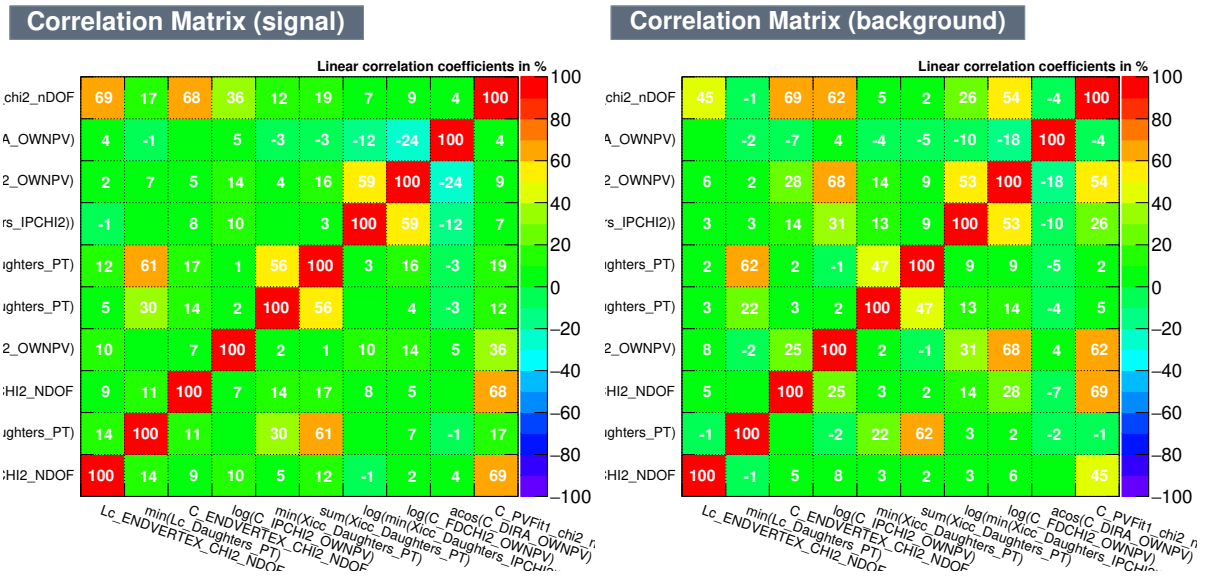

Figure 4.2: The correlation matrices for the final ten training variables used in the multivariate classifier in (left) signal MC and (right) background WS data.

rejection rates versus signal efficiency for the four best performing MVA algorithms are shown in Figure 4.4. All classifiers show a similar level of excellent performance with an expected signal efficiency of 50% corresponding to a background rejection rate of around 98%. The responses from the training and testing phases of the classification process for the four best performing MVA classifiers are shown in Figure 4.5. Based on the Kolmogorov−Smirnov test statistic, the BDT classifier is expected to be susceptible to over-training but this is not be case for the other classifiers.

Optimisation

The choice of which MVA classifier to use was finalised after investigating their obtainable Punzi Figure of Merit (FoM) scores [169] using data from the testing phase. This FoM is used to quantify the performance of the classifiers but, more importantly, is used to find the optimum selection on the MVA response distribution. The Punzi FoM is based only on the efficiency of the signal selection and an estimation of the background; it does not rely on the number of signal events, which is important when the expected signal yield is unknown. The Punzi FoM is defined as

$$\text{FoM} = \frac{\varepsilon(t)}{\frac{\sigma}{2} + \sqrt{B(t)}}, \tag{4.2}$$

where $\varepsilon(t)$ is the signal efficiency as a function of the response value, t, $B(t)$ is the expected number of background events as a function of t and σ is the desired significance, which is the number of standard deviations of signal above background. In this analysis, $\sigma = 5$

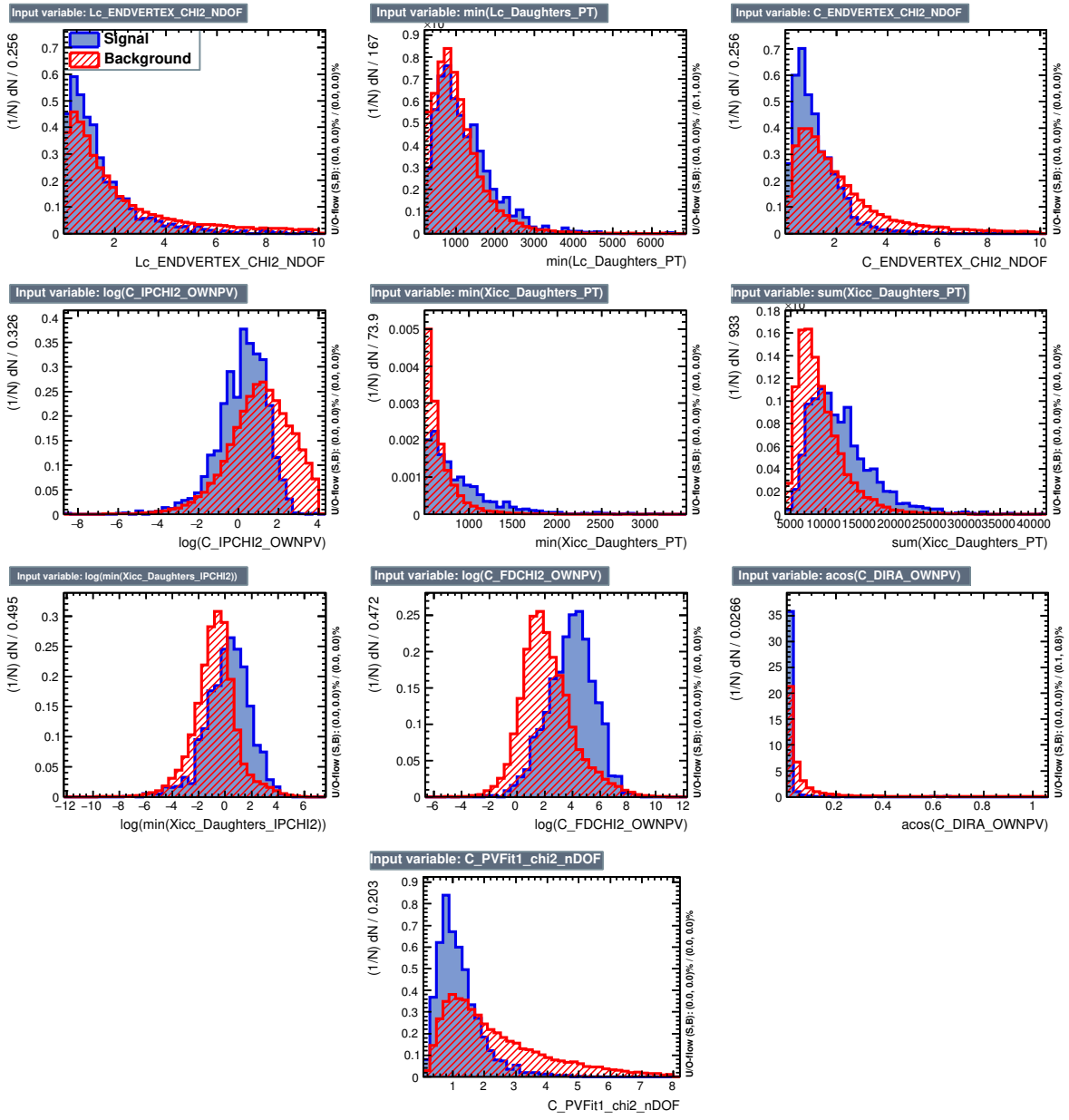

Figure 4.3: A comparison of the distributions of the final ten training variables used to train the multivariate classifier in the (blue) signal and (red) background samples.

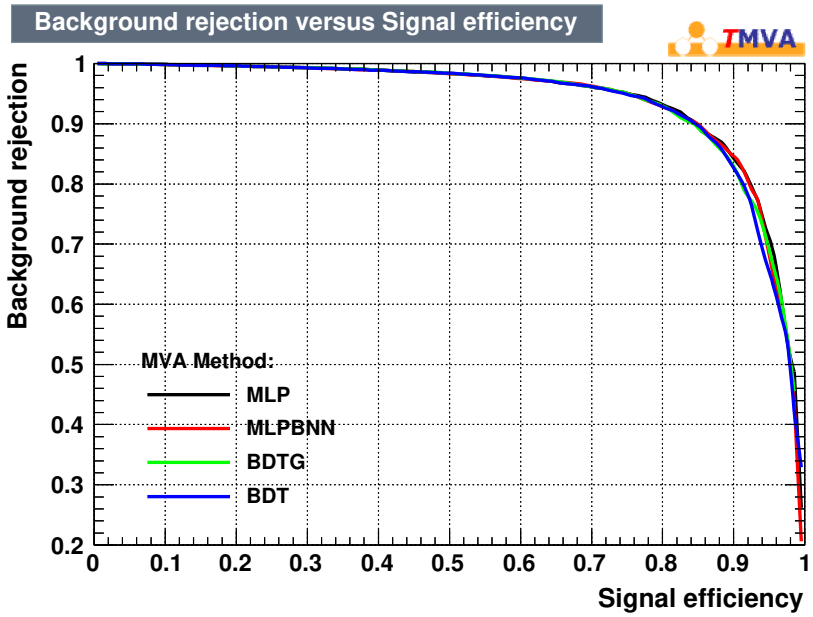

Figure 4.4: The background rejection versus signal efficiency curves for different MVA classifiers. The vertical axis shows the fraction of background events rejected and horizontal axis shows the analogous measure for signal.

since the aim is to discover decays of $\Xi_{cc}^{++} \to \Lambda_c^+ K^- \pi^+ \pi^+$ and this requires a significant signal to be obtained to make this claim. The terms in Equation 4.2 are evaluated as:

$$\varepsilon(t) = \frac{\text{Number of signal events after the response cut } t}{\text{Number of signal events generated}};$$

$$B(t) = \frac{\text{Number of background events after the response cut } t}{C_{\text{scaling}} \times C_{\text{mode}} \times C_{\text{window}}}.$$

The efficiency $\varepsilon(t)$ is defined as the signal efficiency with respect to the MC events passing the GAUSS generator-level cuts. Since $B(t)$ should correspond to the expected background underneath the signal region and not the total number of events in the WS data set, the WS sample is rescaled appropriately by the following factors:

- C_{scaling} – corrects for any downscaling used in the background sample. In this case, $C_{\text{scaling}} = 0.95$ since 5% was used for the training;
- C_{mode} – corrects for the difference in background level between the WS and RS data. This factor is the ratio of the numbers of events in the mass sidebands, $m(\Lambda_c^+ K^- \pi^+ \pi^+) > 3800\,\text{MeV}/c^2$, of WS and RS data. It is found to be equal to 2.1;
- C_{window} – corrects for the mass window used. The C_{window} factor is the ratio between the number of events in the full range of WS sample against the number of events residing in the expected Ξ_{cc}^{++} signal region because the important background level

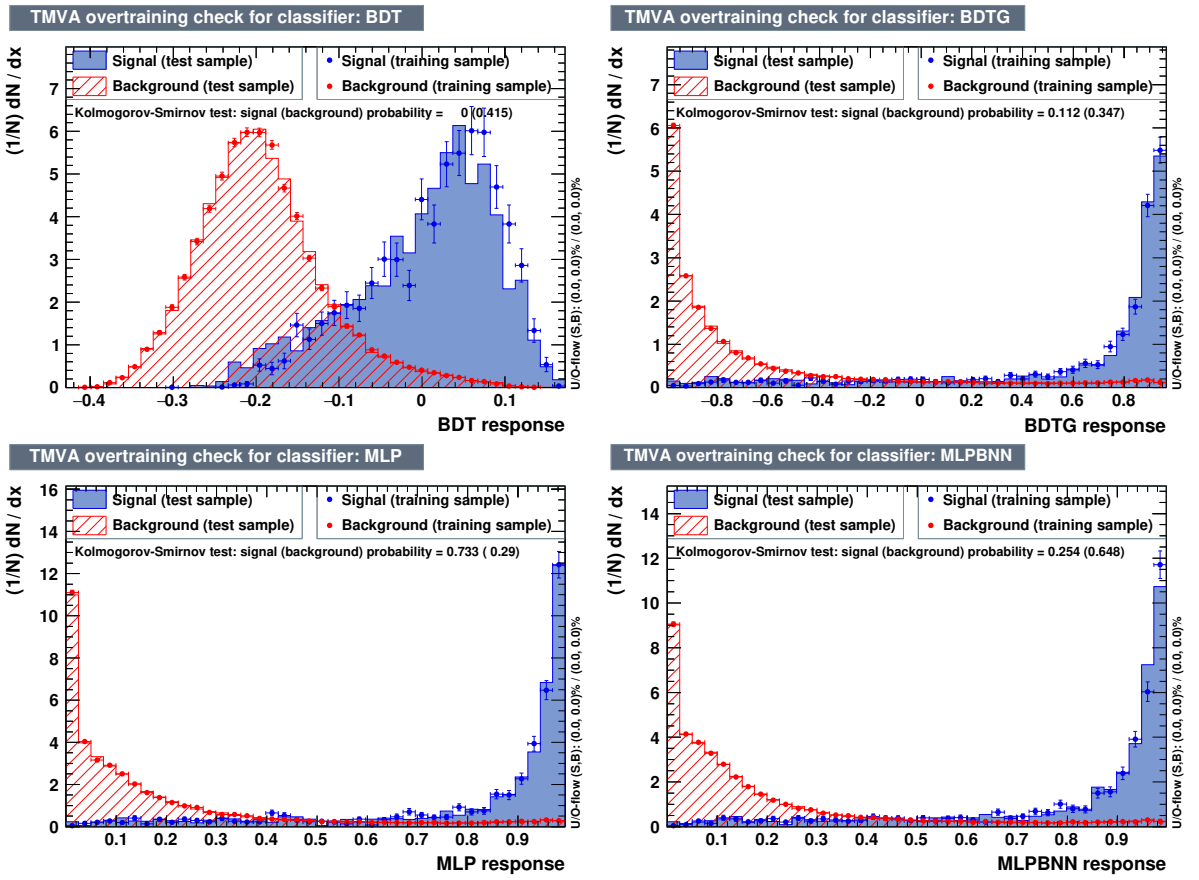

Figure 4.5: The normalised response distributions for the (top left) BDT, (top right) BDTG, (bottom left) MLP and (bottom right) MLPBNN classifiers. The results from training are shown as points with error bars while the testing results are shown as shaded-hatched histograms. The Kolmogorov−Smirnov test scores indicate the compatibility between the training and testing phases.

is that expected underneath the signal peak for FoM optimisation. This factor is found to be approximately 16.

The distribution of the Punzi FoM scores versus the requirement on the response variable for the best performing classifiers is shown in Figure 4.6. The requirement on the response variable for each classifier, which maximises the FoM value, is shown in Table 4.5. Based on the Punzi FoM scores and the resulting signal efficiencies, all algorithms work equally well in separating signal from background. In the end, the MLP classifier, which is a type of feed-forward artificial neural network, is chosen on the grounds that it appears more robust against over-training[6]. The MLP response for each Ξ_{cc}^{++} candidate is required to be greater than the value of 0.94 in the multivariate selection.

[6]The number of hidden layers used in the MLP classifier are varied from the default values provided by TMVA (version 4.2.1) [166] to try to improve its performance but this led to negligible gain.

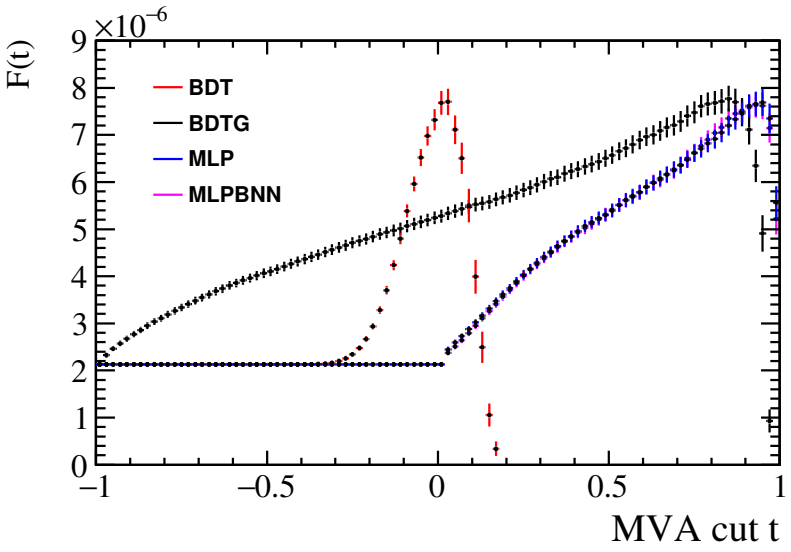

Figure 4.6: The Punzi figure of merit scores, F(t), as a function of the multivariate response for the four best performing classifiers.

Table 4.5: The optimum requirement on the multivariate response and resulting signal efficiency, $\varepsilon_{\text{MVA|presel}}$, for the four best performing classifiers.

Classifier	Optimal response (t)	$\varepsilon_{\text{MVA|presel}}$	FoM ($\times 10^{-6}$)
BDT	0.02	0.501 ± 0.016	7.70 ± 0.28
MLP	0.94	0.499 ± 0.016	7.69 ± 0.28
BDTG	0.84	0.542 ± 0.016	7.77 ± 0.27
MLPBNN	0.92	0.546 ± 0.016	7.63 ± 0.27

Validation Checks

Several cross-checks are performed to ensure that the training used is sensible following the application of the multivariate selection. The yield and retention rates of Ξ_{cc}^{++} candidates in the control modes as a function of the invariant mass are checked; the results of this study are shown in Figure 4.7. No significant peaking structures are seen in the invariant-mass distributions and the retention rate is approximately constant across the entire mass range, as expected. The invariant-mass variables plotted in Figure 4.7 for the WS and DCS data set are the same as the mass estimator given in Equation 4.1 to describe RS data; the only difference is in the charge of the final-state tracks used to form the invariant-mass combinations.

The effect of the expected lifetime of the Ξ_{cc}^{++} baryon on the performance of the MLP classifier is also checked. To do this, the signal MC sample is weighted to emulate other lifetimes other than the default 333 fs. Two different scenarios are examined:

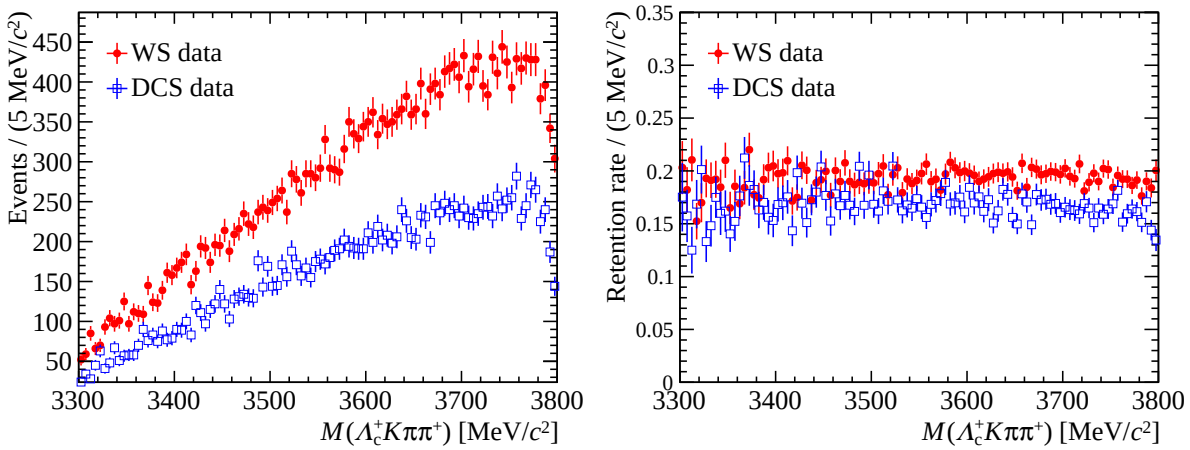

Figure 4.7: The (left) invariant-mass distribution after the multivariate requirement and (right) background retention rate for the WS and DCS data.

1. The MLP classifier is retrained with the weighted MC sample and the optimum requirement on the response is found;

2. The MLP classifier is not retrained but the default MLP is applied to the weighted MC sample and then the optimum requirement on the response is found.

The dependency of the Punzi FoM scores, obtained by the MLP (and BDT) classifier, on the lifetime of the Ξ_{cc}^{++} baryon is shown, in Figure 4.8 for both scenarios described above. The MLP classifier is found to perform better when the lifetime of the Ξ_{cc}^{++} baryon is longer. Figure 4.8 also highlights that the default training (left plot) gives a similar performance to what is obtainable by optimising under each lifetime hypothesis separately (right plot). In summary, the MLP classifier is able to efficiently separate signal from background for a variety of different lifetimes of the Ξ_{cc}^{++} baryon but its performance improves if the lifetime of the Ξ_{cc}^{++} baryon is longer, as would be expected.

4.3.6 Rejection of Specific Backgrounds

After the multivariate selection, multiple Ξ_{cc}^{++} candidates may wrongly exist in the same event. Due to the quark content of protons, it is almost impossible to have more than one real Ξ_{cc}^{++} baryon produced in the same event from pp collisions. However, mistakes in the reconstruction of the Ξ_{cc}^{++} decays may lead to this happening. The last stage of the offline selection targets the removal of fake Ξ_{cc}^{++} candidates that typically arise in decays with several final-state tracks such as $\Xi_{cc}^{++} \to \Lambda_c^+ K^- \pi^+ \pi^+$ decays that have six daughter tracks. Two special types of fake Ξ_{cc}^{++} candidates are removed in this selection.

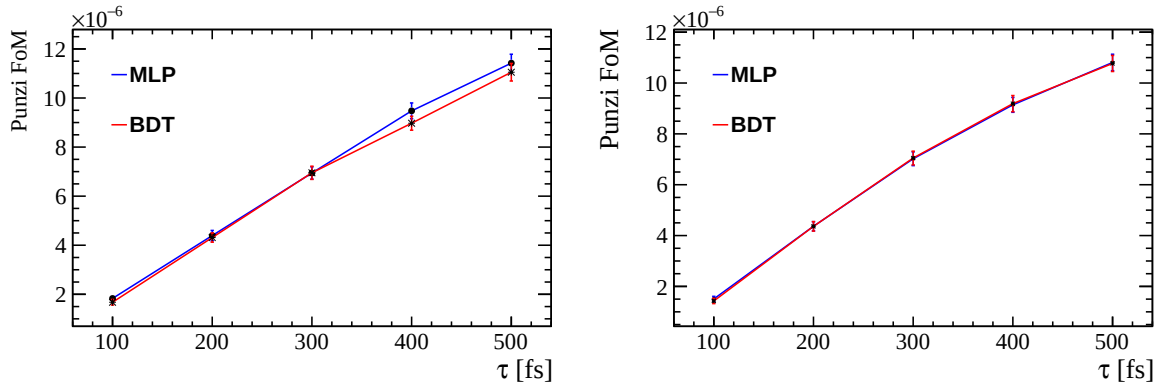

Figure 4.8: The Punzi FoM distributions obtained after weighting the signal MC sample to match Ξ_{cc}^{++} lifetime hypotheses, τ, between 100−500 fs with a (left) full retraining and reoptimisation and with (right) the default training.

Clones

The first type of candidate removed is a cloned candidate. Clones occur when the same set of detector hits is used to create more than one track.[7] These seemingly different tracks are then used to create more than one candidate of the same species in the same event. Since Ξ_{cc}^{++} candidates are reconstructed from a high number of tracks in $\Xi_{cc}^{++} \to \Lambda_c^+ K^- \pi^+ \pi^+$ decays, RS data is expected to contain a non-negligible amount of contamination from cloned candidates. Clones are fake signals and are not included in the fit to the final $m(\Lambda_c^+ K^- \pi^+ \pi^+)$ mass spectrum in RS data.

From knowledge gained by the LHCb collaboration in past analyses, the enclosed angle between cloned tracks, $\Delta\theta_{i,j}$, is known to be close to zero. The opening angles between any pairs of tracks, among all the six tracks, with the same charge in the WS, DCS and MC samples are plotted in Figure 4.9. In both the WS and DCS samples, a peak around the zero angle is seen, consistent in the two samples, which is understood to be caused by clone tracks. The same peak is not seen in simulation because of the truth-matching requirements. Based on these results, if a $\Delta\theta_{i,j} > 0.5$ mrad requirement is imposed on data as part of the specialised selection, then clone contributions may be fully removed without removing the majority of signal. If Ξ_{cc}^{++} candidates are reconstructed from at least one pair of final-state tracks identified to be clones of each other then the Ξ_{cc}^{++} candidate is not kept. This removes 10% of the Ξ_{cc}^{++} candidates in the WS data and more than 20% for the DCS data. Less than 1% of the Ξ_{cc}^{++} candidates in signal MC sample are removed.

The invariant-mass distribution of Ξ_{cc}^{++} candidates arising from expected clones in the WS and DCS data sets, after the multivariate selection, is shown in Figure 4.10.

[7] A true track and its clone are two different computer based objects but are the same physical track.

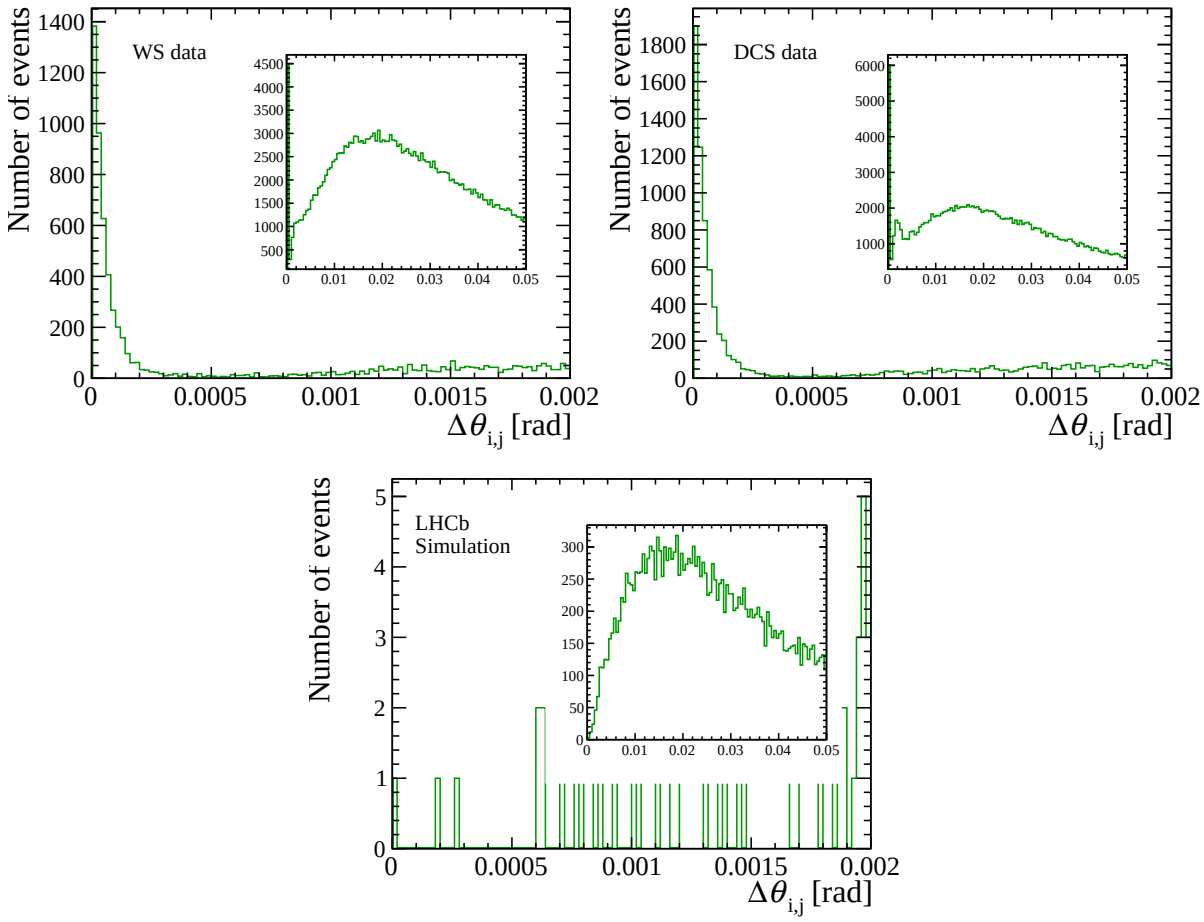

Figure 4.9: Opening angle, $\Delta\theta_{i,j}$, between final-state track of the same charge in the (top left) WS, (top right) DCS and (bottom) MC samples. The insert for each plot gives the same distribution but in a wider angular region.

The cloned candidates, removed by the $\Delta\theta_{i,j} > 0.5\,\text{mrad}$ requirement, have on average a smaller mass than the non-cloned Ξ_{cc}^{++} candidates due to the smaller opening angle of their final-state tracks. No significant peaks are identified in these mass distributions.

Duplications

The second type of candidate recognised as potentially problematic and linked to decays with a large number of final-state tracks, are candidates formed by track-exchanges that are referred to as duplications. Duplications may artificially increase the significance of a signal and so they must be removed when selecting candidates to study in the mass measurement. In the case of the $\Xi_{cc}^{++} \to \Lambda_c^+(\to pK^-\pi^+)K^-\pi^+\pi^+$ decay, duplications can occur from three situations during their reconstruction:

1. The K^- track from the Λ_c^+ decay vertex is swapped with the K^- track produced at the Ξ_{cc}^{++} decay vertex;

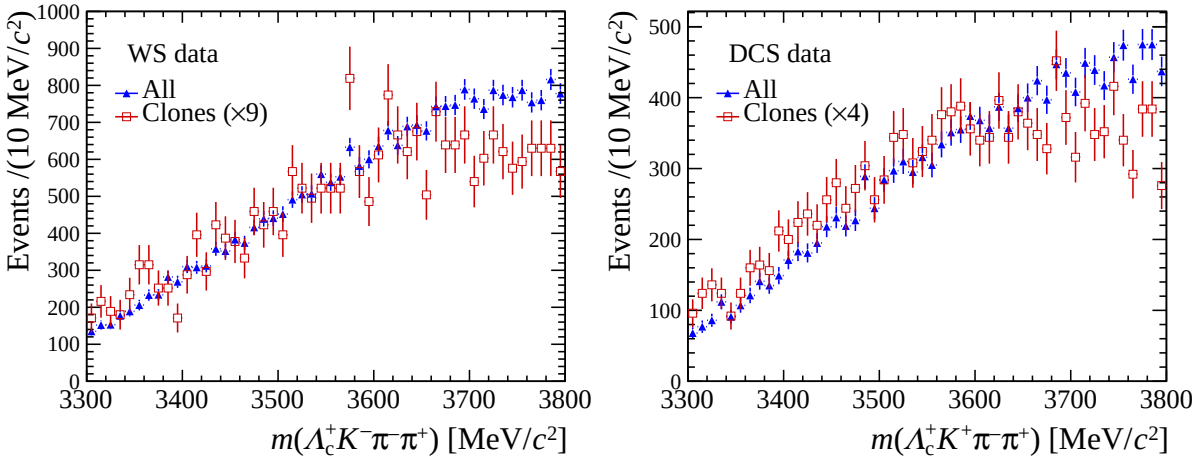

Figure 4.10: The invariant-mass distribution for (blue filled triangle) all Ξ_{cc}^{++} candidates and for (red open square) cloned candidates in the (left) WS and (right) DCS data sets.

2. The π^+ track from the Λ_c^+ decay vertex is swapped with any of the two π^+ tracks originating from the Ξ_{cc}^{++} decay vertex;

3. Track exchanges happen in both situation 1 and situation 2.

The requirements of the HLT2 Turbo lines, such as strict requirements on the reconstructed mass of the Λ_c^+ candidates and their vertex quality fit, will suppress the occurrence of duplications. However, since the phase space available to the decay products in $\Xi_{cc}^{++} \to \Lambda_c^+ K^- \pi^+ \pi^+$ decays is expected to be small, then duplications are still expected to be present in data. Duplications will have exactly the same invariant mass as any non-duplicate Ξ_{cc}^{++} candidate but the mass of their associated Λ_c^+ candidate might be very different from the known mass of the Λ_c^+ baryon.

Using a combination of Run, Fill and track object serial numbers, duplicate candidates are identified. Every electronic channel on the LHCb detector has an associated 'LHCbID' integer, such that every reconstructed object then has an associated set of detector hits and LHCbIDs to uniquely identify it. The invariant-mass distributions for duplications in the MC and WS samples after the multivariate selection are investigated. Normally in simulation, duplications are removed by the truth-matching process since any tracks that are exchanged can then no longer be matched to their true mother particle. Duplications were recovered manually in the MC sample used for this study alone to examine the effects of duplicate candidates. As expected, a peak is seen around the generated value of Ξ_{cc}^{++} baryon ($3597.98\,\text{MeV}/c^2$) used in this particular simulated sample as shown in the left plot of Figure 4.11. However, in the pure combinatorial background (the WS sample), duplications do not create fake peaks, as can be seen in the right plot of Figure 4.11. In the $\Xi_{cc}^{++} \to \Lambda_c^+ K^- \pi^+ \pi^+$ analysis, this duplication removal process discards around 2.7% of the Ξ_{cc}^{++} candidates in WS data after the multivariate selection

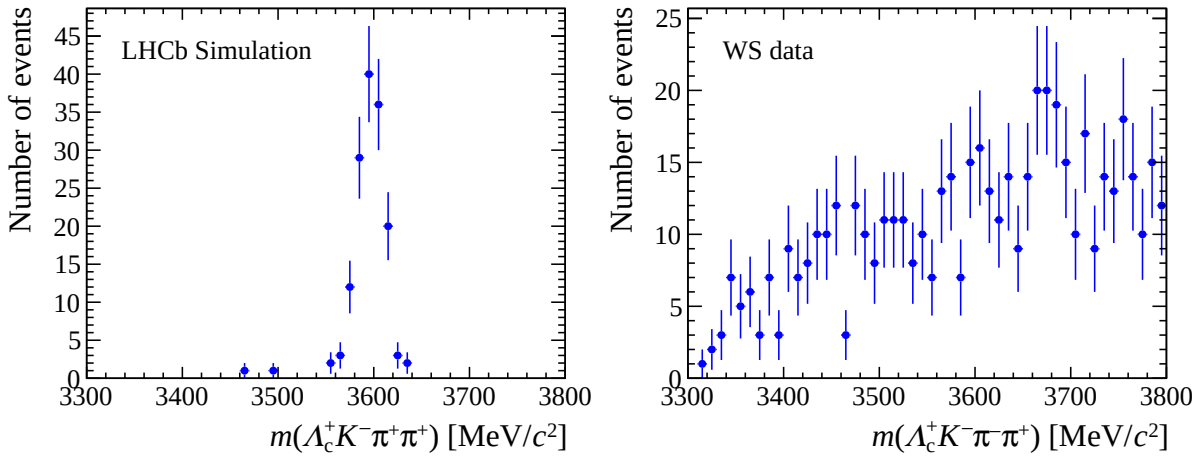

Figure 4.11: The invariant-mass distribution of duplicate Ξ_{cc}^{++} candidates in (left) a track-exchange-allowed MC sample and in (right) the WS data set.

and the removal of clones, and less than 1% for the DCS dataset. In simulation, around 3% of signal decays are removed by this method. The duplication removal rate for WS and DCS data is smaller compared to the MC sample simply because there are fewer possible track-exchange scenarios; three ways in WS decays, one way in DCS decays and five ways in the simulated RS decays.

Candidates identified to be reconstructed from exactly the same six tracks as another Ξ_{cc}^{++} candidate in the same event, and therefore be a duplicate, are removed apart from one candidate in that event. To avoid any biases, the retained Ξ_{cc}^{++} candidate is chosen at random. This strategy of removing duplicate candidate events does not remove events that contain signal candidates as at least one signal decay per event is kept. The duplication removal process will be applied to RS data at the end of all selection steps. However, there is no way to guarantee that the single candidate retained is the real candidate and not one of its duplicates. The fact that duplicates are not removed before the multivariate selection is not an issue because the classifier is trained on a truth-matched MC sample so no duplicates will be present anyway. Duplications also have a slight impact on the Ξ_{cc}^{++} mass measurement, see Section 4.5.2.

Track exchanges is just one mechanism which can give rise to fake multiple candidate in a single event. There are other ways in which multiple candidates can occur and these are examined in detail in Section 4.4.2 when discussing the studies of background.

4.4 Background Studies

In this section, potential backgrounds in the $\Xi_{cc}^{++} \to \Lambda_c^+ K^- \pi^+ \pi^+$ channel are studied. The contribution of fake Ξ_{cc}^{++} signals from background associated to the intermediate

Λ_c^+ candidate, multiple candidates, particle misidentification, and other physical decay processes are briefly discussed. These types of background are studied prior to examination of RS data using the WS and DCS data sets to evaluate each of their likely contributions in the RS channel.

The findings presented in this section provide convincing evidence that the backgrounds discussed will not create fake peaking structures in the $m(\Lambda_c^+ K^- \pi^+ \pi^+)$ invariant mass distribution of RS data. Analogous mass quantities to that used for RS data, $m(\Lambda_c^+ K^- \pi^- \pi^+)$ and $m(\Lambda_c^+ K^+ \pi^- \pi^+)$ for the WS and DCS data set, respectively, are used in the following studies. Additionally, Ξ_{cc}^{++} candidates reconstructed in either the RS, WS or DCS data sets are referred to as Ξ_{cc}^{++} candidates for simplicity and to avoid confusion.

4.4.1 Λ_c^+ Background

The first study performed is a check of the invariant mass of the Ξ_{cc}^{++} candidates, after the multivariate selection, with different associated Λ_c^+ masses. As mentioned in Section 4.3.1, only Λ_c^+ candidates with an invariant mass within $[2270, 2306]\,\mathrm{MeV}/c^2$ are included in the search as part of this analysis.

The Λ_c^+ signal search region is depicted as the middle cross-shaded region of Figure 4.12 and the Λ_c^+ mass sidebands, defined as $[2222, 2258] \cup [2318, 2354]\,\mathrm{MeV}/c^2$, are also shown in Figure 4.12 as the striped-shaded regions. The mass distributions of the Ξ_{cc}^{++} candidates in different Λ_c^+ mass regions are shown in Figure 4.13 for both the WS and DCS data set. The Ξ_{cc}^{++} mass distributions in the signal and sideband Λ_c^+ mass regions are consistent with each other after normalisation. This is the case for both the WS and DCS data set. The results suggest that the combinatorial background of Ξ_{cc}^{++} candidates arising from either signal Λ_c^+ or Λ_c^+ combinatorial background are very similar and that narrow peaking structures are not expected.

4.4.2 Multiple Candidates

As mentioned in Section 4.3.6, events can have more than one Ξ_{cc}^{++} candidate reconstructed and selected by a combination of the trigger and offline selections. In fact, from the Turbo output six Ξ_{cc}^{++} candidates per event on average are observed in the WS data set. After the offline selection, this reduces to 1.28 Ξ_{cc}^{++} candidates per event on average.

Multiple candidates are further examined to see if their presence in background may cause peaking structures in the $m(\Lambda_c^+ K^{-(+)} \pi^- \pi^+)$ mass distributions in WS (DCS) data. Multiple candidates resulting from the following three scenarios are examined:

1. Two or more Ξ_{cc}^{++} candidates in the same event share all six final-state tracks with the same mass assignments;

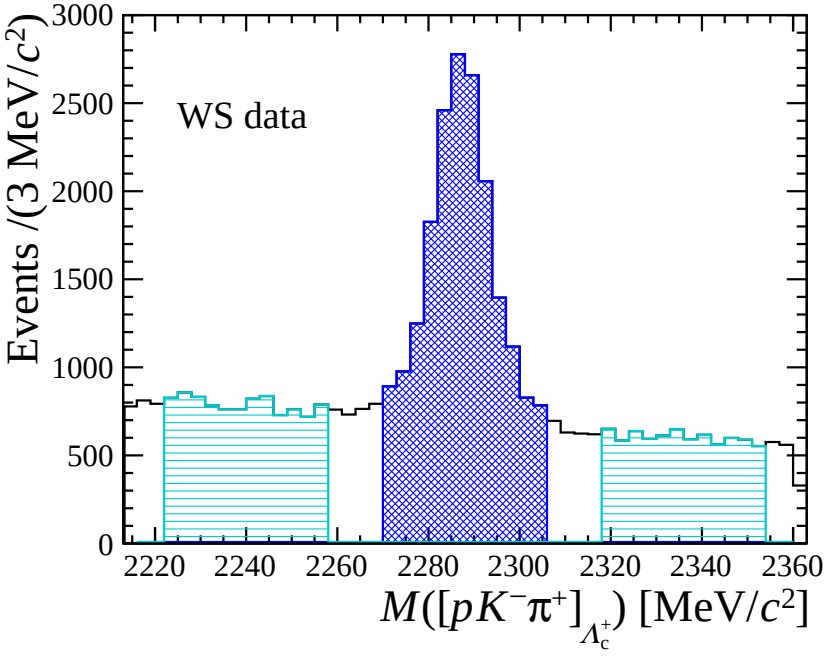

Figure 4.12: The invariant-mass distribution of Λ_c^+ candidates in WS data with the (shaded blue) signal region and the (cyan horizontal) sideband regions shown.

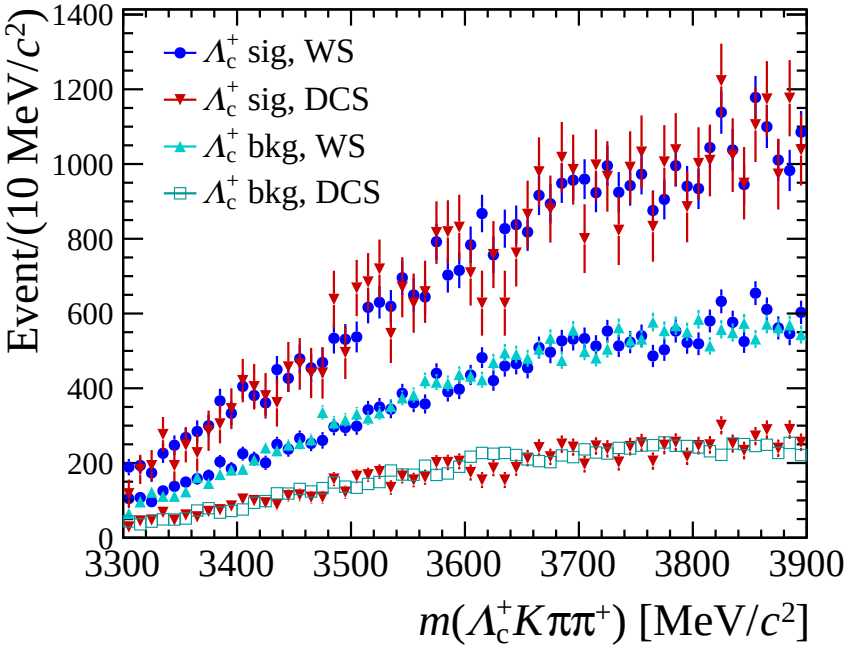

Figure 4.13: Invariant-mass distributions in the WS (DCS) data set for Ξ_{cc}^{++} candidates that reside in the Λ_c^+ signal region, shown as blue circles (red triangles) and in the Λ_c^+ background regions, shown as cyan triangles (open squares). The distributions are scaled to overlap pair-wise, which is why the red and blue data points appear twice.

2. Two or more Ξ_{cc}^{++} candidates in the same event share a few but less than six final-state tracks and the shared tracks have the same mass assignments;

3. Two or more Ξ_{cc}^{++} candidates share either all final-state tracks, or a fraction of them, but at least one shared track has a different mass assignment.

The first case describes duplicate candidates, which are mentioned in Section 4.3.6 when describing the candidate selection, and so are not discussed further here. The second case describes a partial reconstruction, for example when a Λ_c^+ candidate is combined with other kaon, pion and proton tracks in the same event to form another Ξ_{cc}^{++} candidate. In the WS and DCS data sets, the second case proves to be the dominant source of multiple candidates; especially from the same Λ_c^+ candidate being used by two or more different Ξ_{cc}^{++} candidates. The third case corresponds to misidentified background, which is discussed in Section 4.4.3. This type of background is highly suppressed by strict PID requirements.

The $m(\Lambda_c^+ K \pi^+ \pi^+)$ mass distributions in the WS and DCS samples for events containing a singly selected Ξ_{cc}^{++} candidate and those with multiply selected Ξ_{cc}^{++} candidates are shown in Figure 4.14. Duplications are removed in the plots in Figure 4.14 and a number of simulated signals, corresponding approximately to an expected 5σ local statistical significance in RS data, are injected into the plot to indicate what the mass distribution in RS data might look like if signal is present. The WS distributions are scaled by a factor of 0.5 such that they approximately match the number of Ξ_{cc}^{++} candidates found in RS data outside the signal search region. The mass distributions for singular candidate events and multiple candidate events are found to be similar. No significant narrow peaking structures are identified in either control sample.

In conclusion, multiple candidates of the second and third form are not removed because they are not expected to cause peaking mass structures in the background of RS data and that so the selection does not reject potential signal decays.

4.4.3 Misidentified Background

Despite strict PID requirements throughout the selection, both in the trigger and in the offline preselection, background, resulting from tracks being identified as an incorrect particle type, can still be expected. This is usually referred to as a 'reflection' background. For instance, there are a large number of decays from the singly-charmed mesons which, with a single final-state kaon or pion misidentified as a proton, can lead to their manifestation in the same final state as one of the intermediate $\Lambda_c^+ \to pK^-\pi^+$ decays in the overall $\Xi_{cc}^{++} \to \Lambda_c^+(\to pK^-\pi^+)K^-\pi^+\pi^+$ decay chain.

Reflections are generally suppressed by the excellent PID capabilities of the LHCb detector. However, to check for the potential contamination from certain reflections, in

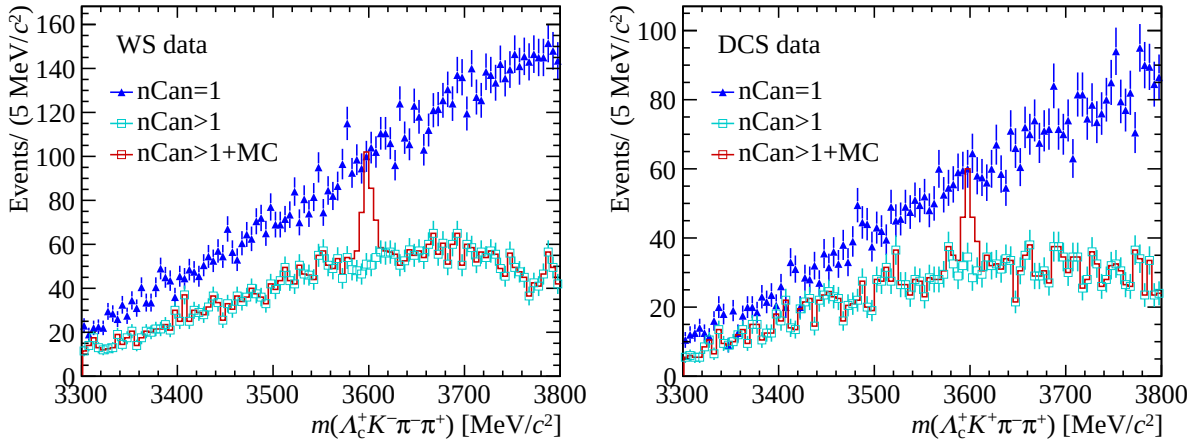

Figure 4.14: Invariant-mass distributions of Ξ_{cc}^{++} candidates, passing the final selection, for (blue triangle) events with exactly one candidate and for (open cyan square) events that have multiple candidates selected. The left (right) plot is for the WS (DCS) sample. The red histogram shows mass distribution for multiple candidate event together with 150 injected signals from simulation.

the region of the mass of the Λ_c^+ baryon, tracks are refitted under different mass hypotheses. The most abundant reflections in this case are from the singly-charmed D^+ and D_s^+ mesons. The reflections investigated are the $D^+ \to K^- \pi^+ \pi^+$ decay with a measured branching fraction of $(9.13 \pm 0.19)\%$ [1], and which would be mistaken as a $\Lambda_c^+ \to p K^- \pi^+$ decay if a pion is misidentified as a proton, and also the $D_s^+ \to K^+ K^- \pi^+$ decay with a branching fraction of $(5.49 \pm 0.27)\%$ [1] that would be wrongly interrupted as a $\Lambda_c^+ \to p K^- \pi^+$ decay if a kaon is misidentified as a proton.

The invariant-mass distributions of the D_s^+ and D^+ reflections are shown in Figure 4.15 after replacing the proton hypothesis in the $\Lambda_c^+ \to p K^- \pi^+$ final state by a K^+ and π^+ hypothesis, respectively. In the two plots, signal D_s^+ and D^+ decays are observed but with contributions below 1% of the total number of selected events. The $m(\Lambda_c^+ K \pi^- \pi^+)$ invariant-mass distributions for events in the signal region of the reflections are shown in Figure 4.16. The signal regions are defined as $\pm 18\,\text{MeV}/c^2$ around the known values of the D_s^+ and D^+ baryons, which are $1968.47\,\text{MeV}/c^2$ and $1869.63\,\text{MeV}/c^2$, respectively [1]. No significant peaking structures are identified for these reflections. Therefore, particle misidentification is not expected to cause issues for the mass measurement of the Ξ_{cc}^{++} baryon in RS data and no events are vetoed because of reflections.

Backgrounds from two misidentified tracks, originating from the Ξ_{cc}^{++} candidate, are not investigated as they are not expected due to charge configuration constraints. Equally, double misidentified background for tracks from the Λ_c^+ candidate are not explicitly investigated as they are expected to be highly suppressed due to the relatively tight requirement on Λ_c^+ mass. Finally, the contribution of the singly-Cabbibo-suppressed $\Xi_{cc}^{++} \to \Lambda_c^+ K^+ K^- \pi^+$ decay, where a K^+ track is reconstructed as a π^+ track, is expected

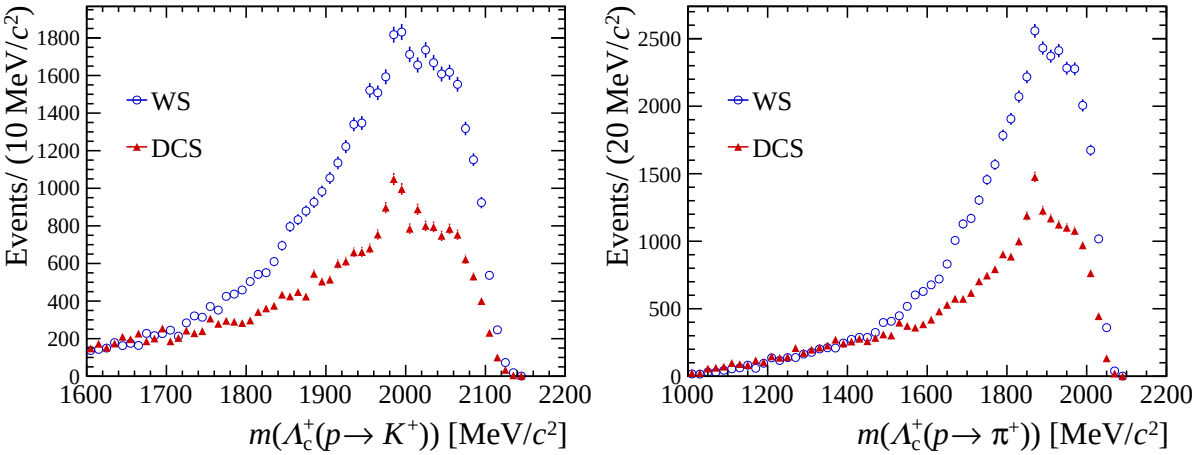

Figure 4.15: Invariant-mass distribution of Λ_c^+ candidates in the WS and DCS data after a proton from the $\Lambda_c^+ \to pK^-\pi^+$ decay is replaced by a (left) K^+ and a (right) π^+ hypothesis, respectively.

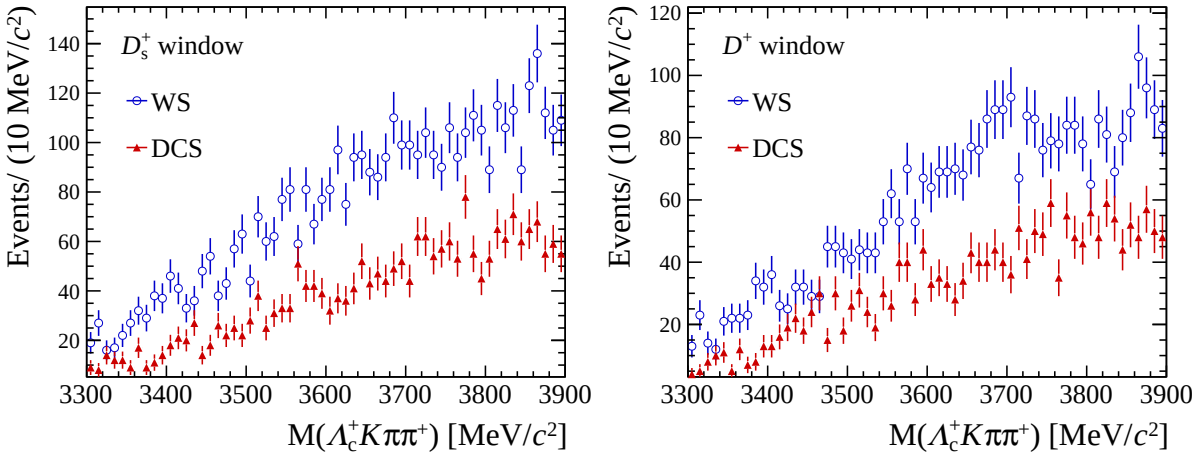

Figure 4.16: Invariant-mass distributions for events residing in the (left) D_s^+ and (right) D^+ signal regions that are plotted in Figure 4.15.

to be negligible due to the expected smaller branching fraction of this decay and the tight particle identification requirements in the selection.

The effect of tightening particle identification requirements in the event selection is also investigated. The $m(\Lambda_c^+ K^-\pi^-\pi^+)$ invariant-mass distribution in WS data, after the full selection, as a function of different particle identification requirements is plotted in Figure 4.17. The tighter PID requirements are compared to the default PID requirements used in the trigger and preselection. The mass distributions are very similar and smoothly shaped and no peaking structures are present. In summary, there is expected to be no issues if particle identification hypotheses are incorrect for the combinatorial background.

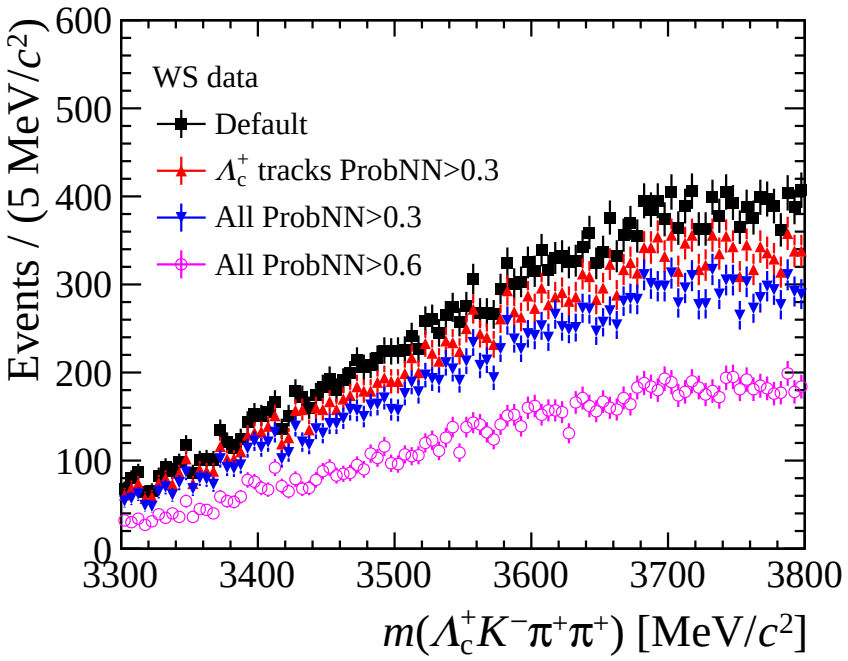

Figure 4.17: Invariant-mass distribution of Ξ_{cc}^{++} candidates in WS data as a function of tighter particle identification requirements applied to final-state tracks.

4.5 Mass Measurement Studies

In this section, appropriate studies that are needed to be performed in order to measure the mass of the Ξ_{cc}^{++} baryon, prior to examination of RS data, are discussed. The signal and background models used to fit the $m(\Lambda_c^+ K^- \pi^+ \pi^+)$ mass distribution in RS data are described in detail and a brief overview of sources of systematic uncertainty connected to the Ξ_{cc}^{++} mass measurement are also discussed. For most of the studies in this section, the signal MC sample simulated under 2016 data-taking conditions and described in Section 4.2.2, is used, as well as 2016 data. The same strategies developed and discussed here are also used for the 2012 RS data.

4.5.1 Mass Models

The mass of the Ξ_{cc}^{++} baryon is measured from the $m(\Lambda_c^+ K^- \pi^+ \pi^+)$ invariant-mass distribution of the Ξ_{cc}^{++} candidates in RS data that passed the full selection. The $m(\Lambda_c^+ K^- \pi^+ \pi^+)$ variable is defined in Equation 4.1 with its terms evaluated after a kinematic refitting by the `DecayTreeFitter` tool to constrain the Ξ_{cc}^{++} candidates to originate from their best associated primary vertex and at the same time to apply momentum scaling corrections.

Signal

The shape of the expected signal mass distribution in RS data is studied with simulated MC events passing the selection discussed in Section 4.3. Sensible empirical models are tested against the signal distribution observed in signal MC events. The invariant-mass distribution of the Ξ_{cc}^{++} candidates is expected to peak somewhere between 3300−3800 MeV/c^2, with a smear given by the convolution of its intrinsic decay width Γ (see Section 1.4.1) with the experimental resolution of the LHCb detector. Any observed mass peak should be dominated by detector resolution effects in this case.

The $m(\Lambda_c^+ K^- \pi^+ \pi^+)$ mass distribution is found to be well described by a Gaussian function convoluted with a Double-Sided-Crystal-Ball (DSCB) function. The DSCB is an extension of the Crystal Ball function [170] and is defined as

$$\mathrm{DSCB}(x;\mu,\sigma_1,n_\mathrm{L},n_\mathrm{H},\alpha_\mathrm{L},\alpha_\mathrm{H}) = N \cdot \begin{cases} e^{-0.5t^2} & \text{if } -\alpha_\mathrm{L} \leq t \leq \alpha_\mathrm{H} \\ e^{-0.5\alpha_\mathrm{L}^2}\left[\frac{\alpha_\mathrm{L}}{n_\mathrm{L}}\left(\frac{\alpha_\mathrm{L}}{n_\mathrm{L}} - \alpha_\mathrm{L} - t\right)\right]^{-n_\mathrm{L}} & \text{if } t < -\alpha_\mathrm{L} \\ e^{-0.5\alpha_\mathrm{H}^2}\left[\frac{\alpha_\mathrm{H}}{n_\mathrm{H}}\left(\frac{\alpha_\mathrm{H}}{n_\mathrm{H}} - \alpha_\mathrm{H} + t\right)\right]^{-n_\mathrm{H}} & \text{if } t > \alpha_\mathrm{H}, \end{cases} \tag{4.3}$$

where $t = (x-\mu)/\sigma_1$, N is a normalisation parameter, μ represents the mean, σ_1 represents its width and α_low (α_high) parameterise the mass value where the distribution of the invariant mass becomes a power-law function on the low-mass (high-mass) side, with n_low (n_high) the exponent of this function. The x parameter is the value of the $m(\Lambda_c^+ K^- \pi^+ \pi^+)$ mass estimator for each Ξ_{cc}^{++} candidate. The DSCB function allows the asymmetric tails of the mass peak, caused by initial and final state radiation, to be fitted.

In the total Gaussian plus DSCB model, the widths of the Gaussian and DSCB components are scaled together such that the resolution width, σ, of the model is defined as $\sigma = \sqrt{f * \sigma_2^2 + (1-f) * \sigma_1^2}$, where σ_2 is the width of Gaussian component, σ_1 is the same as defined in Equation 4.3, and f is the fraction of Gaussian part. Due to the f parameter being highly correlated with other parameters, it is fixed to a value of 0.3. The Gaussian and DSCB components also share a common mean, μ, which will correspond to the central value of the measured mass.

The excellent agreement between this model and the signal MC sample can be seen in Figure 4.18. This model is therefore chosen as the default model to fit the RS data. The fit by the Gaussian plus DSCB model to the MC events uses an unbinned-extended maximum-likelihood method, where the fit parameters converge on the values given in Table 4.6. The mass of the Ξ_{cc}^{+} baryon is set to 3597.98 MeV/c^2 in the simulated sample shown in Figure 4.18. The difference between the fitted and generated mass of the Ξ_{cc}^{++} baryon is covered by the systematic uncertainty that is discussed in Section 4.5.2.

When fitting this model to RS data, all the parameters are fixed to the values given in

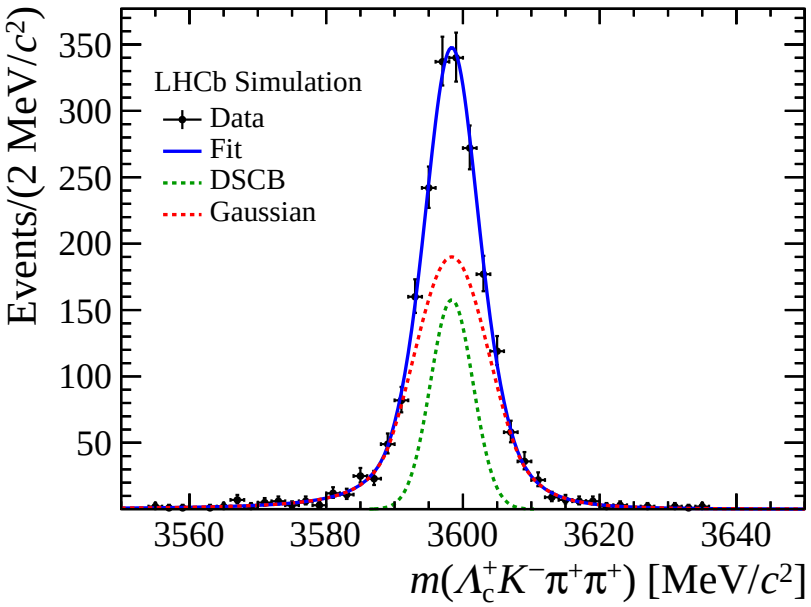

Figure 4.18: Invariant-mass distribution of Ξ_{cc}^{++} candidates in a 2016 MC sample with simulated $\Xi_{cc}^{++} \to \Lambda_c^+ K^- \pi^+ \pi^+$ decays. A Gaussian plus Double-Sided-Crystal-Ball fit is overlaid. The simulated data points are shown in black.

Table 4.6. Only the signal and background yields and the resolution σ and mean μ of the signal are determined from RS data. The resolution found in simulation is approximately $5\,\text{MeV}/c^2$ and so a mass range of $\pm 150\,\text{MeV}/c^2$, centred on any peak, is chosen as the appropriate fit range in RS data.[8] This is large enough to contain all signals and also to constrain the background distribution. The uncertainty associated to choosing the Gaussian plus DSCB function as the default mass model is discussed in Section 4.5.2.

Background

The invariant-mass distributions of Ξ_{cc}^{++} candidates in the WS and DCS data sets are expected to be shaped similarly to combinatorial background in the RS channel. Therefore, the shape of the background may be taken from these data control samples.

The invariant-mass distributions in these data sets after the full selection are given in Figure 4.19, where it can be seen that the reconstructed mass of the Ξ_{cc}^{++} candidates increases linearly before saturating at higher mass values. A second-order Chebyshev function (i.e. a second-order polynomial) with free parameters is shown to describe the mass distributions in both the WS and DCS data sets, well. This second-order polynomial, with a gradient parameter set to the value found by fitting to the WS data set, is hence used as the default model for fitting background in RS data. Alternative fit models and

[8] Due to the imperfect modelling of detector resolution in simulation, the resolution found in simulation may not accurately reflect that in data.

Table 4.6: The value of the mass model parameters from the fit to the simulated data shown in Figure 4.18.

Parameter	Value from fit
μ	$3598.40 \pm 0.14\,\text{MeV}/c^2$
σ (resolution)	$4.88 \pm 0.14\,\text{MeV}/c^2$
$R = \frac{\sigma(\text{DSCB})}{\sigma(\text{Gaussian})}$	1.48 ± 0.24
f(Gaussian)	0.3 (fixed)
α_L	1.8 ± 0.3
n_L	2.1 ± 0.9
α_H	2.1 ± 0.2
n_H	1.9 ± 0.7
If other parameters are fixed to values above	
μ	$3598.40 \pm 0.14\,\text{MeV}/c^2$
σ	$4.88 \pm 0.12\,\text{MeV}/c^2$

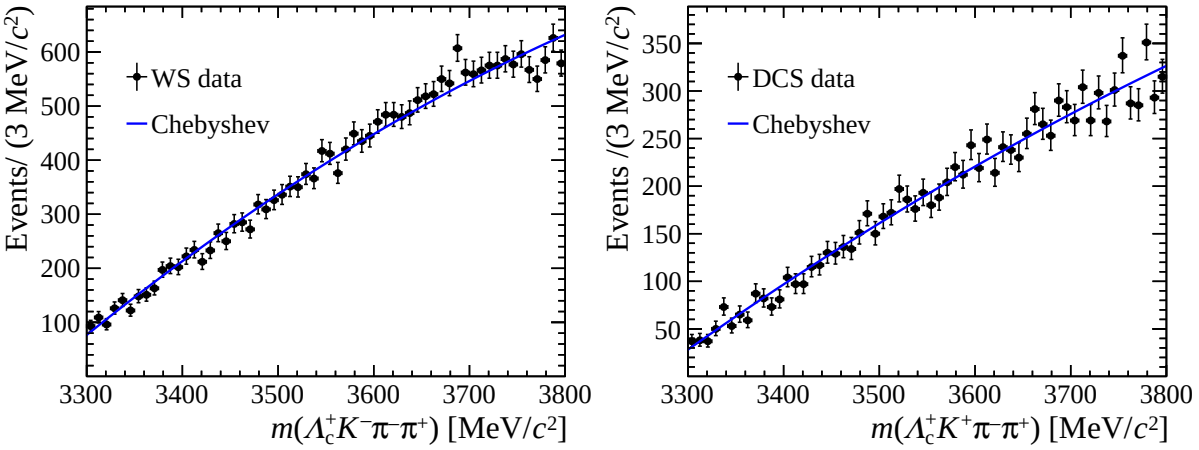

Figure 4.19: Invariant-mass distributions for the (left) WS and the (right) DCS data sets with a second-order Chebyshev polynomial fit overlaid.

mass ranges are used to evaluate the systematic uncertainty associated to this choice of background model. This is discussed in more detail in Section 4.5.2.

4.5.2 Systematic Uncertainties

Several possible sources of systematic uncertainty on the Ξ_{cc}^{++} mass measurements are investigated as part of the $\Xi_{cc}^{++} \to \Lambda_c^+ K^- \pi^+ \pi^+$ analysis. The PhD candidate was not heavily involved in the majority of these studies, apart from uncertainties related to the mass models, momentum scaling and duplications. Therefore, only these systematic uncertainties are discussed in this section. An overview of all the dominant systematic

uncertainties and their source are however listed in Table 4.7 in Section 4.6 for completeness. A total systematic uncertainty of $0.27\,\mathrm{MeV}/c^2$ is found after taking the sum in quadrature of the individual uncertainties and a $0.14\,\mathrm{MeV}/c^2$ uncertainty is found due to the uncertainty on the world-average mass of the Λ_c^+ baryon [1]. Systematic uncertainties noted in Table 4.7 but not discussed in the main text of this section, are calculated using the same methods described in the next chapter of this thesis when it comes to the mass measurement of the Ξ_{cc}^{++} baryon in another decay mode, see Sections 5.5.3 to 5.5.7.

Momentum Scaling Calibration

As mentioned in Section 4.3.4, the momentum of tracks are recalibrated offline using samples of $J/\psi \to \mu^+\mu^-$ and $B^+ \to J/\psi K^+$ decays [164, 165]. This momentum correction is performed according to the data-taking period, the magnet field polarity and the charge of the tracks. The momentum scaling calibration is cross-checked with the masses of several b-hadron decays. The b-hadron masses agree with their known values within ± 0.3‰ after the calibration. This 0.3‰ uncertainty on the momentum of the tracks introduces a systematic uncertainty of $0.22\,\mathrm{MeV}/c^2$ on the observed invariant mass of Ξ_{cc}^{++} candidates. This makes the momentum calibration the dominant source of systematic uncertainty for the Ξ_{cc}^{++} mass measurement, which is not unexpected given the $\Xi_{cc}^{++} \to \Lambda_c^+ K^- \pi^+ \pi^+$ decay is reconstructed from six tracks, each with a momentum uncertainty.

Duplicate Candidates

Duplications are described in Section 4.3.6 as candidates arising from tracks being exchanged during reconstruction to create more than one copy of the same physical Ξ_{cc}^{++} candidate. Normally in simulation, track-exchanges cannot occur after truth-matching requirements are applied. However, for this study, the truth-matching requirements applied to the MC sample are altered to allow track exchanges to occur. When comparing the fit to the the MC sample with and without track-exchange candidates present, the average Ξ_{cc}^{++} mass is altered by $(0.08 \pm 0.04)\,\mathrm{MeV}/c^2$, which is not significant. The change in the value of the signal shape parameters, listed in Table 4.7, is also smaller than their statistical uncertainties when the track-exchange candidates are used. The fraction of track-exchange candidates in the signal component of the fit to RS data is not expected to be very different from that found in the MC sample. However, it is not easy to quantify the difference between data and simulation, so in the end, for a conservative measurement, the value of $0.08\,\mathrm{MeV}/c^2$, is assigned as a systematic uncertainty of the Ξ_{cc}^{++} mass measurement related to excluding track-exchange candidates in the final fit to RS data.

Mass Fit Models

The Gaussian plus DSCB model used to describe the final $m(\Lambda_c^+ K^- \pi^+ \pi^+)$ mass distribution in RS data is ultimately a subjective choice. This fit could introduce some biasing effects on the measured mass of the Ξ_{cc}^{++} baryon. Therefore, the PhD candidate, in collaboration with other LHCb colleagues tested alternative fit models to test the impact on the mass measurement in RS data. This includes using a DSCB function without the Gaussian component to fit the signal, using a linear function to model the background, varying the fitted parameters used in the default model and changing the mass fit ranges. All these studies are conducted after examining the RS data and so the final systematic uncertainties related to the mass model used in the fit RS data is discussed in Section 4.6.1.

4.6 Results

Having finalised the candidate selection, performed detailed studies into potential backgrounds and chosen the models to fit the mass distributions, RS data within the mass region $m(\Lambda_c^+ K^- \pi^+ \pi^+) \in [3300, 3800]\,\text{MeV}/c^2 \cap M([pK^-\pi^+]_{\Lambda_c^+}) \in [2270, 2306]\,\text{MeV}/c^2$ are examined. For simplicity, right-signed data is referred to as data where appropriate.

An unambiguous peak is observed around $3620\,\text{MeV}/c^2$ in both the 2016 and 2012 data sets. The details of the observed signal with 2016 data and the confirmation of the signal with 2012 data is given in Section 4.6.1, while a preliminarily study of the resonant structures in the decay from 2016 data is presented in Section 4.6.2. Finally, the lifetime of the signal is confirmed to be consistent with a weak decay in Section 4.6.3.

4.6.1 Mass Distributions

2016 Results

The invariant-mass distributions of the Ξ_{cc}^{++} candidates in 2016 data and in the WS and DCS data sets, after the selection described in Section 4.3, are shown in Figure 4.20. The mass range in Figure 4.20 is between $3300-3800\,\text{MeV}/c^2$, which corresponds to the entire mass range with the given selection. A significant peak is observed around $3620\,\text{MeV}/c^2$ in the data, whereas the mass distributions in the WS and DCS control modes are smoothly shaped across the entire mass range.

An unbinned extended maximum likelihood fit to the invariant-mass distribution in data is shown in Figure 4.21. The fit is centered between $3470-3770\,\text{MeV}/c^2$ around the peaking structure. The signal component is described by the Gaussian plus DSCB function that is described in Section 4.5. The background component is modelled by

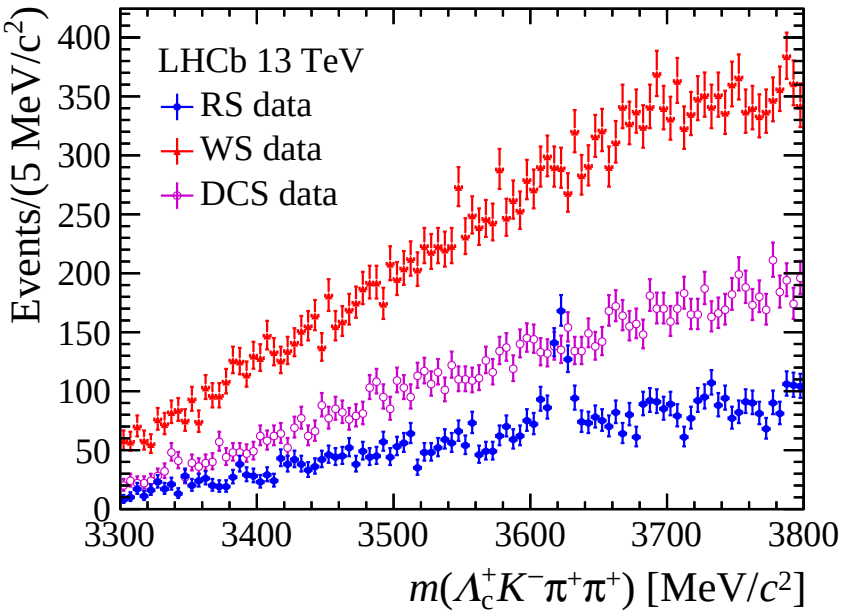

Figure 4.20: Invariant-mass distributions of the right-signed (blue) $\Lambda_c^+ K^- \pi^+ \pi^+$, wrong-signed (red) $\Lambda_c^+ K^- \pi^- \pi^+$ and doubly-Cabibbo-suppressed (magenta) $\Lambda_c^+ K^+ \pi^- \pi^+$ 2016 data after the candidate selection.

a second-order Chebyshev polynomial. All the parameters in the total fit are fixed to the values given in Table 4.6 apart from signal and background yield and the resolution. The mean value from the fit is $\mu = 3621.80 \pm 0.72\,\text{MeV}/c^2$, the mass resolution is $\sigma = 6.63 \pm 0.82\,\text{MeV}/c^2$, which is consistent with the value found in simulation, and the signal yield is 313 ± 30, where all the uncertainties quoted are statistical. The local statistical significance is above 12σ, based on the log-likelihood difference between the hypotheses with and without the signal component in the fit model ($\sqrt{-2\Delta \ln L}$) in accordance with Wilks' theorem [171]. The peak is also shown to consist of Ξ_{cc}^{++} candidates that are formed from real Λ_c^+ combinations as can be seen from the two-dimensional mass scan in Figure 4.22.

2012 Results

As mentioned in Appendix B, the 2012 data is subject to a very similar event selection to the 2016 data. The analogous invariant-mass distribution plots for the 2012 data and the WS and DCS data sets are shown in Figure 4.23.

A peaking structure is also observed around $3620\,\text{MeV}/c^2$ in the 2012 data as shown in the left plot of Figure 4.23 while the invariant-mass spectra from the WS and DCS samples are again smoothly shaped. From the fit to 2012 data, which is shown in the right plot of Figure 4.23, the mean value is $\mu = 3622.62 \pm 1.18\,\text{MeV}/c^2$, the mass resolution is

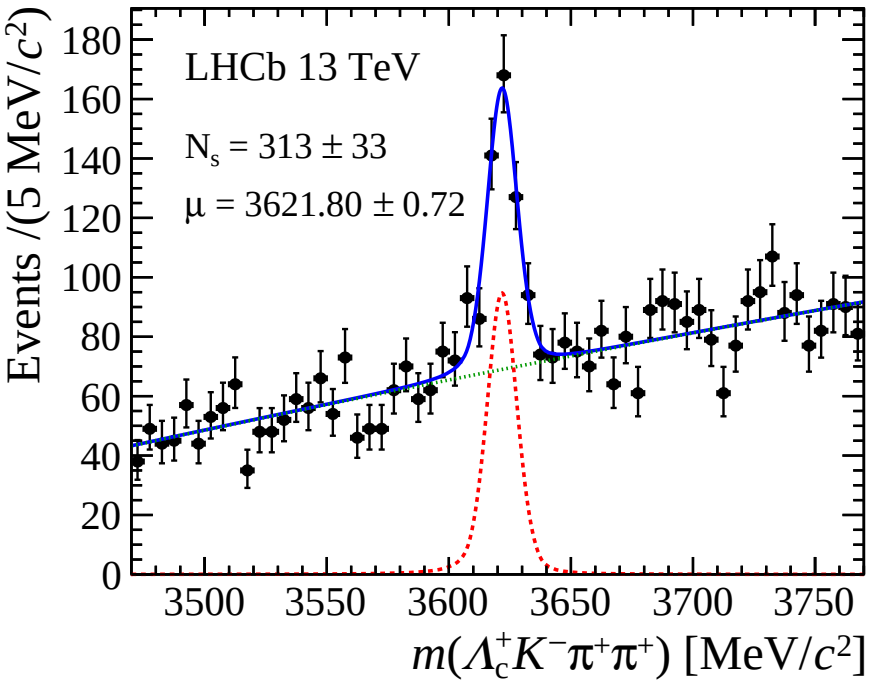

Figure 4.21: Invariant-mass distribution of Ξ_{cc}^{++} candidates in 2016 data after the analysis selection with the projections of the (dashed red line) signal, the (dotted green line) background and the (blue line) total fit overlaid. The black points represent data.

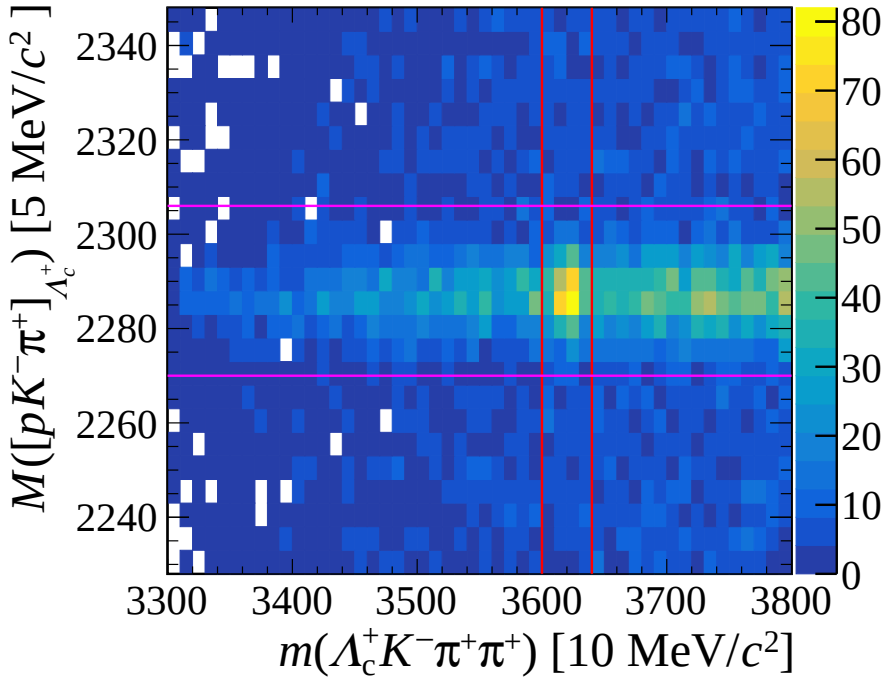

Figure 4.22: Invariant-mass distribution of the Λ_c^+ candidates versus that of the Ξ_{cc}^{++} candidates. The area between the two vertical or horizontal lines indicate the signal regions for the Ξ_{cc}^{++} and Λ_c^+ candidates, respectively.

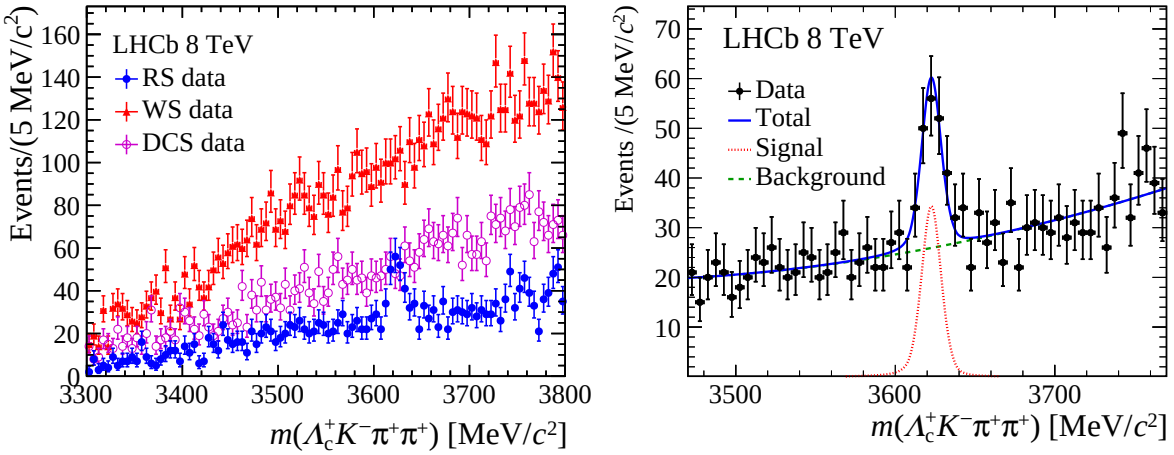

Figure 4.23: (Left) Invariant-mass distribution of the right-sign (blue) $\Lambda_c^+ K^- \pi^+ \pi^+$, wrong-sign (red) $\Lambda_c^+ K^- \pi^- \pi^+$ and doubly-Cabibbo-suppressed (magenta) $\Lambda_c^+ K^+ \pi^- \pi^+$ 2012 data after the selection and (right) the fit to the invariant-mass distribution of Ξ_{cc}^{++} candidates in 2012 data.

$6.70 \pm 1.35\,\text{MeV}/c^2$ and the signal yield is 113 ± 21, where the uncertainties come from the fit. The fit model in Figure 4.23, is identical to the one used on 2016 data. The local statistical significance is above 7.6σ, based on the log likelihood difference between hypotheses with and without the signal component in the fit model. The results with 2012 data are consistent with 2016 data and the yields are expected based on the luminosities, Ξ_{cc}^{++} production cross sections and selection efficiencies involved in the 2012 and 2016 analyses.

Systematic Uncertainty of Mass Model

Having examined the 2016 data, the systematic uncertainty from the choice of fit mass model is examined. Using only a DSCB function to describe the signal peak instead of a Gaussian plus DSCB function results in a change of $0.06\,\text{MeV}/c^2$ to the mass according to the mean of the fit.[9] In another case study, the parameters of the Gaussian plus DSCB function are changed one by one by their statistical uncertainty given in Table 4.7 then the Gaussian plus DSCB function is refitted to the $m(\Lambda_c^+ K^- \pi^+ \pi^+)$ mass distribution in data. Since the uncertainties given in Table 4.7 are correlated, the largest variation resulting from changing the parameters in the fit, $0.07\,\text{MeV}/c^2$, is taken as the systematic uncertainty from this study. Additionally, changing the mass region from $3620 \pm 150\,\text{MeV}/c^2$ to $3620 \pm 100\,\text{MeV}/c^2$ results in a $0.01\,\text{MeV}/c^2$ change in the mean mass of the fit.

[9]Other alternative models were considered to fit the signal, such as a Gaussian and a Breit-Wigner function but these did not describe the signal shape well in simulation so their results were not included in the evaluation of this systematic uncertainty; they would have artificially inflated its value otherwise.

Table 4.7: Systematic uncertainties on the Ξ_{cc}^{++} mass measurement in the $\Xi_{cc}^{++} \to \Lambda_c^+ K^- \pi^+ \pi^+$ channel. The statistical uncertainty is given for reference.

Source	Value (MeV/c^2)
Momentum scaling calibration	0.22
Λ_c^+ bias due to selections	0.01
Ξ_{cc}^{++} bias due to selections	0.11
Ξ_{cc}^{++} unknown lifetime	0.06
Duplicate candidates	0.08
Mass Model	0.07
Total	0.27
Uncertainty of Λ_c^+ mass	0.14
Statistical	0.72

The mean of the fit also changes by a value of 0.02 MeV/c^2 when a linear function is used to model the background with the rest of the fit procedure kept the same as the default. Finally, if the shape of the background component is fixed to the mass distribution in WS data then the mean of the fit changes by 0.07 MeV/c^2. The systematic uncertainties from using alternative mass models discussed are also all correlated. Therefore, the maximum variation of 0.07 MeV/c^2 is quoted as the final uncertainty related to the choice of mass model. When this systematic uncertainty is combined with the uncertainties discussed in Section 4.5.2, a total systematic uncertainty of 0.27 MeV/c^2 is obtained for the Ξ_{cc}^{++} mass measurement.

Mass Measurement Summary

From the 2016 data alone, the measured mass of this new state is $3621.80 \pm 0.72\,\text{MeV}/c^2$. However, this fitted mass value must be corrected by $+0.04\,\text{MeV}/c^2$ and $-0.49\,\text{MeV}/c^2$ due to offline selection biases on the mass of the Λ_c^+ and Ξ_{cc}^{++} baryon, respectively. These mass corrections are discussed in Section 4.5.2. Therefore, the resulting mass of this new state is

$$\mu = 3621.40 \pm 0.72\,(\text{stat}) \pm 0.27\,(\text{syst}) \pm 0.14\,(\Lambda_c^+)\,\text{MeV}/c^2,$$

after taking into account both the statistical and systematic uncertainties. This results in a total uncertainty of less than 1%, which is statistically dominated. The last uncertainty, 0.14 MeV/c^2, is due to the limited knowledge of the mass of the Λ_c^+ baryon.

4.6.2 Resonant Structures

Signs for intermediate resonances are also investigated in the final data sample passing the candidate selection. Possible resonance structures in the 2016 data after examining different combinations of the final-state particles are shown in Figure 4.24. The background contribution in the sidebands of the invariant mass distribution of the Ξ_{cc}^{++} candidates in Figure 4.21 is simply reduced by assigning these candidates negative weights. In the top left plot of Figure 4.24, a clear peak of the $\Sigma_c(2455)^{++}$ baryon, with an expected decay width $1.89^{+0.09}_{-0.18}\,\text{MeV}/c^2$ [1], is observed via its $\Sigma_c(2455)^{++} \to \Lambda_c^+ \pi^+$ decay. In the same plot, a hint of evidence for $\Sigma_c(2520)^{++} \to \Lambda_c^+ \pi^+$ decays is also observed, where the $\Sigma_c(2520)^{++}$ baryon's decay width is expected to be $14.78^{+0.30}_{-0.40}\,\text{MeV}$ [1]. In the top right plot of Figure 4.24, a hint of the $K^{*0} \to K^- \pi^+$ decay is seen but the evidence is not significant. A reminder that the $\Xi_{cc}^{++} \to \Sigma_c^{++} K^{*0}$ decay was mentioned as a possible pathway for the $\Xi_{cc}^{++} \to \Lambda_c^+ K^- \pi^+ \pi^+$ decay in Section 1.4.2. Note that the plots in Figure 4.24 are not corrected for any variations in selection efficiency across phase-space dependent variables.

4.6.3 Lifetime Checks

After extracting a mass measurement of this new state, the decay times of the candidates making up the peaking structures in the 2016 and 2012 data are scrutinized. The invariant-mass distributions of the Ξ_{cc}^{++} candidates with a reconstructed decay time five times larger than the decay-time uncertainty, σ_t, are shown in Figure 4.25. The peak reported previously in the 2016 (2012) data maintains its statistical significance above 12σ (7σ). These findings prove that the Ξ_{cc}^{++} candidates in the peak have a long and non-zero lifetime, making the data consistent with what is expected for a weak decay.

The proper decay time distribution of the Ξ_{cc}^{++} signals in the 2016 data after the candidate selection is shown in Figure 4.26. The simulated MC sample that was used to develop the selection is shown alongside for comparison. The simulated sample is generated with the Ξ_{cc}^{++} lifetime set to 333 fs. The background is subtracted using the `sPlot` method [172]. `sPlot` is a way to unfold the various signal and background components from a data sample via a maximum likelihood fit. In this study, the invariant-mass distribution of the Ξ_{cc}^{++} candidates is used as the discriminate in the `sPlot` method since it is uncorrelated to the decay time distribution. The distributions of the background-subtracted data and 333 fs simulated MC events are consistent with each other. The simulated distributed is then weighted to have a Ξ_{cc}^{++} lifetime of 100 fs and this distribution is also shown in Figure 4.26. The observed distribution is incompatible with a lifetime of 100 fs but similar to that of a lifetime of 333 fs. A similar relationship was seen between the 2012 data and the 2012 MC sample.

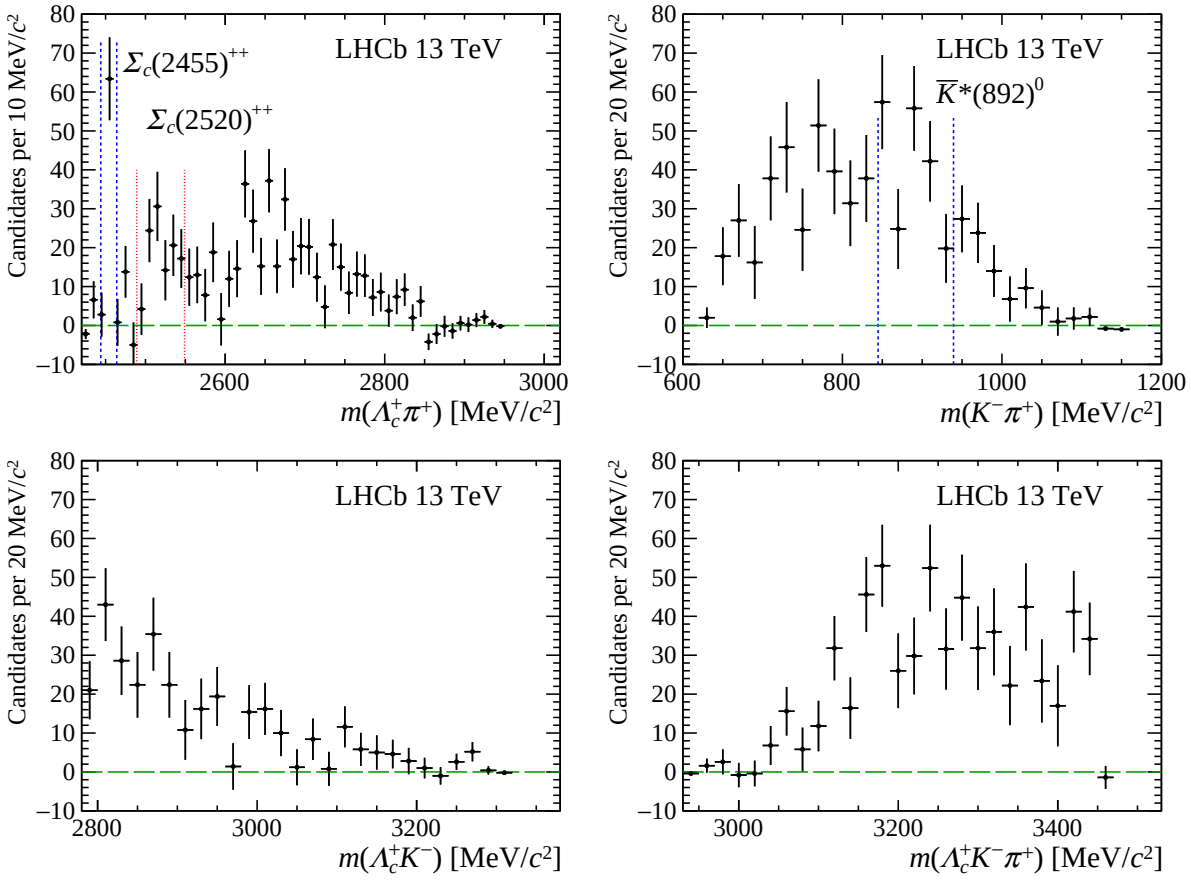

Figure 4.24: Possible intermediate resonances observed in the 2016 background-subtracted data, from the Ξ_{cc}^{++} decay. Any π^+ tracks used in these final-state mass combination plots come directly from Ξ_{cc}^{++} decay vertex.

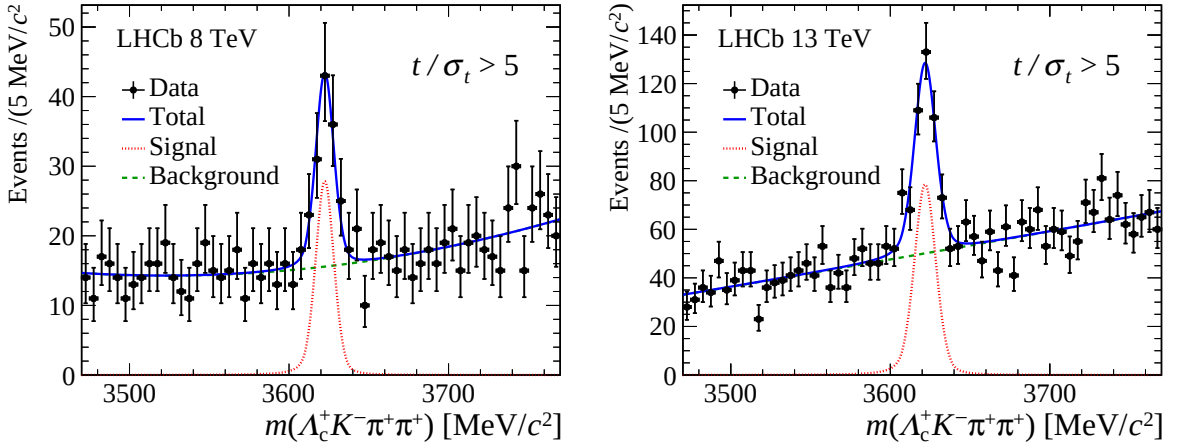

Figure 4.25: Invariant-mass distribution of the Ξ_{cc}^{++} candidates in the (left) 2012 and (right) 2016 data after the selection, with an additional requirement that the Ξ_{cc}^{++} candidate's decay time exceeds 5 standard deviations. The statistical signal significance is above 7σ (12σ) for the 2012 (2016) samples.

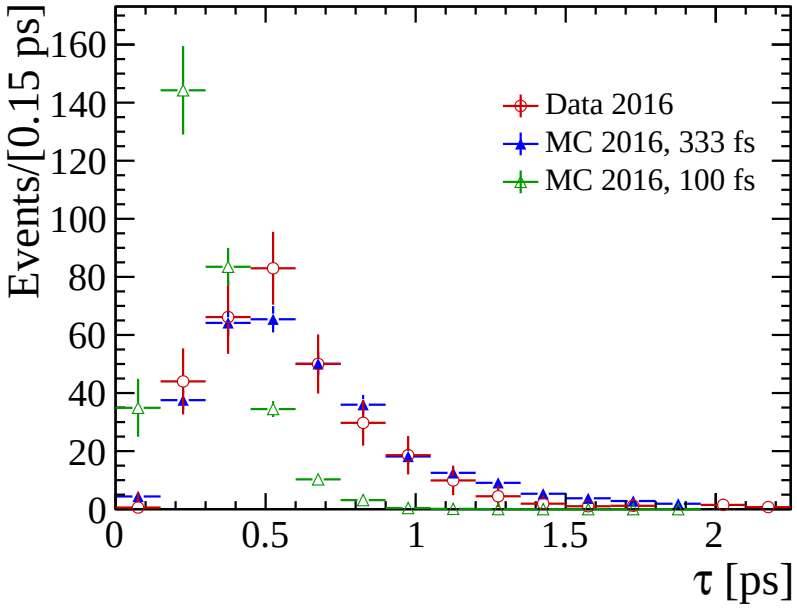

Figure 4.26: Distribution of the decay time of the Ξ_{cc}^{++} candidates in the (red) background-subtracted 2016 data, (blue) simulated 2016 sample with the lifetime of the Ξ_{cc}^{++} baryon set to 333 fs and (green) simulated 2016 sample with the lifetime of the Ξ_{cc}^{++} baryon set to 100 fs. The simulated distributions are normalised to data.

4.6.4 Conclusion and Discussion

A highly significant structure, with a local signal significance greater than twelve standard deviations over background, is observed in the $\Lambda_c^+ K^- \pi^+ \pi^+$ mass spectrum of 2016 LHCb data. This structure must correspond to a new particle state with a mass around 3621.40 MeV/c^2. The structure is also confirmed with consistent mass in a pp data set collected by LHCb in 2012. The signals in these peaking structures also have significant decay lengths and the peak itself remains highly significant after a strict lifetime requirement is applied The new state must be a baryon to conserve baryon number in the final state and must also contain two heavy quarks with at least one a charm quark (so a bcq or ccq state, where $q \in u, d, s$) as it decays weakly to a Λ_c^+ baryon.[10] A bcq state is disfavoured because the peak is too narrow and the measured mass is far from the expected mass of the lightest b-baryon, which is around 5600 MeV/c^2 [1]. Equally, a bcq state could never be doubly electromagnetically charged. All these observations of a narrow peak, a finite lifetime and a mass consistent with expectations of ground state doubly-charmed baryon, means this new state fits the requirements of a weakly decaying Ξ_{cc}^{++} (ccu) baryon.

[10]The state is inconsistent with being a $c\bar{c}uuu$ pentaquark since this would decay to a final state containing a K^+ track and so should be seen in the DCS data set, which is not the case.

These results mark the discovery of the first ever doubly-charmed baryon unambiguously measured. However, as discussed in Section 1.4.3, this is not the first time a doubly-charmed baryon discovery has been claimed. The SELEX collaboration twice reported signals of the Ξ_{cc}^+ (ccd) baryon in their data sets [103, 104]. The mass of the observed Ξ_{cc}^{++} state found in this analysis is greater than that of the Ξ_{cc}^+ peaks reported by the SELEX collaboration by $103 \pm 2\,\text{MeV}/c^2$ [78–80], when considering statistical uncertainty only. This difference would imply an isospin splitting vastly larger than that seen in any other baryon system, which are typically different by only a few MeV/c^2. Consequently, if the structure observed in this analysis is the Ξ_{cc}^{++} state, then the interpretation of the SELEX collaboration's structure as the Ξ_{cc}^+ baryon, which would be the isospin partner of the Ξ_{cc}^{++} baryon, would be strongly disfavored.

Since the $\Xi_{cc}^{++} \to \Lambda_c^+ K^- \pi^+ \pi^+$ result was published the discovery of the Ξ_{cc}^{++} baryon has been commonly accepted. Yet, there have been attempts to reconcile the LHCb and SELEX measurements. One such attempt assumes that the observed Ξ_{cc}^{++} baryon in this analysis is actually the $J^P = {}^3/_2^+$ state, decaying through the strong or electromagnetic interaction, and not actually the $J^P = {}^1/_2^+$ state [173]. Through a subsequent study of the $\Xi_{cc}^{++} \to \Lambda_c^+ K^- \pi^+ \pi^+$ data by the LHCb collaboration, the lifetime of the Ξ_{cc}^{++} baryon was measured to be $0.256^{+0.024}_{-0.022}$ (stat) $\pm$ 0.014 (syst) ps [174], thereby ruling it out to be a strong or electromagnetic decay since the particle does not decay instantaneously.[11] Moving forward, the only way to truly solve this long-term puzzle in the heavy-flavoured sector of particle physics, will be for the LHCb collaboration, or other b-factories, to discover the singly-charged Ξ_{cc}^+ state and to compare the findings to the previous results.

4.7 Chapter Summary

This chapter presented a first-ever search for the doubly-charmed Ξ_{cc}^{++} baryon within LHCb data collected in 2012 and 2016. An introduction to the analysis was first given, where the aims of the analysis were established and the motivation for exploring the $\Xi_{cc}^{++} \to \Lambda_c^+ K^- \pi^+ \pi^+$ channel was explained, after which the strategy of the analysis was explained in a broad sense before finer details on each stage of the analysis were presented. Primarily, the filtering of data to leave behind potential Ξ_{cc}^{++} candidates, based on the attributes of their decays, was explained in great detail. Attempts were also made to highlight the excellent workings of the LHCb detector in helping to separate signal and background candidates in this part of the chapter. Background studies were then presented and then the methodology of designing suitable fit models to describe the mass distributions was given. Finally, the mass measurement results of the

[11] The mass distribution in Figure 4.21 could contain spin-1/2 Ξ_{cc}^{++} candidates originating from the spin-3/2 Ξ_{cc}^{++} state and directly from pp interaction but there is no way to distinguish between them.

$\Xi_{cc}^{++} \to \Lambda_c^+ K^- \pi^+ \pi^+$ analysis were presented with an interpretation of the results also given. The chapter concluded with a discussion on the results of the analysis and talked briefly about the implications and future aims for doubly-charmed-baryon searches.

Chapter 5

Searches for $\Xi_{cc}^{++} \to D^+ p K^- \pi^+$

> "The best that most of us can hope to achieve in physics is simply to misunderstand at a deeper level."
>
> – Wolfgang Pauli, discoverer of the exclusion principle

In this chapter, a first-ever search for the $\Xi_{cc}^{++} \to D^+(\to K^-\pi^+\pi^+)pK^-\pi^+$ decay at LHCb is presented. This Ξ_{cc}^{++} decay mode has never before been examined by any high-energy physics experiments including the LHCb collaboration. Having gleaned knowledge from the $\Xi_{cc}^{++} \to \Lambda_c^+ K^-\pi^+\pi^+$ analysis, the work is solely carried out by the PhD candidate, under the guidance of University of Glasgow personnel. The aim of this analysis is to rediscover the doubly-charmed Ξ_{cc}^{++} (ccu) baryon and to again measure the mass of this state. To accomplish this, evidence of the Ξ_{cc}^{++} baryon decaying to a singly-charmed D^+ meson, a proton, a K^- meson and a π^+ meson is sought. The D^+ meson is reconstructed from two π^+ mesons and a K^- meson. Similarly to the $\Xi_{cc}^{++} \to \Lambda_c^+ K^-\pi^+\pi^+$ analysis, the anti-particle equivalent decay process is also included in this search. Another objective of this analysis is to make a quantitative statement about the ratio between the $\Xi_{cc}^{++} \to \Lambda_c^+ K^-\pi^+\pi^+$ and $\Xi_{cc}^{++} \to D^+ pK^-\pi^+$ branching fractions.

The Ξ_{cc}^{++} baryon was observed in the $\Xi_{cc}^{++} \to \Lambda_c^+ K^-\pi^+\pi^+$ channel by the LHCb collaboration, as discussed in Chapter 4, and the PhD candidate was one of the main proponents of the analysis that led to its discovery [157]. Following this important and exciting result, the PhD candidate chose to pursue a search for an additional decay mode of the Ξ_{cc}^{++} state. This would be important to understand further the dynamics of weakly-decaying doubly-charmed baryons, which are expected to differ significantly from their singly-charmed counterparts due to interference effects between the decay amplitudes of the two heavy-charm quarks. The Cabbibo-favoured $\Xi_{cc}^{++} \to D^+(\to K^-\pi^+\pi^+)pK^-\pi^+$ decay was chosen as a suitable search channel based on its experimentally favourable attributes, primarily the lifetime of the D^+ meson. With a relatively long 1 ps lifetime [1], the decay vertex of the D^+ meson will be significantly displaced from the pp interaction point in this decay chain, meaning combinatorial background arising from the primary

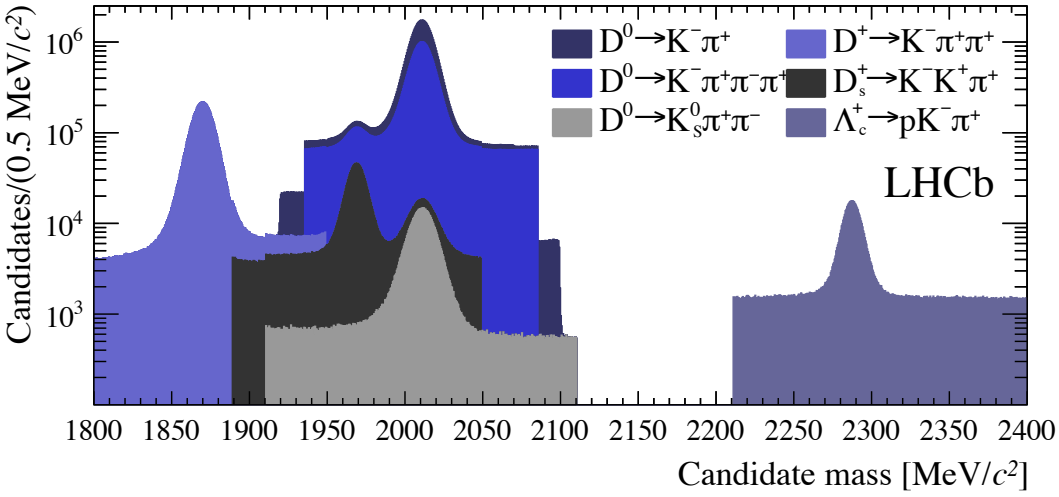

Figure 5.1: Invariant-mass distributions of candidate charm decays that are selected by exclusive Turbo lines with no further offline selection. The plot was reproduced from LHCb trigger performance paper [139].

vertex will be suppressed more easily at all levels of the selection, including the trigger. The trigger at LHCb is excellent at selecting $D^+ \to K^-\pi^+\pi^+$ decays [139]. Invariant-mass distributions of a select set of charm-hadron decays, which are fully reconstructed by exclusive trigger lines, are shown in Figure 5.1. The $D^+ \to K^-\pi^+\pi^+$ sample is shown to have a larger number of signal events compared to background than in the $\Lambda_c^+ \to pK^-\pi^+$ decay.

The structure of this chapter is very similar to the $\Xi_{cc}^{++} \to \Lambda_c^+ K^-\pi^+\pi^+$ analysis presented in Chapter 4, with a candidate selection outlined in Section 5.3 and details of background and mass-measurement studies given in Section 5.4 and Section 5.5, respectively. Therefore, effort is made to highlight the differences between the two analyses when possible and not to repeat details when appropriate. A slightly more concise overview of the candidate selection is presented and further time is spent discussing the background and mass-measurement studies performed by the PhD candidate. Since a branching-fraction measurement is also pursued, more information on the selection efficiencies of this and the past $\Xi_{cc}^{++} \to \Lambda_c^+ K^-\pi^+\pi^+$ analysis are disclosed as efficiencies are paramount to this type of measurement. The results of this analysis are published in Reference [175].

5.1 Analysis Strategy

A sufficiently precise measurement of the mass of the Ξ_{cc}^{++} baryon was obtained through the $\Xi_{cc}^{++} \to \Lambda_c^+ K^-\pi^+\pi^+$ decay mode. However, despite the clear peak of the Ξ_{cc}^{++} state around 3621.40 MeV/c^2, a large mass space is still examined in this analysis. This allows for an independent mass measurement of the Ξ_{cc}^{++} state to be performed and means

that the hypothetical isospin partner of the Ξ_{cc}^{+} state reported by the SELEX collaboration [103, 104] can be explored in an unbiased manner. Following the $\Xi_{cc}^{++} \to \Lambda_c^+ K^-\pi^+\pi^+$ search analysis described in Chapter 4, a dedicated lifetime analysis was carried out by the LHCb collaboration using the same $\Xi_{cc}^{++} \to \Lambda_c^+ K^-\pi^+\pi^+$ data. The lifetime of the Ξ_{cc}^{++} state was measured to be $0.256^{+0.024}_{-0.022}$ (stat) $\pm$ 0.014 (syst) ps [174]. The Ξ_{cc}^{++} baryon is assumed to have a lifetime within its measured uncertainty in the development of this analysis.

Similarly to the $\Xi_{cc}^{++} \to \Lambda_c^+ K^-\pi^+\pi^+$ analysis, mass-search windows are defined for the Ξ_{cc}^{++} baryon and the open-charm hadron (the D^+ meson this time) that are not examined in real data until all aspects of the analysis are finalised. To avoid any personal biases, the analysis is developed using a simulated sample of real-signed (RS) decays and two data sets consisting of the non-physical $\Xi_{cc}^{++} \to D^+ pK^+\pi^+$ and $\Xi_{cc}^{++} \to D^+ pK^-\pi^-$ decays that have wrong-signed (WS) final states. The intermediate D^+ meson is reconstructed in the Cabbibo-favoured $K^-\pi^+\pi^+$ final state in both of the WS decays.

In the simulation of RS decays, the mass of the Ξ_{cc}^{++} baryon is set to the value that was measured in the $\Xi_{cc}^{++} \to \Lambda_c^+ K^-\pi^+\pi^+$ analysis, while the lifetime of the Ξ_{cc}^{++} baryon is set to its measured value. The impact of these assumed mass and lifetime values on certain aspect of the analysis are assessed by varying their values within the simulation. All final-state tracks of the $\Xi_{cc}^{++} \to D^+(\to K^-\pi^+\pi^+)pK^-\pi^+$ decay are distributed uniformly in the phase space of the decay but the effect of strongly-decaying resonances on the efficiency of selecting $\Xi_{cc}^{++} \to D^+ pK^-\pi^+$ is investigated. The p_T spectrum of the Ξ_{cc}^{++} baryon is taken from the same MC event generator that was used in the $\Xi_{cc}^{++} \to \Lambda_c^+ K^-\pi^+\pi^+$ analysis.

The data sets used in this analysis contain decays that are reconstructed at the trigger level using Turbo processing. The offline selection of the $\Xi_{cc}^{++} \to D^+ pK^-\pi^+$ decays is designed to be as similar as possible to the $\Xi_{cc}^{++} \to \Lambda_c^+ K^-\pi^+\pi^+$ channel, with a preselection-plus-multivariate-selection strategy again adopted. The multivariate selection is trained on a simulated RS sample and the WS control modes. The same multivariate classifier configured for selecting $\Xi_{cc}^{++} \to \Lambda_c^+ K^-\pi^+\pi^+$ decays is not necessarily used in this $\Xi_{cc}^{++} \to D^+ pK^-\pi^+$ analysis.

Once the candidate selection, background determination and mass measurement studies are complete, the RS data are scrutinised and the signal significance is determined. Furthermore, the choice of what quantities will be measured is decided before the RS data is examined. A mass measurement is undertaken and the branching fraction of the $\Xi_{cc}^{++} \to D^+ pK^-\pi^+$ channel, relative to the $\Xi_{cc}^{++} \to \Lambda_c^+ K^-\pi^+\pi^+$ branching fraction, is determined if the signal observed is over five standard deviations in significance. If the number of signal events is less than three standard deviations over the background contribution then no mass measurement is performed and an upper limit on the ratio of the $\Xi_{cc}^{++} \to D^+ pK^-\pi^+$ branching fraction relative to the $\Xi_{cc}^{++} \to \Lambda_c^+ K^-\pi^+\pi^+$ branching

fraction will be set instead. The efficiency of selecting events at every stage of the analysis will be determined primarily using simulated RS decays.

5.2 Data Samples

In this section, the data samples that are collected and simulated by LHCb for use in the $\Xi_{cc}^{++} \to D^+ p K^- \pi^+$ search analysis are discussed in detail.

5.2.1 LHCb Data

The data set examined in this analysis is from pp collision data recorded by the LHCb detector in 2016. This is the same data set used for the Run II $\Xi_{cc}^{++} \to \Lambda_c^+ K^- \pi^+ \pi^+$ analysis (see Section 4.2.1), and it corresponds to an integrated luminosity of approximately $1.7\,\text{fb}^{-1}$. Exclusive trigger lines are designed to capture the RS and WS data. The selection requirements of these trigger lines that have Turbo processing enabled are discussed in detail in Section 5.3.

Data, matching to a similar amount of integrated luminosity as the 2016 data sample (see Figure 2.5), were collected by the LHCb detector in 2017. However, this data set was not included in this analysis because no $\Xi_{cc}^{++} \to D^+ p K^- \pi^+$ sample simulated using 2017 data-taking conditions was available; determination of selection efficiencies as a result would be problematic. Data had also started to be gathered in 2018 at the LHCb detector when this analysis was in progress but this data set is not used because it had not been quality checked by the LHCb collaboration. Run II data is the focus of this analysis and Run I data, where the production cross section of the Ξ_{cc}^{++} baryon is smaller, is not considered. Only the 2016 data set used in the $\Xi_{cc}^{++} \to \Lambda_c^+ K^- \pi^+ \pi^+$ analysis is used in the branching-fraction measurement.

5.2.2 Simulation

The GENXICC generator [158] is used to simulate the Ξ_{cc}^{++} signal events for this analysis. For a reminder of the details of this MC-event generator refer to Section 4.2.2. There is however one notable change to GENXICC to point out since the $\Xi_{cc}^{++} \to \Lambda_c^+ K^- \pi^+ \pi^+$ analysis described in Chapter 4; the mass of the Ξ_{cc}^{++} baryon used by the GENXICC generator has been updated from $3597.98\,\text{MeV}/c^2$ to the measured value of $3621.40\,\text{MeV}/c^2$. Additionally, it was found that the Ξ_{cc}^{++} signal p_T spectrum provided by GENXICC does not exactly match the one observed in the background-subtracted $\Xi_{cc}^{++} \to \Lambda_c^+ K^- \pi^+ \pi^+$ data, as shown in Figure 5.2. Since these two p_T distributions do not agree perfectly, procedures are put in place to overcome this difference. This is discussed in more detail in Section 5.7.2.

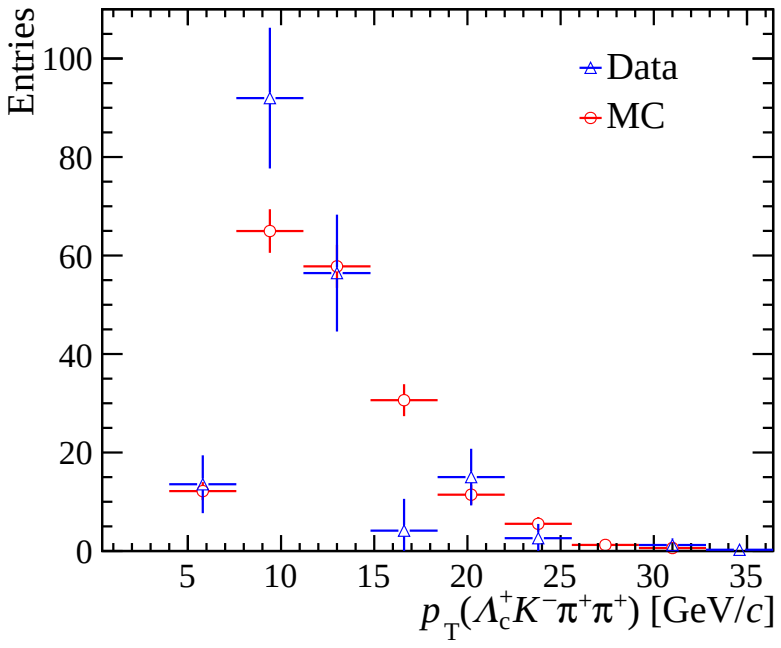

Figure 5.2: A comparison of the Ξ_{cc}^{++} p_T spectrum from $\Xi_{cc}^{++} \to \Lambda_c^+ K^- \pi^+ \pi^+$ decays in (red) simulation and (blue) background-subtracted 2016 data following the application of selection requirements described in Chapter 4.

For this analysis, the final-state particles of both the Ξ_{cc}^{++} and D^+ hadrons are distributed uniformly in the phase space of the decay by the PHSP EvtGen model[1] and approximately twenty million $\Xi_{cc}^{++} \to D^+ p K^- \pi^+$ decays, for both the MagUp and MagDown magnetic conditions, are generated to pass the MC selection requirements detailed in Section 5.3.3. This is ten times the number of MC events than what was available for the $\Xi_{cc}^{++} \to \Lambda_c^+ K^- \pi^+ \pi^+$ analysis. The decay-time distribution of the Ξ_{cc}^{++} baryon is weighted on a per-event basis to give the particle an effective lifetime of 256 ps for the selection studies discussed next.

5.3 Candidate Selection

This section describes the online and offline selection of $\Xi_{cc}^{++} \to D^+ p K^- \pi^+$ decays within the data collected in 2016. To better control the systematic uncertainties associated to the ratio of branching fraction measurement, the selection of $\Xi_{cc}^{++} \to D^+ p K^- \pi^+$ decays is designed to be as similar as possible to the $\Xi_{cc}^{++} \to \Lambda_c^+ K^- \pi^+ \pi^+$ decay mode. The selection of $\Xi_{cc}^{++} \to \Lambda_c^+ K^- \pi^+ \pi^+$ decays is described in Section 4.3.

[1] D^+ mesons commonly decay via an excited $\bar{K}_0^*(1430)$ resonance [1] but a model to simulate such a process was not available at the time this analysis was conducted.

5.3.1 Overview

The $\Xi_{cc}^{++} \to D^+pK^-\pi^+$ and $\Xi_{cc}^{++} \to \Lambda_c^+K^-\pi^+\pi^+$ decay modes are similar in many aspects. Both have six charged tracks in the final state and both contain two displaced vertices. An illustration of the $\Xi_{cc}^{++} \to D^+(\to K^-\pi^+\pi^+)pK^-\pi^+$ decay chain is shown in Figure 5.3. By comparing Figure 4.1 and Figure 5.3, the equivalence in topology of the two Ξ_{cc}^{++} decay modes can be seen. Furthermore, the final-state tracks in the $\Xi_{cc}^{++} \to D^+pK^-\pi^+$ decay will, like all heavy-hadron decays, have large p_T, so there are kinematic parallels between the two channels as well. Therefore, the same kinds of requirements on variables such as FD, IP, DIRA and DOCA *etc.*, which are used to isolate $\Xi_{cc}^{++} \to \Lambda_c^+K^-\pi^+\pi^+$ decays (see Section 4.3.1), will also be useful in selecting $\Xi_{cc}^{++} \to D^+pK^-\pi^+$ decays.

There are however some differences between the two Ξ_{cc}^{++} decay modes. The major difference is in the size of phase space available to the decays. Based on the results of simulation, the $\Xi_{cc}^{++} \to D^+pK^-\pi^+$ decay has an energy release of around 180 MeV, compared to the 560 MeV value for the $\Xi_{cc}^{++} \to \Lambda_c^+K^-\pi^+\pi^+$ decay, see Section 5.5.1. This is due to the difference in mass between the proton (938.27 MeV/c^2) and the pion (134.97 MeV/c^2), being much larger than the difference between the D^+ meson (1869.63 MeV/c^2) and the Λ_c^+ baryon (2268.48 MeV/c^2) [1]. Another distinction between the two Ξ_{cc}^{++} decay modes is in the spatial separation between the open-charm candidate and the decay vertex of the Ξ_{cc}^{++} candidate. Since the lifetime of the D^+ meson is much longer than the Λ_c^+ meson; 1 ps compared to 0.2 ps, respectively [1], then it will, on average, travel further from the pp interaction point. This is an extremely useful feature for helping to select $\Xi_{cc}^{++} \to D^+pK^-\pi^+$ decays.

In summary, the two Ξ_{cc}^{++} search channels analysed and described in this thesis are similar but there are important differences between them. This necessitates that a unique candidate selection should be devised for the $\Xi_{cc}^{++} \to D^+pK^-\pi^+$ decay. Although, the selection structure will be the same; Turbo lines will reconstruct the decays online, after which the combination of a preselection and a multivariate selection will effectively separate any signal events from background. The candidate selection will conclude with a final set of requirements that remove any fake signal Ξ_{cc}^{++} candidates arising from track clones and candidates duplicated during the reconstruction process.

The design of the offline selection is based on information from simulated RS decays and two distinct WS decays; a WS-Plus (WSP) channel, in which all the tracks originating from the Ξ_{cc}^{++} candidate are positively charged and a WS-Minus (WSM) channel where both the kaon and pion produced at the decay vertex of the Ξ_{cc}^{++} candidate are negatively charged. The kinematic distributions of the WSP and WSM data set are expected to be similar to the combinatorial background in the RS $\Xi_{cc}^{++} \to D^+pK^-\pi^+$ decay mode. In

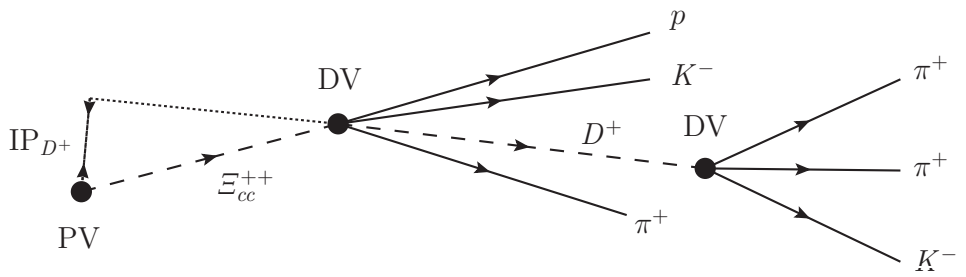

Figure 5.3: The topology of the $\Xi_{cc}^{++} \to D^+(\to K^-\pi^+\pi^+)pK^-\pi^+$ decay.

the case of all three data sets, the intermediate D^+ candidates are reconstructed from the charge conserving $K^-\pi^+\pi^+$ final state. The full decay chains are:

RS: $\Xi_{cc}^{++} \to D^+(\to K^-\pi^+\pi^+)\, p\, K^-\pi^+$;

WSP: $\Xi_{cc}^{++} \to D^+(\to K^-\pi^+\pi^+)\, p\, K^+\pi^+$;

WSM: $\Xi_{cc}^{++} \to D^+(\to K^-\pi^+\pi^+)\, p\, K^-\pi^-$.

The simulated sample and the WS data sets are used to measure and optimise the performance of the multivariate selection prior to examination of RS data. The signal events are represented by signal MC and the background by WSP data. For both the signal and background events, the Ξ_{cc}^{++} candidates are required to pass the full trigger requirements, the offline selections and then mass requirements that are stricter than those present in the trigger; the reconstructed mass of the Ξ_{cc}^{++} candidate is required to be between $[3300, 3800]\,\mathrm{MeV}/c^2$ and the associated D^+ candidate must have a mass between $[1849, 1891]\,\mathrm{MeV}/c^2$, approximately $\pm 3\sigma$ around the known mass of the D^+ meson. Apart from the final hardware-trigger requirement in the ratio of branching-fraction measurement, the full candidate selection is determined before the RS data, within the mass regions detailed above, is examined.

The mass estimator defined in Equation 4.1 is again used in this search analysis but it is reformulated for the $\Xi_{cc}^{++} \to D^+(\to K^-\pi^+\pi^+)pK^-\pi^+$ system, *i.e.*

$$m(D^+pK^-\pi^+) \equiv M(D^+pK^-\pi^+) - M([K^-\pi^+\pi^+]_{D^+}) + M_{\mathrm{PDG}}(D^+), \qquad (5.1)$$

where $M(D^+pK^-\pi^+)$ is the reconstructed mass of the Ξ_{cc}^{++} candidate, $M([K^-\pi^+\pi^+]_{D^+})$ is the measured invariant mass of the $K^-\pi^+\pi^+$ combination corresponding to the intermediate D^+ candidate and $M_{\mathrm{PDG}}(D^+)$ is the known mass of the D^+ meson. The reason for using this mass estimator is again to improve the mass resolution. The gain in resolution is summarised in Section 5.5.3. The final mass measurement is made by fitting the

distribution of this $m(D^+pK^-\pi^+)$ mass estimator in RS data. Analogous mass estimators are used for the WS data sets when discussing the studies of background in Section 5.4.

5.3.2 Trigger Selection

For the mass measurement of the Ξ_{cc}^{++} baryon and the signal significance evaluation in the $\Xi_{cc}^{++} \to D^+pK^-\pi^+$ channel, there is no well-defined L0 trigger requirement; the Ξ_{cc}^{++} candidates must simply pass any L0 trigger line active in 2016. As for the ratio of branching-fractions measurement, the exact L0 trigger requirement imposed on the data is decided upon after the RS data are examined. This makes it the only requirement of the candidate selection not fixed before the RS data are inspected. The reason for this is that the efficiency of the L0 selection cannot be reliably calculated from simulation since the underlying pp interaction is poorly modelled so this efficiency is determined from knowledge of data instead. Depending on the composition of any potentially observed Ξ_{cc}^{++} signal in the RS data, the L0 selection criteria for the branching-fraction measurement is one of the following requirements:

1. The D^+ candidate must be TOS (see Section 2.5.2) with respect to the `L0Hadron` line. This means that at least one daughter track of the D^+ candidate must be associated to a cluster in the HCAL with $E_T > 3.5\,\text{GeV}$;

2. The Ξ_{cc}^{++} candidates must be TIS with respect to `L0Global` line. This means that the Ξ_{cc}^{++} candidate simply has to pass any of the main L0 lines, such as `L0Hadron`, that make requirements on global attributes such as p_T and the number of SPD hits;

3. Both requirements 1 and 2 must be satisfied.

The choice will be exclusively requirement 1 or requirement 2 if the signal candidates predominately satisfy one over the other. The looser requirement − the one that leaves the greater number of candidates − will be adopted. In the case a significant contribution of events (greater than 10%) comes from imposing both requirement 1 and requirement 2 then requirement 3 will be used. If no significant signal (greater than three standard deviations) is seen in data, then the simpler-to-evaluate requirement 2 will be chosen to avoid the complications of the overlapping-trigger categories. Whatever requirement is chosen for this analysis, the analogous requirement is also imposed on the 2016 $\Xi_{cc}^{++} \to \Lambda_c^+K^-\pi^+\pi^+$ data for the branching-fraction measurement.

The same HLT1 trigger requirements used in the $\Xi_{cc}^{++} \to \Lambda_c^+K^-\pi^+\pi^+$ selection are also used in this analysis. Both the Ξ_{cc}^{++} and D^+ candidates are required to be TOS with respect to the `HLT1TrackMVA` line or TOS with respect to the `HLT1TwoTrackMVA` line. As a reminder, the selection criteria of these two trigger lines are listed in Table 4.1.

After passing L0 and HLT1, events need to meet the specific requirements of HLT2. The RS, WSP and WSM decays are each reconstructed by dedicated Turbo lines. The selection criteria of each of these lines is the same, apart from the charge combination of the final-state tracks. The selection requirements of these HLT2 lines were fixed throughout the 2016 data-taking period, when the data used in this analysis was collected. Some of the more important requirements of these trigger lines are summarised next:

- $D^+ \to K^-\pi^+\pi^+$ candidates are reconstructed from three charged tracks that pass appropriate momentum and hadron DLL PID requirements. The combination of these tracks are also subject to requirements; at least one of the three tracks must have $p_{\mathrm{T}} > 1\,\mathrm{GeV}/c$ and $\chi^2_{\mathrm{IP}} > 50$ and at least two of them must have $p_{\mathrm{T}} > 400\,\mathrm{MeV}/c$ and $\chi^2_{\mathrm{IP}} > 10$. The D^+ candidate must also have a very good vertex fit quality and it needs to point back to its associated primary vertex (PV) such that its DIRA value is small. The decay vertex (DV) of the D^+ candidate must be significantly displaced from its associated PV and only D^+ candidates whose reconstructed mass is within $\pm 90\,\mathrm{MeV}/c^2$ of the known D^+ mass are retained;

- $\Xi_{cc}^{++} \to D^+ pK^-\pi^+$ candidates are reconstructed from the D^+ candidates plus three charged tracks that pass appropriate hadron DLL PID and momentum requirements. The selections on the reconstructed Ξ_{cc}^{++} candidate are then the same as in the $\Xi_{cc}^{++} \to \Lambda_c^+ K^-\pi^+\pi^+$ reconstruction; the three tracks and the D^+ candidate are required to form a good fitted vertex ($\chi^2_{\mathrm{vtx}}/\mathrm{ndf} < 60$) with a mass between $[3100, 4000]\,\mathrm{MeV}/c^2$ and the DV of the D^+ candidate must be 10 mm further along the z-axis than the DV of the Ξ_{cc}^{++} candidate.

In general, the selection criteria is similar to the $\Xi_{cc}^{++} \to \Lambda_c^+ K^-\pi^+\pi^+$ analysis but there is a stricter requirement on the reconstructed D^+ decay vertex, as well as differences in the momentum and decay-time requirements of the tracks. Furthermore, there are no requirements on the momentum or the PID score of the proton track in the $\Xi_{cc}^{++} \to D^+ pK^-\pi^+$ selection, since it had been expected that DLL information from RICH-1 would not be essential for identifying the proton when it originates from the Ξ_{cc}^{++} decay vertex. A full overview of the HLT2 trigger requirements for the $\Xi_{cc}^{++} \to D^+ pK^-\pi^+$ analysis is shown in Table 5.1.

After the candidate selection requirements of HLT2, there is already a very pure sample of $D^+ \to K^-\pi^+\pi^+$ decays. The invariant-mass distribution of D^+ candidates in the MagDown WSP data set, which is extracted from the trigger, is shown in Figure 5.4. There is around 6×10^5 D^+ candidates with approximately 80% of them corresponding to real D^+ signal, based on the area of the peak in the invariant-mass spectrum.

Table 5.1: HLT2 trigger requirements for selecting RS, WSP and WSM decays. The requirements highlighted in red are different to their analogous requirement in the $\Xi_{cc}^{++} \to \Lambda_c^+ K^- \pi^+ \pi^+$ analysis, see Table 4.2.

Candidate	Variable	Requirement
Daughters of D^+	Track quality	$\chi^2/\text{ndf} < 3$
	Momentum	$p > 1\,\text{GeV}/c$
	Transverse momentum	$p_\text{T} > 250\,\text{MeV}/c$
	Arithmetic sum of daughter p_T	$> 3\,\text{GeV}/c$
	Impact parameter significance	$\chi^2_\text{IP} > 4$
	Proton momentum	$> 10\,\text{GeV}/c$
	Kaon PID	$\text{DLL}_{K\pi} > 5$
	Pion PID	$\text{DLL}_{K\pi} < 5$
	Maximum p_T	$> 1\,\text{GeV}/c$
	Second maximum p_T	$> 400\,\text{MeV}/c$
	Maximum χ^2_IP	> 50
	Second maximum χ^2_IP	> 10
D^+ mother	Vertex quality	$\chi^2_\text{vtx}/\text{ndf} < 6$
	Cosine of DIRA	> 0.99995
	Decay time	$\tau > 0.4\,\text{ps}$
	Mass	$[1759, 1959]\,\text{MeV}/c^2$
Daughters of Ξ_{cc}^{++}	Track quality	$\chi^2/\text{ndf} < 3$
	Transverse momentum	$p_\text{T} > 500\,\text{MeV}/c$
	Momentum	$p > 1\,\text{GeV}/c$
	Kaon PID	$\text{DLL}_{K\pi} > 10$
	Pion PID	$\text{DLL}_{K\pi} < 0$
Ξ_{cc}^{++} mother	Vector sum of daughter p_T	$> 2\,\text{GeV}/c$
	Vertex quality	$\chi^2_\text{vtx}/\text{ndf} < 60$
	DV of D^+ w.r.t. Ξ_{cc}^{++}	$(z_{D^+} - z_{\Xi_{cc}^{++}}) > 0.01\,\text{mm}$
	Distance of closest approach	$\text{DOCA} < 10\,\text{mm}$
	Mass	$[3100, 4000]\,\text{MeV}/c^2$

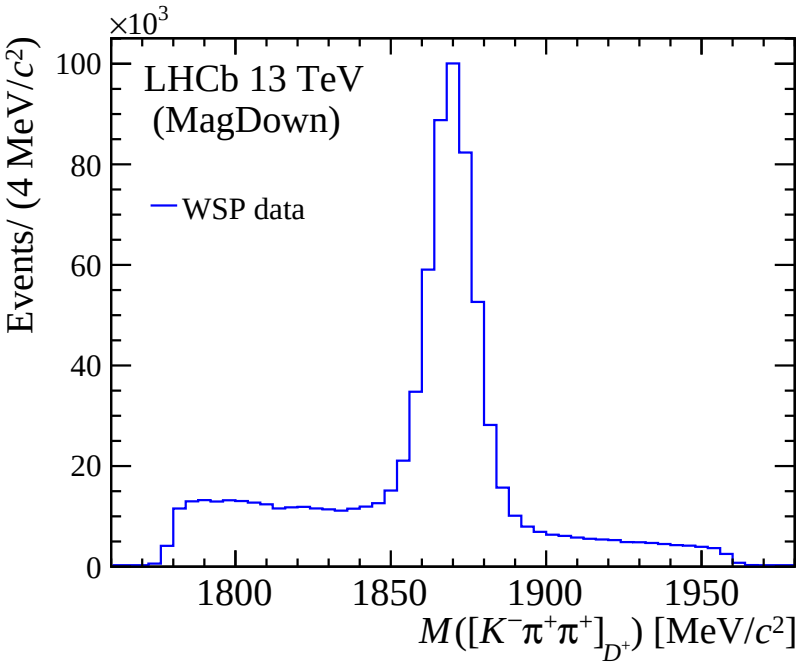

Figure 5.4: Invariant-mass distribution of the D^+ candidates from events recorded under MagDown conditions and straight from the output of the WSP trigger line.

5.3.3 MC Sample Setup

For the same reasons discussed in Section 4.3.3, the DLL PID requirements listed in Table 5.1 are not directly applied to the MC sample. Instead, the functionality of the `PIDCalib` package [161] to reshape distributions of decay observables, through the use of weights, is utilised such that the PID requirements are effectively mimicked in the MC sample. The details of this procedure are fully described in Appendix C. All other selection criteria in the HLT2 trigger lines are directly applied to the MC sample however.

Generator-level requirements are also applied to the simulated sample via the Gauss software package [145] such that all $\Xi_{cc}^{++} \to D^+pK^-\pi^+$ decays are produced within the geometric acceptance of the LHCb detector, all charged particles have a polar angle between 10 mrad to 400 mrad relative to the z-axis and the mother Ξ_{cc}^{++} particle has p_T greater than 3 GeV/c. Based on the number of events passing these requirements relative to the number generated, the geometric acceptance (and generator) efficiency of such a selection is 0.0989 ± 0.0003 for $\Xi_{cc}^{++} \to D^+pK^-\pi^+$ decays.

The process of truth-matching, which was explained in Section 4.3.3, is also applied to the $\Xi_{cc}^{++} \to D^+pK^-\pi^+$ MC sample. All reconstructed tracks are required to belong to the correct particle type and to be associated to the correct particle decay. Aside from true signal events, this form of truth-matching accepts events classed as low-mass background events, where not all generated final-state particles are matched to their reconstructed equivalents but the resulting mother candidate is still only 100 MeV/c^2 less than the

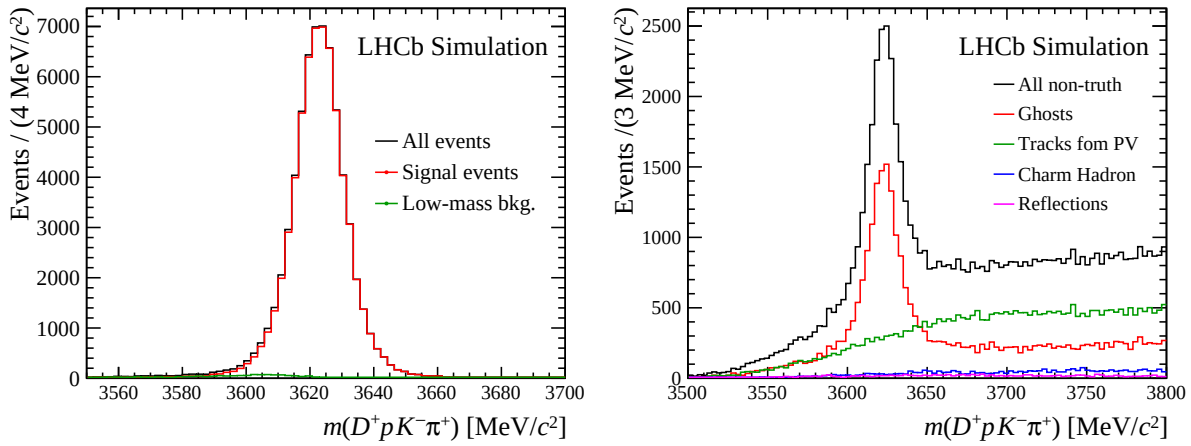

Figure 5.5: Invariant-mass distributions of the Ξ_{cc}^{++} candidates in (left) truth-matched $\Xi_{cc}^{++} \to D^+pK^-\pi^+$ MC and (right) non-truth-matched $\Xi_{cc}^{++} \to D^+pK^-\pi^+$ MC.

expected mass. Events that are rejected by the truth-matching are different types of background resulting from combinatorics, ghosts, secondary charm decays and reflections from particle misidentification. The invariant-mass distribution of the Ξ_{cc}^{++} candidates in (non-)truth-matched simulation is shown in the left (right) of Figure 5.5.

5.3.4 Offline Processing and Preselection

The same data processing techniques used in the $\Xi_{cc}^{++} \to \Lambda_c^+K^-\pi^+\pi^+$ analysis (see Section 4.3.4) are also applied to the RS, WSP and WSM data sets offline; a full kinematic refitting with the `DecayTreeFitter` (DTF) tool [162] is applied such that all the Ξ_{cc}^{++} candidates originate from their best associated PV and simultaneously the momentum scaling calibration of tracks is then performed.

The first layer of the offline selection is again a preselection, which seeks to improve the signal purity of the data samples by removing recognizable background events. The requirements of the preselection are chosen based on data extracted from the WSP Turbo line and on the MC events passing the same requirements as WS data plus the generator-level and truth-matching requirements discussed in Section 5.3.3. Using the WSP events to represent background and the MC events as signal decays, different requirements on various quantities of the $\Xi_{cc}^{++} \to D^+pK^-\pi^+$ decays are investigated to find the combination which retains nearly all signal events, while removing a non-negligible amount of background events. The selection criteria includes loose requirements on `ProbNN` PID scores for all final-state particles, topological information and ghost tracks. Additionally, all tracks are required to have momentum between $[2, 150]\,\text{GeV}/c$ and pseudorapidity, η, between $[1.5, 5.0]$ such that their associated PID information can be calibrated with `PIDCalib`. All the Ξ_{cc}^{++} candidates are required to originate from their associated PV ($\log(\chi^2_{\text{IP}}) < 4$),

Table 5.2: The preselection requirements that are applied to data offline.

Particle	Requirement	Signal efficiency
All tracks	$2 \leq p \leq 150\,\text{GeV}/c$	$(97.83 \pm 0.09)\%$
	$1.5 \leq \eta \leq 5.0$	$(99.96 \pm 0.01)\%$
	`ProbNNghost` < 0.9	$(99.86 \pm 0.02)\%$
Proton	`ProbNNp` > 0.1	$(98.74 \pm 0.07)\%$
Kaons	`ProbNNk` > 0.1	$(96.78 \pm 0.11)\%$
Pions	`ProbNNpi` > 0.1	$(98.24 \pm 0.08)\%$
Ξ_{cc}^{++} candidate	$\log(\chi^2_{\text{IP}}) < 4$	$(100.0 \pm 0.00)\%$
	$\chi^2_{\text{vtx}}/\text{ndf} < 10$	$(100.0 \pm 0.00)\%$
	$p_{\text{T}} > 4.5\,\text{GeV}/c$	$(100.0 \pm 0.00)\%$
	$\chi^2_{\text{vtx}} < 60$ (with DTF refit)	$(99.90 \pm 0.02)\%$

to have a good vertex from the initial fit ($\chi^2_{\text{vtx}}/\text{ndf} < 10$) and also from the refit by the `DTF` tool ($\chi^2_{\text{vtx}} < 60$). Furthermore, only the Ξ_{cc}^{++} candidates with $p_{\text{T}} > 4.5\,\text{GeV}/c$ are retained. The final requirements chosen for the preselection are listed in Table 5.2, along with their corresponding efficiencies. The efficiency of each requirement is based on signal MC events and is relative to the number of events passing the trigger and then after the number of events passing the requirement listed above itself in the Table.[2] Several of the requirements retain all signal events, as desired. The p_{T} and χ^2_{vtx} requirements are slightly stricter than the analogous ones in the preselection of the $\Xi_{cc}^{++} \to \Lambda_c^+ K^- \pi^+ \pi^+$ analysis, see Table 4.3.

The invariant-mass distribution of the Ξ_{cc}^{++} candidates in the RS, WSP and WSM samples, outside the mass-search regions of the analysis, after the preselection, are shown in Figure 5.6. Both the WSP and WSM distributions are shaped similarly to the RS one. The difference in the number of events is merely an artefact of the total charge combination in the final state of the decay mode. The zero-net charge of the WSM mode means these decays are more readily reconstructed by the trigger than WSP decays, which have a plus-four charge in the final state, while the plus-two-charged RS decay is in between both in terms of the number of events. The combination of the requirements in Table 5.2 reject around 30% of the events in both the WS data sets.

5.3.5 Multivariate Selection

Following the preselection, a one-step multivariate (MVA) selection is used to further improve the signal purity of the RS data sample by primarily removing combinatorial

[2]The `ProbNN` efficiencies listed in Table 5.2 are not derived from `PIDCalib` but are directly calculated from the number of MC events before and after the application of the PID requirement.

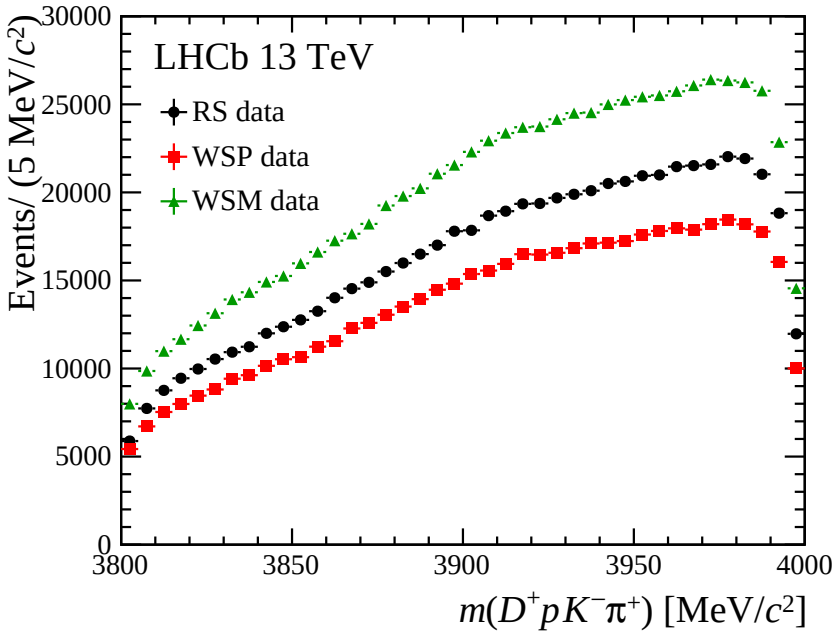

Figure 5.6: Invariant-mass distribution of the Ξ_{cc}^{++} candidates in (black circles) RS data, (red squares) WSP data and (green triangles) WSM data in the 3800−4000 MeV/c^2 region after the preselection.

background arising from the primary vertex. The concept of using MVA techniques in the context of a classification problem in particle physics search analyses is explained in detail in Section 4.3.5, so this will not be discussed further here, however the principles are the same for this $\Xi_{cc}^{++} \to D^+pK^-\pi^+$ analysis. MVA classifiers are trained to recognise signal and background after which a requirement on the response output of the classifier can be placed such that these two types of events can be effectively separated. The TMVA package [166] is once again used to carry out the multivariate selection. A few classifying algorithms are trialled to find the one most suitable for this analysis but only the results of some of the better performing classifiers are discussed in this section.

The simulated RS $\Xi_{cc}^{++} \to D^+pK^-\pi^+$ sample is used to train the classifiers to recognise signal, while events within the invariant-mass region $[3550, 3700]$ MeV/c^2 in the WSP (WSM) data set is used as the default (cross-check) sample for background training. Events in both the signal and background samples are required to pass the trigger and preselection, and also truth-matching and generator level cuts in the case of signal. The narrow $[3550, 3700]$ MeV/c^2 mass region is chosen because the kinematic distributions of the candidates outside this range may differ significantly from the actual background in the signal region of the RS data. The invariant mass-distributions in the sidebands, $[3800, 4000]$ MeV/c^2, of both the WSP and WSM data show a similar level of agreement to the same distribution in the RS data, as can be seen in Figure 5.6. The WSP sample

is however chosen as the primary background training source since it is the least likely to contain real signal $\Xi_{cc}^{+} \to D^+pK^-$ decays following a partial reconstruction of the $\Xi_{cc}^{++} \to D^+pK^-\pi^+$ decay.[3] To retain a large number of signal events, the hardware-trigger requirements are not applied to the signal and background samples. Following the standard TMVA approach, both the signal and background samples are split randomly into two equally sized but disjoint subsamples; one for the training and the other for the testing phase. Approximately 1.2×10^4 events are used to train the classifiers to recognise both signal and background. The optimisation of the MVA response requirement, described next, is determined from the testing sample only.

Different classifiers are initially studied with different sets of training variables. The training variables used in the $\Xi_{cc}^{++} \to \Lambda_c^+K^-\pi^+\pi^+$ analysis, see Table 4.4, are used as a starting point before alterations are made to allow the classifier to perform better. Given the limited sample size of the signal MC sample, the approach was to prune the variable list as much as possible to reduce the risk of over-training. Several training variables are ultimately discarded if they are either highly correlated with other variables or are not greatly used by the MVA algorithm. The final fifteen training variables opted for are listed in Table 5.3 in order of the best discriminating power.[4] The variables chosen relate to lifetime, p_T and topological information. Remember that charm hadrons have characteristically long lifetimes and their daughters have relatively hard p_T distributions. Particle identification variables are not used in the training due to their imperfect modeling in simulation. The distributions of each of these training variables in the signal and background sample are shown in Figure 5.7. The correlation matrices of the training variables from the MC and WSP samples are shown in Figure 5.8.

Variants of the Boosted Decision Tree (BDT) and Multilayer Perceptron (MLP) classifying algorithms are found to give the best performance based on their signal efficiency and background rejection rates, which are shown in Figure 5.9. Excellent performance is obtained for all classifiers, with a signal efficiency of 95% corresponding to a background rejection of approximately 80%. The hyper-parameter values that are default in TMVA version 4.2.1 [166] are used in each classifier.

Ultimately, the MLP neural network is chosen as the classifier of choice for this multivariate selection, since it was able to achieve a competitive Punzi FoM score [169] and it seems insensitive to over-training based on the Kolmogorov–Smirnov test statistic, see Figure 5.10. It also meant that the same type of classifier is used in both the

[3]WSM data could contain real $\Xi_{cc}^{+} \to D^+pK^-$ decays if they are combined with a random π^+ moving sufficiently slowly. However, by applying the HLT2 requirements to simulated $\Xi_{cc}^{+} \to D^+pK^-$ decays it was found that most MC events are rejected anyway.

[4]The MLP classifier implements a variable ranking that uses the sum of the weights-squared of the connections between the neurons in the input layer and the first hidden layer.

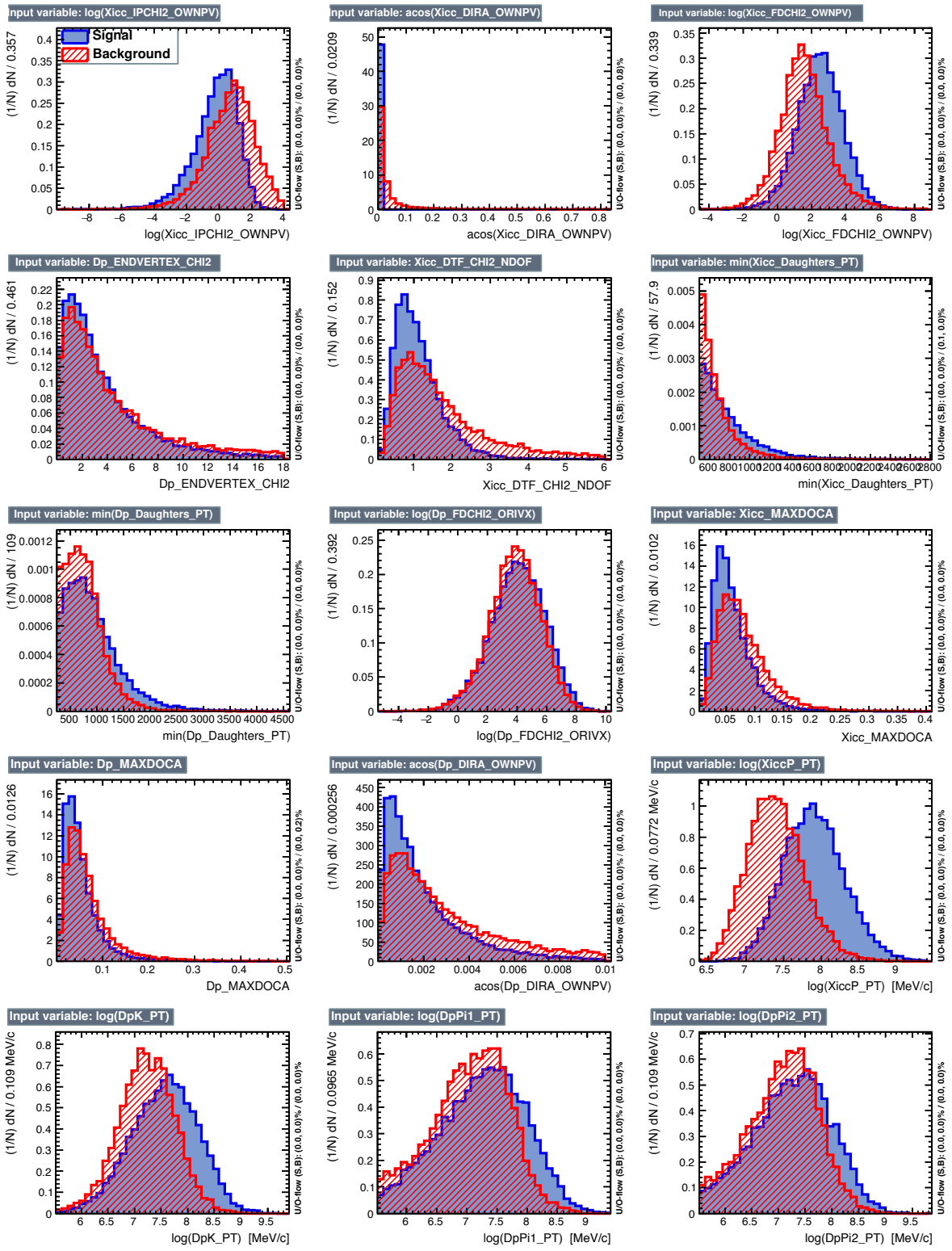

Figure 5.7: A comparison of the distributions of the final fifteen training variables used to train the multivariate classifier in the (blue) signal and (red) background samples.

Table 5.3: The final fifteen variables used to train the multivariate classifier. The variables in red are also used to train the classifier in the $\Xi_{cc}^{++} \to \Lambda_c^+ K^- \pi^+ \pi^+$ analysis, see Table 4.4, but with the D^+ particle hypothesis replacing the Λ_c^+ particle hypothesis. The 'log' symbol denotes the natural logarithmic.

Training variables
1) $\cos^{-1}$(DIRA) of Ξ_{cc}^{++} to its PV
2) Smallest p_T among the daughters (D^+, p, K^-, and π^+) of the Ξ_{cc}^{++}
3) Maximum DOCA of Ξ_{cc}^{++}
4) Maximum DOCA of D^+
5) $\log(\chi^2_{IP})$ of Ξ_{cc}^{++} to its PV
6) χ^2_{vtx}/ndf of the Ξ_{cc}^{++} vertex fit (DTF refit)
7) Smallest p_T among the final daughters of the D^+
8) log(FD χ^2) of Ξ_{cc}^{++} from its PV
9) $\cos^{-1}$(DIRA) of D^+ to its PV
10) $\log(p_T)$ of K^- coming from D^+
11) $\log(p_T)$ of p coming from Ξ_{cc}^{++}
12) $\log(p_T)$ of π^+ (2) coming from D^+
13) $\log(p_T)$ of π^+ (1) coming from D^+
14) log(FD χ^2) of D^+ from its origin vertex
15) χ^2_{vtx}/ndf of the D^+ vertex fit

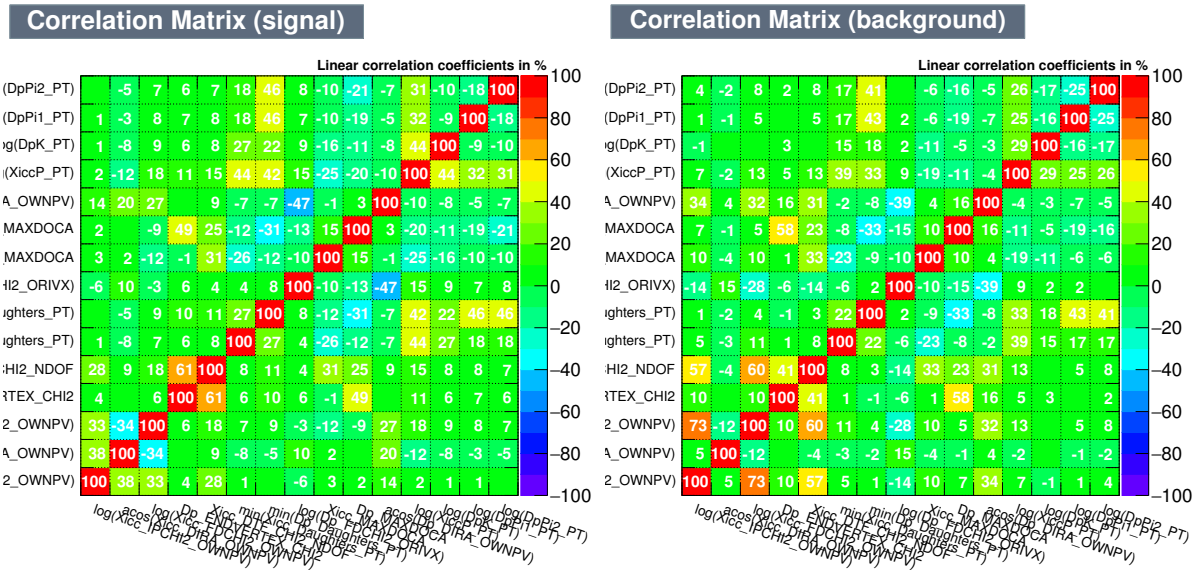

Figure 5.8: The correlation matrices for the final fifteen training variables used in the multivariate classifier in (left) signal MC and (right) background WSP data.

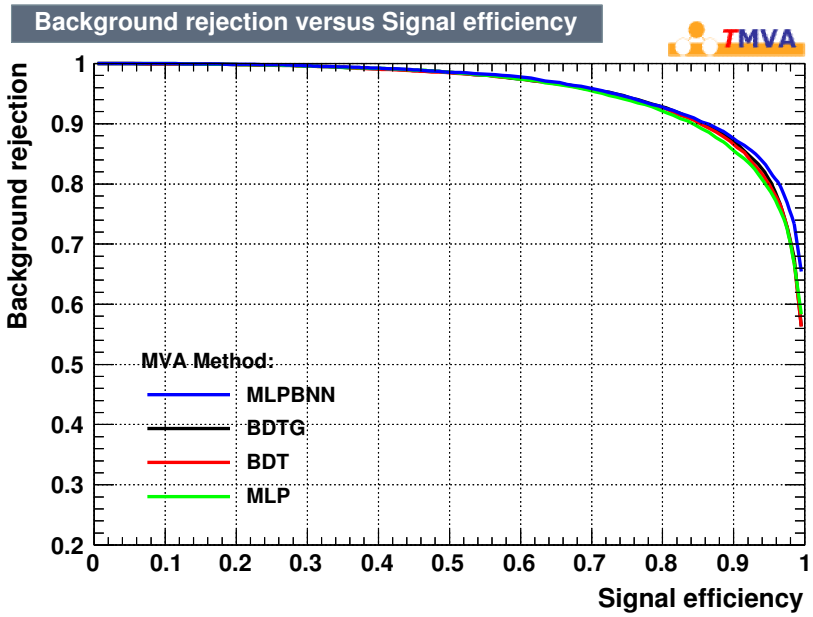

Figure 5.9: The background rejection rate versus signal efficiency curves for different multivariate classifiers. The vertical axis shows the fraction of background events rejected and horizontal axis shows the analogous measure for signal.

$\Xi_{cc}^{++} \to D^+pK^-\pi^+$ and $\Xi_{cc}^{++} \to \Lambda_c^+K^-\pi^+\pi^+$ candidate selections, which makes the efficiency of this stage of the selection in both channels easier to compare. The Punzi FoM scores, with a target significance of five standard deviations, as a function of response output for the best performing classifiers are shown in the left plot of Figure 5.10. As a reminder, the Punzi FoM is defined in Equation 4.2 and the reasons for using this figure of merit in search analyses such as this one is explained in Section 4.3.5. The background scaling factors for the $\Xi_{cc}^{++} \to D^+pK^-\pi^+$ channel are calculated to be: $C_{\text{scaling}} = 0.5$, $C_{\text{mode}} = 1.4$ and $C_{\text{window}} = 151.8$, following the same studies performed in Section 4.3.5 but with the WSP data set replacing the WS data set of the $\Xi_{cc}^{++} \to \Lambda_c^+K^-\pi^+\pi^+$ analysis. The response distribution from the training and testing phases of the classification process for the MLP classifier is shown in the right plot of Figure 5.10.

The optimal requirement, t, on the response from the four best performing classifiers, including the MLP classifier, is shown in Table 5.4 along with corresponding signal and background retention rates. In summary, the MLP response for each Ξ_{cc}^{++} candidate is required to be greater than the value of 0.89 in the multivariate selection.

Validation Checks

Similar cross-checks as carried out in the $\Xi_{cc}^{++} \to \Lambda_c^+K^-\pi^+\pi^+$ selection are performed in this analysis, following the application of the multivariate method. The multivariate variable's dependency on the lifetime of the Ξ_{cc}^{++} baryon is not scrutinized, since its

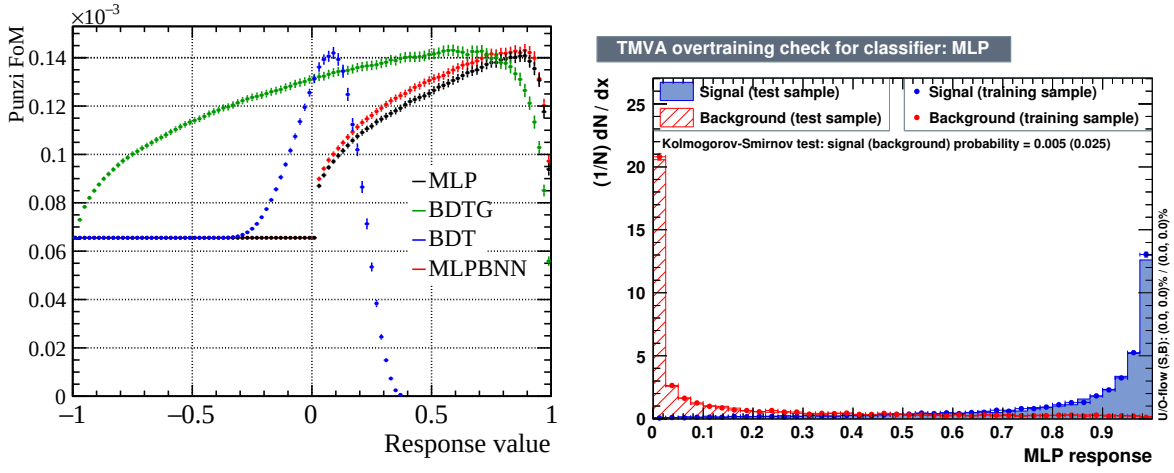

Figure 5.10: (left) The Punzi figure of merit scores as a function of the multivariate response for the four best performing classifiers and (right) the normalised response distribution for the MLP classifier,

Table 5.4: The optimum requirement on the response for the four best performing classifiers with signal and background efficiencies given with respect to the preselection.

Classifier	Optimal response t	Sig. $\varepsilon_{\text{MVA\|Presel}}$	Bkg. $\varepsilon_{\text{MVA\|Presel}}$	FoM ($\times 10^{-4}$)
BDT	0.09	0.671 ± 0.005	0.037 ± 0.001	1.41 ± 0.03
BDTG	0.59	0.722 ± 0.004	0.047 ± 0.001	1.43 ± 0.02
MLP	0.89	0.624 ± 0.004	0.029 ± 0.001	1.41 ± 0.02
MLPBNN	0.89	0.632 ± 0.005	0.029 ± 0.001	1.43 ± 0.03

lifetime has been measured to within a small value range and this uncertainty is not expected to significantly affect the performance of the multivariate method. The potential effects of the multivariate selection on data are checked by studying its impact on the WS control modes. Firstly, the resulting yield and retention rates of the Ξ_{cc}^{++} candidates, after the multivariate selection, are checked in the control modes as a function of the invariant mass of the Ξ_{cc}^{++} candidates. The plot on the right of Figure 5.11 shows that the multivariate selection slightly favours Ξ_{cc}^{++} candidates with a smaller reconstructed mass in WS data but otherwise there is no significant peaking structures in the invariant-mass distribution as is evident by the distribution in the left plot of Figure 5.11. Therefore, it is safely assumed that the MVA classifier does not artificially sculpt peaking structures in the combinatorial background in the RS channel. Note that in Figure 5.11 the range is between $3500-3800\,\text{MeV}/c^2$. A negligible number of Ξ_{cc}^{++} candidates are accepted with a mass less than $3500\,\text{MeV}/c^2$ by the multivariate selection.

Secondly, the effect of imposing stricter PID requirements on the expected Punzi FoM after the multivariate selection is also investigated. The LHCb collaboration have noticed

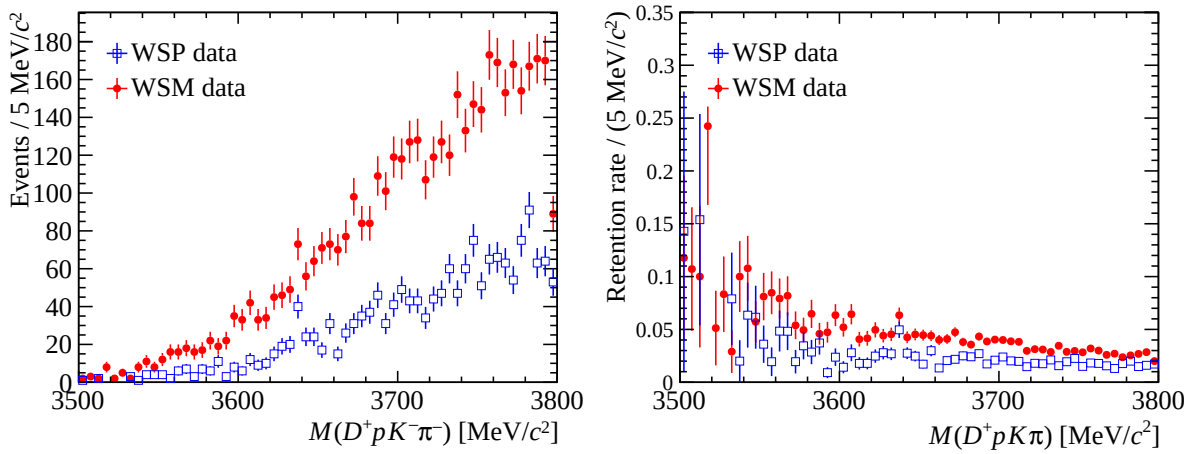

Figure 5.11: (left) Invariant-mass distribution and (right) background retention rate in the data control modes after the multivariate requirement.

from previous analyses that tighter PID requirement tend not to improve the Punzi FoM score. This is found to also be the case for this analysis. When the thresholds of the `ProbNN` requirements listed in Table 5.2 are increased, one at a time for each final-state particle with the `ProbNN` > 0.1 requirement remaining fixed for all other particles, the Punzi FoM is approximately constant. One-dimensional FoM scans of the `ProbNN` requirement, where the WSP data set has been used for the background source, are shown in Figure 5.12. The FoM is not significantly improved when using the stricter PID requirements compared to when using the ones in the preselection.

5.3.6 Rejection of Specific Backgrounds

Like in the $\Xi_{cc}^{++} \to \Lambda_c^+ K^-\pi^+\pi^+$ selection, requirements tailored to remove clone and duplicate candidates also make up the final part of this candidate selection. A recap of these two types of special candidates is given in this section.

Clones

The meaning of clones is thoroughly discussed in Section 4.3.6. However, it is perhaps worth discussing them briefly again here in order to explain what they are in the context of $\Xi_{cc}^{++} \to D^+pK^-\pi^+$ decays. Simply put, clones are Ξ_{cc}^{++} candidates from the same event that have used the same track more than once and they can arise from mistakes in the reconstruction of $\Xi_{cc}^{++} \to D^+pK^-\pi^+$ decays. They are identified by examining the angles between tracks of the same charge that are used to reconstruct a Ξ_{cc}^{++} candidate. Any two same-charged-final-state tracks that are too close to each other are assumed to be clones of each other and are expected to lead to the reconstruction of a cloned

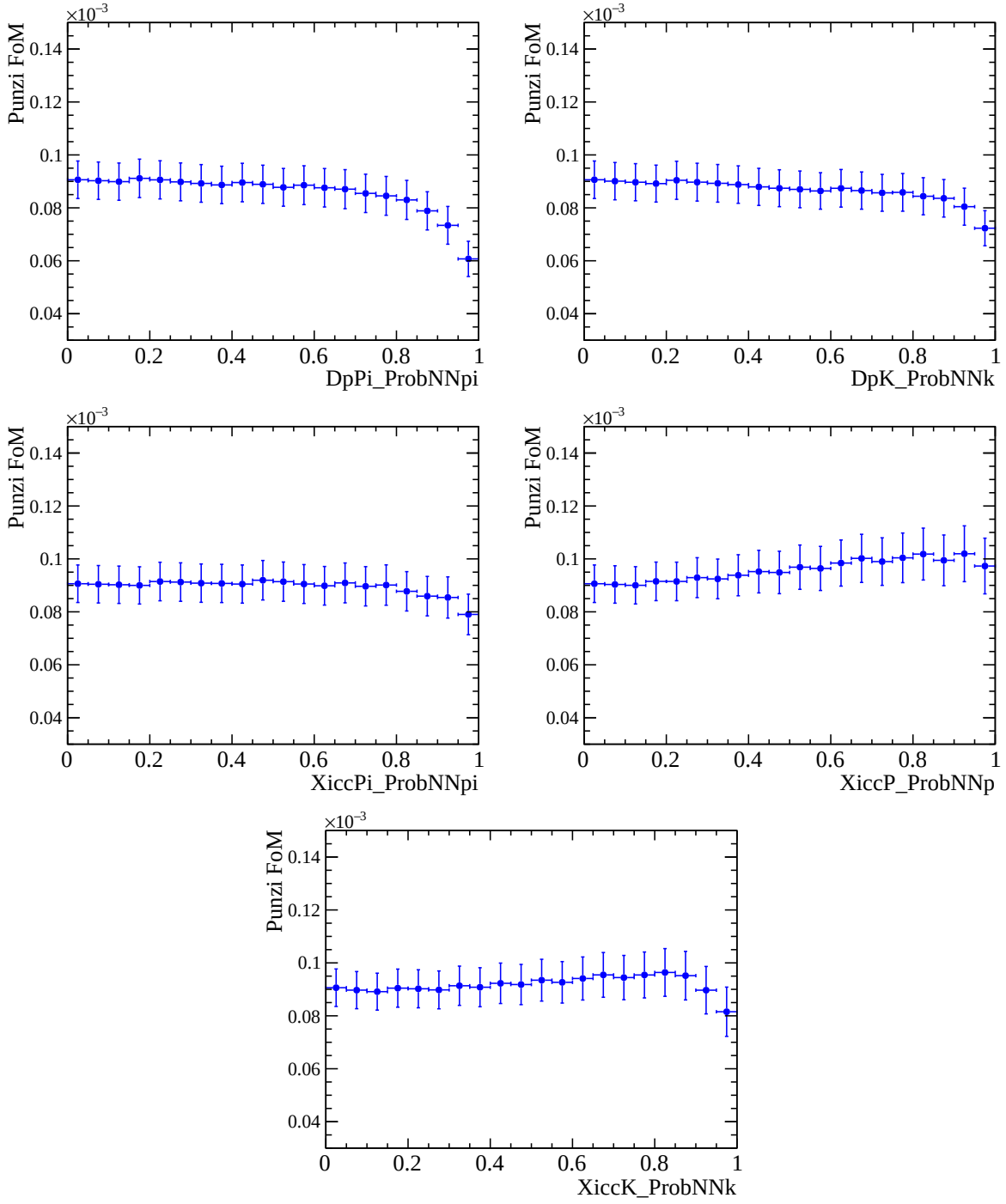

Figure 5.12: The Punzi FoM as a function of the ProbNN requirement on (top left) both the π^+ tracks coming directly from the D^+ candidate, on (top right) the K^- track coming directly from the D^+ candidate, on (middle, left) the π^+ track coming directly from the Ξ_{cc}^{++} candidate, on (middle, right) the p track coming directly from the Ξ_{cc}^{++} candidate and on (bottom) the K^- track coming directly from the Ξ_{cc}^{++} candidate. The ProbNN requirements used in the final selection are detailed in Table 5.2.

Ξ_{cc}^{++} candidate. Therefore, to deal with this form of fake signal candidate, the angle between any two tracks of the same charge is required to be greater than 0.5 mrad. If a Ξ_{cc}^{++} candidate has been formed from at least one pair of these suspected cloned tracks, then the candidate is removed as part of this specialised selection.

The opening angle between any pairs of tracks, among all the six tracks, with the same charge in the WSP, WSM and MC samples are plotted in Figure 5.13. In both the WSP and WSM samples, a peak around the zero angle is seen, consistent in the two samples, which is understood to be caused by clone tracks. Clones cannot easily occur in MC samples that have been truth-matched. This is reflected by the fact that there is no abundant peak near the zero-angle in the MC sample. This procedure removes around 31.4% of events in WSP data, 7.9% of events in WSM data and less than 0.2% of signal MC events. Based on these results, if a $\Delta\theta_{\mathrm{i,j}} > 0.5$ mrad requirement is imposed on data then clone contributions may be fully removed without removing a noticeable fraction of the signal candidates. The higher number of clones in the WSP sample is expected if one considers the ten possible combinations of same-charged-final-state tracks in the WSP data set compared to the six in the WSM sample.

The invariant-mass distribution of the Ξ_{cc}^{++} candidates arising from the expected clones in the WSP and WSM data set, after the multivariate selection, is shown in Figure 5.14. Note that the mass distribution of the expected cloned tracks has been normalised to the distribution with all candidates present. The cloned candidates have on average a smaller mass than the non-cloned Ξ_{cc}^{++} candidates due to the smaller opening angle of their final-state tracks. Within statistical uncertainty, clones are shown not to form significant peaking structures in the invariant mass distribution of either the WS data samples. Thus, clones are not expected to cause issues for fitting the background component of the mass distribution in the final RS data sample. The results presented in Figure 5.13 and Figure 5.14, have a stricter `ProbNN` requirement (`ProbNNghost` < 0.6) imposed on all final-state tracks to ensure no ghost tracks are present, however this requirement is not used in the final selection. Refer to Section 4.3.1 for the definition of a ghost track. A narrow range of the `ProbNNghost` distribution for all final-state tracks is shown in Figure 5.15 for expected cloned candidates and non-cloned candidates. The distributions are very similar and so demonstrates that clones and non-cloned candidates are equally likely to be identified as a clone.

Duplications

The procedure to cope with duplications in the context of the $\Xi_{cc}^{++} \to \Lambda_c^+ K^- \pi^+ \pi^+$ selection is carefully explained in Section 4.3.6. Duplications are treated in the same way

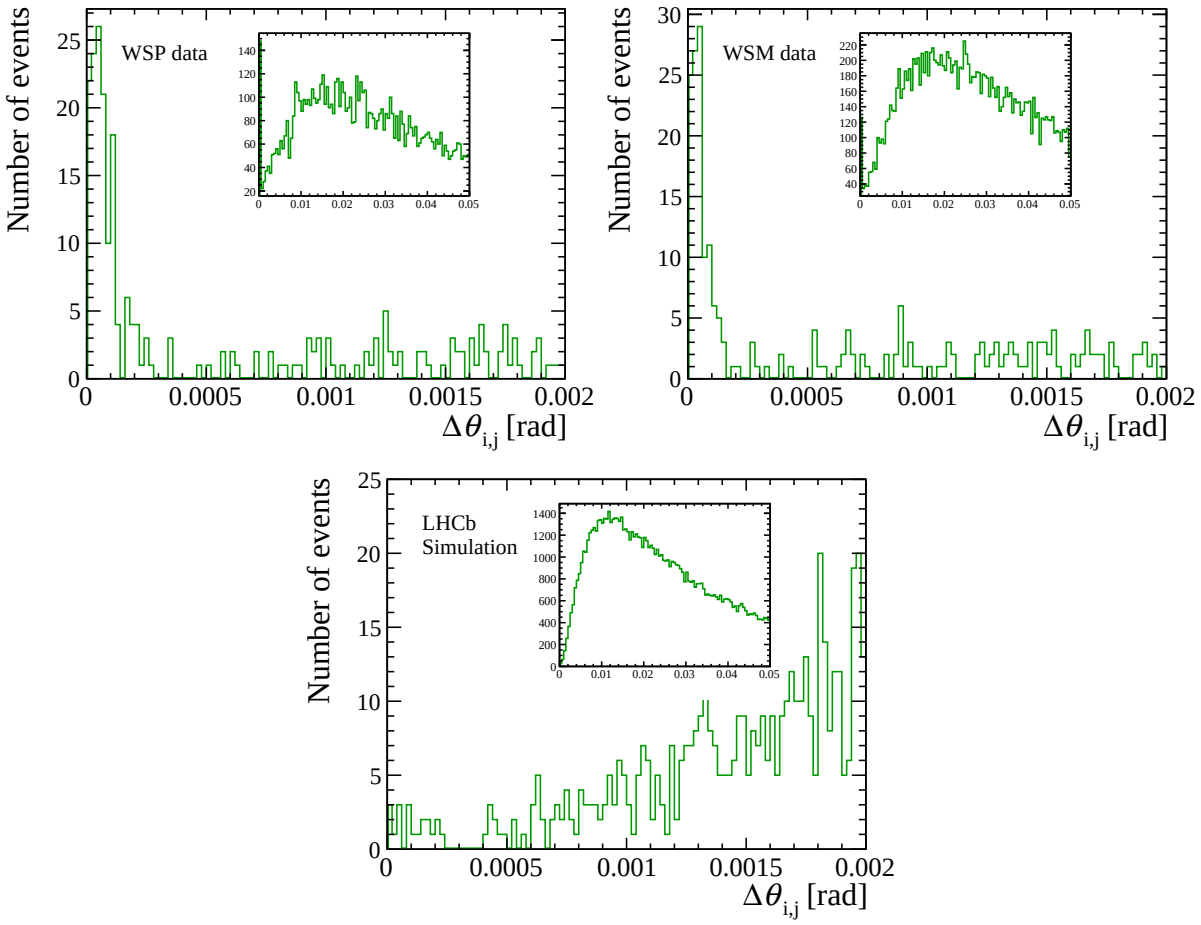

Figure 5.13: Opening angle, $\Delta\theta_{i,j}$, between final-state track of the same charge in the (top left) WSP, (top right) WSM and (bottom) MC samples. The insert for each plot gives the same distribution but in a wider angular region.

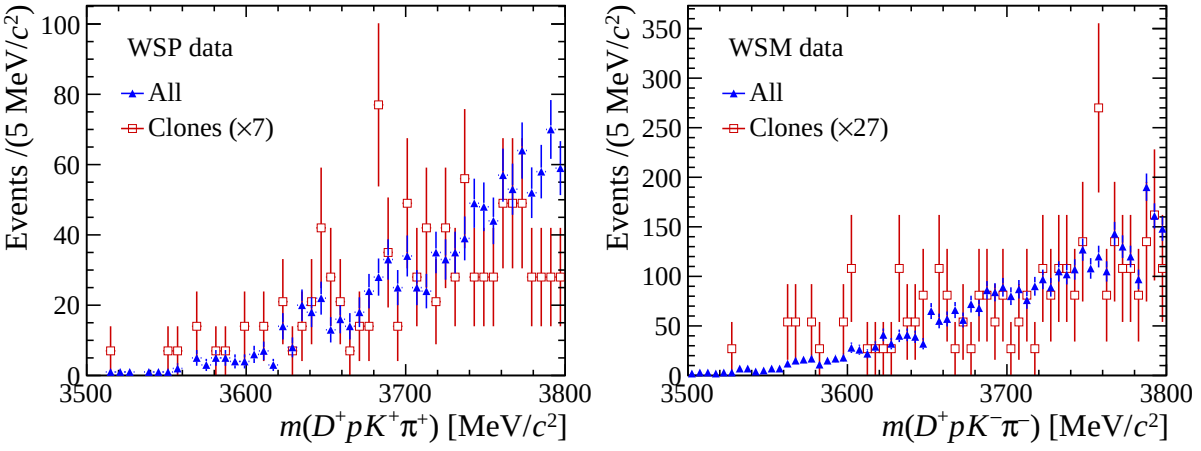

Figure 5.14: Normalised Ξ_{cc}^{++} invariant mass distribution for (blue triangles) all candidates and (red squares) clone candidates, for (left) WSP and (right) WSM samples.

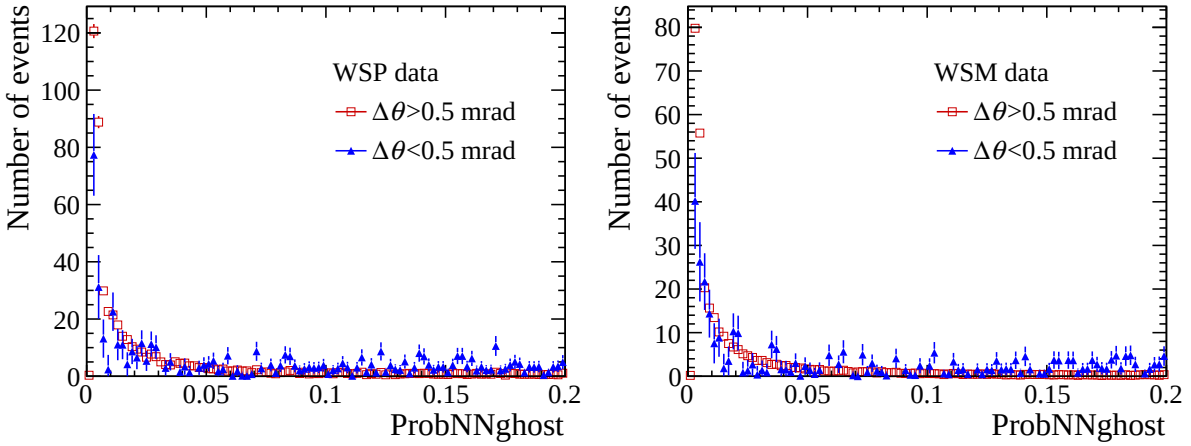

Figure 5.15: The ghost track probability of the (left) WSP data set and (right) WSM data set (after the full selection) separated out into events in terms of the angles between tracks with the same charge.

in this analysis and therefore the procedure to remove them will not be extensively described again. However, an explanation to the origin of duplications specifically in the $\Xi_{cc}^{++} \to D^+ pK^-\pi^+$ channel is given in this section.

Duplicate candidates occur when the same final-state tracks are used to reconstruct more than one candidate because the tracks are wrongly interchanged during the reconstruction of the decay chain. For $\Xi_{cc}^{++} \to D^+(\to K^-\pi^+\pi^+)pK^-\pi^+$ decays, this can happen due to three situations:

1. The K^- track from the D^+ decay vertex is swapped with the K^- track produced at the Ξ_{cc}^{++} decay vertex;

2. The π^+ track from the Ξ_{cc}^{++} decay vertex is swapped with any of the two π^+ tracks originating from the D^+ decay vertex;

3. Track exchanges happen in both situation 1 and situation 2.

The situations described above are easier to visualise when referring to Figure 5.3. The duplicate candidates resulting from these track-exchange situations will have exactly the same invariant mass as any non-duplicate Ξ_{cc}^{++} candidate but the mass of their associated D^+ candidate might differ vastly from the known mass of the D^+ baryon. Therefore, the constraints on the mass and vertex quality of the D^+ candidates in the HLT2 lines of this analysis, see Table 5.1, should reduce the possibility of duplications being accepted. However, this is never a guarantee and it is assumed that duplications will remain in the data samples, even after the multivariate selection. If duplications are identified, then only one of the Ξ_{cc}^{++} candidates from such an event, chosen at random, is retained. This

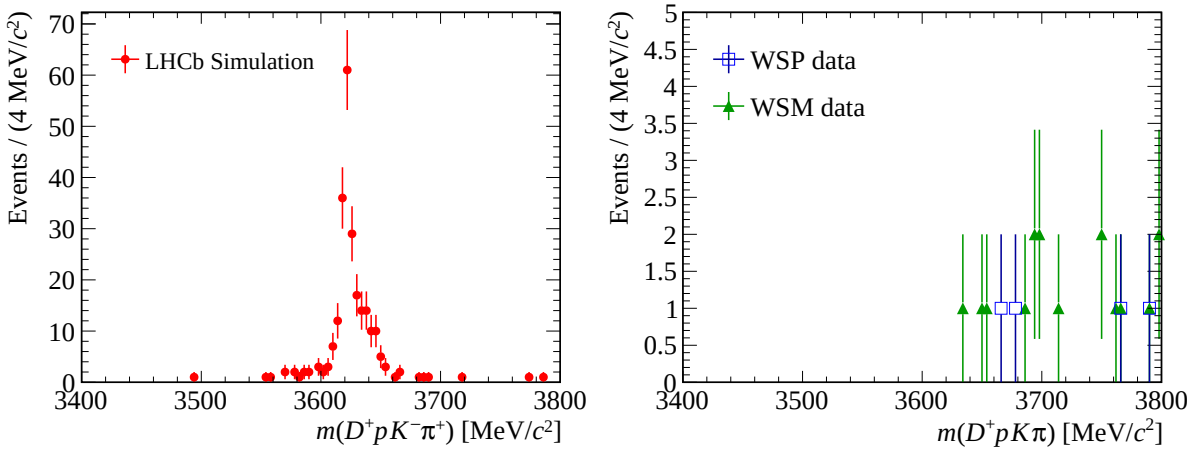

Figure 5.16: The invariant-mass distribution of duplicate Ξ_{cc}^{++} candidates in (left) a track-exchange-allowed MC sample and in (right) the WS control samples.

removal process is performed after the preselection, the multivariate selection and the removal of clones.

The invariant-mass distribution of duplications in the MC, WSP and WSM samples, after the multivariate selection, is shown in Figure 5.16. Note that the MC sample has a modified version of the truth-matching requirement applied so to allow duplications. In the top plot of Figure 5.16, a peak is seen around the generated mass of the Ξ_{cc}^{++} baryon of this track-exchange-allowed MC sample. However, in the case of the WS samples, which should represent combinatorial background in the RS channel, there is no peak. Instead, the masses of the Ξ_{cc}^{++} candidates identified as duplicates are far from expected signal region of the Ξ_{cc}^{++} baryon, as shown in the bottom plots of Figure 5.16. Keep in mind, there are more pairs of identical tracks in the RS decays compared to both the WS decays, so the number of duplications for each real Ξ_{cc}^{++} candidate in the RS data set is expected to be larger. In the WS samples, after the multivariate selection and removal of clones, the number of multiple candidates reconstructed from the swap of tracking is less than 1%. Like in the $\Xi_{cc}^{++} \to \Lambda_c^+K^-\pi^+\pi^+$ analysis, it was decided that only one Ξ_{cc}^{++} candidates, chosen at random, should be retained from events containing duplications, while the rest are removed.

Track exchanges are not the only means by which fake Ξ_{cc}^{++} candidates can be reconstructed in the same event as a real Ξ_{cc}^{++} candidate. The more general discussion of multiple candidates as a potential form of background takes place in Section 5.4.3.

5.4 Background Studies

In this section, different types of background are studied in the $\Xi_{cc}^{++} \to D^+pK^-\pi^+$ channel. Aside from combinatorial background, which will dominate, background may arise

through resonances, multiple candidates and the misidentification of particles. The effect of these types of background on the invariant-mass distribution of the Ξ_{cc}^{++} candidates in the RS data is explored via the WS control modes, before the RS data itself is scrutinised.

In the following studies, candidates reconstructed in the WSP or WSM data sets are referred to as Ξ_{cc}^{++} candidates for simplicity and to avoid confusion. The mass variables plotted in this section for the WS control modes take the same form as the mass estimator defined in Equation 5.1 but of course reformulated to reflect the appropriate charges of the final-state tracks that are reconstructed in the samples.

5.4.1 D^+ Background

One source of background could be from unrelated tracks forming the D^+ candidate. Given that the event selection requires the daughter tracks of the D^+ candidate to be significantly displaced from the PV, see Figure 5.3, then this form of combinatorial background should not be abundant. Equally, as discussed before, $D^+ \to K^-\pi^+\pi^+$ decays are cleanly reconstructed with a high purity using the LHCb detector, even when produced promptly at the PV, so combinatorial D^+ background is not expected to cause issues.

Nevertheless, the invariant-mass distribution of the Ξ_{cc}^{++} candidates in the WS control modes, before and after the multivariate selection and from different regions of the D^+ mass spectrum is plotted to check the resulting distribution. For this study alone, the offline mass requirement on the D^+ candidate is not enforced to allow a larger mass range to be examined. The D^+ mass spectrum from the WSM data set is shown in Figure 5.17 where the blue-shaded region ($1849-1891\,\mathrm{MeV}/c^2$) represents the signal region. The lower-mass sideband ($1780-1840\,\mathrm{MeV}/c^2$) and the upper-mass sideband ($1910-1960\,\mathrm{MeV}/c^2$) regions are shown as the green-shaded and red-shaded areas, respectively, in Figure 5.17.

The mass distributions of the corresponding Ξ_{cc}^{++} candidates from the D^+ mass regions detailed above, before and after the multivariate selection, are shown in Figure 5.18. The Ξ_{cc}^{++} mass distributions in the signal and sideband mass regions are consistent with each other after normalisation. This was also found to be the case for the WSP data set. After the multivariate selection, the mass distribution of the Ξ_{cc}^{++} candidates in the D^+ signal region is slightly different from that observed in the sideband regions; although, the statistical uncertainties are too large to draw a definite conclusion. If the effect is real, it may be caused by the training variables linked to the D^+ candidate causing the multivariate classifier to select Ξ_{cc}^{++} candidates with different kinematic properties in the signal and sideband regions.

However, within statistical uncertainty, the results shown in Figure 5.18, suggest that the background arising from either the signal D^+ or D^+ combinatorial background

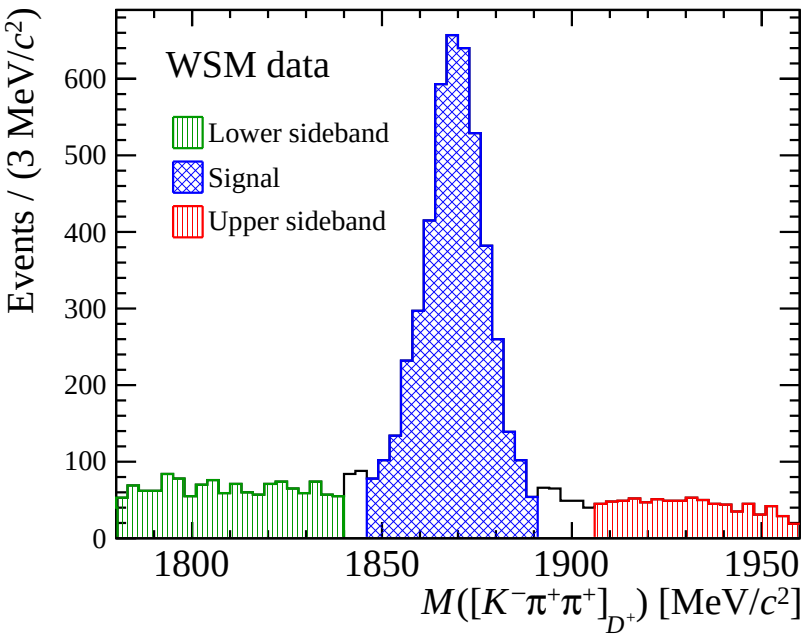

Figure 5.17: Invariant-mass distribution of D^+ candidates in the WSM data, after the multivariate selection, indicating the (blue-shaded) signal region, the (green-shaded) lower-sideband region and the (red-shaded) upper-sideband region.

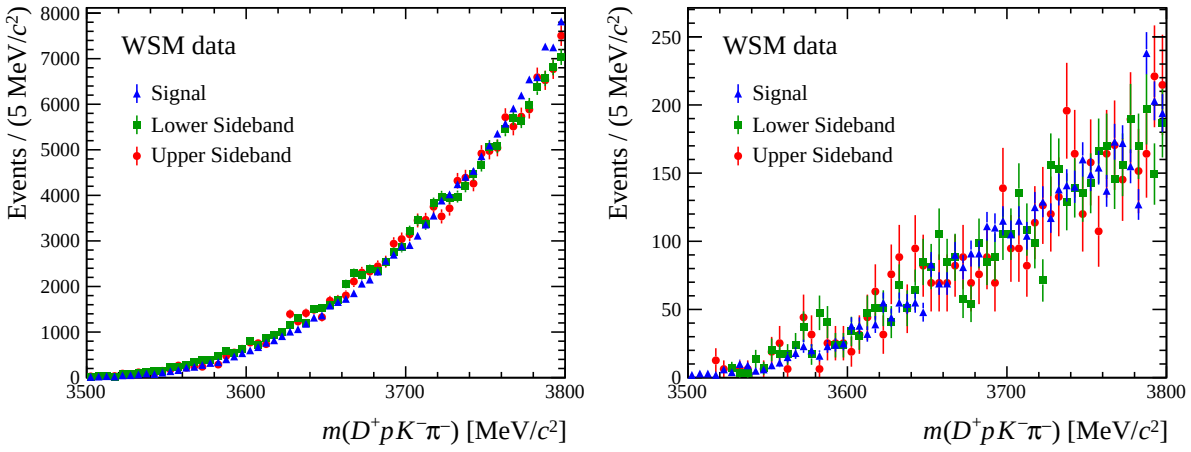

Figure 5.18: Invariant-mass distributions of Ξ_{cc}^{++} candidates in the WSM data set. The left (right) plot shows the distribution in the D^+ signal region and D^+ sideband regions before (after) applying the multivariate selection.

are very similar and that narrow peaking structures are not expected in the combinatorial background in the RS channel. In any case, the majority of combinatorial D^+ background is removed by the strict offline D^+ mass requirement used in the event selection.

5.4.2 Sub-decay Structures

Resonances are a very important discussion point when it comes to the branching fraction of the $\Xi_{cc}^{++} \to D^+pK^-\pi^+$ decay, as discussed in Section 1.4.2. However, they may also cause substructures to form in the invariant-mass spectrum of the Ξ_{cc}^{++} candidates in the RS data. Possible resonant decays in the $\Xi_{cc}^{++} \to D^+pK^-\pi^+$ channel include: $\Sigma_c^{++} \to D^+p$, $\Lambda^0 \to pK^-$, $\Sigma^0 \to pK^-$ and $\bar{K}^{*0} \to K^-\pi^+$ decays but they are all below threshold if $3620\,\mathrm{MeV}/c^2$ is accepted as the mass of the Ξ_{cc}^{++} baryon. Therefore, resonances are not expected to significantly impact the mass spectrum in the RS data. Although, if they do appear in the RS channel then this is not an issue; if the Ξ_{cc}^{++} candidates proceed through a resonance this is insignificant for the mass measurement study. For the ratio of branching fractions measurement, the effect of resonances on the efficiency of the event selection is discussed in Appendix D. A problem associated to resonances would be if some kinematic correlation existed between them and uncorrelated tracks such that the invariant mass of the combined objects peaks in the signal Ξ_{cc}^{++} mass region. This would imply that they have a common origin and, therefore, that the reconstruction has failed. Yet, this is proven not to be the case for either the WSP or the WSM data set.

On the other hand, resonances are expected in the combinatorial background of the RS channel. The WS data sets are explored to evaluate the likely presence of resonances in background and, at the same time, to further understand the control modes. In the WSP data set, $\Delta^{++} \to p\pi^+$ decays could be expected, while for the WSM data set, $\Lambda^0(1520) \to pK^-$ decays could contribute. Both these resonant decays are not available to the RS channel due to the charge of its final-state tracks. The invariant-mass distributions for partial-decay-product combinations of the WSP and WSM decays are shown in Figure 5.19 and Figure 5.20, respectively. Peaks of potential structures caused by resonances are marked by the blue-vertical lines in the plots of Figure 5.19 and Figure 5.20. Resonant decays of $\Delta^{++} \to p\pi^+$ and $\Lambda^0(1520) \to pK^-$ are likely seen, while others are not significant. Events in these marked regions are projected into the mass space of its associated Ξ_{cc}^{++} candidate and the resulting distributions are shown in Figure 5.21 and Figure 5.22 for the WSP and WSM data set, respectively. The size of the bins in these histograms are in keeping with the expected mass resolution of the Ξ_{cc}^{++} baryon in the RS channel following studies with simulation, see Section 5.5.1.

In summary, no significant peaking structures are observed in the Ξ_{cc}^{++} invariant-mass projections in either the WSP or WSM data set and so resonances are not expected

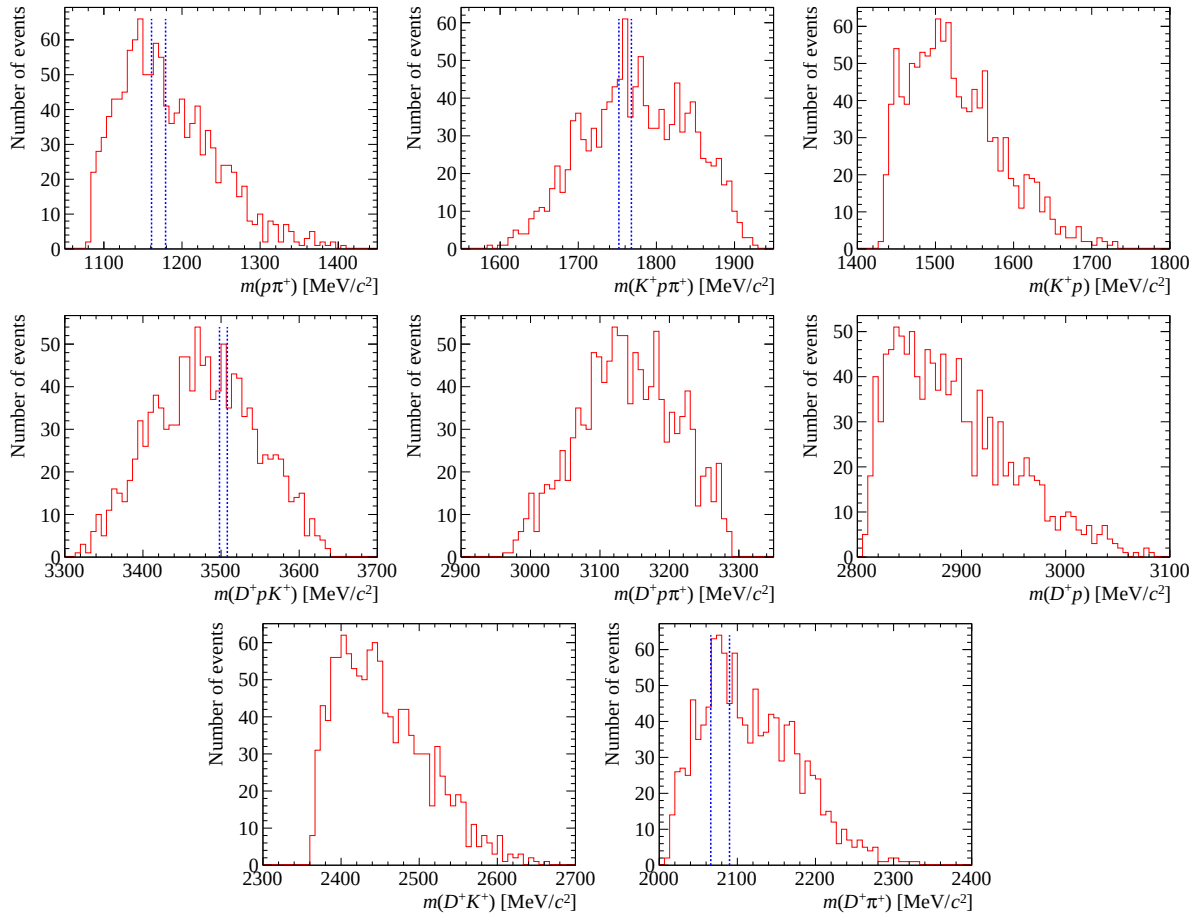

Figure 5.19: Invariant-mass distributions of combinations of partial-decay products in the WSP $\Xi_{cc}^{++} \to D^+pK^+\pi^+$ decay. The blue-vertical lines indicate the mass regions of interest for searches of possible resonances.

to be a problem from the point of view of background.

5.4.3 Multiple Candidates

The reconstruction of $\Xi_{cc}^{++} \to D^+pK^-\pi^+$ decays also invites the possibility of multiple Ξ_{cc}^{++} candidates existing in the same event; some of which are not real candidates. One type of fake multiple candidate, duplications, has already been discussed in Section 5.3.6. Multiple candidates as a source of background has also been deliberated in Section 4.4.2 when discussing $\Xi_{cc}^{++} \to \Lambda_c^+K^-\pi^+\pi^+$ decays. The same categories of multiple candidates identified in Section 4.4.2 will also be discussed here. As a reminder, those categories are:

1. Two or more Ξ_{cc}^{++} candidates in the same event share all six final-state tracks with the same mass assignments;

2. Two or more Ξ_{cc}^{++} candidates in the same event share a few but less than six final-state tracks and the shared tracks have the same mass assignments;

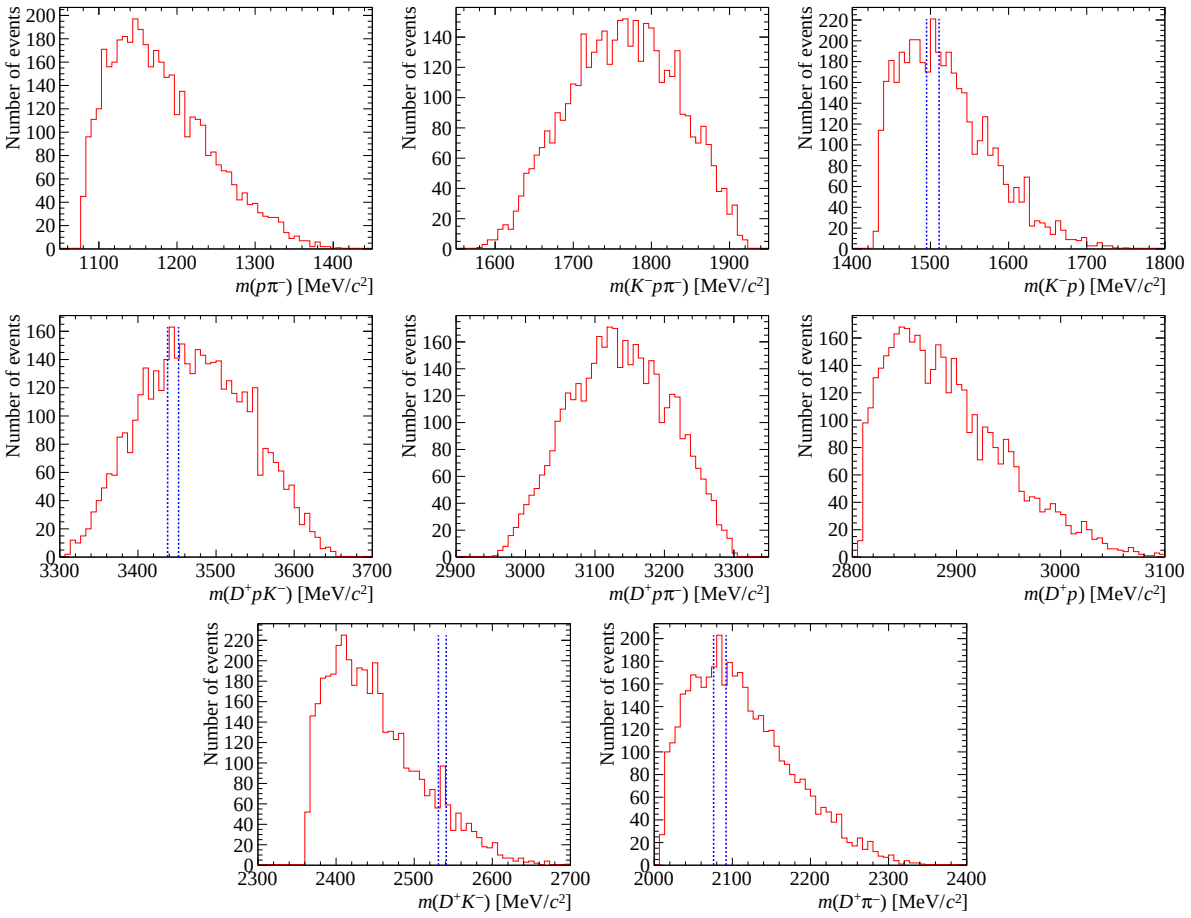

Figure 5.20: Invariant-mass distributions of combinations of partial-decay products in the WSM $\Xi_{cc}^{++} \to D^+pK^-\pi^-$ decay. The blue-vertical lines indicate the mass regions of interest for searches of possible resonances.

3. Two or more Ξ_{cc}^{++} candidates share either all final-state tracks, or a fraction of them, but at least one shared track has a different mass assignment.

Category one is the aforementioned duplicate candidates of Section 5.3.6. Category three corresponds to background from tracks being misidentified; Section 5.4.4 is dedicated to this type of background so it will not be discussed further here. Category two covers partially-reconstructed background. This happens to be the dominant type of multiple candidate that leads to fake Ξ_{cc}^{++} candidates in this analysis, according to the control modes. Partially-reconstructed background, in relation to multiple candidates, can occur from a real D^+ baryon combining with unrelated kaon, pion or proton tracks to form more than one Ξ_{cc}^{++} candidate in the same event.

The invariant-mass distributions for each event containing a singly-selected Ξ_{cc}^{++} candidate and events with multiple Ξ_{cc}^{++} candidates, after the event selection, including the removal of clones and duplicates, are shown in Figure 5.23. Within their statistical uncertainty, the two distributions are found to be similar with no peaking structures visible

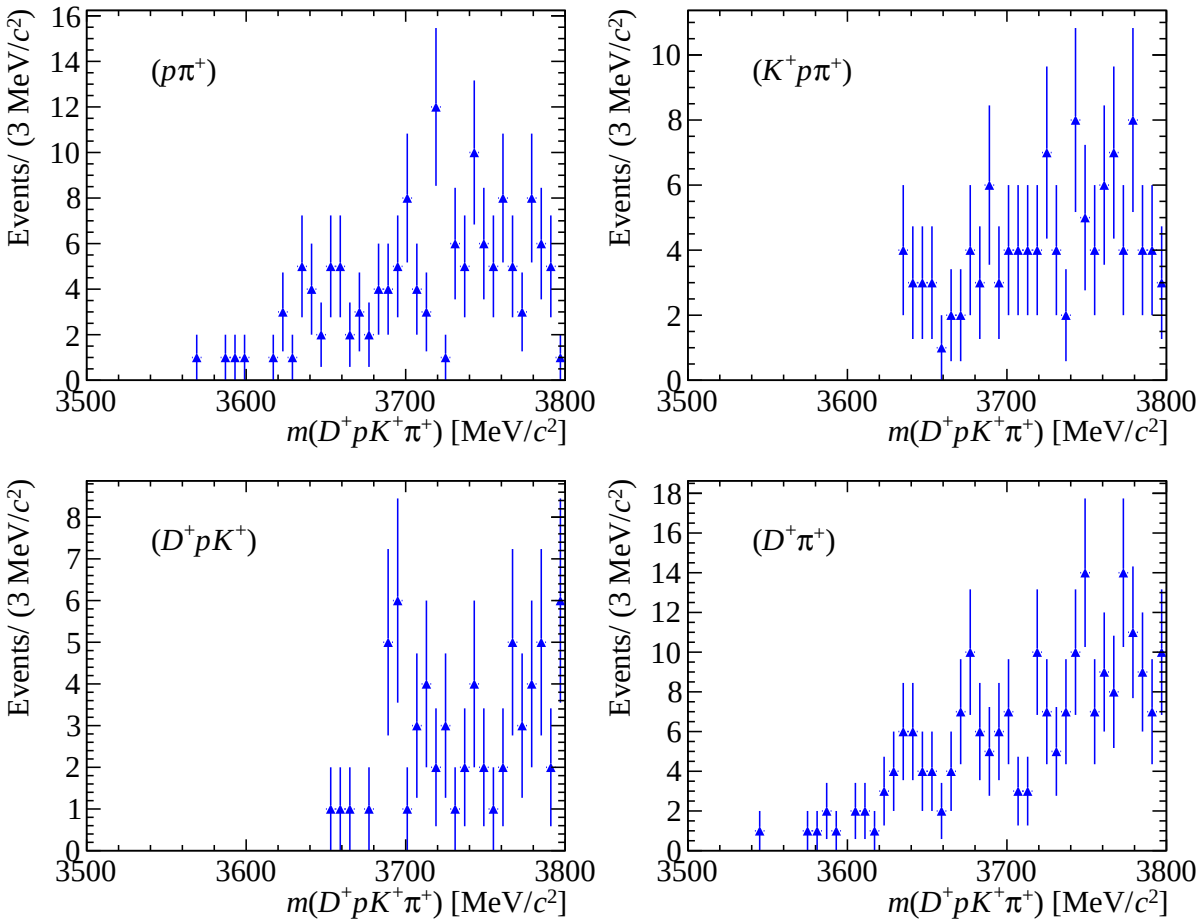

Figure 5.21: Invariant-mass distribution of Ξ_{cc}^{++} candidates in the WSP data set for events between the regions marked by blue-vertical lines in Figure 5.19.

in either case. Category two multiple candidates constitute around 6.9% (7.9%) of all the remaining Ξ_{cc}^{++} candidates in the WSP (WSM) data set.

In the end, category two and category three multiple candidates are not removed as part of the selection to ensure all real signal events are retained. This is the same strategy as was adopted for the $\Xi_{cc}^{++} \to \Lambda_c^+K^-\pi^+\pi^+$ selection. In any case, the results shown in Figure 5.23 demonstrate that these two types of backgrounds are not expected to create significant narrow peaking structures in the Ξ_{cc}^{++} signal region of the RS data. Category one multiple candidates, namely duplications, are however removed as part of the candidate selection, as was mentioned in Section 5.3.6.

5.4.4 Misidentified Background

The final background that is investigated is misidentified background. Strict particle identification requirements are used by the trigger and in the offline preselection but misidentified background should still be expected. Firstly, the misidentification of particles can give rise to reflection backgrounds, albeit in the $D^+ \to K^-\pi^+\pi^+$ channel there

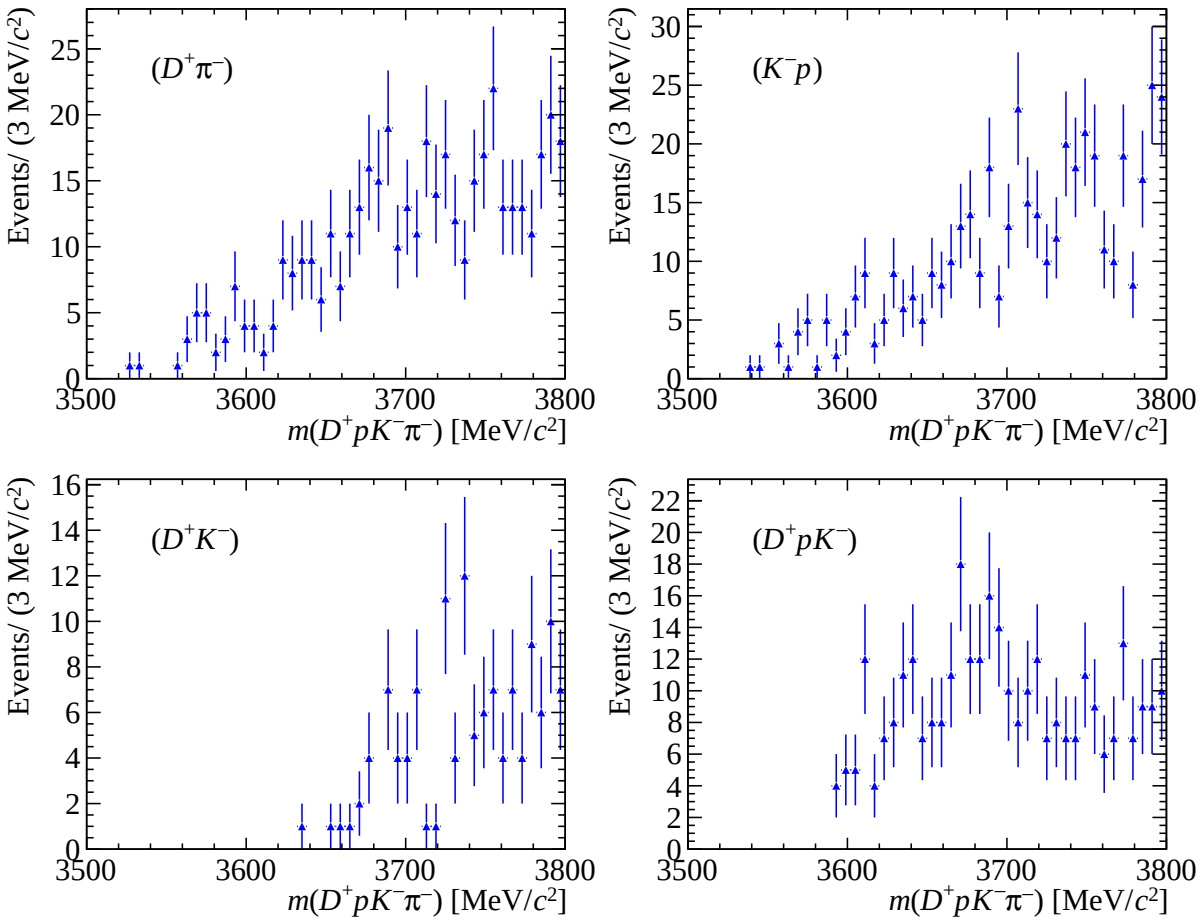

Figure 5.22: Invariant-mass distribution of Ξ_{cc}^{++} candidates in the WSM data set for events between the regions marked by blue-vertical lines in Figure 5.20.

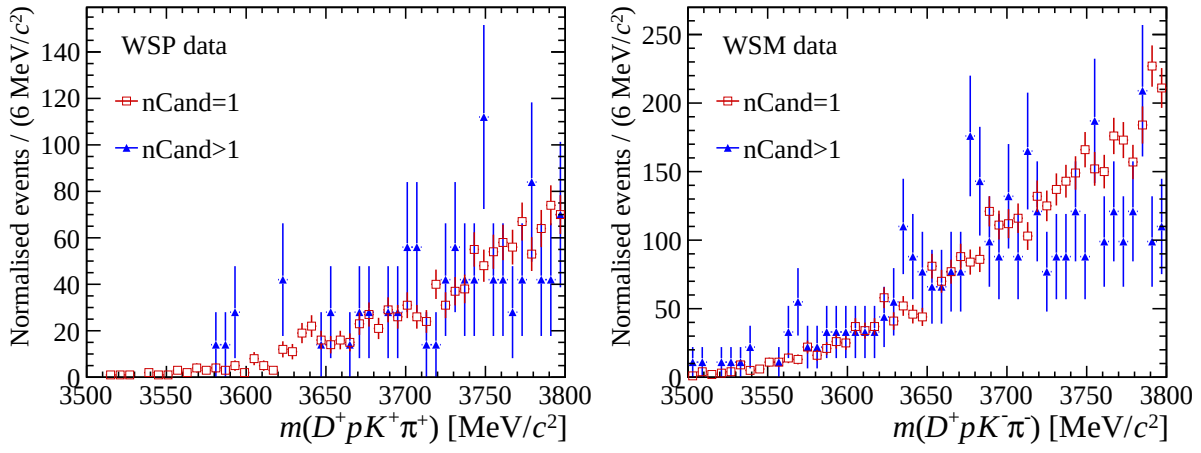

Figure 5.23: Normalised invariant-mass distribution of Ξ_{cc}^{++} candidates, passing the final selection, for (red squares) events with exactly one candidate and for (blue triangles) events that have multiple candidates selected. The left (right) plot is for the WSP (WSM) data set.

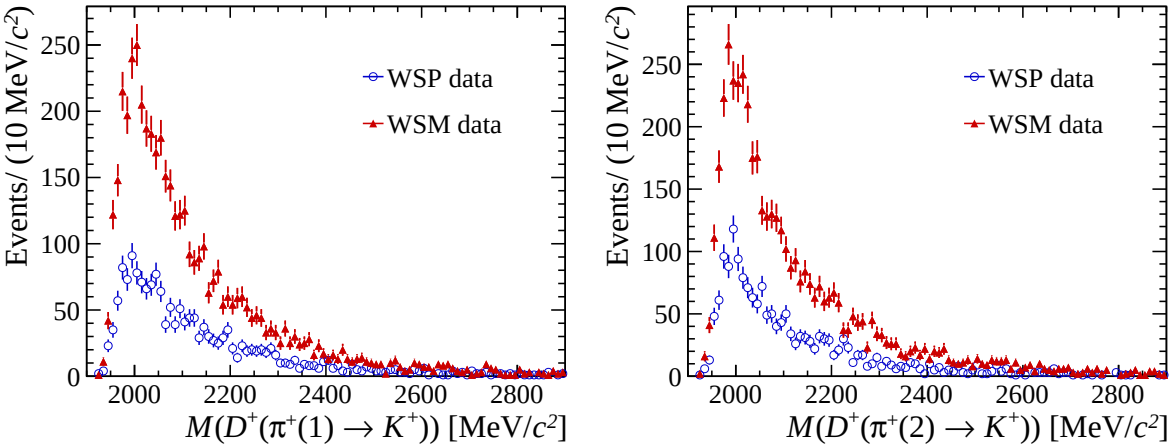

Figure 5.24: Invariant-mass distribution of $D^+ \to K^-\pi^+\pi^+$ decays in the (blue circles) WSP data set and in the (red triangles) WSM data sets, after a (left) $\pi^+(1)$ and (right) $\pi^+(2)$ track are replaced with the a K^+ hypothesis.

is realistically only the possibility of $D_s^+ \to K^+K^-\pi^+$ reflections. With a branching fraction of $(5.45 \pm 0.17)\%$, compared to $(8.98 \pm 0.28)\%$ for the $D^+ \to K^-\pi^+\pi^+$ decay [1], they should not greatly contaminate the $D^+ \to K^-\pi^+\pi^+$ sample. They are still studied in order to be thorough.

The invariant-mass distributions of the D_s^+ reflection background after replacing the π^+ tracks coming directly from the D^+ decay vertex, one at a time, with a K^+ particle hypothesis, are shown in Figure 5.24. The contribution of $D_s^+ \to K^+K^-\pi^+$ decays are found to be negligible with no clear peak around 1968.34 MeV/c^2, the known mass of the D_s^+ meson [1]. Note that the pion tracks in the $D^+ \to K^-\pi^+\pi^+$ decay are distinguished by their p_T such that the $\pi^+(2)$ track represents the higher momentum pion in the event and $\pi^+(1)$ track corresponds to the one with the smaller p_T. The $m(D^+pK\pi)$ invariant-mass distributions for events within the signal region of the D_s^+ mesons are shown in Figure 5.25. The signal region is defined as ± 22 MeV/c^2 around the known value of the D_s^+ meson. No significant peaking structures are identified for these reflections in the data control modes. Hence, reflections are not expected to cause problems for the mass measurement of the Ξ_{cc}^{++} baryon in the RS data. Reflections that mimic the full $\Xi_{cc}^{++} \to D^+(\to K^-\pi^+\pi^+)pK^-\pi^+$ decay are not considered in this analysis since there are no competitive ones that share the same topology.

Lastly, the effect of identifying a particle incorrectly that arise from combinatorial background is investigated. The $m(D^+pK^+\pi^+)$ invariant-mass distribution in WSP data, after the event selection, as a function of different particle identification requirements, is plotted in Figure 5.26. It can be seen that the uncorrelated D^+, p, K^+ and π^+ tracks of the WSP data set produce a smoothly varying mass distribution when combined, as expected. Additionally, the distribution remains smooth and without peaks when stricter particle

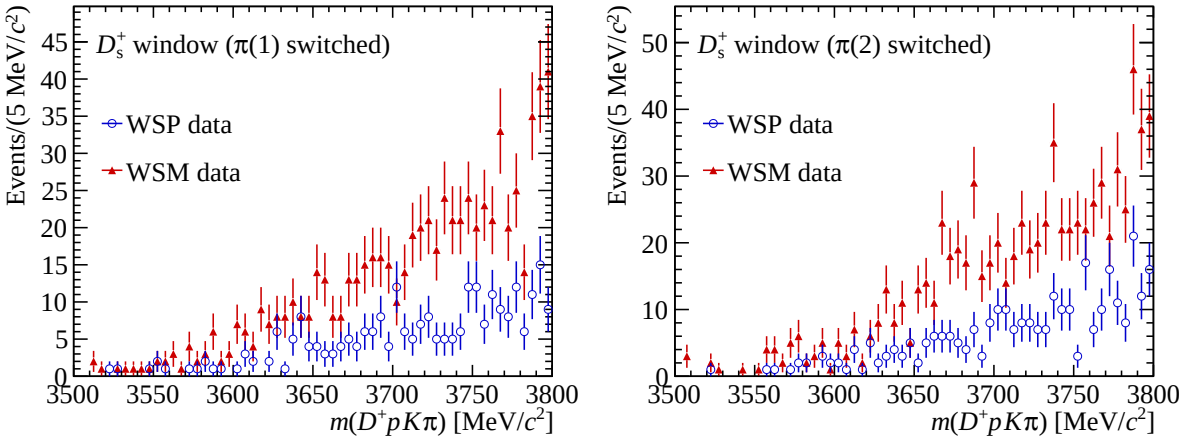

Figure 5.25: Invariant-mass distribution for events residing in the D_s^+ signal regions that are plotted in Figure 5.24 for the (blue circles) WSP data set and the (red triangles) WSM data set.

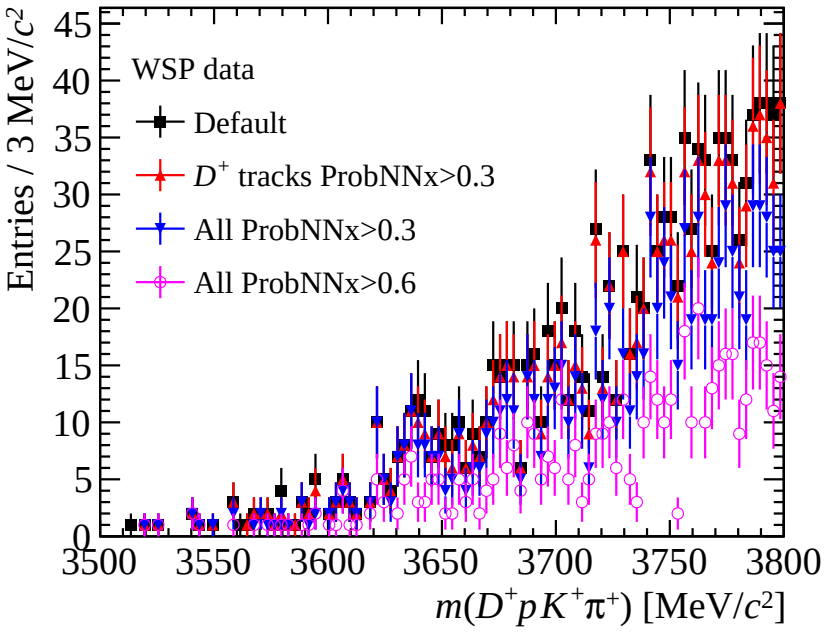

Figure 5.26: Invariant-mass distribution of the Ξ_{cc}^{++} candidates in WSP data as a function of tighter particle identification requirements applied to final-state tracks.

identification requirements than used in the preselection, see Table 5.2, are applied. So similarly to reflections, combinatorial background should not be affected if the particle hypothesis for a track is incorrect.

5.5 Mass Measurement Studies

In this section, studies related to the mass measurement of the Ξ_{cc}^{++} baryon in the $\Xi_{cc}^{++} \to D^+pK^-\pi^+$ channel are discussed. This includes the design of the mass model used to fit the $m(D^+pK^-\pi^+)$ mass distribution in the RS data set, as well an investigation of all possible sources of uncertainty which could impact the mass measurement. The latter subject is focused on more extensively since the PhD candidate conducted all the systematic uncertainty studies in this channel, which was not the case for the $\Xi_{cc}^{++} \to \Lambda_c^+K^-\pi^+\pi^+$ analysis.

5.5.1 Mass Models

The mass of the Ξ_{cc}^{++} baryon is measured from a fit to the invariant-mass distribution of the Ξ_{cc}^{++} candidates in the RS data that pass the event selection described in Section 5.3. The fitted variable is the $m(D^+pK^-\pi^+)$ mass estimator from Equation 5.1 where its terms are evaluated after a kinematic refitting by the `DecayTreeFitter` tool such that the Ξ_{cc}^{++} candidates are constrained to originate from their best associated primary vertex and momentum-scaling corrections are applied.

Signal

The shape of the expected signal-mass distribution in the RS data set is studied with simulated signal MC events that pass the full event selection. Several models are trialled to find the one which best describes the signal shape in simulation. In the end, the same model used to fit the signal observed in the $\Xi_{cc}^{++} \to \Lambda_c^+K^-\pi^+\pi^+$ data, a Gaussian function combined with a DSCB function (see Equation 4.3) is chosen as the default model for this analysis. The full details of this model are described in Section 4.5.1 and so the technicalities will not be reiterated here. The good agreement between this model and the signal MC sample can be seen in Figure 5.27, where the difference between the fit and any data point is always less than three standard deviations. A reminder that the Ξ_{cc}^{++} baryon has a generated mass of $3621.40\,\text{MeV}/c^2$ in this simulated sample.

When the Gaussian plus DSCB model is fitted to the signal MC events using an unbinned extended maximum-likelihood method, the parameters of the model converge on the values listed in Table 5.5. The mass extracted by the fit is different to the generated value by almost five sigma, statistically; the biases in the selection that cause this effect are discussed in the subsequent sub-sections. The other values listed in Table 5.5 are also not the same as those detailed in Table 4.6 for the $\Xi_{cc}^{++} \to \Lambda_c^+K^-\pi^+\pi^+$ analysis, in fact, the mass resolution, σ, is much improved; $(2.84 \pm 0.11)\,\text{MeV}/c^2$ versus $(4.88 \pm 0.12)\,\text{MeV}/c^2$ in favour of the $\Xi_{cc}^{++} \to D^+pK^-\pi^+$ channel. Hence, if a signal of Ξ_{cc}^{++} baryons is observed

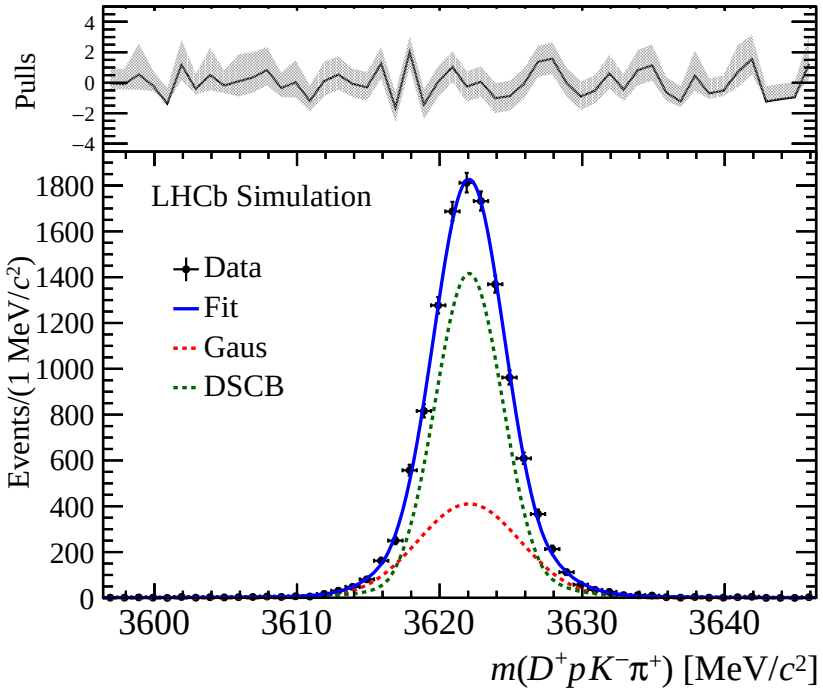

Figure 5.27: Invariant-mass distribution of Ξ_{cc}^{++} candidates in a 2016 MC sample with simulated $\Xi_{cc}^{++} \to D^+pK^-\pi^+$ decays. The fit from a Gaussian plus Double-Sided-Crystal-Ball model is overlaid. The simulated data points are shown in black.

in the RS data set, it is expected that it will correspond to a very distinctive narrow peak in the $m(D^+pK^-\pi^+)$ invariant-mass distribution.

However, the mass resolution of any signal in the RS data is expected to be different from that in simulation because the detector cannot be modelled perfectly. Despite this limitation, the mass resolution should be roughly proportional to the momentum resolution. Thus, the 2.84 MeV/c^2 resolution found in simulation can be used to estimate the resolution expected in the RS data by scaling it by the ratio between the Q-value of the RS decay found in data over that in simulation. The Q-value of a decay is a measure of the energy available to its decay products so for the $\Xi_{cc}^{++} \to D^+pK^-\pi^+$ decay it is defined as

$$Q(\Xi_{cc}^{++}) \equiv \mu(\Xi_{cc}^{++}) - M_{\text{PDG}}(D^+) - M(p) - M(K^-) - M(\pi^+), \tag{5.2}$$

where $\mu(\Xi_{cc}^{++})$ is the mean value of the fit to the $m(D^+pK^-\pi^+)$ distribution, $M_{\text{PDG}}(D^+)$ is the world-average mass of the D^+ meson (1869.63 MeV/c^2) and $M(p)$, $M(K^-)$ and $M(\pi^+)$ are the reconstructed masses of the proton, kaon and pion tracks, respectively. In simulation, the Q-value for the $\Xi_{cc}^{++} \to D^+pK^-\pi^+$ decay is found to be approximately 180 MeV. For comparison, the Q-value for the $\Xi_{cc}^{++} \to \Lambda_c^+K^-\pi^+\pi^+$ decay in data was determined to be much larger at around 560 MeV following the Ξ_{cc}^{++} mass measurement

Table 5.5: The value of the mass model parameters from the fit to the simulated data shown in Figure 5.27.

Parameter	Value from fit
μ	$3622.07 \pm 0.13\,\text{MeV}/c^2$
σ (resolution)	$2.82 \pm 0.11\,\text{MeV}/c^2$
$R = \frac{\sigma(\text{DSCB})}{\sigma(\text{Gaussian})}$	0.67 ± 0.14
f(Gaussian)	0.3 (fixed)
a_L	2.60 ± 0.11
n_L	1.80 ± 0.09
a_R	2.07 ± 0.13
n_R	2.36 ± 0.18
If other parameters are fixed to the values above	
μ	$3622.05 \pm 0.13\,\text{MeV}/c^2$
σ	$2.84 \pm 0.11\,\text{MeV}/c^2$

in that channel.

During the fit to the RS sample, only the mean value of the signal component (μ), and the resolution parameter (σ) of the total fit are free parameters to be determined from the RS data. The parameters that govern the shape of the radiative tails (a_L, n_L, a_R and n_R) and the relative fractions between the Gaussian and DSCB parts in the fit model (R) are fixed to the values listed in Table 5.5.

Background

The invariant-mass distribution of the Ξ_{cc}^{++} candidates in the WS control modes is expected to be shaped similarly to the combinatorial background observed in the RS data set. Therefore, the background model can be determined from fitting to either the WSP or WSM data set.

The invariant-mass distributions of the WS data sets after the full event selection are shown in Figure 5.28. From both data sets, the reconstructed mass of the Ξ_{cc}^{++} candidates can be seen to increase between $3500{-}3800\,\text{MeV}/c^2$. Furthermore, no Ξ_{cc}^{++} candidates with an invariant mass less than $3500\,\text{MeV}/c^2$ are found to pass the event selection, despite the accepted $3300{-}3800\,\text{MeV}/c^2$ search range. A second-order Chebyshev function, with two unfixed parameters, suitably describes the mass distributions in both the WSP and WSM data set. Therefore, this Chebyshev function, with its parameters starting values based on the fit results shown in the right plot of Figure 5.28 is used as the default model for fitting background in the RS data set.[5] Alternative fit models and different mass

[5] The starting values of the background model parameters are based on the fit to the WSM data set, rather than the WSP data set, because it has a greater number of events for a more reliable fit. Although, there is insignificant difference between these values.

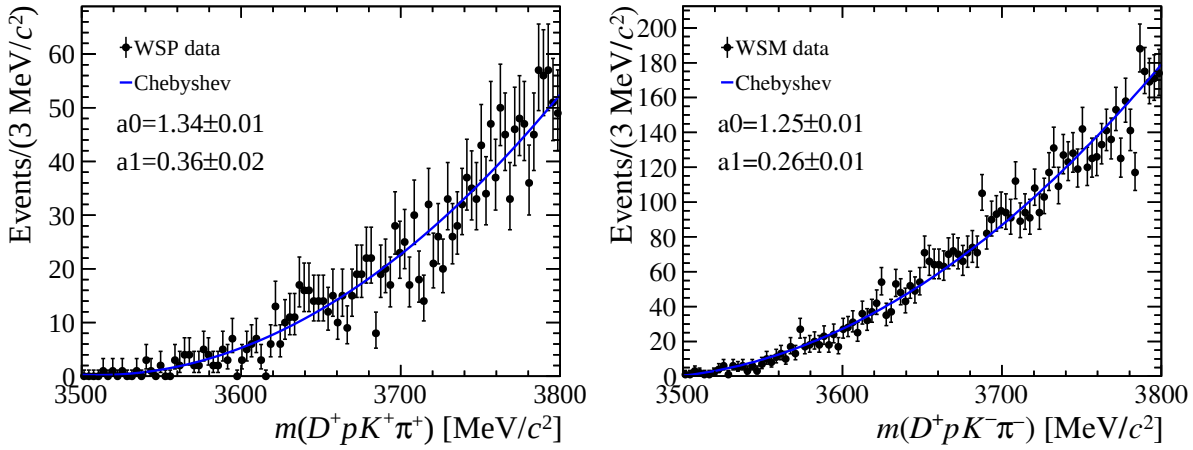

Figure 5.28: Invariant-mass distribution of Ξ_{cc}^{++} candidates in the (left) WSP and (right) WSM data set with a second-order Chebyshev polynomial fit overlaid. The parameters of the Chebyshev function from the fit are shown.

ranges can be used to evaluate the systematic uncertainty associated to this choice of background model after the RS data are examined.

Systematic Uncertainties

The subsequent sections describe the studies into possible sources of systematic uncertainty for the mass measurement of the Ξ_{cc}^{++} baryon. The signal MC sample described in Section 5.2.2, simulated under 2016 data-taking conditions, is used for the majority of these systematic uncertainty studies and the distribution of the $m(D^+pK^-\pi^+)$ quantity is always the variable fitted to extract any mass information, unless stated otherwise.

5.5.2 Momentum Scaling Calibration

A possible source of uncertainty on the mass measurement could arise from the momentum calibration of tracks that was mentioned in Section 5.3.4. The performance of this calibration is discussed in Section 4.5.2, where, as a reminder, it was found that the masses of heavy hadrons agree with their world-average values within ±0.3‰ after the momentum-scaling calibration is applied. This uncertainty on the momentum of the final-state tracks should introduce an associated uncertainty on the invariant mass of the Ξ_{cc}^{++} candidates.

This effect is investigated using a simulated MC sample where the momentum-scaling-correction factor is changed in steps of 0.3‰ using the `DecayTreeFitter` tool. The resulting change in the $m(D^+pK^-\pi^+)$ mass estimator for each Ξ_{cc}^{++} candidate is then plotted as shown in Figure 5.29. The distribution is fitted with a Gaussian plus DSCB function that returns a mean value of $(0.06 \pm 0.01)\,\text{MeV}/c^2$. Therefore, an initial

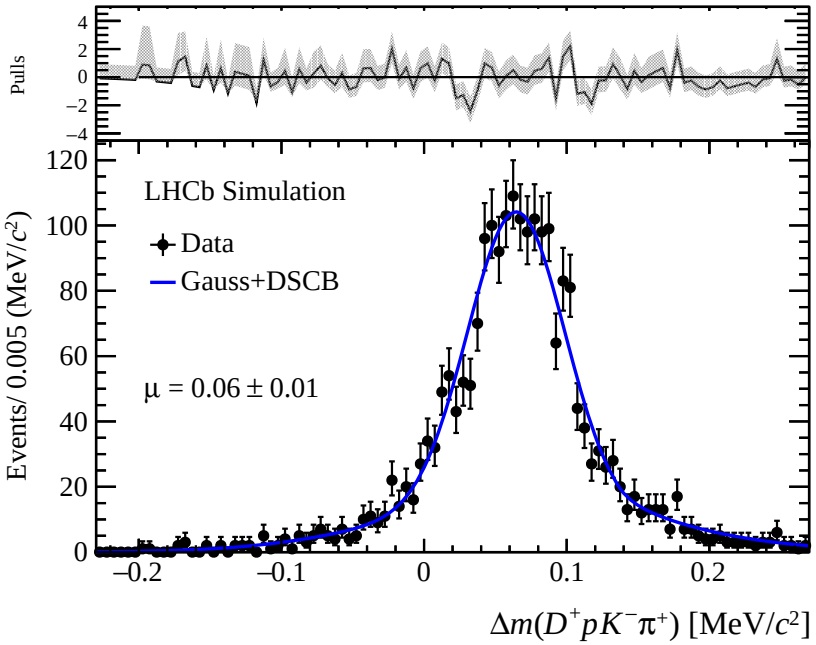

Figure 5.29: The change in the $m(D^+pK^-\pi^+)$ mass estimator for each Ξ_{cc}^{++} candidate from an additional momentum scaling correction of 0.3‰. The fit in blue is given by a Gaussian plus Double-Sided-Crystal-Ball model.

systematic uncertainty of $0.06\,\text{MeV}/c^2$ is associated to the Ξ_{cc}^{++} mass measurement due to the track momentum scaling.[6] This systematic uncertainty is smaller than the equivalent $0.21\,\text{MeV}/c^2$ uncertainty found for the $\Xi_{cc}^{++} \to \Lambda_c^+K^-\pi^+\pi^+$ decay. This is however expected given that the uncertainty of the momentum-scaling correction is proportional to the energy release of the decay, see Appendix A.

5.5.3 Bias of the D^+ Mass

From past analyses using data sets directly extracted from Turbo lines, the LHCb collaboration has observed that the masses of several open-charm hadrons are shifted from their known value due to the selection criteria favouring candidates with longer lifetimes, see Appendix A. This includes the D^+ meson, which is biased by approximately $0.2\,\text{MeV}/c^2$, while, to give a sense of comparison, it is around $0.8\,\text{MeV}/c^2$ for the Λ_c^+ baryon.

According to the results from simulation, the reconstructed Ξ_{cc}^{++} mass is also biased by $0.2\,\text{MeV}/c^2$ because of this bias on the D^+ mass. It can however be reduced if the $m(D^+pK^-\pi^+)$ mass estimator is used to fit the signal instead of the standard $M(D^+pK^-\pi^+)$ mass variable. The difference between the mean of the $m(D^+pK^-\pi^+)$ distribution found from a fit to simulation and the value of the Ξ_{cc}^{++} baryon's mass set in

[6] Since the $0.06\,\text{MeV}/c^2$ value was obtained using simulation, where the kinematic properties of particles might differ to that in data, it needs to be appropriately scaled by the ratio between the energy released in the $\Xi_{cc}^{++} \to D^+pK^-\pi^+$ decay in the RS data and the 180 MeV value found from simulation.

the simulation is found to be only $(-0.05 \pm 0.02)\,\text{MeV}/c^2$. Therefore, the mass estimator defined in Equation 5.1 brings up an improvement in resolution of $0.15\,\text{MeV}/c^2$.

In summary, by using the $m(D^+pK^-\pi^+)$ mass estimator to measure the mass of the Ξ_{cc}^{++} baryon in the RS data, the resolution is expected to be improved but a systematic uncertainty of $0.02\,\text{MeV}/c^2$ should be assigned to the mass measurement to account for a lifetime biasing effect caused by the Turbo processing of the data.

5.5.4 Bias of the Ξ_{cc}^{++} Mass

The mass of the observed Ξ_{cc}^{++} baryon is also expected to be biased from lifetime requirements used in the offline selection. The trigger lines do not use any lifetime related variables in their selection criteria, except from the DIRA variable, but the offline selections do make use of lifetime information on the Ξ_{cc}^{++} baryon.

To check if the offline selections bias the observed mass of the Ξ_{cc}^{++} baryon, the MC sample is compared with and without any requirements related to the Ξ_{cc}^{++} baryon applied. The $m(D^+pK^-\pi^+)$ mass variable is fitted for both cases and a difference of $(0.35 \pm 0.06)\,\text{MeV}/c^2$ is found for a simulated sample with a Ξ_{cc}^{++} lifetime of 256 fs. The MC sample is then weighted to a range of Ξ_{cc}^{++} lifetimes that reflect its measured uncertainty. The difference between the fitted mean from the $m(D^+pK^-\pi^+)$ distribution and the generated mass of the MC sample, as a function of the lifetime, is plotted in Figure 5.30. By fitting a second-order polynomial to the data points in Figure 5.30, the largest variation of this mass difference quantity from the uncertainty at the nominal 256 ps lifetime is found to be $0.07\,\text{MeV}/c^2$ at 236 ps.

In the end, $0.35\,\text{MeV}/c^2$ is used to correct the measured Ξ_{cc}^{++} mass that has an uncertainty of $0.06\,\text{MeV}/c^2$ due to the limited number of events in the simulation. This $0.06\,\text{MeV}/c^2$ systematic uncertainty is assigned to the mass measurement to account for biases in the offline selection. It also has an additional uncertainty of $0.07\,\text{MeV}/c^2$ due to its lifetime dependency.

5.5.5 Uncertainty on the D^+ Mass

The world-average mass of the D^+ meson has an uncertainty of $0.09\,\text{MeV}/c^2$ [1]. For comparison, the uncertainty on the mass of the Λ_c^+ baryon is greater at $0.14\,\text{MeV}/c^2$ [1].

This uncertainty on the mass of the D^+ meson will propagate through to the measurement of the Ξ_{cc}^{++} baryon's mass. Using the `DecayTreeFitter` tool, the mass of the D^+ meson is set to values between $1869.27-1689.99\,\text{MeV}/c^2$ (approximately ± 3 standard deviations) in a simulation of $\Xi_{cc}^{++} \to D^+pK^-\pi^+$ decays, after which the corresponding change in mass of the Ξ_{cc}^{++} candidates is examined. The relationship between the change of the D^+ mass and the Ξ_{cc}^{++} mass per candidate is found to be almost exactly linear,

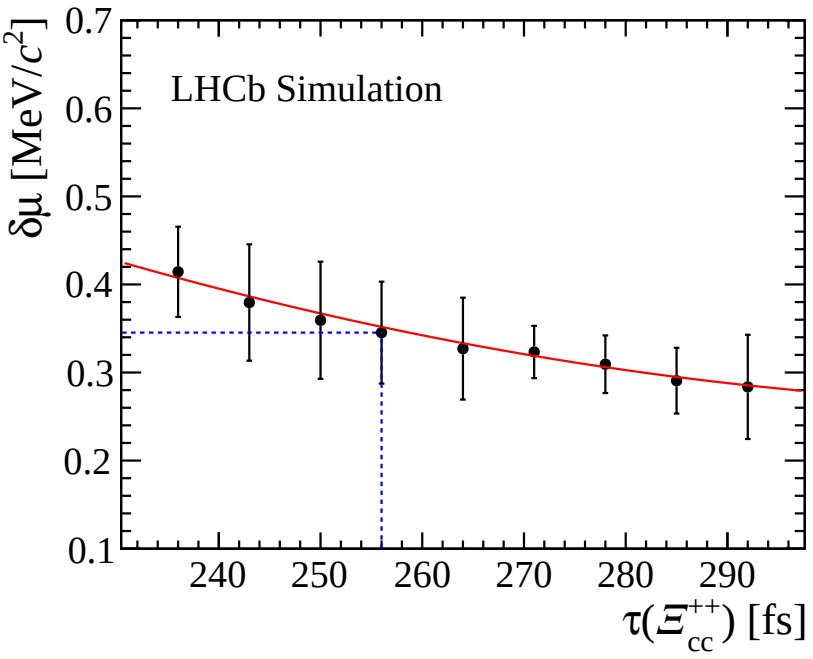

Figure 5.30: The bias of the measured mass as a function of the lifetime of the Ξ_{cc}^{++} baryon in simulation for values between 236 fs to 292 fs. The fit shown in red is a second-order polynomial. The dotted blue lines indicates the measured lifetime of the Ξ_{cc}^{++} baryons and the corresponding value of the bias.

as can be seen from fit parameters given in Figure 5.31. The mass variables plotted are the $M(D^+pK^-\pi^+)$ and $M([K^-\pi^+\pi^+]_{D^+})$ quantities. Therefore, with an uncertainty of $0.09\,\text{MeV}/c^2$ on the mass of D^+ meson, a systematic uncertainty of $0.09\,\text{MeV}/c^2$ is assigned to the measured mass of the Ξ_{cc}^{++} baryon in the $\Xi_{cc}^{++} \to D^+pK^-\pi^+$ channel.

5.5.6 Final State Radiation

In $\Xi_{cc}^{++} \to D^+pK^-\pi^+$ decays, low energy photons are expected to be produced along with the kaons, pions and proton. However, the trigger only uses charged tracks to reconstruct the Ξ_{cc}^{++} candidates. Therefore, the invariant-mass of the Ξ_{cc}^{++} candidates is biased towards smaller values due to the loss of energy carried away by these untracked photons. The effect of this final-state radiation is studied using simulated MC events produced by the GENXICC generator where photons, enabled by the PHOTOS software package [150], are also allowed in the final-state. The methodology, described next, for estimating the uncertainty from final-state radiation was adopted from similar studies used by the LHCb collaboration when measuring the mass difference between the D^+ and D^0 states [176].

The momentum values of all final-state tracks in the $\Xi_{cc}^{++} \to D^+pK^-\pi^+$ decay are firstly smeared to simulate the effect of the tracking resolution. This is done by varying the magnitude of the momentum by a value randomly sampled from a Gaussian distribution,

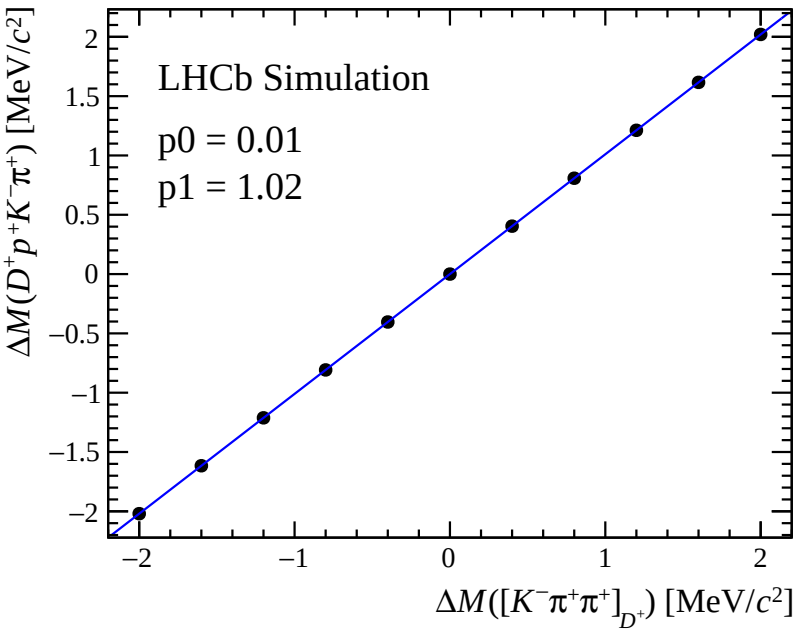

Figure 5.31: The change of the measured Ξ_{cc}^{++} mass in simulation as function of the change in mass of the D^+ meson. The distribution is fitted with a linear function.

which has a zero mean value and a standard deviation equal to the scaled value of the momentum resolution obtained by the LHCb detector. As mentioned in Section 2.3.3, the relative uncertainty on the momentum resolution ($\delta p/p$) of a track passing the LHCb detector varies from 0.5% to 1.0% depending on its momentum, p. The directions of the tracks through the LHCb detector are then also smeared, independently from the magnitude of the momentum, by again sampling from a Gaussian distribution with mean of zero. However, this time the resolution of this Gaussian function is a function of the momentum of the track, then scaled by an appropriate factor.[7] By choosing different scale factors, different sizes of resolution effects can be created. For instance, when the scale factor is set to unity, the nominal resolution at LHCb is achieved.

The masses of the Ξ_{cc}^{++} candidates are then calculated from the smeared momentum of its daughter tracks using basic relativistic kinematic laws. The distribution of the $m(D^+ p K^- \pi^+)$ variable for the Ξ_{cc}^{++} candidates after a select level of smearing, which results in an effective resolution of 2.5 MeV/c^2, is shown in the left plot of Figure 5.32. The mass distribution is fitted with the default mass model, a Gaussian plus DSCB function, to obtain a mean mass value. In the right plot of Figure 5.32, the bias on the mass of the Ξ_{cc}^{++} candidates is plotted against the resolution width obtained by the smearing procedure. The mass bias can be seen to be quite stable over the entire studied resolution range. The data points are fitted with a linear function, which estimates a mass bias of

[7]The formula for the resolution as a function of momentum is taken from the `RapidSim` package [177].

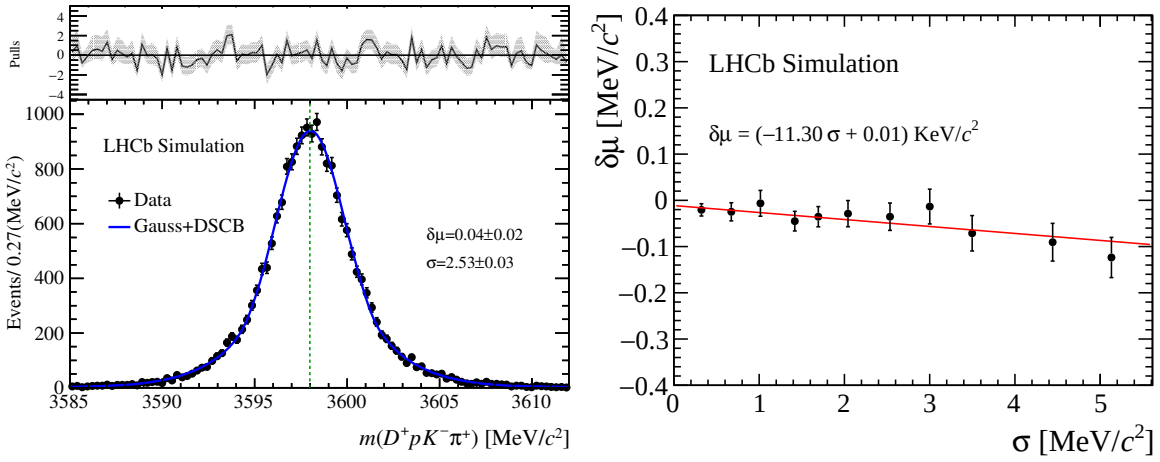

Figure 5.32: (Left) An example of a smeared Ξ_{cc}^{++} mass distribution in simulation where the dotted-green-vertical line represents the generated mass ($3597.8\,\text{MeV}/c^2$) of the MC sample and (right) the fitted mean mass of the Ξ_{cc}^{++} candidates in simulation as a function of the mass resolution.

$(+0.03 \pm 0.01)\,\text{MeV}/c^2$ for $2.8\,\text{MeV}/c^2$, the signal mass resolution found from simulated $\Xi_{cc}^{++} \to D^+pK^-\pi^+$ decays in Section 5.5.1.

In conclusion, a correction of $0.03\,\text{MeV}/c^2$ will be applied to the measured mass of the Ξ_{cc}^{++} baryon to account for the loss of final-state radiation in the RS data. The systematic uncertainly associated to this correction is $0.01\,\text{MeV}/c^2$, which is very insignificant.

5.5.7 Stability with respect to MVA Selection

As discussed in Section 5.5.4, the measured mass of the Ξ_{cc}^{++} baryon in the RS data is biased due to requirements in the offline selection exploiting reconstructed decay-time information; this includes the multivariate selection. Therefore, the change in the mass of the Ξ_{cc}^{++} candidates after varying the requirement on the response of the MLP classifier is also examined in simulation. A reminder that the requirement fixed in the event selection is for the Ξ_{cc}^{++} candidates to have a MLP response value greater than 0.89.

The change in the mass obtained using the default fit to the $m(D^+pK^-\pi^+)$ distribution, is shown in Figure 5.33, as a function of the multivariate requirement imposed on the Ξ_{cc}^{++} candidates. The number of MC events passing the multivariate selection ranges between $\pm 15\%$ when the response threshold is varied between $0.85-0.91$. The mean value from the fit is also found to be very stable, with a variation of only $\pm 0.06\,\text{MeV}/c^2$ after considering its associated statistical uncertainty. Half of this variation, $0.03\,\text{MeV}/c^2$, is taken as the systematic uncertainty associated to the multivariate selection.

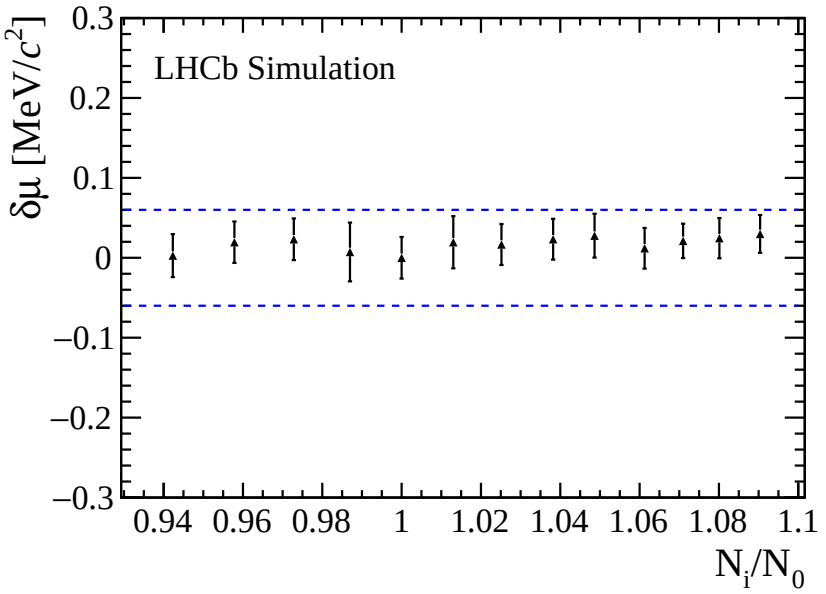

Figure 5.33: The change in the fitted Ξ_{cc}^{++} mass, μ, when the MLP response requirement is varied between 0.85 and 0.91. The x-axis represents the number of signal events, N_i, relative to that passing the nominal multivariate requirement, N_0. The y-axis shows the change of μ with respect to the nominal value. The blue-dotted-lines represent a range of $\pm 0.06\,\mathrm{MeV}/c^2$ around the zero value.

Table 5.6: Systematic uncertainties of the mass measurement of the Ξ_{cc}^{++} baryon in the $\Xi_{cc}^{++} \to D^+ p K^- \pi^+$ channel.

Source	Value (MeV/c^2)
Momentum scaling calibration	0.07
D^+ bias due to selections	0.05
Ξ_{cc}^{++} bias due to selections	0.06
Ξ_{cc}^{++} lifetime	0.07
Final-state radiation	0.01
Uncertainty of D^+ mass	0.09
Multivariate selection stability	0.03
Total	0.17

Summary of Systematic Uncertainties

An overview of all the systematic uncertainties discussed in this section along with their source are listed in Table 5.6. A total systematic uncertainty of $0.17\,\mathrm{MeV}/c^2$ is found after taking the sum in quadrature of the individual uncertainties that are considered uncorrelated. This is smaller than the $0.31\,\mathrm{MeV}/c^2$ systematic uncertainty found for the mass measurement in the $\Xi_{cc}^{++} \to \Lambda_c^+ K^- \pi^+ \pi^+$ channel. No systematic uncertainty dominates but the effects from final-state radiation is negligible. The effects of the choice of fit model on the mass measurement are investigated after the RS data is examined.

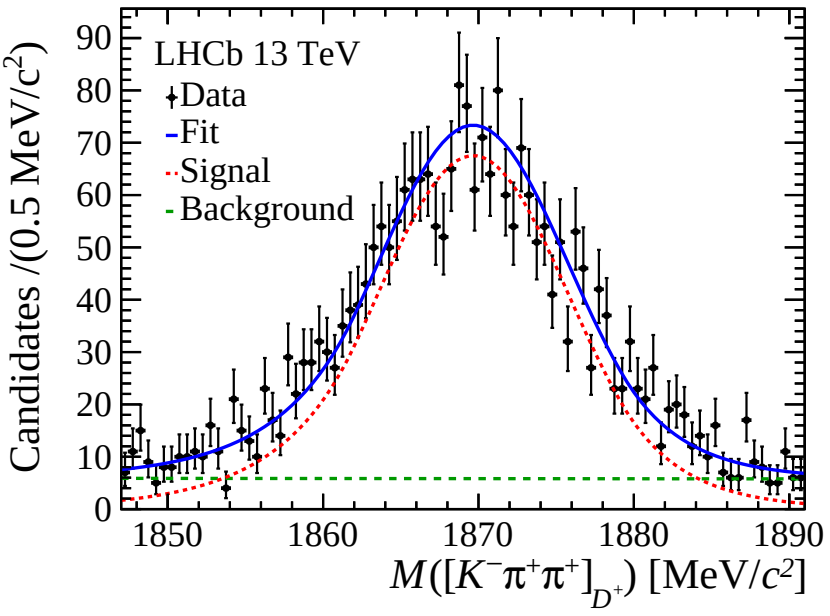

Figure 5.34: Invariant-mass distribution of the D^+ candidates after the analysis selection. The black points represent data. Overlaid is the fit to data which is indicated by the continuous (blue) line with the individual signal and background components of the fit represented by the dotted (red) line and dashed (green) line, respectively.

5.6 Mass Distributions

Having completed all necessary studies on backgrounds, chosen the mass models to describe any signal observed and decided upon all aspects of the candidate selection for the mass measurement, based on simulation and the control modes, the RS data within the mass region $m(D^+pK^-\pi^+) \in [3300, 3800]\,\text{MeV}/c^2 \cap M([K^-\pi^+\pi^+]_{D^+}) \in [1849, 1891]\,\text{MeV}/c^2$ are examined. For simplicity, the right-signed data will just be referred to as data where appropriate in this section.

The invariant-mass distribution of $M([K^-\pi^+\pi^+]_{D^+})$ for D^+ candidates after the event selection, including the L0 requirement is shown in Figure 5.34. The Gaussian plus DSCB model, which was originally designed to measure the Ξ_{cc}^{++} signal, see Section 5.5.1, is used to model the signal component and a linear function is used to fit the background contribution. Apart from the yield, all parameters describing the signal model are fixed to values obtained from a simulated sample of $\Xi_{cc}^{++} \to D^+ pK^-\pi^+$ decays, while all the parameters in the background model are free. The mass spectrum contains 2697 D^+ candidates, with a purity of around 80% expected, based on the results of the fit shown in Figure 5.34. This demonstrates the event selection described in Section 5.3. can at least select $D^+ \to K^-\pi^+\pi^+$ decays displaced from the pp interaction point.

The invariant-mass distribution of the Ξ_{cc}^{++} candidates in the 2016 data and in the WSP and WSM data sets, after the event selection, apart from L0 trigger requirement,

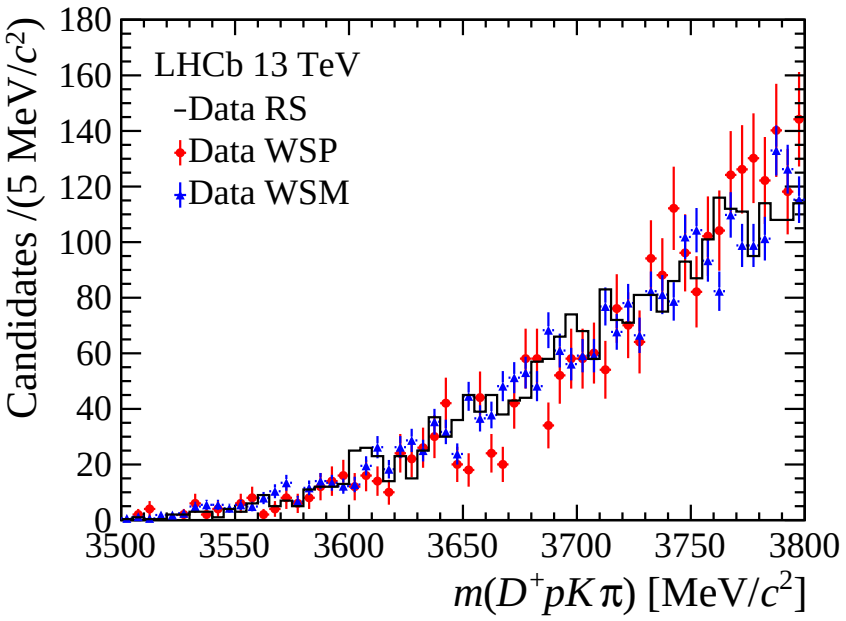

Figure 5.35: Invariant-mass distributions of right-sign (black)$D^+pK^-\pi+$, wrong-sign-plus (red) $D^+pK^+\pi^+$ and wrong-sign-minus (blue) $D^+pK^-\pi^-$ data combinations are shown. The control samples have been normalised to the right-sign sample.

is shown in Figure 5.35. The mass range in shown is between $3500-3800\,\text{MeV}/c^2$, which corresponds to the range of masses that are populated following the event selection. In fact, only one Ξ_{cc}^{++} candidate is observed in the mass range from the kinematic threshold of the $\Xi_{cc}^{++} \to D^+pK^-\pi^+$ decay ($3441\,\text{MeV}/c^2$) to $3500\,\text{MeV}/c^2$. It is clear that no excess of event is observed around $3620\,\text{MeV}/c^2$ in the data where a Ξ_{cc}^{++} signal would be expected, given the results in the $\Xi_{cc}^{++} \to \Lambda_c^+K^-\pi^+\pi^+$ analysis. In fact, all samples have similarly smoothly shaped distributions across the entire mass range.

As mentioned previously, the L0 hardware trigger was to be decided after examining data. Following the initial results shown in Figure 5.35, requirement 2, as defined in Section 5.3.1, is chosen as the L0 selection criteria for this analysis. The $m(D^+pK^-\pi^+)$ distribution in data with the L0 requirment imposed is shown in Figure 5.36. The mass distribution in data is well described by the second-order Chebyshev function, which was designed to model only background in the RS channel. Again it is obvious that there is no peak around the region indicated by the vertical dashed lines, where in Figure 4.21 there was a significant peak. The shape of the combinatorial background in the $\Xi_{cc}^{++} \to D^+pK^-\pi^+$ channel compared to the $\Xi_{cc}^{++} \to \Lambda_c^+K^-\pi^+\pi^+$ decay mode is also very different; likely a result of the different energy releases from each decay.

The local p-value was then calculated as a function of the invariant mass of the Ξ_{cc}^{++} candidate in the $\Xi_{cc}^{++} \to D^+pK^-\pi^+$ data [175] by a colleague of the PhD candidate. The resulting distribution is shown in Figure 5.37. The local p-value is defined

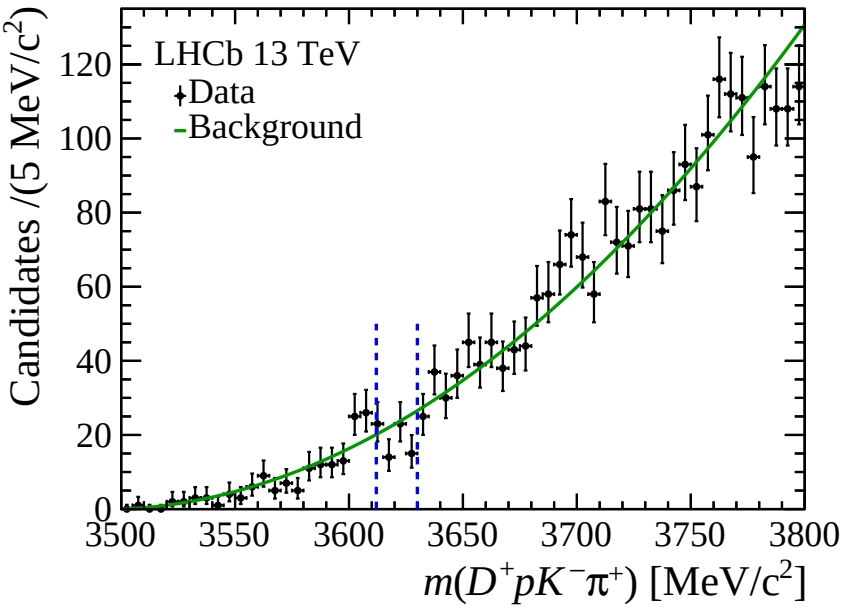

Figure 5.36: Invariant-mass distribution of the Ξ_{cc}^{++} candidates from data passing the selection, with the fit result overlaid. The black points represent data. The two vertical parallel dashed (blue) lines define the region where the signal is expected and the continuous (green) line represents the combinatorial background.

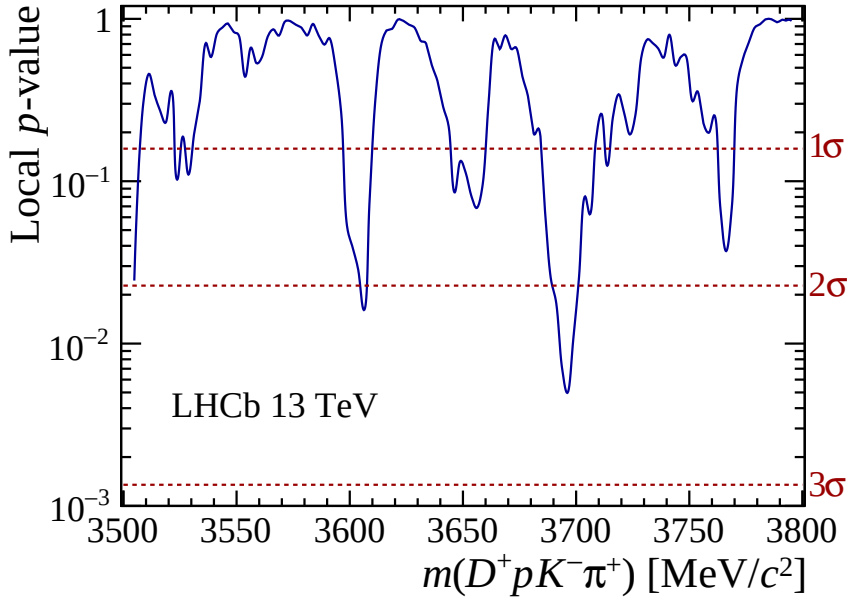

Figure 5.37: The local p-value expressing the compatibility of the mass distribution of the $\Xi_{cc}^{++} \to D^+pK^-\pi^+$ data with the background-only hypothesis. The horizontal dashed (red) lines indicate p-values of 1, 2 and 3σ local significance [175].

as the probability of observing data that is less compatible with the background-only hypothesis than the data set. The likelihoods are evaluated with Poisson statistics using the predicted number of background candidates and the observed number of signal candidates in regions of $\pm 3\sigma$ around each hypothetical mass, where $\sigma = 2.8\,\text{MeV}/c^2$ is the Ξ_{cc}^{++} mass resolution determined from simulated $\Xi_{cc}^{++} \to D^+pK^-\pi^+$ decays. The global p-value, including the look-elsewhere effect in the mass range 3500–3800 MeV/c^2, is 26% and only one Ξ_{cc}^{++} candidate is observed in the mass range from the kinematic threshold of 3441 MeV/c^2 to 3500 MeV/c^2. Hence, no significant signal is observed in the mass range from the kinematic threshold to 3800 MeV/c^2. Additionally, there is no excess of candidates near the mass of 3520 MeV/c^2, where the hypothetical isospin partner of the state that was reported by the SELEX collaboration would be expected, see Figure 1.8.

An upper limit on the ratio of branching fractions between the $\Xi_{cc}^{++} \to D^+pK^-\pi^+$ and $\Xi_{cc}^{++} \to \Lambda_c^+K^-\pi^+\pi^+$ decay modes is set in Section 5.1 to determine the suppression of the $\Xi_{cc}^{++} \to D^+pK^-\pi^+$ branching fraction. Since no evidence of $\Xi_{cc}^{++} \to D^+pK^-\pi^+$ decays is observed, this hints at a low branching fraction for the decay mode.

5.7 Ratio of Branching Fractions

In this section, the methodology for determining the upper limit on the ratio of branching fractions measurement between the $\Xi_{cc}^{++} \to \Lambda_c^+K^-\pi^+\pi^+$ and the $\Xi_{cc}^{++} \to D^+pK^-\pi^+$ decay modes in the 2016 data is outlined. Like in Section 5.6, the RS data is now referred to as data to ease reading and the $\Xi_{cc}^{++} \to \Lambda_c^+K^-\pi^+\pi^+$ decay is also interchangeably referred to as the normalisation channel.

The ratio of branching fractions between the Ξ_{cc}^{++} decay modes, $\mathcal{R}$, is determined as

$$\begin{aligned}
\mathcal{R} &= \frac{\mathcal{B}(\Xi_{cc}^{++} \to D^+pK^-\pi^+)}{\mathcal{B}(\Xi_{cc}^{++} \to \Lambda_c^+K^-\pi^+\pi^+)} \\
&= \frac{\mathcal{B}(\Xi_{cc}^{++} \to D^+(\to K^-\pi^+\pi^+)pK^-\pi^+)}{\mathcal{B}(\Xi_{cc}^{++} \to \Lambda_c^+(\to pK^-\pi^+)K^-\pi^+\pi^+)} \times \frac{\mathcal{B}(\Lambda_c^+ \to pK^-\pi^+)}{\mathcal{B}(D^+ \to K^-\pi^+\pi^+)} \\
&= \frac{N(D^+pK^-\pi^+)}{N(\Lambda_c^+K^-\pi^+\pi^+)} \times \frac{\varepsilon(\Lambda_c^+K^-\pi^+\pi^+)}{\varepsilon(D^+pK^-\pi^+)} \times \frac{\mathcal{L}_{\text{Int}}(\Lambda_c^+K^-\pi^+\pi^+)}{\mathcal{L}_{\text{Int}}(D^+pK^-\pi^+)} \times \frac{\mathcal{B}(\Lambda_c^+ \to pK^-\pi^+)}{\mathcal{B}(D^+ \to K^-\pi^+\pi^+)} \\
&= \alpha_s \times N(D^+pK^-\pi^+), \qquad (5.3)
\end{aligned}$$

where N refers to the yield of the Ξ_{cc}^{++} decay modes, $\mathcal{B}$ denotes a branching fraction, ε means the efficiency of selecting the Ξ_{cc}^{++} decay mode and $\mathcal{L}_{\text{Int}}$ stands for the integrated luminosity of the data set used to search for the Ξ_{cc}^{++} decay mode. As mentioned in Section 5.2, the 2016 data sets used in both the Ξ_{cc}^{++} search analyses correspond to the same value of integrated luminosity, hence the luminosity terms cancel out in $\mathcal{R}$. The

single-event-sensitivity parameter, α_s, is introduced for convenience and is defined as

$$\alpha_s = \frac{\varepsilon(\Lambda_c^+ K^-\pi^+\pi^+)}{N(\Lambda_c^+ K^-\pi^+\pi^+)\,\varepsilon(D^+ pK^-\pi^+)} \times \frac{\mathcal{B}(\Lambda_c^+ \to p\,K^-\pi^+)}{\mathcal{B}(D^+ \to K^-\pi^+\pi^+)}, \tag{5.4}$$

such that it encapsulates the ratio of efficiencies and the signal yield of the normalisation channel. The branching fractions of the intermediate open-charm hadron decays are taken to be their world-average value:

$\mathcal{B}(D^+ \to K^-\pi^+\pi^+) = (8.98 \pm 0.28)\%$;

$\mathcal{B}(\Lambda_c^+ \to pK^-\pi^+) = (6.23 \pm 0.33)\%$,

where it can be seen that $\mathcal{B}(D^+ \to K^-\pi^+\pi^+)$ is larger than $\mathcal{B}(\Lambda_c^+ \to pK^-\pi^+)$ [1].

5.7.1 Normalisation Yield

The yield in the normalisation channel, $N(\Lambda_c^+ K^-\pi^+\pi^+)$, is obtained from the same fit described in Section 4.5 and using the same Run II data set detailed in Section 4.2. The only difference is that the L0 trigger requirement stated in Section 5.6 is now applied to these data. The $m(\Lambda_c^+ K^-\pi^+\pi^+)$ mass distribution in the 2016 data after this extra hardware-trigger requirement is applied is shown in Figure 5.38. The signal yield is found to be 184 ± 29 according to the results of the fit.

5.7.2 Signal Remodelling

As highlighted in Section 5.2.2, differences were found between the kinematic properties of the signal produced in simulation and that measured in the $\Xi_{cc}^{++} \to \Lambda_c^+ K^-\pi^+\pi^+$ data. The difference in the p_T distributions from data and simulation, shown in Figure 5.2, is attributed to the imperfect modelling of Ξ_{cc}^{++} signal by the GENXICC generator, since the offline selection is understood not to cause any kinematic biases. Therefore, a weighting procedure is adopted to make the p_T distribution of Ξ_{cc}^{++} candidates from simulation align with data, before these simulated samples are used to help calculate selection efficiencies in Section 5.7.3.

Correction factors, which are a function of the p_T of the Ξ_{cc}^{++} candidates, are applied to simulated MC events. Since there was no evidence of $\Xi_{cc}^{++} \to D^+ pK^-\pi^+$ decays in the 2016 data, $\Xi_{cc}^{++} \to D^+ pK^-\pi^+$ MC events are weighted against the signal observed in the $\Xi_{cc}^{++} \to \Lambda_c^+ K^-\pi^+\pi^+$ data, as are the $\Xi_{cc}^{++} \to \Lambda_c^+ K^-\pi^+\pi^+$ MC events. A comparison between the p_T distribution of the Ξ_{cc}^{++} candidates in the $\Xi_{cc}^{++} \to \Lambda_c^+ K^-\pi^+\pi^+$ data and the signal $\Xi_{cc}^{++} \to D^+ pK^-\pi^+$ MC events is shown in Figure 5.39. The final p_T correction factors applied to simulated Ξ_{cc}^{++} decays are shown in Figure 5.40 where the p_T binning scheme is $[4.0 : 8.8 : 11.0 : 13.2 : 17.4 : 35.0]$ GeV/c for both decay modes.

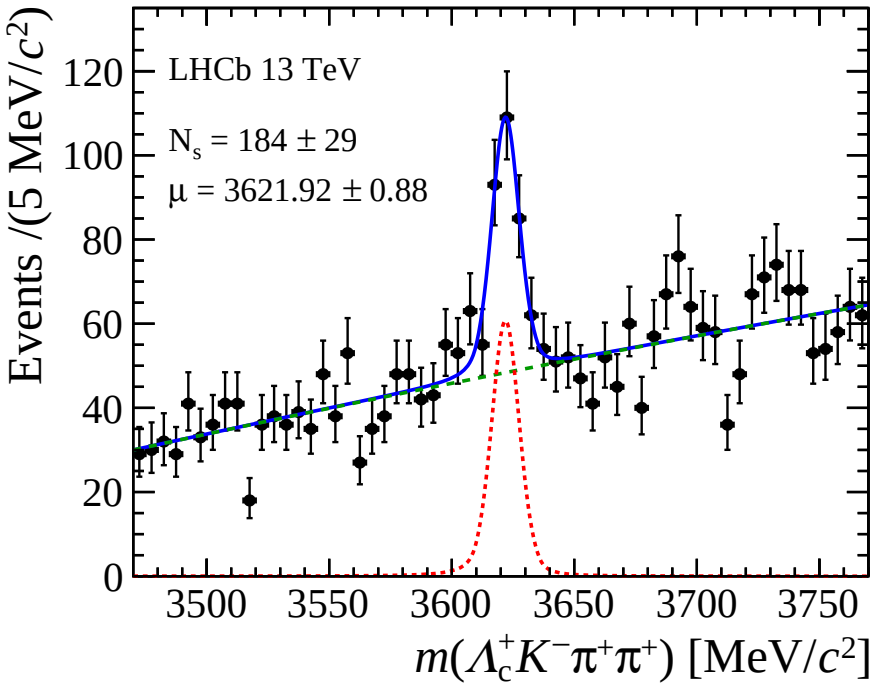

Figure 5.38: Invariant-mass distribution of the Ξ_{cc}^{++} candidates in 2016 data after the selection described in Section 4.3 and an additional L0 trigger requirement is applied. The same fit model as shown in Figure 4.21 is overlaid.

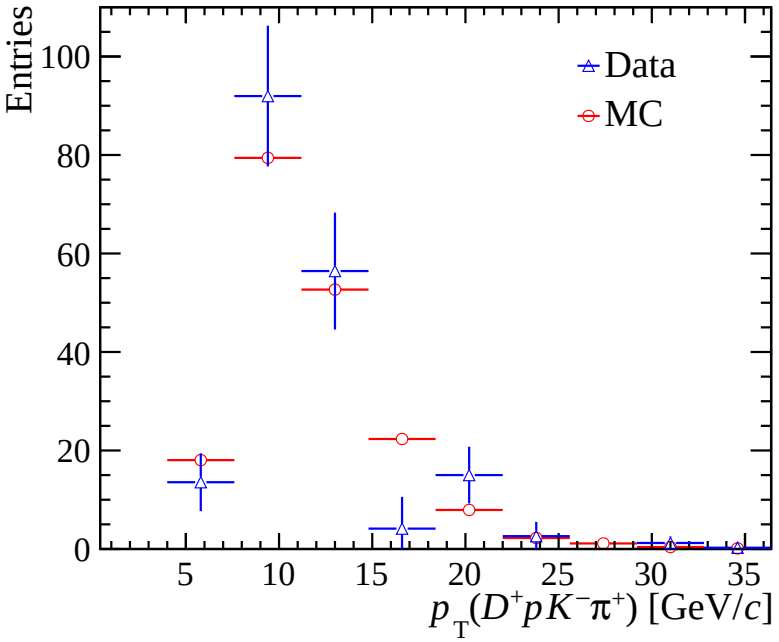

Figure 5.39: Comparison of the Ξ_{cc}^{++} p_T distribution in the background-subtracted $\Xi_{cc}^{++} \to \Lambda_c^+ K^- \pi^+ \pi^+$ data and a simulation of $\Xi_{cc}^{++} \to D^+ p K^- \pi^+$ decays.

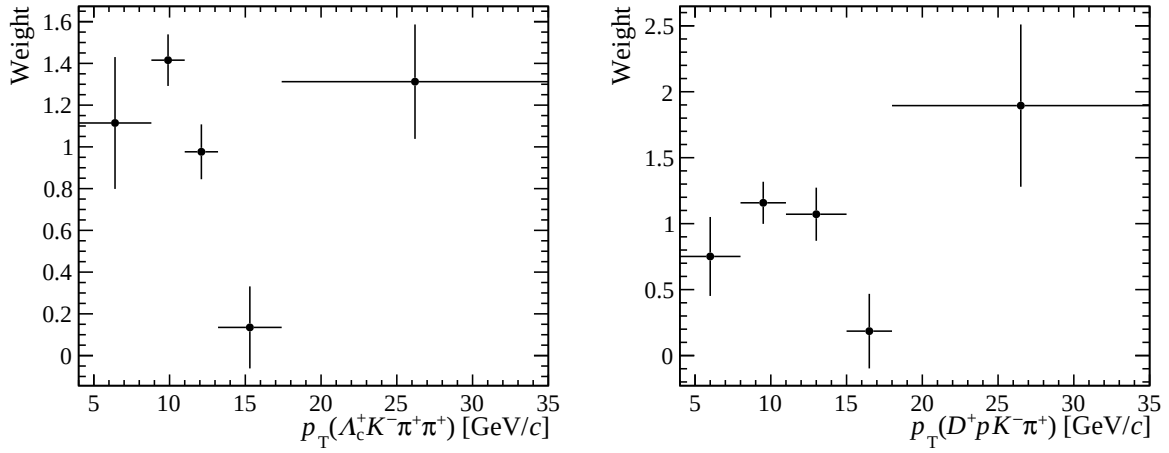

Figure 5.40: The Ξ_{cc}^{++} p_T (x-axis) correction factors (y-axis) between data and MC for the (left) $\Xi_{cc}^{++} \to \Lambda_c^+K^-\pi^+\pi^+$ channel and (right) $\Xi_{cc}^{++} \to D^+pK^-\pi^+$ channel.

5.7.3 Efficiencies

To set an upper limit on the ratio $\mathcal{R}$, it is necessary to evaluate the ratio of efficiencies between the $\Xi_{cc}^{++} \to D^+pK^-\pi^+$ and $\Xi_{cc}^{++} \to \Lambda_c^+K^-\pi^+\pi^+$ decay modes. The efficiency ratio may be factorised as

$$\frac{\varepsilon(\Lambda_c^+K^-\pi^+\pi^+)}{\varepsilon(D^+pK^-\pi^+)} = \frac{\varepsilon^{\text{Acc}}_{\Lambda_c^+K^-\pi^+\pi^+}}{\varepsilon^{\text{Acc}}_{D^+pK^-\pi^+}} \frac{\varepsilon^{\text{Sel|Acc}}_{\Lambda_c^+K^-\pi^+\pi^+}}{\varepsilon^{\text{Sel|Acc}}_{D^+pK^-\pi^+}} \frac{\varepsilon^{\text{PID|Sel}}_{\Lambda_c^+K^-\pi^+\pi^+}}{\varepsilon^{\text{PID|Sel}}_{D^+pK^-\pi^+}} \frac{\varepsilon^{\text{L0|PID}}_{\Lambda_c^+K^-\pi^+\pi^+}}{\varepsilon^{\text{L0|PID}}_{D^+pK^-\pi^+}} \frac{\varepsilon^{\text{HLT|L0}}_{\Lambda_c^+K^-\pi^+\pi^+}}{\varepsilon^{\text{HLT|L0}}_{D^+pK^-\pi^+}}, \tag{5.5}$$

where the efficiencies are evaluated for the geometric acceptance (Acc), the reconstruction and selection excluding particle-identification requirements (Sel), the particle-identification requirements (PID), the software-trigger requirements (L0) and first-level hardware-trigger requirements (HLT1). The efficiency of the HLT2 requirements are contained within the reconstruction and selection efficiency since both the Ξ_{cc}^{++} searches described in this thesis are Turbo analyses. Each factor is the efficiency relative to all previous steps in the order given above. The individual efficiencies are evaluated with simulated Ξ_{cc}^{++} decays, except for ones related to PID, which are derived from data using the `PIDCalib` [161].

The efficiencies are also corrected for known differences between simulation and data by applying the p_T-weighting factors, discussed in Section 5.7.2, to the MC events. The only exception is the geometric acceptance which is directly calculated by Gauss [145]. The efficiencies are determined assuming a uniform distribution of the decay products in the phase space for both decay channels. However, recall that in the $\Xi_{cc}^{++} \to \Lambda_c^+K^-\pi^+\pi^+$ 2016 data, there was clear evidence of $\Sigma_c(2455)^{++} \to \Lambda_c^+\pi^+$ resonant decays, as well as hints of the $\Sigma_c(2520)^{++}$ and K^{*0} resonances. The reason a global efficiency is calculated, even though the resonant structure in data is not modelled in the used simulated samples, is discussed in Appendix D.

Acceptance Efficiency

In Section 5.3.3, the geometric acceptance for $\Xi_{cc}^{++} \to D^+ p K^- \pi^+$ decays at the LHCb detector was established as 0.0989 ± 0.0003. For the $\Xi_{cc}^{++} \to \Lambda_c^+ K^- \pi^+ \pi^+$ channel, this efficiency was calculated in the exact same way *i.e.* based on the number of MC events passing selections detailed in Section 4.3.3; it is found to be 0.0987 ± 0.0002. Therefore, the acceptance efficiencies for both decay modes are found to be almost the same. This is expected given their topologies are similar and they both have six final-state tracks.

Reconstruction and Selection Efficiency

The reconstruction and selection efficiency is evaluated as the number of MC events passing the dedicated HLT2 trigger and offline selections described in Section 5.3 and Section 4.3 for the $\Xi_{cc}^{++} \to D^+ p K^- \pi^+$ and $\Xi_{cc}^{++} \to \Lambda_c^+ K^- \pi^+ \pi^+$ decay mode, respectively. The particle identification requirements are however not included.

The selection and reconstruction efficiency is measured to be $(0.74 \pm 0.02) \times 10^{-3}$ for the $\Xi_{cc}^{++} \to \Lambda_c^+ K^- \pi^+ \pi^+$ decay mode, while for the $\Xi_{cc}^{++} \to D^+ p K^- \pi^+$ channel it is found to be $(1.59 \pm 0.01) \times 10^{-3}$; approximately twice that of the $\Xi_{cc}^{++} \to \Lambda_c^+ K^- \pi^+ \pi^+$ decay. This is due to the decay times of the D^+ candidates in $\Xi_{cc}^{++} \to D^+ p K^- \pi^+$ decays being longer, on average, than the Λ_c^+ candidates in $\Xi_{cc}^{++} \to \Lambda_c^+ K^- \pi^+ \pi^+$ decays, which leads to better suppression of signal and combinatorial background from the primary vertex.

Particle identification efficiency

The particle identification efficiency, is defined as the number of MC events passing the PID requirements used throughout the entire candidate selection, which was developed independently for both Ξ_{cc}^{++} decay modes. Since PID discriminants are not perfectly modelled in simulation, signal MC events cannot be directly used to calculate this efficiency. Instead, the signal MC events passing the selection and reconstruction requirements are first calibrated against data using `PIDCalib`, which then returns the appropriate efficiency. A more thorough explanation of this procedure is presented in Appendix C.

`PIDCalib` determines the PID efficiency to be 0.714 ± 0.013 and 0.706 ± 0.001 for the $\Xi_{cc}^{++} \to \Lambda_c^+ K^- \pi^+ \pi^+$ and $\Xi_{cc}^{++} \to D^+ p K^- \pi^+$ channels, respectively. The uncertainties quoted are statistical only, with the difference in the sizes of the uncertainties just a reflection of the difference in the number of MC events generated for each decay mode. These efficiencies are also very close in value, which is expected given the loose and similar nature of the particle identification requirements imposed on each decay mode.

Hardware trigger efficiency

The chosen L0 requirement, decided upon in Section 5.3.2, means only candidates that are triggered independently of the final-state tracks of the Ξ_{cc}^{++} candidate are to be used in the branching fraction ratio measurement. In other words, only events that passed the hardware trigger based on information from the muon and calorimeter systems but that are not part of the reconstructed Ξ_{cc}^{++} event are kept. By the definition of the L0 requirement, the ratio of these efficiencies is equal to one if the kinematic distributions of the Ξ_{cc}^{++} candidate in the $\Xi_{cc}^{++} \to D^+ p K^- \pi^+$ and $\Xi_{cc}^{++} \to \Lambda_c^+ K^- \pi^+ \pi^+$ decay modes are identical. Therefore, the ratio of these efficiencies is not derived from MC events but is simply assumed to be one. However, these efficiencies can be different if the respective selection requirements of the $\Xi_{cc}^{++} \to D^+ p K^- \pi^+$ and $\Xi_{cc}^{++} \to \Lambda_c^+ K^- \pi^+ \pi^+$ analyses select different kinematic regions of the Ξ_{cc}^{++} candidates. Hence, a sizeable systematic uncertainty is also assigned to this ratio of efficiencies, which is explained more in Section 5.7.4.

Software Trigger Efficiency

Finally, the efficiency of the HLT1 requirements is calculated directly from the MC events passing the requirements laid out in Table 4.1 since these trigger lines are well understood in simulation.

The HLT1 trigger efficiency for the $\Xi_{cc}^{++} \to \Lambda_c^+ K^- \pi^+ \pi^+$ decay mode is found to be 0.943 ± 0.010, while for the $\Xi_{cc}^{++} \to D^+ p K^- \pi^+$ channel it is measured to be 0.953 ± 0.003. With the strict requirements of the HLT2 lines, it is understandable that the HLT1 trigger efficiencies are very high for both channels. The L0 trigger requirement is directly applied to the MC events for the HLT1 efficiency to be determined.

Total Efficiency

The efficiencies of each stage of the analysis for both the Ξ_{cc}^{++} decay modes are summarized in Table 5.7. The total combined ratio of efficiencies, $\varepsilon(\Lambda_c^+ K^- \pi^+ \pi^+)/\varepsilon(D^+ p\, K^- \pi^+)$, is determined to be 0.461 ± 0.014.

5.7.4 Systematic Uncertainties

With the observed value of the normalisation yield, $N(\Lambda_c^+ K^- \pi^+ \pi^+)$, and the total relative efficiency, $\varepsilon(\Lambda_c^+ K^- \pi^+ \pi^+)/\varepsilon(D^+ p\, K^- \pi^+)$ at hand, along with the measured values of $\mathcal{B}(D^+ \to K^- \pi^+ \pi^+)$ and $\mathcal{B}(\Lambda_c^+ \to p K^- \pi^+)$, then according to Equation 5.4, the single-event sensitivity parameter α_s equates to $(1.74 \pm 0.29) \times 10^{-3}$.

Table 5.7: Efficiencies for selecting the Ξ_{cc}^{++} decays according to simulation and the ratio of these efficiencies. The uncertainties stated are only statistical.

Efficiency	$\Xi_{cc}^{++} \to \Lambda_c^+ K^-\pi^+\pi^+$	$\Xi_{cc}^{++} \to D^+pK^-\pi^+$	Ratio
ε^{Acc}	0.0987 ± 0.0002	0.0989 ± 0.0003	0.998 ± 0.003
$\varepsilon^{\text{Sel\|Acc}}$	$(0.74 \pm 0.016) \times 10^{-3}$	$(1.59 \pm 0.009) \times 10^{-3}$	0.462 ± 0.010
$\varepsilon^{\text{PID\|Sel}}$	0.714 ± 0.013	0.706 ± 0.001	1.011 ± 0.013
$\varepsilon^{\text{L0\|PID}}$	–	–	1.000
$\varepsilon^{\text{HLT1\|L0}}$	0.943 ± 0.010	0.953 ± 0.003	0.990 ± 0.010
Total	$(4.884 \pm 0.148) \times 10^{-5}$	$(1.059 \pm 0.007) \times 10^{-4}$	0.461 ± 0.014

The remaining part of this section will discuss the sources of systematic uncertainty associated to the evaluation of the single-event sensitivity parameter. Note that, uncertainties related to the mass measurement of the Ξ_{cc}^{++} baryon are of negligible importance here since the ratio of the total branching fractions measurement is insensitive to this.

Uncertainty on Normalisation Yield

In Section 4.6, it was ascertained that the measured mass of the Ξ_{cc}^{++} baryon from the $\Xi_{cc}^{++} \to \Lambda_c^+ K^-\pi^+\pi^+$ data is affected by the signal and background mass model used to the fit the $m(D^+pK^-\pi^+)$ mass distribution of Ξ_{cc}^{++} candidates. Now with the additional L0 trigger requirement applied to this data set, the variation in the accompanying signal yield is studied by using alternative mass models and fit ranges, one at at time.

For the signal model, a double-Gaussian function is trialled, while for the background model, the second-order Chebyshev function is changed to a first-order polynomial. The fit range is changed from $3650 \pm 150\,\text{MeV}/c^2$ to $3650 \pm 100\,\text{MeV}/c^2$. This results in the α_s parameter changing by 1.8% with the new fit range, 2.1% with the new signal model and 1.3% with the different background model. Taking the sum in quadrature of these variations, returns a 3.1% systematic uncertainty on α_s as a result of the uncertainty on the signal yield in the normalisation channel.

PID Calibration Uncertainty

The efficiency of the particle identification requirements in selecting $\Xi_{cc}^{++} \to D^+pK^-\pi^+$ and $\Xi_{cc}^{++} \to \Lambda_c^+ K^-\pi^+\pi^+$ decays is obtained using the PIDCalib software [161]. As explained in Appendix C, `PIDCalib` uses a data-driven method to calculate the efficiencies. However, an incorrect average PID efficiency could be calculated by `PIDCalib` if the binning size of the kinematic variables of signal and the data calibration samples are not optimum. Therefore, to calculate an uncertainty associated to this PID efficiency, the number of bins is doubled then halved and the PID efficiency is then recalculated by

`PIDCalib`. The largest deviation from the nominal ratio of efficiencies results in a 1.5% change on the α_s parameter.

Uncertainty of MC remodelling

The reconstruction and selection efficiency in both the Ξ_{cc}^{++} decay modes is calculated using MC events, which are correct for the observed difference in production kinematics of the Ξ_{cc}^{++} candidates between simulation and data, see Section 5.7.2. The p_T binning scheme in Section 5.7.2, which dictates the correction factors that are applied to the MC events might also not be optimum. Thus, the binning size is doubled then halved to investigate the impact on the reconstruction and selection efficiency. The maximum change in the value of α_s from the modelling of the MC sample is around 1.2%.

Ξ_{cc}^{++} Lifetime Uncertainty

Equally, the reconstruction and selection efficiency in both the Ξ_{cc}^{++} decay modes is calculated using MC events where the lifetime of the Ξ_{cc}^{++} baryon is set to its measured value of approximately 256 ps in simulation. A reminder that the lifetime measured by the LHCb collaboration was $0.256^{+0.024}_{-0.022}$ (stat) $\pm$ 0.014 (syst) ps [174].

The effect that the uncertainty on this lifetime measurement has on reconstruction and selection efficiency is also investigated. The decay time of Ξ_{cc}^{++} candidates in both decay modes are weighted in simulation to give effective lifetimes of 232 fs (-1σ) and 280 fs ($+1\sigma$) for the Ξ_{cc}^{++} baryon. The reconstruction and selection efficiencies are then reevaluated with these weighted MC samples in the same way as before. The maximum variation of the α_s parameter as a result is found to be 5.8%. Half of this value is assigned as a systematic uncertainty due to the uncertainty on the lifetime of the Ξ_{cc}^{++} baryon.

Uncertainty on L0 Trigger Efficiency

To a good approximation, the ratio of efficiencies of the hardware-trigger requirement should be one, which is the value quoted for this efficiency ratio. As explained in Section 5.7.3, the efficiencies may not be the same if the selection requirements for each decay mode pick out Ξ_{cc}^{++} candidates with slightly different kinematic properties. This will ultimately affect the objects that are triggered in the event. Therefore, comparing any differences in the p_T distributions of the Ξ_{cc}^{++} candidates between each decay mode is a sensible course of action to estimate the validity of this assumed unity ratio. However, because no signal is observed in $\Xi_{cc}^{++} \to D^+ p K^- \pi^+$ data, this means that MC events can only used to investigate this comparison and that is despite the L0 trigger being poorly modelled in simulation.

Table 5.8: Statistical and systematic uncertainties on the single-event-sensitivity parameter, α_s, used in the ratio of branching fractions measurement.

Source of uncertainty	Uncertainty on α_s (%)
Statistical	16.8
PID calibration	1.5
Simulation modelling	1.2
Lifetime uncertainty	2.9
Mass fit model	3.1
L0 efficiency	3.5
Total	17.7%

With both the Ξ_{cc}^{++} decays corrected by the p_T weights discussed in Section 5.7.2, the hardware-trigger efficiency for the $\Xi_{cc}^{++} \to \Lambda_c^+ K^- \pi^+ \pi^+$ channel is determined to be 0.291 ± 0.010 based on the number of MC events passing the L0 requirement, while for the $\Xi_{cc}^{++} \to \Lambda_c^+ K^- \pi^+ \pi^+$ channel, it is found to be 0.320 ± 0.003. This corresponds to a relative efficiency of 0.909 ± 0.010 between the decay modes. Since this is not consistent with a value of one, within the statistical uncertainty, the systematic uncertainty that is assigned should be large enough to account for this difference. The systematic uncertainty is calculated by reweighting the p_T spectrum of the Ξ_{cc}^{++} candidates in simulation from both channels such that they match each other. When these p_T weights are used, the ratio of efficiencies is found to increase by around 3.5%. This 3.5% variation is quoted as the systematic uncertainty on the α_s parameter due to the assumed L0 trigger efficiency.

Summary of Uncertainties on α_s

All systematic uncertainties are considered uncorrelated and are added in quadrature to give a total systematic uncertainty of 5.8%. The uncertainty on the lifetime is considered to be 100% correlated between the two modes, since it is the same mother particle. This means that the statistical uncertainty on the measured signal yield in the $\Xi_{cc}^{++} \to \Lambda_c^+ K^- \pi^+ \pi^+$ channel is the dominant uncertainty on the α_s parameter. It is thus expected that the systematic uncertainties on α_s will have a negligible effect on the upper limit set on the ratio $\mathcal{R}$. Taking the sum in quadrature of the statistical (16.8%) and systematic uncertainty (5.8%) gives a total uncertainty of 17.7%. Sources of systematic uncertainty and their effects on the single-event-sensitivity parameter α_s are summarized in Table 5.8 along with the final statistical uncertainty. The statistical entry in Table 5.8 includes the uncertainty on the intermediate singly-charmed hadron branching fractions.

5.7.5 Upper Limits

In this analysis, no significant $\Xi_{cc}^{++} \to D^+pK^-\pi^+$ signal is observed in the 2016 data so the $N(D^+pK^-\pi^+)$ term in Equation 5.3 should be viewed as a possible signal yield rather than a definite one. Instead, an upper limit is set on the ratio of branching fractions $\mathcal{R}$ at 3621.40 MeV/c^2, the mass of the Ξ_{cc}^{++} state measured in the $\Xi_{cc}^{++} \to \Lambda_c^+K^-\pi^+\pi^+$ data. The `CLs` method [178] is chosen to evaluate the upper limit on the ratio $\mathcal{R}$ since it can determine the ratio of Confidence Levels (CL) between the signal-plus-background and background-only hypotheses in the $\Xi_{cc}^{++} \to D^+pK^-\pi^+$ mass distribution and the statistical techniques that underpin the method are relatively simple.

To interpret any search result in high-energy physics, the test statistic in the experiment that comprises the result must be identified. For the search of $\Xi_{cc}^{++} \to D^+pK^-\pi^+$ decays, the test statistic is number of Ξ_{cc}^{++} candidates, N_{obs}, that are counted in the 3612−3630 MeV/c^2 mass region.[8] This mass region, indicated by the dashed-blue lines in Figure 5.36, corresponds to approximately three standard deviations around the measured mass of the Ξ_{cc}^{++} baryon when using the 2.84 MeV/c^2 mass resolution found in simulation.

For this analysis, the `CLs` method returns a score for every assumed value of $\mathcal{R}$, based on the test statistic, which indicates the level of confidence for that value of $\mathcal{R}$. The `CLs` score for a possible value of ratio $\mathcal{R}$ is calculated as follows

$$\texttt{CLs} = \frac{P(N_b + N_s \leq N_{obs})}{P(N_b \leq N_{obs})}, \tag{5.6}$$

where N_s is sampled from the distribution of the expected number of signal candidates for a given ratio $\mathcal{R}$, N_b is derived from the distribution shown in Figure 5.36, where the expected number of background candidates is given by the background-only fit and P indicates the probability that these statistical quantities are smaller than N_{obs}.

The value of N_b is found by fitting a second-order Chebyshev function to the data. The data points in the mass region $3612 < m(D^+pK^-\pi^+) < 3630$ MeV/c^2 are removed for the fit and N_b is determined by performing an integral extrapolation. The value of N_b is independent of the binning scheme of the mass distribution since it is calculated from an unbinned likelihood fit. The probability requirements in the numerator and denominator of Equation 5.6 are tested by running a large number of pseudoexperiments sampling from a Poisson distribution with statistical means of $N_b + N_s$ and N_b, respectively. The uncertainty on α_s is taken into account into Equation 5.6 by first sampling from a Gaussian distribution with a mean of 1.74×10^{-3} and a standard deviation of 0.31×10^{-3}, the values of the α_s parameter and its uncertainty, respectively. The value of N_s that is fed into the Poisson distribution for the number of signal candidates in the pseudoexperiments is then

[8] The number of candidates is not extrapolated from any fitting procedure since negative yields can arise; it is instead conducted as a simple single channel counting experiment.

determined from a fixed value of α_s, sampled from the Gaussian distribution discussed before and the presumed value of $\mathcal{R}$. This broadens the distribution of the number of observed candidates appropriately.

The derived CL curve as a function of possible $\mathcal{R}$ values is shown as the black line in Figure 5.41. This curve results from $N_{obs} = 66$ and $N_b = 79.8$ as observables and running 1×10^6 pseudoexperiments for each hypothetical value of $\mathcal{R}$.[9] The upper limit on $\mathcal{R}$ is set at < 0.017 at the 90% CL and < 0.021 at the 95% CL.

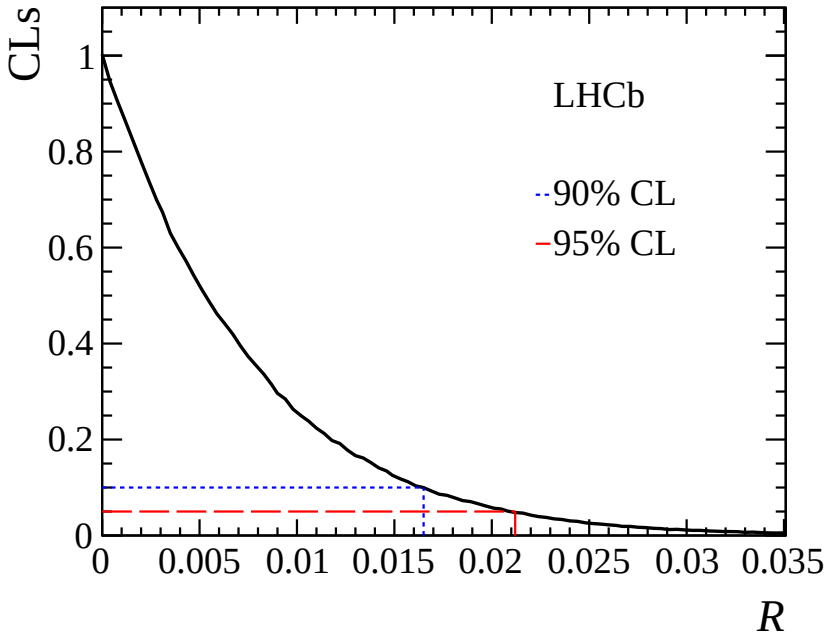

Figure 5.41: The scores from the `CLs` method for each value of the assumed ratio of branching fractions $\mathcal{R}$. Observed values are shown by the solid black line while the set upper limit at the 90% (95%) CL are indicated by the dotted-blue (dashed-red) line.

5.7.6 Summary of Branching Fraction Ratio Measurement

The upper limits set on the measured branching fraction ratio $\mathcal{R}$ at the known mass of the Ξ_{cc}^{++} state are

$$\mathcal{R} = \frac{\mathcal{B}(\Xi_{cc}^{++} \to D^+ p K^- \pi^+)}{\mathcal{B}(\Xi_{cc}^{++} \to \Lambda_c^+ K^- \pi^+ \pi^+)} < 0.017\ (0.021)\ @\ 90\%\ (95\%)\ \text{CL}$$

There limits were set using the `CLs` method [178]. The test statistic used was the number of candidates counted in the mass region where a Ξ_{cc}^{++} signal was expected.

[9] Note that the value of N_b is greater than N_{obs} but this is expected as the fitted curve is consistently higher across all bins in the signal mass region, see Figure 5.36.

5.7.7 Conclusion and Discussion

Following a clear observation of the Ξ_{cc}^{++} baryon through the $\Xi_{cc}^{++} \to \Lambda_c^+ K^- \pi^+ \pi^+$ decay mode, a search for the Cabibbo-favoured $\Xi_{cc}^{++} \to D^+ p K^- \pi^+$ decay is performed using pp collision data recorded by the LHCb experiment at a centre-of-mass energy of 13 TeV and which corresponds to an integrated luminosity of $1.7\,\text{fb}^{-1}$. The $\Xi_{cc}^{++} \to D^+ p K^- \pi^+$ decay was pursued based on its desirable experimental attributes. However, no significant signal of Ξ_{cc}^{++} decays is observed in the $3300-3800\,\text{MeV}/c^2$ mass range, despite the reconstruction and selection efficiencies of the $\Xi_{cc}^{++} \to D^+ p K^- \pi^+$ decay being higher than in the $\Xi_{cc}^{++} \to \Lambda_c^+ K^- \pi^+ \pi^+$ decay. The selection was able to pick out a very pure sample of D^+ candidates displaced from the primary vertex.

Instead of making a mass measurement of the Ξ_{cc}^{++} baryon, an upper limit on the ratio of branching fractions between the $\Xi_{cc}^{++} \to D^+ p K^- \pi^+$ and the $\Xi_{cc}^{++} \to \Lambda_c^+ K^- \pi^+ \pi^+$ decay is set as less than $1.7\,(2.1) \times 10^{-2}$ at the 90% (95%) confidence level at the known mass of the Ξ_{cc}^{++} baryon. This limit was obtained using the `CLs` method [178], after a full consideration of the statistical and systematic uncertainties in the analysis. The limit is also derived assuming a uniform phase space model in the efficiency determination. This result implies that there is at least two orders of magnitude difference between the branching fractions of these two Ξ_{cc}^{++} decay modes.

A better theoretical understanding of the resonant and nonresonant contributions underpinning the $\Xi_{cc}^{++} \to D^+ p K^- \pi^+$ and $\Xi_{cc}^{++} \to \Lambda_c^+ K^- \pi^+ \pi^+$ decay processes is now required to understand this suppression. It is likely that the nonresonant contribution to the $\Xi_{cc}^{++} \to D^+ p K^- \pi^+$ decay, see the left Feynman diagram of Figure 1.7, is quite small, if the theoretical work on pseudo-two-body decays is to be accepted [99]. Dynamical effects or spin constraints in the resonance structures could also be suppressing the $\Xi_{cc}^{++} \to D^+ p K^- \pi^+$ decay. Lastly, and perhaps most importantly, the reduced phase space available to the decay products of the $\Xi_{cc}^{++} \to D^+ p K^- \pi^+$ decay compared to the $\Xi_{cc}^{++} \to \Lambda_c^+ K^- \pi^+ \pi^+$ decay, with energy releases of around 180 MeV and 560 MeV in each mode, respectively, will contribute to this suppression. The fact that the $\Xi_{cc}^{++} \to D^+ p K^- \pi^+$ decay is close to its energy production threshold, may be another factor for its lack of evidence in the 2016 LHCb data. The full data set collected by the LHCb detector in Run II, or with data taken in the future with the upgraded LHCb detector [179], may reveal evidence of the $\Xi_{cc}^{++} \to D^+ p K^- \pi^+$ decay and shed more light on the production and decay dynamics of the Ξ_{cc}^{++} baryon in the process.

5.8 Chapter Summary

This chapter presented a search for $\Xi_{cc}^{++} \to D^+(\to K^-\pi^+\pi^+)pK^-\pi^+$ decays, the first of its kind at any high-energy physics experiment. The aim of this work was to rediscover the doubly-charmed Ξ_{cc}^{++} baryon within the data collected in 2016 at the LHCb detector and at the same time to learn more about its decay dynamics. An introduction to the analysis was first given, where the aims of the analysis were established and the motivation for exploring the $\Xi_{cc}^{++} \to D^+ pK^-\pi^+$ decay mode was explained, after which the strategy of the analysis was described intermingled with updates and referrals back to the $\Xi_{cc}^{++} \to \Lambda_c^+ K^-\pi^+\pi^+$ analysis. A concise explanation of the way in which potential $\Xi_{cc}^{++} \to D^+ pK^-\pi^+$ decays were selected from within data was given by referring back to any similarities discussed in the $\Xi_{cc}^{++} \to \Lambda_c^+ K^-\pi^+\pi^+$ search but also by highlighting any differences between the two Ξ_{cc}^{++} decay modes. Background studies were then presented and the methodology of designing suitable fit models to describe the mass distributions was given. Next, mass distributions associated to potential $\Xi_{cc}^{++} \to D^+ pK^-\pi^+$ decays were presented with an interpretation of the results also given. Finally, a procedure for comparing the branching ratios when the Ξ_{cc}^{++} baryon decays to the $D^+ pK^-\pi^+$ and the $\Lambda_c^+ K^-\pi^+\pi^+$ final states are presented. The chapter concluded with a discussion on the implications of not observing a significant number of $\Xi_{cc}^{++} \to D^+ pK^-\pi^+$ decays and discussed the need for future theoretical and experiment work into the Ξ_{cc}^{++} baryon.

Chapter 6

Charm Baryon Trigger Studies

"Be sure you positively identify your target before you pull the trigger."

– Tom Flynn, American author and journalist

This chapter primarily describes the development and performance of a new multi-purpose and multivariate-based trigger line that was designed by the PhD candidate to reconstruct $\Xi_c^+ \to pK^-\pi^+$ decays. The motivation and techniques for creating this trigger line are also established in this chapter. This new $\Xi_c^+ \to pK^-\pi^+$ HLT2 trigger line was merged into the LHCb software after the first LHC technical stop of 2018 and was active for approximately the last $1.3\,\text{fb}^{-1}$ of the pp collision data recorded that year. This trigger line is discussed, along with many others, in Reference [139].

6.1 Introduction and Motivation

The main aim of this work was to create a $\Xi_c^+ \to pK^-\pi^+$ trigger line that would support searches for doubly-charmed baryons. A reminder that doubly-charmed baryons are typically reconstructed from singly-charmed hadrons in combination with other particles at LHCb. This was the case for the $\Xi_{cc}^{++} \to \Lambda_c^+ K^-\pi^+\pi^+$ and $\Xi_{cc}^{++} \to D^+ pK^-\pi^+$ analyses discussed in Chapters 4 and 5, respectively. Search channels of doubly-charmed baryons involving the Ξ_c^+ (usc) baryon, have also been explored by the LHCb collaboration and they will continue to be studied in the future; this is where the introduction of a new versatile $\Xi_c^+ \to pK^-\pi^+$ trigger becomes particularly important.[1] Additionally, inclusive Ξ_c^+ trigger lines at LHCb are used to study heavy-flavoured baryons containing either a single b quark or both a c and b quark. Thus, the breadth of potential uses for a new multivariate-based $\Xi_c^+ \to pK^-\pi^+$ trigger line is vast.

Since the start of Run I, there has been an inclusive $\Xi_c^+ \to pK^-\pi^+$ trigger in use at LHCb. This trigger line uses simple rectangular cut-based selections to separate

[1] The Ξ_{cc}^{++} baryon was rediscovered in 2017 through the $\Xi_{cc}^{++} \to \Xi_c^+(\to pK^-\pi^+)\pi^+$ decay mode by the LHCb collaboration using Run II data [180].

signal events from background. However, based on the promising results when using multivariate techniques in other inclusive-charm trigger lines at the start of Run II at LHCb [181], it was expected that a multivariate-based $\Xi_c^+ \to pK^-\pi^+$ trigger line would give a better performance. Ideally, the use of a multivariate selection would mean that the $\Xi_c^+ \to pK^-\pi^+$ trigger is more sensitive to Ξ_c^+ baryons originating from the primary vertex and from decays of heavy hadrons than the existing line. To achieve this, the selection criteria of the trigger is intended not to make use of any quantities that are dependent on the source of the Ξ_c^+ baryon. To be prudent, the new multivariate-based line is planned to co-exist with the original cut-based trigger rather than replace it.

6.2 Technicalities

The structure of the trigger system at LHCb is explained in Section 2.5 but a brief recap is given in this section, along with information on the history of Turbo processing that is required to understand the design of the new trigger. The particular multivariate method used in this new trigger is also discussed in this section.

6.2.1 Turbo Streams

The role of a trigger is to make quick and intelligent selections in order to keep only interesting events for offline analyses. The trigger at LHCb is organised in three levels; the hardware Level-0 trigger (L0) and two software High-Level triggers (HLT1 and HLT2); this results in a very flexible and efficient system [136].

In Run II, the collision energy of protons was increased from 7 TeV to 13 TeV at the LHC and the pp bunch crossing rate was increased from 15 MHz to 30 MHz. In these collision conditions, beauty and charm hadrons are produced inside the LHCb detector acceptance at rates exceeding 50 kHz and 1 MHz, respectively. To cope with this higher production rate with the same limited computing storage as in Run I, LHCb introduced Turbo processing into the HLT software at the start of Run II. In this setup, event objects that are reconstructed in HLT2 are now saved to a dedicated stream, where data sets are stored in more manageable memory sizes [140]. Turbo event objects may then be directly used by analysts without any further offline processing. The $\Xi_{cc}^{++} \to \Lambda_c^+ K^-\pi^+\pi^+$ analysis of Chapter 4 makes uses of Ξ_{cc}^{++} candidates from the Turbo stream; the discovery of the Ξ_{cc}^{++} baryon can therefore be partially attributed to the great success of Turbo processing.

A drawback of the Turbo stream in 2015 was that any information associated to tracks or detector responses that are not used by a trigger line to evaluate its decision is simply discarded. To overcome this issue, the Turbo++ stream was introduced in 2016

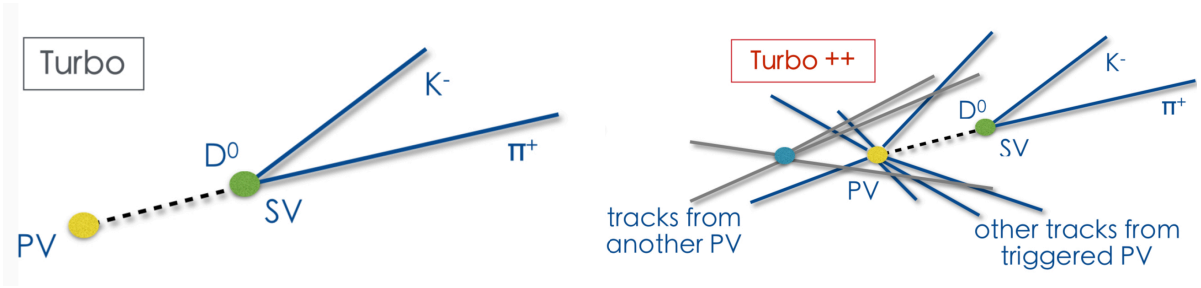

Figure 6.1: Illustrations of the different event objects that are saved in memory under the different Turbo streams for a triggered $D^0 \to K^-\pi^+$ event.

to persist the triggered candidate plus all the reconstructed objects in the event [182].[2] An illustration of the potential events objects that may be saved in a triggered event containing $D^0 \to K^-\pi^+$ decays, under the different turbo schemes, is shown in Figure 6.1.

The new $\Xi_c^+ \to pK^-\pi^+$ trigger will be a HLT2 line with Turbo++ processing enabled. Hence, all tracks in events that fire the $\Xi_c^+ \to pK^-\pi^+$ trigger will be saved to disk; this allows for maximum robustness and flexibility offline. It is also beneficial for the trigger to be inclusive to cover possible decay modes that are not covered by the exclusive triggers. A reminder that inclusive selections do not depend on a complete reconstruction of signal decays, allowing for an efficient selection of a broader range of decay channels.[3]

6.2.2 Bonsai Boosted Decision Tree

During Run I at LHCb, the algorithms used in the HLT software commonly used simple cut-based selections to perform the online event reconstruction, *i.e.* an event is selected based on a series of individual criteria combined through a chain of logical AND statements. Examples include the typical high p_T and large IP requirements of HLT1 that are discussed in Section 2.5.2. However, this means that the inevitable correlations among the discriminating variables of an event are ignored, which is wasteful.

On the other hand, it is known that multivariate classifiers such as Artificial Neural Networks are more powerful at discriminating between signal and background events, as mentioned in Section 4.3.5. For this reason, there was a rise of multivariate-based HLT trigger lines being used in Run II. One particular multivariate classifier that was found to be useful in the LHCb trigger was a Decision Tree (DT) classifier [181]. DTs are

[2]The Turbo Selective Persistence (TurboSP) model was introduced in 2017 as a middle ground between the Turbo and the Turbo++ streams. An arbitrary set of additional event object can be saved in memory along with the triggered candidate. TurboSP employs the same algorithms used in the offline Stripping of data and allows analysts do a lot more physics for a small cost in the event memory size.

[3]To facilitate searches for higher resonances of doubly-charmed baryons, additional reconstruction objects are persisted in the existing exclusive doubly-charmed trigger lines during data-taking in 2018.

constructed by looping over the variates of the data set and repeatedly performing one-dimensional splits of the data to form tree-like structures if imagined pictorially. To limit the effects of over-training, DTs are often boosted [183]; this is the basic BDT classifier that was previously discussed in the candidate selections of the Ξ_{cc}^{++} search analyses.

Despite its great discriminating ability, the BDT algorithm can take a long time to determine its response. In order for the BDT classifier to be compatible with the strict timing requirements of HLT, the LHCb collaboration sometimes use a slightly modified version of the standard BDT, known as the Bonsai BDT (BBDT) [184]. This method involves training the BDT classifier using discretised information from a set of variables to learn about signal and background events. This way, the multi-dimensional phase space of the input training variables is divided into set regions. The BBDT response is then only evaluated for these regions and this relational information can be converted into a simple one-dimensional look-up table, which can be embedded into the HLT2 software. Due to the limited computing resources at LHCb, the size of the look-up table needs to be carefully considered. The size is determined by the number of training variables and the number of bins for each variable. Therefore, the minimum set of uncorrelated variables, discretised in a coarse binning, is needed to train the BBDT algorithm such that the size of the multivariate look-up table is kept small.

The BBDT method is used in the multivariate-based $\Xi_c^+ \to pK^-\pi^+$ trigger, whose development and implementation is discussed next. The configuration, training and optimisation of this type of BDT classifier is detailed in Section 6.3.3.

6.3 Trigger Development

Following the standard approach of most multivariate-based triggers at LHCb, the selection criteria of this new $\Xi_c^+ \to pK^-\pi^+$ trigger line is implemented into two stages:

1. Firstly, through a cut-based preselection that aims to remove combinatorial background and control the CPU requirements of the HLT2 data throughput. The selection requirements are loose enough so as not to favour a particular source of the Ξ_c^+ baryons;

2. Secondly, using a BBDT classifier to perform a multivariate selection to efficiently separate signal events from combinational background. To preserve the inclusive nature of the trigger line, only loose requirements that are based on the decay time of a Ξ_c^+ candidate are used.

As mentioned in Section 6.1, the output of the new $\Xi_c^+ \to pK^-\pi^+$ trigger is written to the Turbo++ stream. The next few sub-sections describe in detail the different stages of

the selection and the data and MC samples used to develop and test the trigger offline before it is added into the HLT software to officially trigger data.

6.3.1 Data Samples

The selection requirements of the new multivariate-based trigger are chosen by studying different sources of Ξ_c^+ baryons. The properties of signal $\Xi_c^+ \to pK^-\pi^+$ decays are based on a mixture of different simulated samples where the Ξ_c^+ baryons are produced either at the primary vertex (prompt) or from other heavy-flavoured hadrons (secondaries). Specifically, the following simulated decays are used to investigate signal:

Prompt: $\Xi_c^+ \to pK^-\pi^+$;

Secondary charm: $\Xi_{cc}^+ \to (\Xi_c^+ \to pK^-\pi^+)\pi^+\pi^-$;

Secondary beauty: $\Xi_{bc}^+ \to (\Xi_c^+ \to pK^-\pi^+)(J/\psi \to \mu^+\mu^-) \,|\, \Xi_{bc}^0 \to (\Xi_c^+ \to pK^-\pi^+)\pi^-$.

Approximately equal sized samples of these decays are generated under MagUp and MagDown magnetic conditions for the trigger selection studies. The decay-time distribution of the mother particle in each simulation are weighted such that the lifetime of the mother is equal to its most up-to-date predicted or measured value [74, 185]. The effective lifetimes of the mother particles in each simulation are summarised in Table 6.3.

Background is represented by Stripped data that was collected during the first few days of data taking in 2015. Events are recorded with a pass-through trigger, whereby no filtering takes place, *i.e.* no selection or rejection criteria is imposed on this data, beyond requiring the data to pass any active L0 line. All possible kaon, pion and proton candidate tracks are combined offline to form the following wrong-signed-plus (WSP), wrong-signed-minus (WSM) and Doubly-Cabbibo-Suppressed (DCS) decay modes:

WSP: $\Xi_c^+ \to pK^+\pi^+$;

WSM: $\Xi_c^+ \to pK^-\pi^-$;

DCS: $\Xi_c^+ \to pK^+\pi^-$,

where the WSP and WSM decays are both expected to have similar kinematic properties to the combinatorial background reconstructed in the $\Xi_c^+ \to pK^-\pi^+$ signal mass region. These data sets are combined to form a single background sample that is used to develop the trigger selection. These three different sources of background are used in order to increase the statistics for developing the trigger selection.

6.3.2 Preselection

Firstly, all events are required to pass the `L0Global` trigger line and then need to satisfy either the `Hlt1TrackMVA` or `Hlt1TwoTrackMVA` trigger line before they can be evaluated by the new $\Xi_c^+ \to pK^-\pi^+$ HLT2 trigger. The requirements of the `Hlt1(Two)TrackMVA` trigger line are disclosed in Table 4.1.

At this stage, the combination of three reconstructed tracks, which have simply passed L0 and HLT1, will still lead to a huge amount of combinatorial background. To allow the BBDT classifier to evaluate the response of each event at an adequate speed, the number of events reaching the multivariate selection is controlled by a preselection. The requirements of the preselection are modelled on the selection criteria of the original $\Xi_c^+ \to pK^-\pi^+$ HLT2 trigger line, which is given in Table 6.1, and their efficiencies are based on the signal and background samples described in Section 6.3.1. The background events in the simulated samples are removed by a simple truth-matching procedure that requires the Ξ_c^+ baryon and its decay products to correspond to the correct particle type.

The final set of requirements chosen for the preselection are shown in Table 6.2. They include loose particle identification and momentum related requirements on the daughter tracks and a constraint on the quality of the reconstructed vertex of the Ξ_c^+ baryon. The particle identification requirements of the preselection are directly applied to the MC events rather than through any data-driven means after cross-checks uncovered no discernible difference between the procedures. Since the new multivariate-basedtrigger needs to be insensitive to the source of Ξ_c^+ baryons, the directional and angular based variables listed in Table 6.1 are not used in the preselection of the new trigger.

The number of events that pass the total requirements of the L0 and HLT1 trigger lines and the preselection are listed in Table 6.3 and Table 6.4 for the signal MC samples and background data sets, respectively. The signal efficiency from the combined requirements in the trigger and preselection is around $30-40\%$ based on the number of signal MC events that pass. This efficiency is dependent on the source of the Ξ_c^+ baryons with a slightly higher efficiency observed for the prompt $\Xi_c^+ \to pK^-\pi^+$ decay. The significance requirement on the impact parameter (IP) of the daughter tracks, $\chi^2_{\text{IP}} > 4$, is particularly useful for removing background according to the WSP, WSM and DCS data sets.

6.3.3 Multivariate Selection

The TMVA package version 4.2.1 [166] with ROOT version 6.12.04 [167] is used to develop the multivariate selection. As mentioned in Section 6.2.2, the new $\Xi_c^+ \to pK^-\pi^+$ trigger line will exploit the fast-thinking BBDT algorithm, which uses discretised input training variables. This procedure limits where data can be split in order to better control the growth and shape of the decision tree.

Table 6.1: Selection criteria of the cut-based $\Xi_c^+ \to pK^-\pi^+$ trigger. The variables highlighted in red are strongly dependent on the production point of the Ξ_c^+ baryon.

Candidate	Variable	Requirement
Daughter of Ξ_c^+	Momentum	$p > 1\,\text{GeV}/c$
	Transverse momentum	$p_\text{T} > 200\,\text{MeV}/c$
	Impact parameter significance	$\chi^2_\text{IP} > 6$
	Arithmetic sum of p_T	$(p_\text{T}(p) + p_\text{T}(K^-) + p_\text{T}(\pi^-)) > 3\,\text{GeV}/c$
	Second maximum p_T	$p_\text{T}(2\,\text{tracks}) > 400\,\text{MeV}/c$
	Maximum χ^2_IP	$\chi^2_\text{IP}(2\,\text{tracks}) > 16$
	Second maximum χ^2_IP	$\chi^2_\text{IP}(1\,\text{track}) > 9$
proton	Particle identification	$\text{DLL}_{p\pi} > 5$ & $\text{DLL}_{pK} > 5$
	Momentum	$p > 10\,\text{GeV}/c$
kaon	Particle identification	$\text{DLL}_{K\pi} > 5$
pion	Particle identification	$\text{DLL}_{K\pi} < 5$
Ξ_c^+ candidate	Reconstructed mass	$m \in [2392, 2543]\,\text{MeV}/c^2$
	Cosine of Direction Angle	DIRA> 0.99995
	Lifetime	$\tau > 0.1\,\text{ps}$
	Vertex quality	$\chi^2_\text{vtx}/\text{ndf} < 10$
	Vertex displacement	$\chi^2_\text{BPVVD} > 25$
	HLT1 trigger	`Hlt1*Track*_TOS` $= 1$

Table 6.2: Selection criteria of the new $\Xi_c^+ \to pK^-\pi^+$ trigger line prior to the multivariate selection. No source dependent variables of the Ξ_c^+ baryon are used.

Candidate	Variable	Requirement
Daughter of Ξ_c^+	Momentum	$p > 1\,\text{GeV}/c$
	Transverse momentum	$p_\text{T} > 200\,\text{MeV}/c$
	Impact parameter significance	$\chi^2_\text{IP} > 4$
	Particle identification	`ProbNNghost` < 0.9
proton	Momentum	$p > 10\,\text{GeV}/c$
	Particle identification	`ProbNNp` > 0.1
		$\text{DLL}_{p\pi} > 5$ & $\text{DLL}_{pK} > 5$
kaon	Particle identification	$\text{DLL}_{K\pi} > 5$
		`ProbNNk` > 0.1
pion	Particle identification	`ProbNNpi` > 0.1
Ξ_c^+ candidate	Reconstructed mass	$m \in [2392, 2543]\,\text{MeV}/c^2$
	Vertex quality	$\chi^2_\text{vtx}/\text{ndf} < 50$
	HLT1 trigger	`Hlt1(Two)TrackMVADecision_Dec` $= 1$
	L0 trigger	`L0Global_Dec` $= 1$

Table 6.3: The number of signal $\Xi_c^+ \to pK^-\pi^+$ decays from simulation that pass the preselection from different sources, with the corresponding effective lifetime of the mother particle given and the TMVA training weights for each signal sample.

Source of Ξ_c^+ baryon	Mother lifetime	MC events	Weight
$\Xi_c^+ \to pK^-\pi^+$	$\Xi_c^+ = 442\,\text{fs}$	21,851	2.0
$\Xi_{cc}^+ \to (\Xi_c^+ \to pK^-\pi^+)\pi^+\pi^-$	$\Xi_{cc}^+ = 80\,\text{fs}$	74,304	2.0
$\Xi_{bc}^+ \to (\Xi_c^+ \to pK^-\pi^+)(J/\psi \to \mu^+\mu^-)$	$\Xi_{bc}^+ = 250\,\text{fs}$	97,772	1.0
$\Xi_{bc}^0 \to (\Xi_c^+ \to pK^-\pi^+)\pi^-$	$\Xi_{bc}^0 = 100\,\text{fs}$	29,088	1.0

Table 6.4: The number of background events which pass the preselection from different sources with the corresponding TMVA training weights for each sample.

Source	Events	Weight
$\Xi_c^+ \to pK^+\pi^+$	23,337	2.0
$\Xi_c^+ \to pK^-\pi^-$	24,307	2.0
$\Xi_c^+ \to pK^+\pi^-$	24,010	1.0

The BBDT classifier is trained using the approximately 220,000 signal MC events and 50,000 background events that pass the requirements of the L0 and HLT1 trigger lines and the preselection. Both the signal and background samples are randomly split into two disjoint subsets by TMVA; one is used for training, while the other is used for testing the decisions made by the BBDT. When training the BBDT classifier to recognise signal, a higher priority is subjectively given to the Ξ_{cc}^+ decay sample over the Ξ_{bc}^+ and Ξ_{bc}^0 decays. To do this, global weights are applied to the MC events in TMVA such that the effective sample sizes obey a normalised $2:2:1$ ratio for the prompt, the secondary charm and the secondary beauty decay modes, respectively. Keep in mind, the trigger is also naturally expected to be more efficient at selecting particles with longer lifetimes. The background samples similarly have global weights applied to them to give combinatorial background greater importance for training. The background weights are summarised in in Table 6.4.

To train the BBDT, the aim is to use 5–8 attributes of the $\Xi_c^+ \to pK^-\pi^+$ decay and discretise this information into 3–7 bins for each training variable. Variables that are highly dependent on the source of the Ξ_c^+ baryon are not used in training so that the BBDT classifier learns common Ξ_c^+ traits. After initial checks with a large number of training variables, inspired by the ones used in other BDT-based inclusive charm triggers [181], seven training variables are chosen. This includes; the vertex χ^2/ndf of the Ξ_c^+ candidates, the distance of closest approach (DOCA) between any pairwise combination of the proton, kaon and pion tracks and the combined p_T of the proton, kaon and pion tracks, since the corresponding distribution in background is much softer. Information on the lifetime of the Ξ_c^+ candidates is partially exploited using the flight distance χ^2

Table 6.5: Binning schemes of the discretised training variables used in the multivariate selection of the $\Xi_c^+ \to pK^-\pi^+$ trigger line.

Training variable	Binning scheme						#Bins
Ξ_c^+ vertex χ^2_{vtx}/ndf	0	1.67	3.33	6.67	13.33	-	5
Ξ_c^+ MAXDOCA [mm]	0	0.1	0.3	0.5	-	-	4
minimal p_{T} of decay products [MeV/c]	200	300	400	550	700	1000	6
Ξ_c^+ p_{T} [GeV/c]	0	1	2	4	6	9	6
log(sum χ^2_{IP} of decay products))	2	3	4	5	6	-	5
log(minimal χ^2_{IP} of decay products)	1	2	3	4	5	-	5
log(Ξ_c^+ flight distance χ^2)	-2	2	3.5	5	6.5	8	6

variable and the combination of the daughters' χ^2_{IP} values. The seven selected variables and their distributions in each individual signal and background sample are displayed in Figure 6.2. Based on the distributions shown in Figure 6.2, the binning schemes listed in Table 6.5 are chosen for the BBDT algorithm. The intervals are greater than the variable resolution but are small enough to resolve steeply varying discriminating features. The breakdown of these discretised variables in the signal and background samples for training in TMVA are shown in Figure 6.3 and the correlations between the variables are shown in Figure 6.4. In general, the correlations are weak, apart from a link between the vertex quality of the Ξ_c^+ baryon and the arithmetic sum of the χ^2_{IP} of its decay products; the same trend is not observed in the background sample however, so these final seven training variables are considered to be sensible choices. The over-training check using the BBDT method, with 850 decision trees, is shown in Figure 6.5; there is no hint of overtraining based on the Kolmogorov−Smirnov test scores. The excellent separation between signal and background that is achieved by the BBDT method is also highlighted in Figure 6.5.

After training the BBDT, a look-up table is generated that contains the values of the discretised training variables and their corresponding BBDT response. The table is locally added into the Moore software package [137] so that the multivariate selection can be optimised using dedicated data sets provided by LHCb; this is discussed next.

6.3.4 Optimisation and Performance

To determine the most suitable selection requirement to impose on the BBDT response of each event, the potential retention rate and signal efficiency of the new $\Xi_c^+ \to pK^-\pi^+$ trigger is investigated.[4] The signal efficiency is determined using the simulated Ξ_c^+ decay

[4]The efficiencies of inclusive charm triggers were limited by the output rate to storage in Run I.

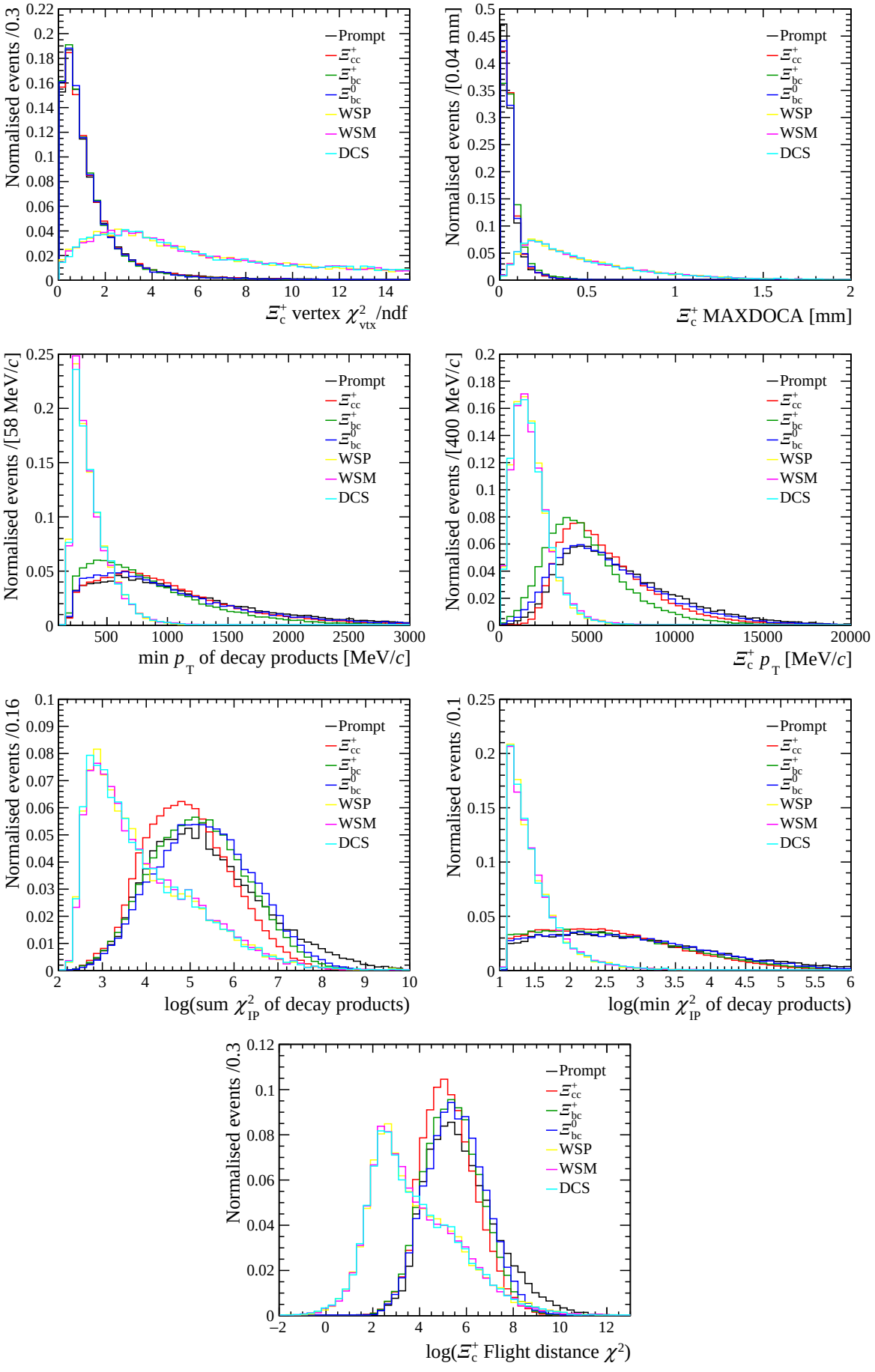

Figure 6.2: Comparison of the training variable distributions in the simulated signal samples and the data background samples.

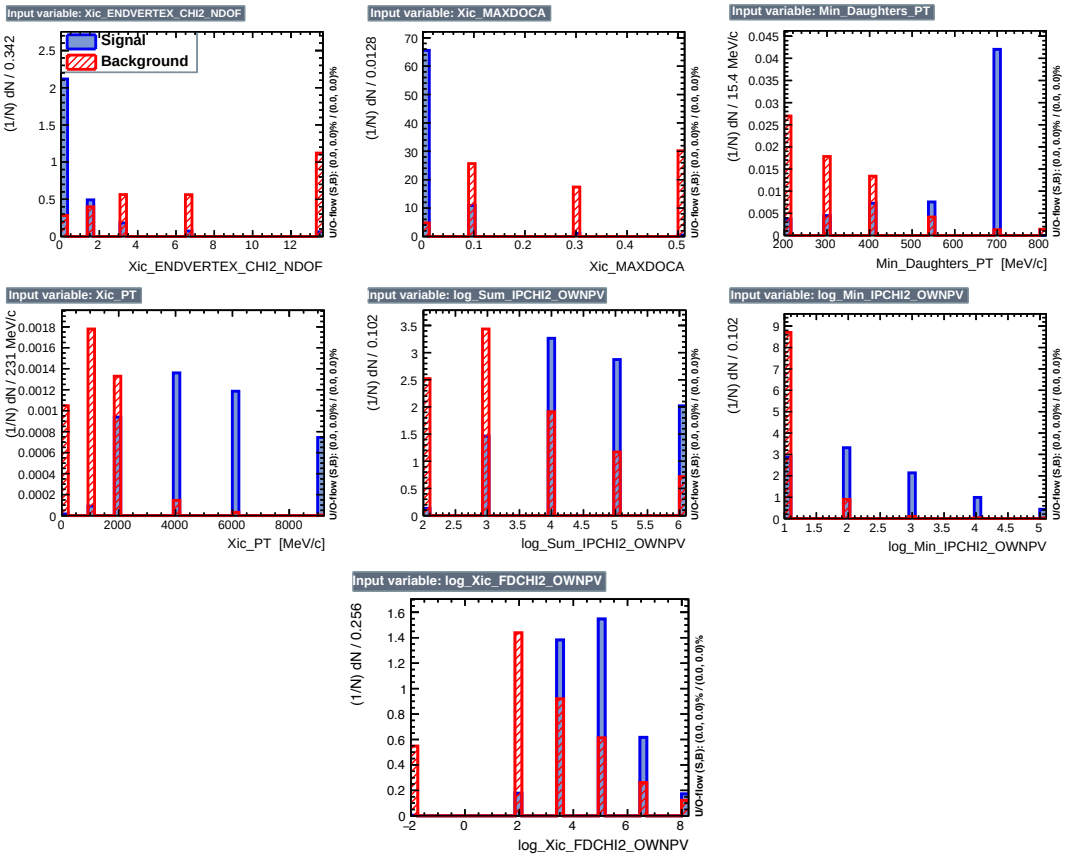

Figure 6.3: Distribution of the discretised (blue) signal and (red) background variables used to train the multivariate in the $\Xi_c^+ \to pK^-\pi^+$ trigger line.

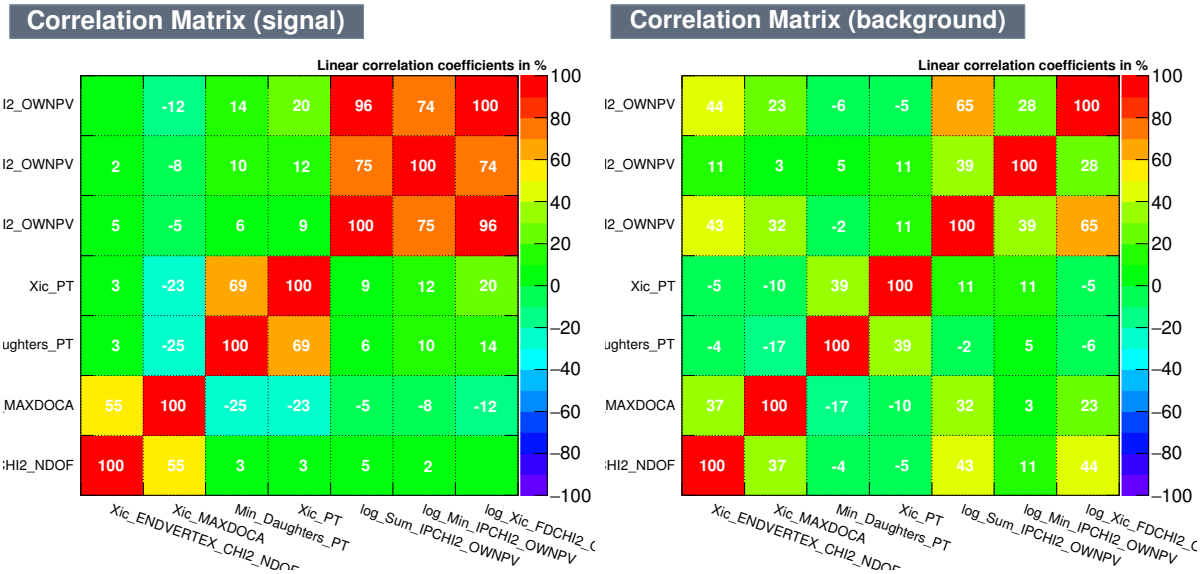

Figure 6.4: Correlation matrix of the variables used to train the multivariate in the $\Xi_c^+ \to pK^-\pi^+$ trigger line for the (left) signal and (right) background samples.

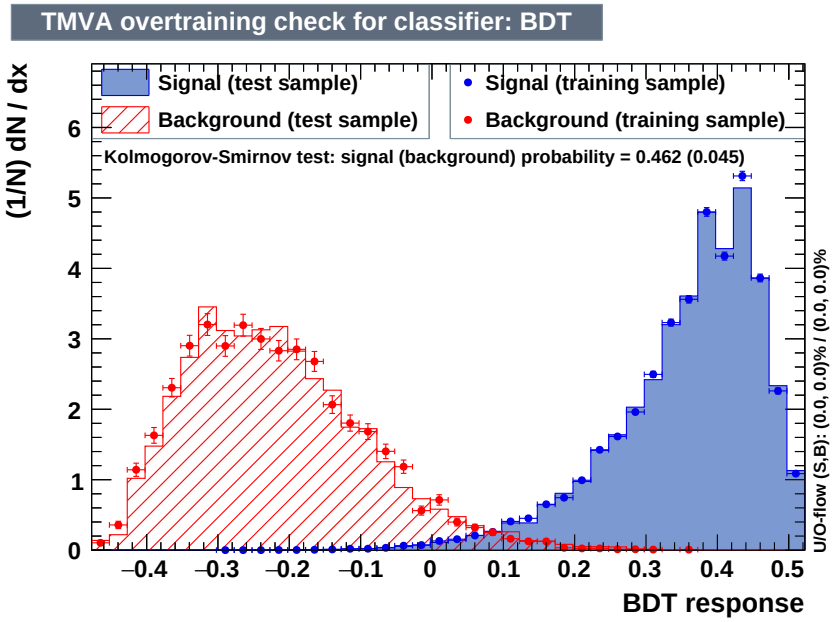

Figure 6.5: The normalised response distribution for the BBDT classifier. The results from training are shown as points with error bars, while the testing results are shown as shaded-hatched histograms. The Kolmogorov−Smirnov test scores indicate the compatibility between the training and testing phases.

samples that are discussed in Section 6.3.1, while the rate and CPU usage of the trigger is evaluated using 50,000 HLT1 accepted events from 2017 data, which passed the `Hlt1Global` line at the rate of 110 kHz, and that are officially used by the LHCb collaboration to test all trigger lines before they are deployed for official data taking.

The new multivariate-based $\Xi_c^+ \to pK^-\pi^+$ trigger line is found to have the desired qualities of a HLT2 trigger; namely retention rates in keeping with other trigger lines and a low CPU time. The rates and efficiencies of the new multivariate trigger, under different working points, is compared to the results when using the original cut-based trigger line in Table 6.6. The measured efficiencies of the new multivariate-based trigger are improved with respect to the existing cut-based one for all sources of Ξ_c^+ baryons but the statistical uncertainty is quite large in some cases due to the low number of MC events. In particular, the efficiency of selecting Ξ_c^+ baryons originating from the doubly-heavy Ξ_{bc}^0 baryon is improved by over a factor of two, when using a minimum BBDT > 0.25 requirement. The retention rates of the other HLT2 lines also remain the same with and without this new multivariate $\Xi_c^+ \to pK^-\pi^+$ trigger being added. To keep a reasonable rate and high efficiency, the BBDT working point is chosen to be 0.25, since a retention rate of around 40 Hz is reasonably low for an inclusive Turbo++ trigger line.[5]

[5]Note that the HLT2 rate allowance for inclusive lines is approximately 2 kHz in Run II but in reality this is only reached by some of the simple two and three body topological trigger lines.

Table 6.6: The rate and efficiency of the multivariate and cut-based lines evaluated with MC samples. The preferred working point of BBDT>0.25 is highlighted in red.

Trigger line	Rate [Hz]	ε_{prompt} [%]	$\varepsilon_{\Xi_{cc}^+}$ [%]	$\varepsilon_{\Xi_{bc}^+}$ [%]	$\varepsilon_{\Xi_{bc}^0}$ [%]
Cut-based	11.0 ± 4.9	2.61 ± 0.33	3.79 ± 0.17	2.03 ± 0.09	3.55 ± 0.29
BBDT > 0.15	83.6 ± 13.6	3.68 ± 0.41	4.95 ± 0.23	5.75 ± 0.18	9.87 ± 0.65
BBDT > 0.20	52.8 ± 10.8	3.44 ± 0.37	4.64 ± 0.21	5.34 ± 0.15	9.13 ± 0.45
BBDT > 0.25	39.6 ± 9.3	3.12 ± 0.33	4.14 ± 0.19	4.43 ± 0.13	7.74 ± 0.38
BBDT > 0.30	15.4 ± 5.8	2.73 ± 0.27	3.21 ± 0.15	3.51 ± 0.10	6.25 ± 0.27

Table 6.7: The mass resolution, signal yield and signal purity from the multivariate and cut-based $\Xi_c^+ \to pK^-\pi^+$ trigger lines.

Trigger	Resolution (MeV/c^2)	Yield per fb^{-1}	Purity ($\pm 2.5\,\sigma$)
Cut-based	6.46 ± 0.04	1.51×10^8	0.247
Multivariate-based	6.55 ± 0.05	2.06×10^8	0.123

The measured CPU time for the new trigger line using the preferred BBDT threshold is around 2.8 ms for each event processed, which is also acceptable.

6.4 Mass Distributions

Following the development and optimisation of the new trigger, the line was officially merged into the Moore software in July 2018 to start triggering on data. The results from the trigger line were initially monitored to check that its performance was as expected from the offline testing phase. The performance of the multivariate $\Xi_c^+ \to pK^-\pi^+$ trigger is ultimately judged by the yield of the retained $\Xi_c^+ \to pK^-\pi^+$ signal.

The invariant-mass distribution of Ξ_c^+ candidates reconstructed by the multivariate and cut-based $\Xi_c^+ \to pK^-\pi^+$ trigger line, during Run 211050 and Run 211944, which corresponds to an integrated luminosity of around 1.34 pb^{-1}, is shown in Figure 6.7. In both cases, a Gaussian function and a second-order polynomial are used to model the signal and background shapes of the $m(pK^-\pi^+)$ mass distribution, respectively, to estimate the mass resolution and yield of Ξ_c^+ baryons. Firstly, the mass resolution is consistent with one another, within their statistical uncertainty, and in both cases, the mean value is in keeping with the 2467.87 ± 0.30 MeV/c^2 world-average mass of the Ξ_c^+ baryon [1]. However, the signal efficiency is found to be better for the multivariate trigger by a factor of 1.36 ± 0.01. Yet notably, the signal-to-background ratio (the purity) in the $\pm 2.5\,\sigma$ signal region decreases by approximately half. A comparison of the signal qualities of the Ξ_c^+ candidates reconstructed by both triggers is summarised in Table 6.7.

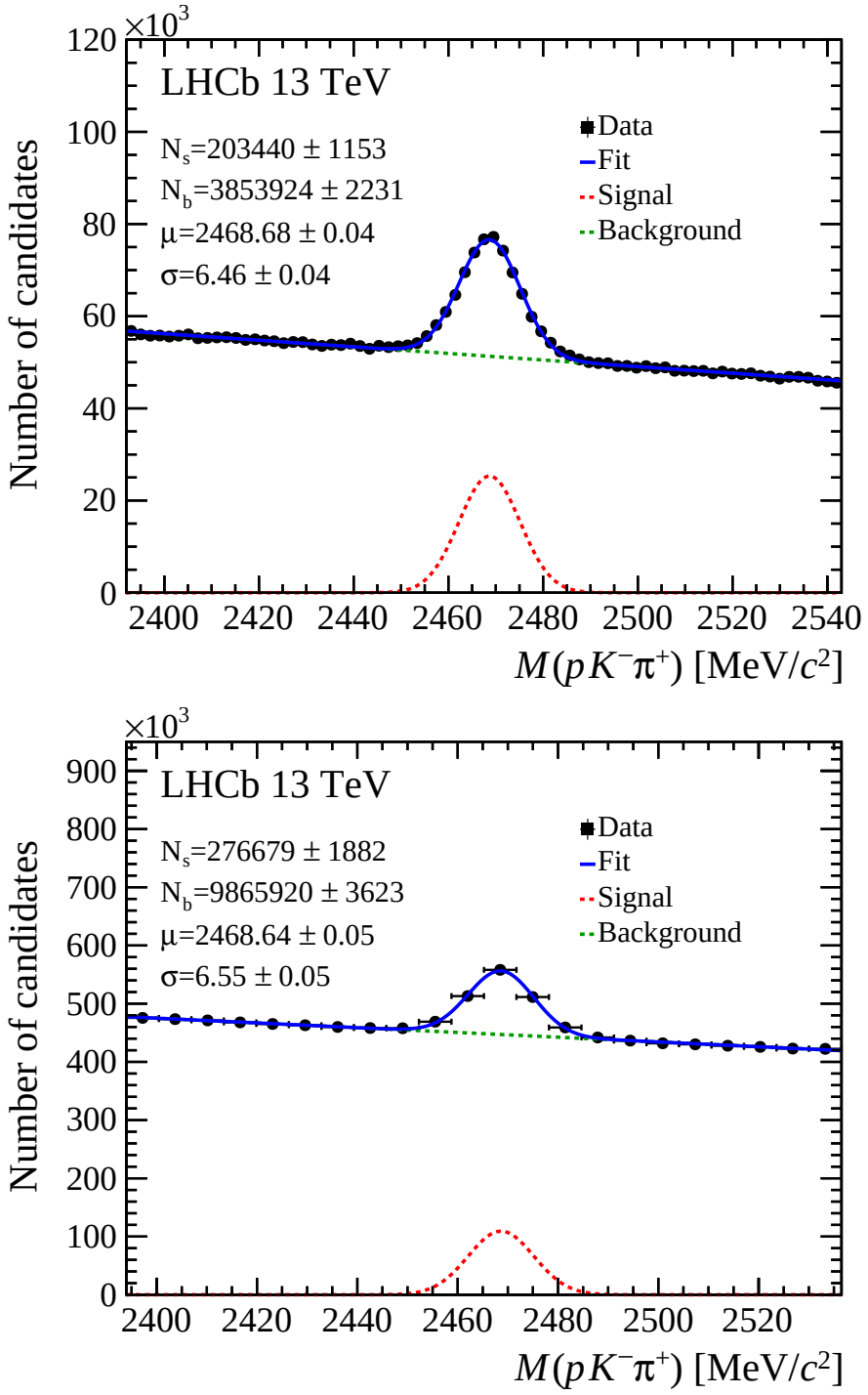

Figure 6.6: Invariant-mass distribution of Ξ_c^+ candidates from the (top) cut-based and (bottom) multivariate-based $\Xi_c^+ \to pK^-\pi^+$ trigger line. The (red) signal and (green) combinatorial background components of the fit are overlaid. The values of the signal and background yield from the fit are inserted on each plot.

6.5 Conclusion and Discussion

A new inclusive trigger line was developed for reconstructing $\Xi_c^+ \to pK^-\pi^+$ decays that uses the Bonzai Boosted DecisionTree method to efficiently separate signal events from background. The new multivariate-based trigger line is able to achieve a 36% gain in the yield of Ξ_c^+ candidates compared to the cut-based trigger line. Based on results with simulated events, the multivariate-based trigger is more sensitive to Ξ_c^+ baryons produced at the primary vertex and from other heavy hadrons including doubly-charmed baryons as well, with the caveat of having a higher rate. The unique selling point of this trigger line is that it achieves these improvements without using variables in its selection that are highly correlated to the origin of the Ξ_c^+ baryon. In this sense, the multivariate-based trigger is a more multi-purpose line; it is envisioned to be used for anything from spectroscopy studies to doubly-charmed-baryon searches in Run II and beyond into Run III.

The fact that the new multivariate trigger has a worse signal purity compared to the cut-based line is not a major concern. Analysts intending to use the multivariate-based $\Xi_c^+ \to pK^-\pi^+$ trigger can exploit the higher signal efficiency of the line to impose offline requirements on the Ξ_c^+ candidates and their daughters, such as on particle identification scores, to improve the purity, while benefiting from the larger sample of $\Xi_c^+ \to pK^-\pi^+$ decays straight from the trigger. Ultimately, the decision was always to maximize the signal efficiency and due to the limited computing resources at LHCb, it was decided that no more requirements, or training variables, can be utilised to suppress background further by the trigger. The final trigger configuration is thus a balance between the benefits for physics analyses and a sensible consideration of the bandwidth of the trigger.

6.6 Chapter Summary

This chapter described the development of a new HLT2 trigger line that was active during data taking from July 2018 to December 2018 and which is expected to be used in Run III. The new trigger uses a multivariate selection, implemented via a look-up table, to remove combinatorial background and retain signal events. Firstly, the motivation for developing a new trigger line is clearly explained before greater detail is given on the way in which the LHCb collaboration saves data more efficiently using their trigger, having entered into the more complex production environment of Run II. The BBDT method, a type of multivariate selection, which is the basis of the new trigger, is then thoroughly discussed. Next, a comprehensive overview of the design, testing and optimisation of the trigger is presented. The chapter concludes by disclosing the performance details of the new trigger and then discussing the results.

Chapter 7

Conclusion

"I have made this longer than usual because I've not had time to make it shorter."

– Blaise Pascal, French mathematician and philosopher

This thesis primarily presented two separate searches for the Ξ_{cc}^{++} particle, a doubly-charmed baryon with a *ccu* quark configuration. Intermingled with these core analyses, a study into the effects of the magnetic field on the measurements of the RICH-1 sub-detector at LHCb was described and the development of a new trigger line was explained.

7.1 Summary

The concept of doubly-charmed baryons was first introduced in Chapter 1 when the quark model was used to motivate their existence. The general properties, decay mechanisms and uses of doubly-charmed baryons are then described throughout the chapter within the framework of the Standard Model of particle physics. Chapter 1 concluded with a review of the expected promising search channels for doubly-charmed baryons that then inspired the main analyses detailed in this thesis.

The data examined in all the studies presented in this thesis were recorded by the LHCb detector at CERN in Geneva, Switzerland. This high-energy physics experiment was expertly designed for the study of particles that contain the relatively heavy charm and beauty quarks. In Chapter 2, each of the sub-detectors that comprise the LHCb detector were extensively described to give the reader a sense of their excellent performance capabilities. Time and emphasis is particularly given to the systems that are pivotal in the searches of doubly-charmed baryons.

The RICH systems of the LHCb detector was the focus of Chapter 3. A preliminary study was presented on the performance of the RICH-1 sub-detector, where the Cherenkov angle of tracks was measured without any knowledge of the momentum of the tracks. The aim of this study was to pinpoint the cause for a difference in the Cherenkov angle resolution from data and simulation. Despite not being able to locate the source of this

discrepancy, a method was successfully developed that allowed for saturated tracks to be selected without any direct momentum information. This method, implemented with the reconstruction software of the LHCb detector, has uses in various studies at LHCb where momentum information is not available or would bias a result.

The first search for the Ξ_{cc}^{++} baryon was described in Chapter 4. This analysis involved the study of the doubly-Cabibbo-favoured $\Xi_{cc}^{++} \to \Lambda_c^+ K^- \pi^+ \pi^+$ decay using two independent samples of the proton-proton collision data recorded by the LHCb detector in 2012 and 2016. The 2016 sample corresponded to an integrated luminosity of $1.7\,\text{fb}^{-1}$ of data and served as the main data sample for the analysis, while the 2012 sample matched to $1.1\,\text{fb}^{-1}$ of data but was recorded under less energetic collision conditions. Potential $\Xi_{cc}^{++} \to \Lambda_c^+ K^- \pi^+ \pi^+$ decays were selected and efficiently separated from background contributions using an artificial neural network. The neural network was trained to recognise $\Xi_{cc}^{++} \to \Lambda_c^+ K^- \pi^+ \pi^+$ decays using kinematic and topological attributes of the decay. An account of the methodology behind the fit to extract the mass of the Ξ_{cc}^{++} baryon and the cross-checks into potential sources of background are also given. Ultimately, the analysis resulted in the first-ever discovery of a doubly-charmed baryon, after a peak with a statistical significance greater 12σ was observed in the final $\Lambda_c^+ K^- \pi^+ \pi^+$ mass spectrum. The mass of the newly-found state was measured to be

$$m(\Xi_{cc}^{++}) = 3621.40 \pm 0.72\,(\text{stat}) \pm 0.27\,(\text{syst}) \pm 0.14\,(\Lambda_c^+)\,\text{MeV}/c^2,$$

where the first and second uncertainties was statistical and systematic, respectively, while the last uncertainty was due to the limited knowledge on the mass of the singly-charmed Λ_c^+ baryon. The measured mass was in line with the majority of theoretical predictions for a ground-state doubly-charmed baryon. The signal was also found to be consistent with that of a weakly decaying state. The general reaction to this result was wide-spread with many in the field regarding it as a hugely important moment in flavour physics.

Following the success of the $\Xi_{cc}^{++} \to \Lambda_c^+ K^- \pi^+ \pi^+$ analysis, the aim of the work described in Chapter 5 was to re-discover the Ξ_{cc}^{++} state through another decay mode. The $\Xi_{cc}^{++} \to D^+ p K^- \pi^+$ channel was chosen based on its experimentally favourable attributes. The same 2016 data sample and a very similar data selection process to that used in the $\Xi_{cc}^{++} \to \Lambda_c^+ K^- \pi^+ \pi^+$ analysis were deployed in this study. Rigorous mass model studies and background checks were also again carried out before data containing potential signal was scrutinized. In the end, no clear signal of the $\Xi_{cc}^{++} \to D^+ p K^- \pi^+$ decay was observed in the 2016 data. Instead, an upper limit was set on its branching fraction relative to the $\Xi_{cc}^{++} \to \Lambda_c^+ K^- \pi^+ \pi^+$ discovery channel at the 90% (95%) confidence level, which was measured to be

$$\frac{\mathcal{B}(\Xi_{cc}^{++} \to D^+ p K^- \pi^+)}{\mathcal{B}(\Xi_{cc}^{++} \to \Lambda_c^+ K^- \pi^+ \pi^+)} < 1.7\,(2.1) \times 10^{-2}.$$

This result helps gauge the amount of data needed in the future before a discovery of the rarer $\Xi_{cc}^{++} \to D^+ pK^-\pi^+$ decay is possible and, more importantly, it aids towards a better understanding of the decay mechanisms of doubly heavy-flavoured baryons.

Finally, Chapter 6 described the development of a new trigger line that was designed to capture $\Xi_c^+ \to pK^-\pi^+$ decays using a multivariate classifier based on the Boosted Decision Tree method. The selection criteria of the trigger was also designed in such a way to be minimally dependent on the lifetime of the Ξ_c^+ baryon. The final product showed a 36% increase in the number of Ξ_c^+ signals compared to the previous trigger line still in use at the LHCb detector. This included marginally better sensitivity to Ξ_c^+ baryons originating from doubly-heavy baryons, based on the results with simulation. The new trigger is also more inclusive and less sensitive to the source of the Ξ_c^+ baryon.

7.2 Outlook

Before any of the research described in this thesis had begun, no doubly-charmed baryon had ever been unambiguously observed. Since then, huge progress has been made in the doubly-charmed baryon sector by the LHCb collaboration. In 2017, the first-ever doubly-charmed baryon, the Ξ_{cc}^{++} (ccu) state, was discovered in the $\Xi_{cc}^{++} \to \Lambda_c^+ K^-\pi^+\pi^+$ channel [157] by LHCb, who then followed this up with a confirmation of the same state through the $\Xi_{cc}^{++} \to \Xi_c^+\pi^+$ decay mode in 2018 [180]. Soon after that, LHCb measured the lifetime of the Ξ_{cc}^{++} baryon, confirming the weakly decaying nature of the discovered Ξ_{cc}^{++} baryon [174]. Most recently, an upper limit of a relative branching fraction of the rarer $\Xi_{cc}^{++} \to D^+ pK^-\pi^+$ decay mode of the Ξ_{cc}^{++} baryon was established [175].

Yet, for all these milestones, there remains countless more studies that need to be performed in this field of research. If doubly-charmed baryons are going to be used to reduce theoretical uncertainties in models of quantum chromodynamics, it will be necessary to discover more than just one or two states. Since the conflict between the claimed Ξ_{cc}^+ state reported by the SELEX group and the observation of the Ξ_{cc}^{++} state by LHCb prevails, another search for the Ξ_{cc}^+ state remains the priority. This result is hotly anticipated by the particle physics community and with increased data in Run II, LHCb are hopeful of resolving this long-term puzzle sooner rather later. Note that the lifetime of the spin-1/2 Ξ_{cc}^+ state is now expected to have a lifetime between 80–100 fs given the 256 fs lifetime measurement of the Ξ_{cc}^{++} state. Other important follow-up studies that are planned by LHCb include a measurement of the production cross section of the Ξ_{cc}^{++} baryon and searches for the Ω_{cc}^+ (ccs) doubly-charmed baryon, which LHCb should still be sensitive to with Run II data, despite its expected smaller production rate than the Ξ_{cc} baryons. From the biased point of the view of the author, the $\Xi_{cc}^{++} \to D^+ pK^-\pi^+$ decay mode should be given more attention and it should be the focus of a search within the already available

2017 and 2018 data. Furthermore, decay modes of doubly-charmed baryons that include a singly-charmed Ξ_c^+ baryon in the final state can be examined with improved efficiency using the multivariate-based trigger line that offers a greater yield of Ξ_{cc}^+ candidates than what was possible before.

The spectroscopy of excited doubly-charmed states will also help probe QCD calculations, since the dynamics of doubly-heavy baryons is expected to be different from that of singly-heavy baryons. However, observations of excited states are likely to require significantly larger data samples than are currently available at LHCb. As a point of interest, the LHCb collaboration also has a programme of searches for the doubly-heavy Ξ_{bc} baryons as well. The $\Xi_c^+ \to pK^-\pi^+$ trigger described in Chapter 6 can contribute to these search efforts.

Thinking further ahead then to Run III and the LHC High-Luminosity phase [186], several more studies should be possible with the vastly greater amounts of data. Certainly, a more accurate measurement of the Ξ_{cc}^{++} baryon's mass is attainable, given that the dominant uncertainty is statistical in nature at the moment. An improvement in measured lifetime of the Ξ_{cc}^{++} baryon, where the overall uncertainty is quite large, is equally expected with the acquisition of more data. Additionally, even though the newly discovered Ξ_{cc}^{++} baryon is expected to have a spin of a half, a direct spin measurement may be possible following a full angular analysis with more data. It is also conceivable that CP-violation studies might be possible with doubly-charmed baryons.

Finally, it would be fair to say that the LHCb collaboration has almost solely written the book on doubly-charmed baryons thus far. Yet, it is actually the hope of LHCb and other groups that doubly-charmed baryons can be confirmed by other experiments as well. The prospects for a synergy with LHCb and the Belle-II experiment [187] in Japan appear promising with the upgraded Belle detector offering a complimentary environment for searches of doubly-charmed baryon to that of LHCb. In summary, the experimental field of doubly-charmed-baryon physics has really just been born in the last few years but no doubt it has an exciting and 'charming' future ahead of it.

Appendix A

Biases from Turbo Processing

This appendix describes a bias that is found to exist following the processing of data by the Turbo software at LHCb. This bias leads to the masses of certain open-charm hadrons being shifted from their known value. This includes a shift of $0.8\,\text{MeV}/c^2$ for the Λ_c^+ baryon from $\Lambda_c^+ \to pK^-\pi^+$ decays and $0.2\,\text{MeV}/c^2$ for the D^+ meson in $D^+ \to K^-\pi^+\pi^+$ decays. The LHCb collaboration first noticed this effect during a measurement of the masses and iospin splitting of the Σ_c baryons [188].

One hypothesis considered by the LHCb collaboration for the cause of this phenomenon was from the offline momentum scaling of tracks, which was first mentioned in Section 4.5.2. As a reminder, the masses of heavy hadrons are found to agree within $\pm 0.3‰$ of their known values after this calibration procedure. However, following studies performed on Run II data, before the time of the PhD candidate, it was found that the large biases of charm hadron masses were not due to incorrect momentum scaling, but due to selection requirements on decay time related variables that favoured candidates with longer lifetime. These variables include the decay time, the χ^2_{IP} of decay products and the DIRA variable. It was found that if the selection criteria of Turbo lines favour candidates with longer decay time then it also favours candidates with larger invariant mass. This can be problematic for studies involving short-lived particles.

The momentum-scaling correction factors for different decay modes, scaled by their energy release, Q, are shown in Figure A.1. The values given are before any corrections are applied to account for the lifetime-biasing effect discussed above. Notably, the shift of the reconstructed Λ_c^+ mass is very large and inconsistent with the other heavy hadrons. The shift of $0.8\,\text{MeV}/c^2$ in the reconstructed Λ_c^+ mass in data results in a correction of $\alpha = \Delta\text{M}/Q \approx 1.1‰$. In Figure A.1, final-state radiation in each decay mode has been corrected for and in the case of any b-hadrons, the masses of their decay products (*i.e.* the Λ_c^+ and J/ψ particles) have been constrained to their known values. From Figure A.1 it can be seen that the detached J/ψ meson's mass has a correction consistent with zero,

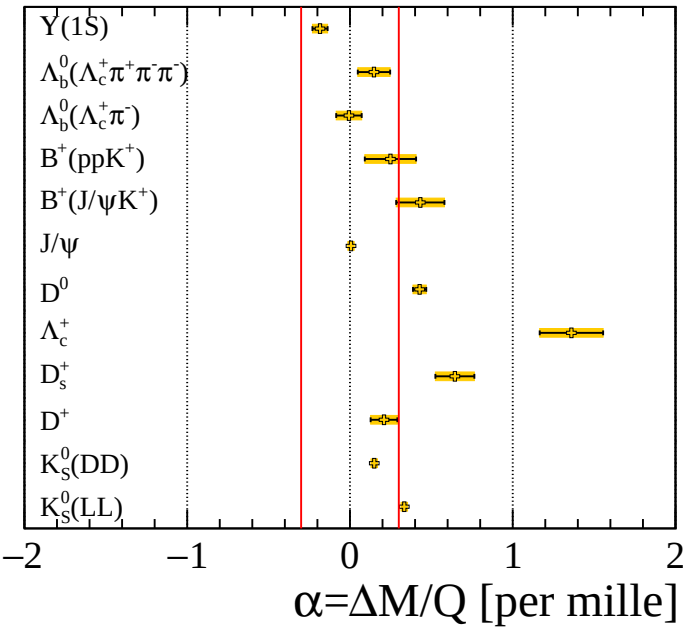

Figure A.1: The momentum-scaling-correction factor, $\alpha = \Delta M/Q$, for different decay modes of heavy hadrons.

the corrections for the b-hadrons and the K_S^0 meson are mostly within the $\pm 0.3‰$ level but the corrections for the open-charm hadrons are significantly larger.

To validate the idea that selection requirements related to lifetime information are causing this mass biasing effect, the reconstructed mass of the Λ_c^+ baryon is independently checked for the $\Xi_{cc}^{++} \to \Lambda_c^+ K^- \pi^+ \pi^+$ analysis by LHCb colleagues of the PhD candidate. This procedure was carried out using simulated events, where the generated mass of the Λ_c^+ baryon is equal to its world-average $2268.48\,\mathrm{MeV}/c^2$ value [1]. Following the application of the Turbo selection requirements stated in Table 4.2, a large mass bias of approximately $1.3\,\mathrm{MeV}/c^2$ is found for the reconstructed Λ_c^+ baryon. The $\Xi_{cc}^{++} \to \Lambda_c^+(\to pK^-\pi^+)K^-\pi^+\pi^+$ decays are then reconstructed and selected using lifetime unbiased selections, namely no information related to the decay time of the Λ_c^+ baryon is utilised. The mean value of the mass of the Λ_c^+ baryon for events in different reconstructed decay-time intervals is shown in the left plot of Figure A.2. The first bin corresponds to no requirements on decay-time information. The average Λ_c^+ mass in this bin is already higher than the generated value used in simulation by around $0.4\,\mathrm{MeV}/c^2$ because the momentum scaling calibration is not applied in simulation. Consistently, the observed mean mass is found to increase when tighter requirements are imposed on the reconstructed decay time of Λ_c^+ baryons. The distribution of the average mass of the reconstructed Λ_c^+ candidate after its decay time is required to be greater than the value of the left bin boundary is also shown in the left plot of Figure A.2.

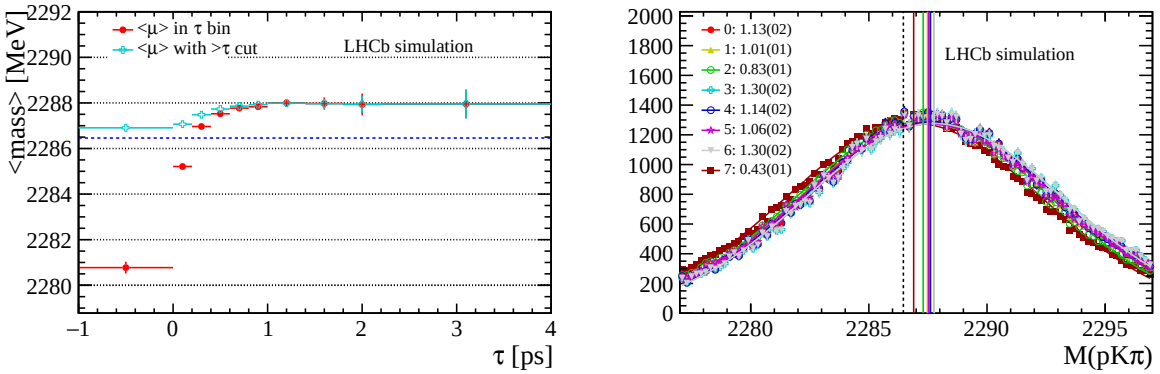

Figure A.2: Information on Λ_c^+ baryons from a simulated $\Xi_{cc}^{++} \to \Lambda_c^+ K^- \pi^+ \pi^+$ sample; (left) the mean value of the Λ_c^+ mass for (red) events in each bin of reconstructed decay time and (cyan) passing the decay-time requirement of left boundary of each bin; and (right) the invariant-mass distribution of Λ_c^+ particles for selections 0–7, which are described in the main text, with the corresponding bias and uncertainty shown in the legend. The blue-dashed horizontal (vertical) line in the left (right) plot shows the generated Λ_c^+ mass value used in the simulation.

The Λ_c^+ mass distribution after seven variations of the selection criteria is shown in the right plot of Figure A.2. The vertical lines correspond to mean value of the mass distribution after a set selection, while the legend gives the bias of the mass for each distribution for each selection variation, where the uncertainty is given in brackets. Selection 7 is the case when there is no requirements related to decay time applied, in which the mass is biased by $0.4\,\text{MeV}/c^2$, consistent with the left plot of Figure A.2. Selections 0–6 make use of different combinations of the lifetime related requirements in the $\Xi_{cc}^{++} \to \Lambda_c^+ K^- \pi^+ \pi^+$ Turbo line (Λ_c^+ decay-time, track χ^2_{IP}, DIRA variable *etc.*, see Table 4.2). Selection 6 corresponds to the case when all of the decay-time-related requirements are applied and this results in a bias of approximately $0.9\,\text{MeV}/c^2$. These findings show that the bias clearly depends on the strictness of the selection. It is expected that for particles with a relatively long lifetime, the same selection would yield a smaller bias. This was the case for the D^+ meson compared to the Λ_c^+ meson.

The shift in mass for the heavy hadrons after correcting for this selection bias, is shown in Figure A.3, from which it can be concluded that the values are now in good agreement as they reside within the quoted uncertainty $\pm 0.3‰$. It can be concluded for these results that the momentum scaling calibration works suitably well for these heavy hadrons.[1] In summary, the momentum scaling calibration in Run II works well and the

[1]The bias due to selections can in principle affect the detached J/ψ candidates, which are used to make the default momentum calibration. However, after comparing the observed mean mass in the prompt J/ψ sample (where no decay time information is used) with that in the detached J/ψ sample, a bias which is negligible compared to the quoted systematic uncertainty is observed.

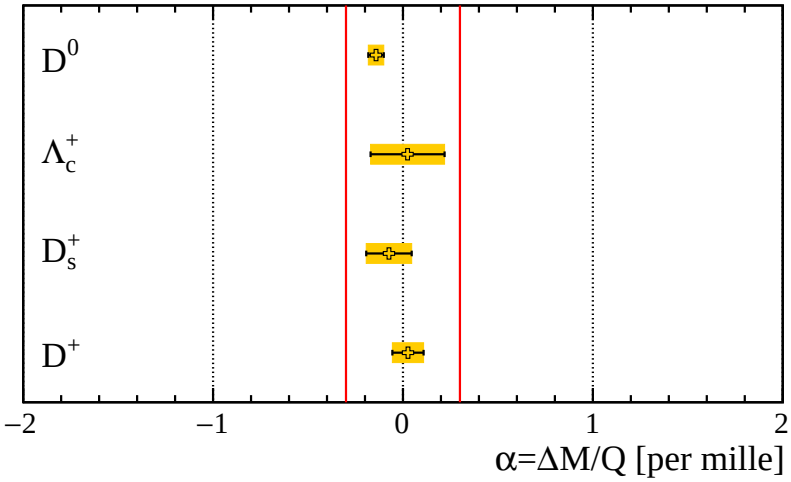

Figure A.3: Momentum-scaling-correction factors, $\alpha = \Delta M/Q$, for a select set of charm hadrons after the correction of lifetime-biasing requirements.

quoted systematic uncertainty of 0.3‰ is sufficient to cover the variations among various decay modes of heavy hadrons.

Appendix B

$\Xi_{cc}^{++} \to \Lambda_c^+ K^- \pi^+ \pi^+$ Run I Analysis

Before the $\Xi_{cc}^{++} \to \Lambda_c^+ K^- \pi^+ \pi^+$ analysis was upgraded to include Run II data, the PhD candidate was highly involved in the event selection of 2012 data. This selection was adapted however, following the final design of the 2016 candidate selection, as is explained in this Appendix. The offline selection is very similar to the one used for the 2016 data, the major difference is in the online processing of data. A brief overview of the selection studies carried out on the 2012 data is given here.

B.1 Data and MC Samples

The selection was devised using the 2012 data and 2012 MC samples, recorded, and simulated, under equal amounts of time of MagUp and MagDown magnetic field conditions. The Ξ_{cc}^{++} candidates are taken from the output of three dedicated Stripping lines, which like the Turbo lines in the analysis of 2016 data, reconstruct RS, WS and DCS decays.

B.2 Selection

The selection requirements used in these stripping lines are summarised in Table B.1. By comparing the selection criteria in Table B.1 with those in Table 4.2, one can see that a few requirements in the Stripping are tighter than those in Turbo. Hence, identical online selections cannot be adopted for the 2012 and 2016 data sets.[1]

Based on the idea that requirements of both data sets should be as similar as possible, three different strategies are trialled for the offline selections of the 2012 data:

[1] Apart from the transverse momenta of the Λ_c^+ tracks, the PID of the π^+ track from Λ_c^+ candidates and the maximum DOCA of the Ξ_{cc}^{++} candidate, other selection requirements are generally more loose.

1. The preselection requirements are made to be as similar to the ones used in the 2016 analysis (tight) and the MVA classifier is trained with the 2012 data and MC samples;

2. The preselection requirements are kept reasonably loose and the MVA classifier is trained with the 2012 data and MC samples;

3. The preselection requirements are made to be as similar to the ones used in the 2016 analysis but the 2016 MVA classifier is directly applied to the 2012 data instead.

For the MVA training and the optimisation of the multivariate selection, the same procedure as used in the analysis of 2016 data is adopted *i.e.*, the same training variables (see Section 4.4) are used, the same MVA classifiers are tested (MLP, MLPBNN, BDT, BDTG), and the Punzi figure of merit is used to optimise the MVA selection. In case that there is no significant improvement for the first and the second strategies, the third strategy is preferred, since it makes the comparison of the efficiencies between the 2012 and 2016 selections slightly easier.

The correlation matrices between the training variables in the signal and background samples for scenario one (tighter cuts) and scenario two (looser cuts) are shown in Figure B.1. The background rejection versus signal efficiency curves are shown in Figure B.2 and the MVA output distributions for the over-training tests are shown in Figure B.3 and Figure B.4 for scenario one and scenario two, respectively. The FoM as a function of the requirement on the MVA response, for all three scenarios, is shown in Figure B.5. The optimal values of the MVA selections and the corresponding signal efficiencies, FoM values and the expected number of background events is given in Table B.2. From these results, it can be seen that scenario one and scenario two do improve the Punzi FoM score, especially for scenario two with looser preselection requirements but not significantly. Equally, there was concerns of some of the classifiers becoming over-trained, especially the BDT method, as can be seen from the Kolmogorov−Smirnov test scores in Figures B.3 and B.4. Therefore, the preferred course of action is to choose scenario three and apply the same 2016 multivariate classifier (the MLP) directly to the 2012 data. The preselection requirements are made to be the same as those used in the 2016 data, except for the tighter requirements that are already used in the stripping lines.

Table B.1: Selection criteria of the stripping lines used in the analysis of 2012 data. The requirements highlighted in red are different to their analogous requirement in the 2016 Turbo lines, show in Table 4.2.

Candidate	Variable	Requirement
Daughters of Λ_c^+	Track quality	$\chi^2/\text{ndf} < 3$
	Momentum	$p > 1\,\text{GeV}/c$
	Transverse momentum	$p_\text{T} > 250\,\text{MeV}/c$
	Arithmetic sum of daughter p_T	$> 3\,\text{GeV}/c$
	Impact parameter significance	$\chi^2_\text{IP} > 6$
	Proton momentum	$> 10\,\text{GeV}/c$
	Proton PID	$\text{DLL}_{\pi} > 5$ & $\text{DLL}_{pK} > 5$
	Kaon PID	$\text{DLL}_{K\pi} > 5$
	Pion PID	$\text{DLL}_{K\pi} < 0$
	Maximum p_T	$> 1\,\text{GeV}/c$
	Second maximum p_T	$> 400\,\text{MeV}/c$
	Maximum χ^2_IP	> 16
	Second maximum χ^2_IP	> 9
Λ_c^+ mother	Vertex quality	$\chi^2_\text{vtx}/\text{ndf} < 10$
	Cosine of DIRA	> 0.99995
	Decay time	$\tau > 0.15\,\text{ps}$
	Mass	$[2200, 2350]\,\text{MeV}/c^2$
Daughters of Ξ_{cc}^{++}	Track quality	$\chi^2/\text{ndf} < 3$
	Transverse momentum	$p_\text{T} > 500\,\text{MeV}/c$
	Momentum	$p > 1\,\text{GeV}/c$
	Kaon PID	$\text{DLL}_{K\pi} > 10$
	Pion PID	$\text{DLL}_{K\pi} < 0$
Ξ_{cc}^{++} mother	Vector sum of daughter p_T	$> 2\,\text{GeV}/c$
	Vertex quality	$\chi^2_\text{vtx}/\text{ndf} < 60$
	DV of Λ_c^+ w.r.t. Ξ_{cc}^{++}	$(z_{\Lambda_c^+} - z_{\Xi_{cc}^{++}}) > 0.01\,\text{mm}$
	Distance of Closest Approach	$\text{DOCA} < 5\,\text{mm}$

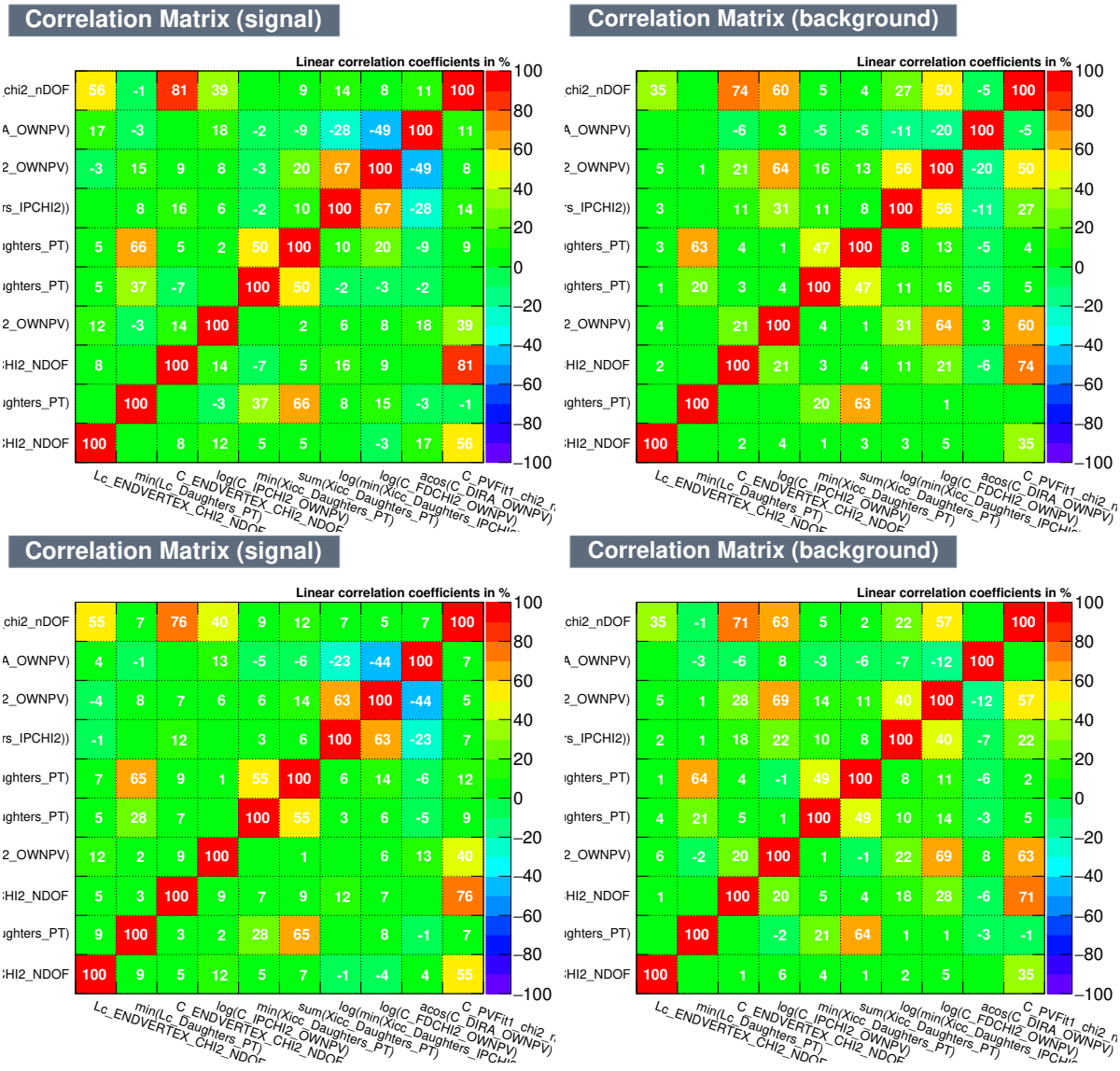

Figure B.1: Correlation matrices for the ten variables used in the multivariate classifier for (left) signal and (right) background with (top) scenario one (tighter preselection) and (bottom) scenario two (looser preselection) compared. These plots are for the 2012 data.

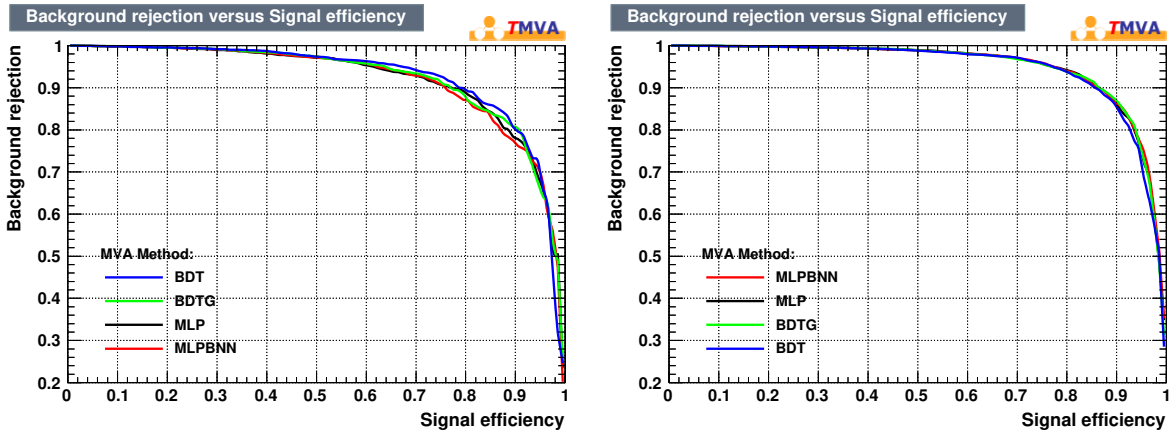

Figure B.2: Background rejection versus signal effficiency curves for four multivariate classifiers in the 2012 sample with (left) scenario one (tighter preselection) and (right) scenario two (looser preselection) compared.

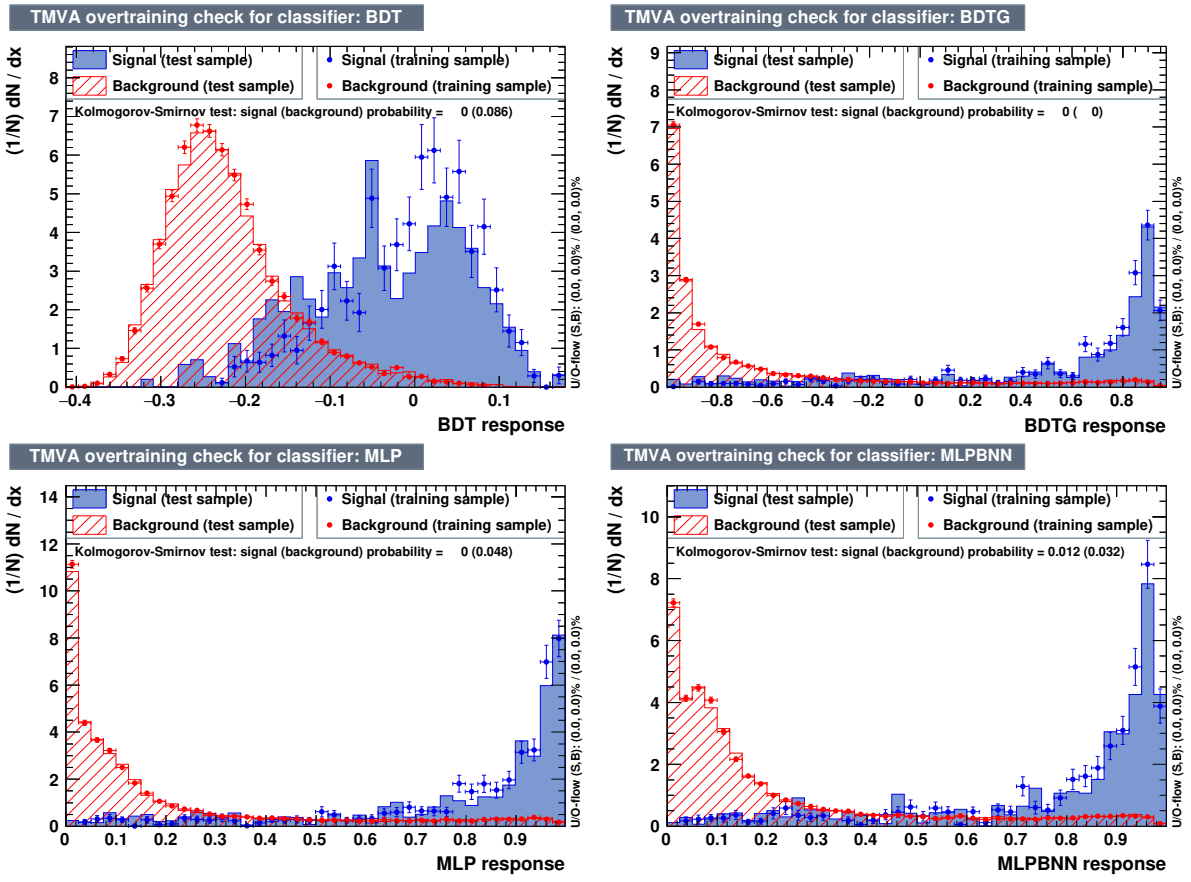

Figure B.3: Response curves of four classifiers for scenario one (tighter preselection): (top left) BDT, (top right) BDTG, (bottom left) MLP and (bottom right) MLPBNN.

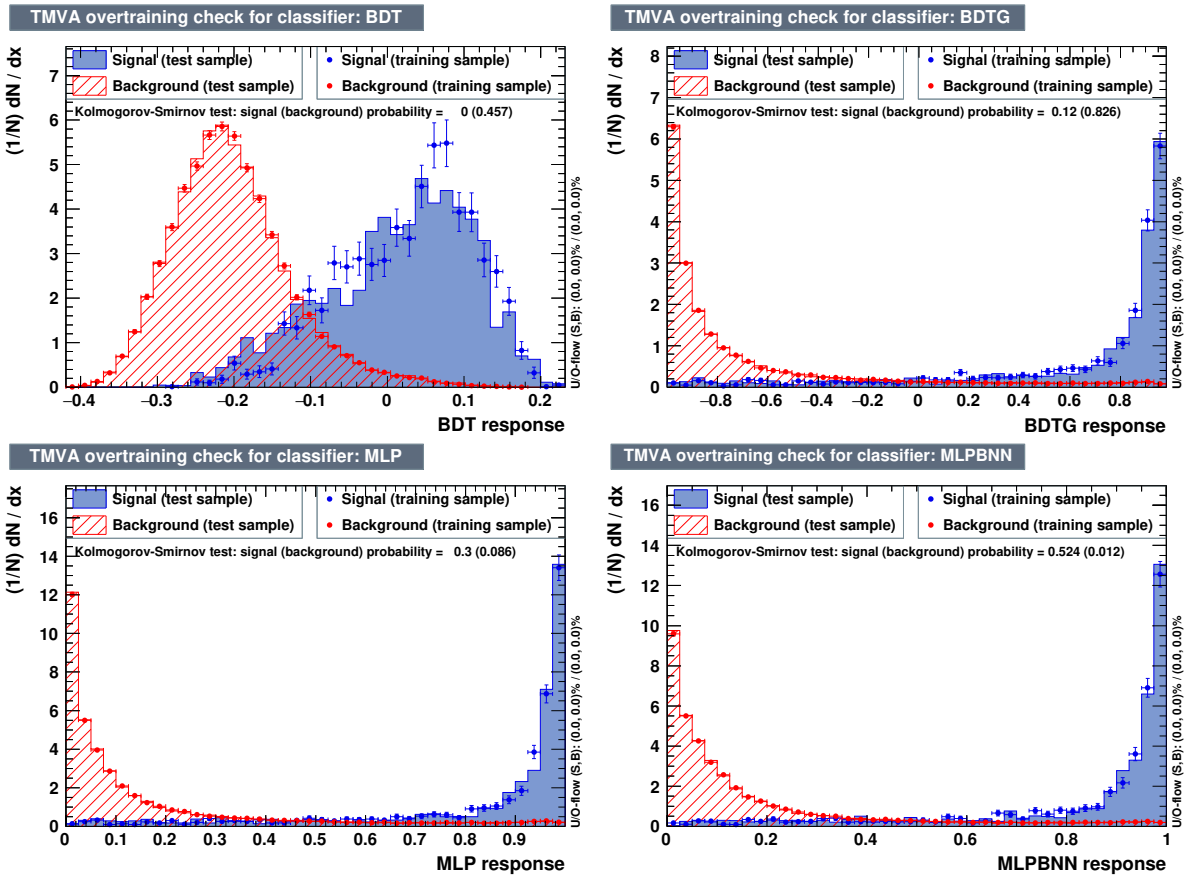

Figure B.4: Response curves of four selectors for scenario two (looser preselection): (top left) BDT, (top right) BDTG, (bottom left) MLP and (bottom right) MLPBNN.

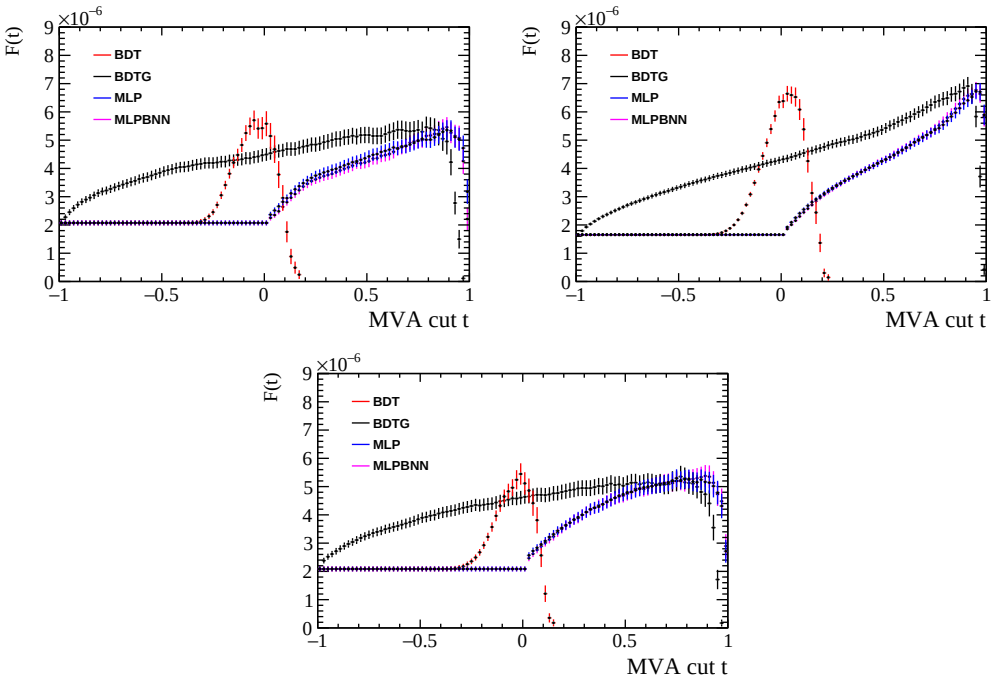

Figure B.5: Punzi figure of merit, F(t), dependency on the response requirement for four different multivariate classifiers in the 2012 data. The top left and top right figures are for scenarios one and two, while the bottom figure refers to scenario three.

Table B.2: The optimal response requirements for four multivariate classifiers with the corresponding relative signal efficiencies, figure of merit (FoM) scores and the expected number of background events in the signal region, all given. Here $\varepsilon_{\mathrm{MVA|Presel}}$ is defined as the relative signal efficiency of the classifier with respect to the preselection, Results for the three different selection scenarios are shown.

	Classifier	Optimal cut t	$\varepsilon_{\mathrm{MVA|Presel}}$	FoM ($\times 10^{-6}$)	#Expected bkg.
Scenario 1	BDT	-0.06	0.634 ± 0.028	5.70 ± 0.34	187
	MLP	$+0.88$	0.554 ± 0.029	5.36 ± 0.35	157
	BDTG	$+0.78$	0.505 ± 0.029	5.46 ± 0.38	120
	MLPBNN	$+0.88$	0.548 ± 0.029	5.46 ± 0.36	146
Scenario 2	BDT	$+0.02$	0.532 ± 0.019	6.64 ± 0.28	604
	MLP	$+0.94$	0.547 ± 0.019	6.72 ± 0.28	627
	BDTG	$+0.90$	0.443 ± 0.019	6.91 ± 0.32	367
	MLPBNN	$+0.94$	0.534 ± 0.019	6.78 ± 0.28	583
Scenario 3	BDT	-0.02	0.496 ± 0.021	5.45 ± 0.38	118
	MLP	$+0.74$	0.626 ± 0.020	5.30 ± 0.32	220
	BDTG	$+0.76$	0.487 ± 0.021	5.35 ± 0.38	111
	MLPBNN	$+0.88$	0.473 ± 0.021	5.38 ± 0.38	108

Appendix C

PID Calibrations with PIDCalib

The hadron PID efficiencies of final-state tracks in both the $\Xi_{cc}^{++} \to \Lambda_c^+ K^- \pi^+ \pi^+$ and $\Xi_{cc}^{++} \to D^+ p K^- \pi^+$ analyses are estimated from data samples using `PIDCalib` [161].

Clean samples of proton, pion and kaon tracks in data are obtained without any use of particle identification requirements but using only kinematic and topological information. Kaon and pion calibration tracks come from tagged $D^{*+} \to D^0(\to K^-\pi^+)\pi^+$ decays. The `sPlot` technique [172] is used to subtract the background contribution in this decay channel. As for the protons calibration sample, they are taken from $\Lambda^0 \to p\pi^-$ decays, since Λ^0 baryons are abundantly produced at LHCb and their relatively long decay times already allow for inherently good background discrimination.

The PID efficiencies are calculated as functions of momentum, p, and pseudorapidity, η, with MagUp and MagDown samples evaluated separately [189]. The binning scheme used for all final-state tracks in the studies of Ξ_{cc}^{++} decays is given in Table C.1. Note that different binning schemes were investigated for each unique track type but the differences were negligible so the same binning-scheme for each track was adopted. The two-dimensional p-η distributions from the data samples used to calibrate the MC events under the chosen binning scheme are shown in Figure C.1. The efficiencies in bins of (p, η) in simulation are then weighted using the (p, η) efficiencies found using the data calibration samples to estimate the average PID efficiency. These weights, used to correct the efficiency differences between simulation and data, are also extracted by `PIDCalib` and used in the preselection and multivariate selections of both the Ξ_{cc}^{++} search analyses.

Table C.1: The binning scheme used for the PID calibration of all final-state tracks in the studies of Ξ_{cc}^{++} decays.

Variable	Binning scheme
p (GeV/c)	2 : 5.6 : 9.2 : 1.28 : 1.64 : 20 : 26 : 32 : 38 : 44 : 50 : 56 : 62 : 68 : 74 : 80 : 90 : 100 : 110 : 120 : 150
η	1.5 : 2.25 : 2.5 : 2.75 : 3 : 3.25 : 3.5 : 3.75 : 4 : 4.33 : 5

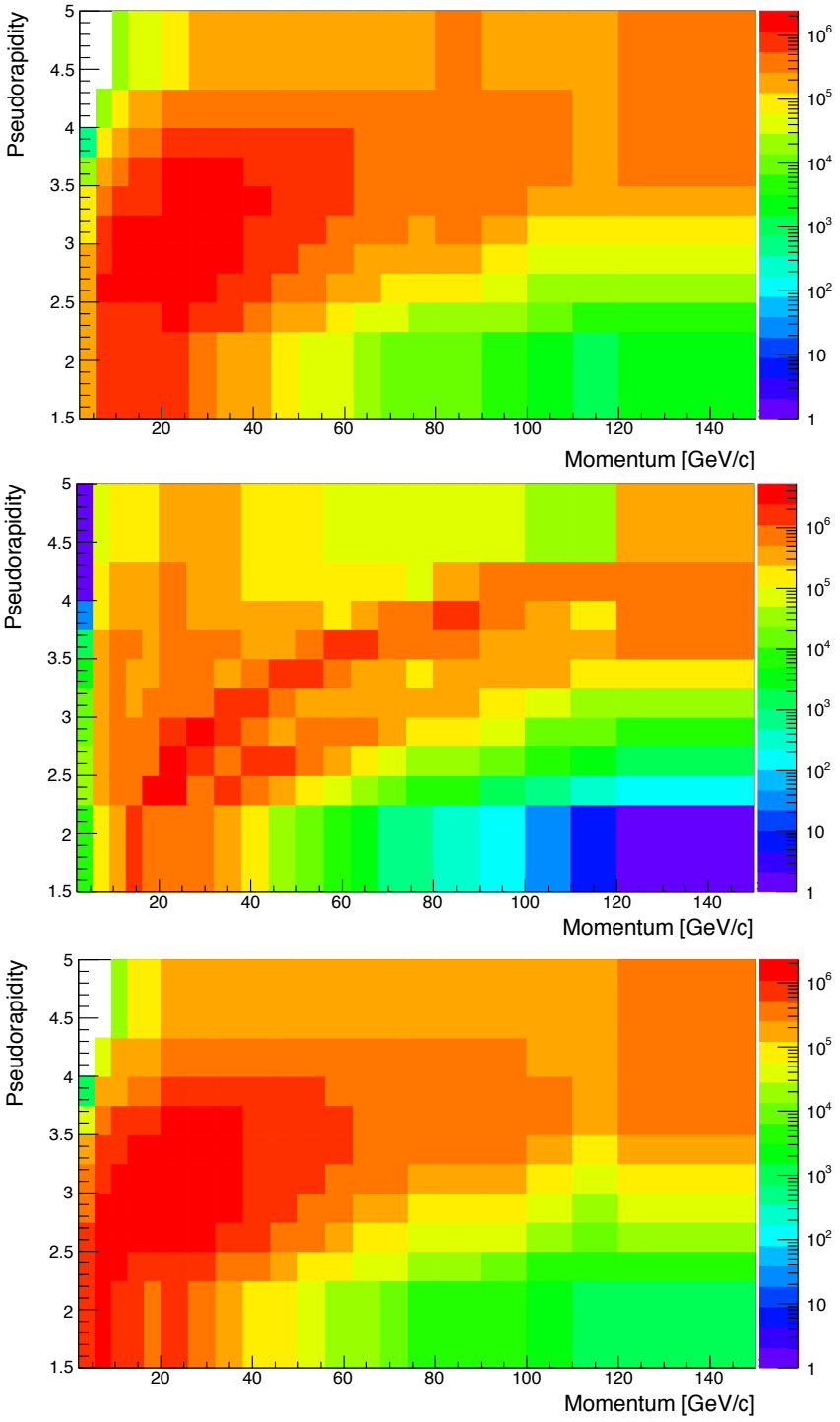

Figure C.1: Two-dimensional distributions of momentum, p, and pseudorapidity, η, variables for (top) kaons, (middle) protons and (bottom) pions for the 2016 MagDown data calibration samples. The z-axis gives the number of events on a logarithmic scale.

Appendix D

Efficiencies in Phase Space

The efficiencies calculated for the ratio of branching fractions measurement in Section 5.7 are averaged over the entire phase space assuming that there are no significant structures in the invariant-mass distribution caused by strongly-decaying resonances.

This appendix describes studies into the phase-space distribution of the Ξ_{cc}^{++} candidates in the $\Xi_{cc}^{++} \to D^+ p K^- \pi^+$ and $\Xi_{cc}^{++} \to \Lambda_c^+ K^- \pi^+ \pi^+$ decay modes in both data and simulation and the possible implications of such results on the selection efficiencies.

The invariant-mass distributions of combinations of tracks originating from the Ξ_{cc}^{++} baryon as well as the open-charm track (the D^+ meson or Λ_c^+ baryon) are shown in Figure D.1 and Figure D.2 for the $\Xi_{cc}^{++} \to D^+ p K^- \pi^+$ and $\Xi_{cc}^{++} \to \Lambda_c^+ K^- \pi^+ \pi^+$ decay modes. Both the results from data and simulation are shown and the distributions correspond to the Ξ_{cc}^{++} candidates that have passed their respective selection requirements, apart from that of the hardware-trigger.[1] In almost all cases, the results in data and simulation look similar, apart from in the $\Lambda_c^+ K^-$ and $\Lambda_c^+ \pi^+$ combination.

However, the more important distribution to check is the ratio of efficiencies between the $\Xi_{cc}^{++} \to D^+ p K^- \pi^+$ and $\Xi_{cc}^{++} \to \Lambda_c^+ K^- \pi^+ \pi^+$ decay modes, particularly in the simulated MC events as the ratio of branching fractions measurement is sensitive to this quantity only and the efficiencies quoted in Section 5.7.3 are determined using MC samples. The ratio of efficiencies, from arbitrarily comparing different track combinations in the $\Xi_{cc}^{++} \to D^+ p K^- \pi^+$ and $\Xi_{cc}^{++} \to \Lambda_c^+ K^- \pi^+ \pi^+$ decay modes, are shown in Figure D.3. The distributions are mostly flat across the invariant mass ranges studied in the respective decay modes but due to the difference in the masses of the final-state particles there is inevitably some observed variation. However, it can safely be assumed that the efficiency ratio does not vary hugely depending on potential resonant structures and that evaluating efficiencies using simulated events is safe. A systematic uncertainty is therefore not assigned for the effect of potential resonances on selecting Ξ_{cc}^{++} candidates.

[1] Background is subtracted using the `sPlot` method [172] in the case of $\Xi_{cc}^{++} \to \Lambda_c^+ K^- \pi^+ \pi^+$ data whereas the $\Xi_{cc}^{++} \to D^+ p K^- \pi^+$ data represents all Ξ_{cc}^{++} candidates passing the event selection.

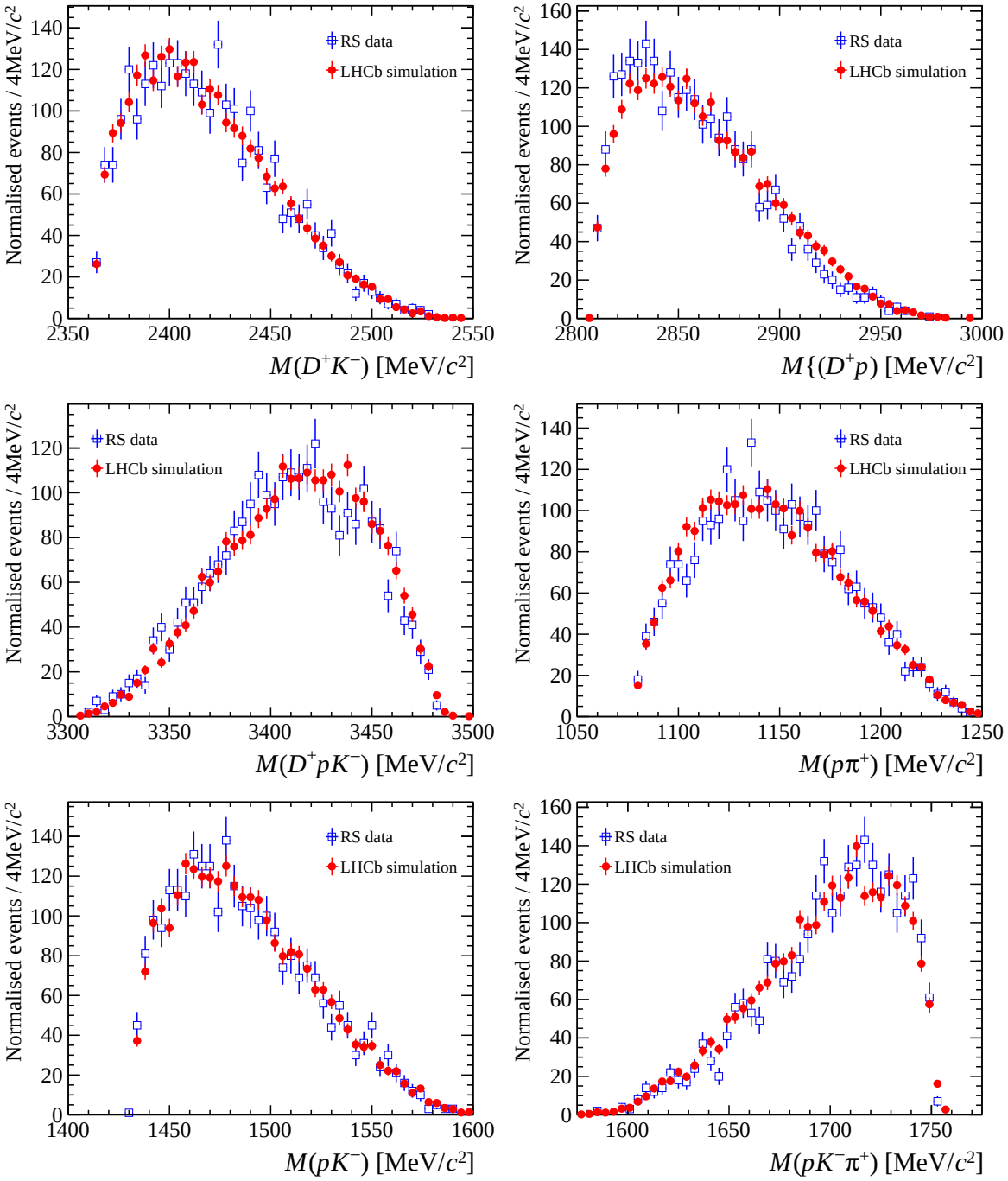

Figure D.1: Projections from the invariant-mass combinations of tracks originating from the Ξ_{cc}^{++} candidate in (red) simulated $\Xi_{cc}^{++} \to D^+pK^-\pi^+$ and (blue) $\Xi_{cc}^{++} \to D^+pK^-\pi^+$ data. The distributions from simulated events have been normalised to data.

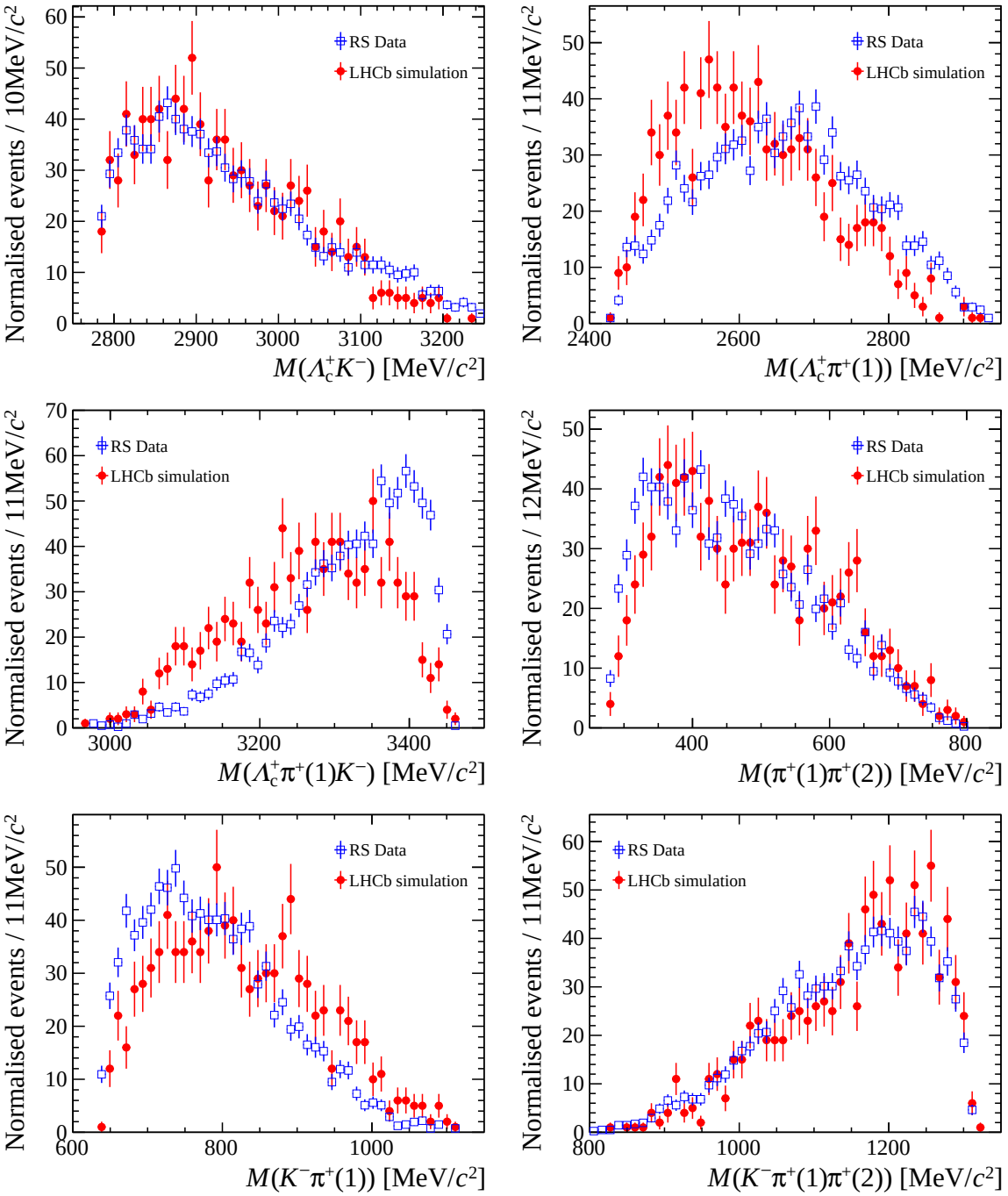

Figure D.2: Projections from the invariant-mass combinations of tracks originating from the Ξ_{cc}^{++} candidate in (red) simulated $\Xi_{cc}^{++} \to \Lambda_c^+ K^-\pi^+\pi^+$ and (blue) $\Xi_{cc}^{++} \to \Lambda_c^+ K^-\pi^+\pi^+$ background-subtracted data. The distributions from simulated events have been normalised to data.

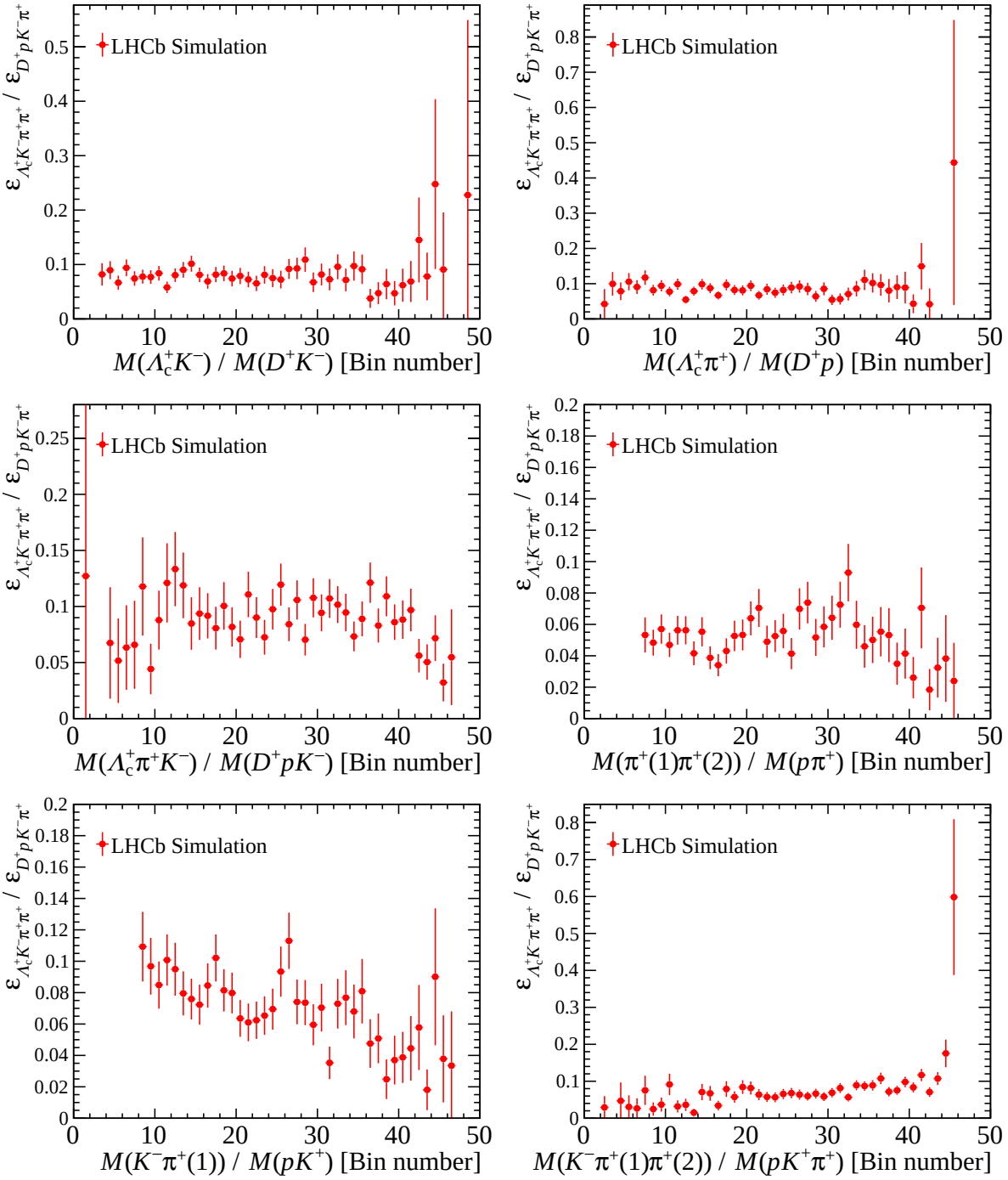

Figure D.3: The ratio of efficiencies between chosen track combinations from the $\Xi_{cc}^{++} \to D^+pK^-\pi^+$ and $\Xi_{cc}^{++} \to \Lambda_c^+K^-\pi^+\pi^+$ decay modes for matching bins in the respective invariant-mass distributions shown in Figures D.1 and Figures D.2.

Bibliography

[1] Particle Data Group, M. Tanabashi *et al.*, *Review of Particle Physics*, Phys. Rev. **D98** (2018), no. 3 030001.

[2] F. Halzen and A. D. Martin, *Quarks and Leptons: An Introductory Course In Modern Particle Physics*, 1984.

[3] W. Pauli, *The connection between spin and statistics*, Phys. Rev. **58** (1940) 716.

[4] Planck, P. A. R. Ade *et al.*, *Planck 2015 results. XIII. Cosmological parameters*, Astron. Astrophys. **594** (2016) A13, arXiv:1502.01589.

[5] DONUT, K. Kodama *et al.*, *Observation of tau neutrino interactions*, Phys. Lett. **B504** (2001) 218, arXiv:hep-ex/0012035.

[6] E. Majorana, *Teoria simmetrica dell'elettrone e del positrone*, Il Nuovo Cimento (1924-1942) **14** (2008) 171.

[7] Super-Kamiokande, Y. Fukuda *et al.*, *Evidence for oscillation of atmospheric neutrinos*, Phys. Rev. Lett. **81** (1998) 1562, arXiv:hep-ex/9807003.

[8] M. E. Peskin and D. V. Schroeder, *An Introduction to quantum field theory*, Addison-Wesley, Reading, USA, 1995.

[9] ATLAS, G. Aad *et al.*, *Observation of light-by-light scattering in ultraperipheral Pb+Pb collisions with the ATLAS detector*, Phys. Rev. Lett. **123** (2019), no. 5 052001, arXiv:1904.03536.

[10] F. Englert and R. Brout, *Broken symmetry and the mass of gauge vector mesons*, Phys. Rev. Lett. **13** (1964) 321.

[11] P. W. Higgs, *Broken symmetries and the masses of gauge bosons*, Phys. Rev. Lett. **13** (1964) 508.

[12] G. S. Guralnik, C. R. Hagen, and T. W. B. Kibble, *Global conservation laws and massless particles*, Phys. Rev. Lett. **13** (1964) 585.

[13] ATLAS, G. Aad *et al.*, *Observation of a new particle in the search for the Standard Model Higgs boson with the ATLAS detector at the LHC*, Phys. Lett. **B716** (2012) 1, arXiv:1207.7214.

[14] CMS, S. Chatrchyan *et al.*, *Observation of a new boson at a mass of 125 GeV with the CMS experiment at the LHC*, Phys. Lett. **B716** (2012) 30, arXiv:1207.7235.

[15] G. Arnison *et al.*, *Experimental observation of isolated large transverse energy electrons with associated missing energy at* $\sqrt{s} = 540\,\text{GeV}$, Physics Letters B **122** (1983), no. 1 103 .

[16] G. Arnison *et al.*, *Experimental observation of lepton pairs of invariant mass around 95* GeV/c^2 *at the CERN SPS collider*, Physics Letters B **126** (1983), no. 5 398 .

[17] UA2, M. Banner *et al.*, *Observation of Single Isolated Electrons of High Transverse Momentum in Events with Missing Transverse Energy at the CERN anti-p p Collider*, Phys. Lett. **B122** (1983) 476.

[18] S. L. Glashow, *Partial-symmetries of weak interactions*, Nuclear Physics **22** (1961), no. 4 579 .

[19] A. Salam and J. C. Ward, *Weak and electromagnetic interactions*, Il Nuovo Cimento (1955-1965) **11** (1959) 568.

[20] M. Gell-Mann, *Isotopic spin and new unstable particles*, Phys. Rev. **92** (1953) 833.

[21] K. Nishijima, *Charge Independence Theory of V Particles*, Prog. Theor. Phys. **13** (1955), no. 3 285.

[22] M. Gell-Mann, *The Eightfold Way: A Theory of Strong Interaction Symmetry*, tech. rep., 3, 1961. doi: 10.2172/4008239.

[23] V. E. Barnes *et al.*, *Observation of a hyperon with strangeness minus three*, Phys. Rev. Lett. **12** (1964) 204.

[24] H. Fritzsch, M. Gell-Mann, and H. Leutwyler, *Advantages of the color octet gluon picture*, Physics Letters B **47** (1973), no. 4 365 .

[25] E598, J. J. Aubert *et al.*, *Experimental Observation of a Heavy Particle J*, Phys. Rev. Lett. **33** (1974) 1404.

[26] J.-E. Augustin *et al.*, *Discovery of a Narrow Resonance in* e^+e^- *Annihilation*, Phys. Rev. Lett. **33** (1974) 1406.

[27] S. W. Herb *et al.*, *Observation of a Dimuon Resonance at 9.5 GeV in 400-GeV Proton-Nucleus Collisions*, Phys. Rev. Lett. **39** (1977) 252.

[28] CDF Collaboration, F. Abe *et al.*, *Observation of Top Quark Production in $\overline{p}p$ Collisions with the Collider Detector at Fermilab*, Phys. Rev. Lett. **74** (1995) 2626.

[29] D0 Collaboration, S. Abachi *et al.*, *Search for high mass top quark production in $p\overline{p}$ collisions at $\sqrt{s} = 1.8$* TeV, Phys. Rev. Lett. **74** (1995) 2422.

[30] E. D. Bloom *et al.*, *High-energy inelastic $e-p$ scattering at 6° and 10°*, Phys. Rev. Lett. **23** (1969) 930.

[31] M. Breidenbach *et al.*, *Observed behavior of highly inelastic electron-proton scattering*, Phys. Rev. Lett. **23** (1969) 935.

[32] LHCb, R. Aaij *et al.*, *Observation of an excited B_c^+ state*, Phys. Rev. Lett. **122** (2019), no. 23 232001, arXiv:1904.00081.

[33] M. Gell-Mann, *A schematic model of baryons and mesons*, Physics Letters **8** (1964), no. 3 214 .

[34] G. Zweig, *An SU(3) model for strong interaction symmetry and its breaking. Version 2*, in *Developments In The Quark Theory Of Hadrons. Vol. 1. 1964 - 1978* (D. B. Lichtenberg and S. P. Rosen, eds.), pp. 22–101. 1964.

[35] Belle Collaboration, S.-K. Choi *et al.*, *Observation of a narrow charmoniumlike state in exclusive $B^\pm \to K^\pm \pi^+ \pi^- J/\psi$ decays*, Phys. Rev. Lett. **91** (2003) 262001.

[36] D0 Collaboration, V. M. Abazov *et al.*, *Evidence for a $B_s^0 \pi^\pm$ state*, Phys. Rev. Lett. **117** (2016) 022003.

[37] G. Cotugno, R. Faccini, A. D. Polosa, and C. Sabelli, *Charmed baryonium*, Phys. Rev. Lett. **104** (2010) 132005.

[38] LHCb, R. Aaij *et al.*, *Observation of the resonant character of the $Z(4430)^-$ state*, Phys. Rev. Lett. **112** (2014), no. 22 222002, arXiv:1404.1903.

[39] LHCb, R. Aaij *et al.*, *Observation of $J/\psi\phi$ structures consistent with exotic states from amplitude analysis of $B^+ \to J/\psi\phi K^+$ decays*, Phys. Rev. Lett. **118** (2017), no. 2 022003, arXiv:1606.07895.

[40] LHCb, R. Aaij *et al.*, *Observation of $J/\psi p$ Resonances Consistent with Pentaquark States in $\Lambda_b^0 \to J/\psi K^- p$ Decays*, Phys. Rev. Lett. **115** (2015) 072001, arXiv:1507.03414.

[41] LHCb, R. Aaij *et al.*, *Observation of a narrow pentaquark state, $P_c(4312)^+$, and of two-peak structure of the $P_c(4450)^+$*, Phys. Rev. Lett. **122** (2019) 222001, arXiv:1904.03947.

[42] D. J. Gross and F. Wilczek, *Ultraviolet behavior of non-abelian gauge theories*, Phys. Rev. Lett. **30** (1973) 1343.

[43] H. D. Politzer, *Reliable perturbative results for strong interactions?*, Phys. Rev. Lett. **30** (1973) 1346.

[44] C. Berger *et al.*, *A study of jets in electron positron annihilation into hadrons in the energy range 3.1 to 9.5* GeV, Physics Letters B **78** (1978), no. 1 176 .

[45] R. Baier, D. Schiff, and B. G. Zakharov, *Energy loss in perturbative QCD*, Ann. Rev. Nucl. Part. Sci. **50** (2000) 37, arXiv:hep-ph/0002198.

[46] G. P. Salam, *Perturbative QCD for the LHC*, in *Proceedings, 35th International Conference on High energy physics (ICHEP 2010): Paris, France, July 22-28, 2010*, vol. ICHEP2010, p. 556, 2010. arXiv:1103.1318. doi: 10.22323/1.120.0556.

[47] F. Siringo, *Perturbation theory of non-perturbative QCD*, arXiv:1507.05543.

[48] K. G. Wilson, *Confinement of quarks*, Phys. Rev. D **10** (1974) 2445.

[49] S. R. Beane, W. Detmold, K. Orginos, and M. J. Savage, *Uncertainty Quantification in Lattice QCD Calculations for Nuclear Physics*, J. Phys. **G42** (2015), no. 3 034022, arXiv:1410.2937.

[50] L. Liu, H.-W. Lin, K. Orginos, and A. Walker-Loud, *Singly and doubly charmed $J = 1/2$ baryon spectrum from lattice QCD*, Phys. Rev. D **81** (2010) 094505.

[51] Z. S. Brown, W. Detmold, S. Meinel, and K. Orginos, *Charmed bottom baryon spectroscopy from lattice QCD*, Phys. Rev. D **90** (2014) 094507.

[52] PACS-CS, Y. Namekawa *et al.*, *Charmed baryons at the physical point in 2+1 flavor lattice QCD*, Phys. Rev. **D87** (2013), no. 9 094512, arXiv:1301.4743.

[53] H. D. Politzer and M. B. Wise, *Effective field theory approach to processes involving both light and heavy fields*, Physics Letters B **208** (1988), no. 3 504 .

[54] S. Bethke, *World Summary of α_s*, Nucl. Phys. (2012) , arXiv:1210.0325.

[55] H. D. Politzer and M. B. Wise, *Leading logarithms of heavy quark masses in processes with light and heavy quarks*, Physics Letters B **206** (1988), no. 4 681 .

[56] D. Ebert, R. N. Faustov, V. O. Galkin, and A. P. Martynenko, *Masses and weak decay rates of doubly heavy baryons*, in *Proceedings, 13th International Seminar on High-Energy Physics: Quarks 2004: Pushkinskie Gory, Russia, May 24-30, 2004*, 2004. arXiv:hep-ph/0411082.

[57] S. L. Glashow, J. Iliopoulos, and L. Maiani, *Weak interactions with lepton-hadron symmetry*, Phys. Rev. D **2** (1970) 1285.

[58] J. H. Christenson, J. W. Cronin, V. L. Fitch, and R. Turlay, *Evidence for the* 2π *decay of the* k_2^0 *meson*, Phys. Rev. Lett. **13** (1964) 138.

[59] M. Kobayashi and T. Maskawa, *CP-Violation in the Renormalizable Theory of Weak Interaction*, Progress of Theoretical Physics **49** (1973) 652.

[60] N. Cabibbo, *Unitary symmetry and leptonic decays*, Phys. Rev. Lett. **10** (1963) 531.

[61] A. De Rujula, H. Georgi, and S. L. Glashow, *Hadron masses in a gauge theory*, Phys. Rev. **D12** (1975) 147.

[62] S. S. Gershtein, V. V. Kiselev, A. K. Likhoded, and A. I. Onishchenko, *Spectroscopy of doubly heavy baryons*, Acta Phys. Hung. **A9** (1999) 133, arXiv:hep-ph/9811212, [Yad. Fiz.63,334(2000)].

[63] S. S. Gershtein, V. V. Kiselev, A. K. Likhoded, and A. I. Onishchenko, *Spectroscopy of doubly charmed baryons:* Ξ_{cc}^+ *and* Ξ_{cc}^{++}, Mod. Phys. Lett. **A14** (1999) 135, arXiv:hep-ph/9807375.

[64] C. Itoh, T. Minamikawa, K. Miura, and T. Watanabe, *Doubly charmed baryon masses and quark wave functions in baryons*, Phys. Rev. D **61** (2000) 057502.

[65] S. S. Gershtein, V. V. Kiselev, A. K. Likhoded, and A. I. Onishchenko, *Spectroscopy of doubly heavy baryons*, Phys. Rev. D **62** (2000) 054021.

[66] V. V. Kiselev and A. K. Likhoded, *Baryons with two heavy quarks*, Phys. Usp. **45** (2002) 455, arXiv:hep-ph/0103169, [Usp. Fiz. Nauk172,497(2002)].

[67] D. Ebert, R. N. Faustov, V. O. Galkin, and A. P. Martynenko, *Mass spectra of doubly heavy baryons in the relativistic quark model*, Phys. Rev. **D66** (2002) 014008, arXiv:hep-ph/0201217.

[68] D.-H. He *et al.*, *Evaluation of spectra of baryons containing two heavy quarks in bag model*, Phys. Rev. **D70** (2004) 094004, arXiv:hep-ph/0403301.

[69] C.-H. Chang, C.-F. Qiao, J.-X. Wang, and X.-G. Wu, *Estimate of the hadronic production of the doubly charmed baryon Ξ_{cc} under GM-VFN scheme*, Phys. Rev. **D73** (2006) 094022, arXiv:hep-ph/0601032.

[70] W. Roberts and M. Pervin, *Heavy baryons in a quark model*, Int. J. Mod. Phys. **A23** (2008) 2817, arXiv:0711.2492.

[71] A. Valcarce, H. Garcilazo, and J. Vijande, *Towards an understanding of heavy baryon spectroscopy*, Eur. Phys. J. **A37** (2008) 217, arXiv:0807.2973.

[72] J.-R. Zhang and M.-Q. Huang, *Doubly heavy baryons in QCD sum rules*, Phys. Rev. **D78** (2008) 094007, arXiv:0810.5396.

[73] Z.-G. Wang, *Analysis of the ${}^1/_2{}^+$ doubly heavy baryon states with QCD sum rules*, Eur. Phys. J. **A45** (2010) 267, arXiv:1001.4693.

[74] M. Karliner and J. L. Rosner, *Baryons with two heavy quarks: Masses, production, decays, and detection*, Phys. Rev. **D90** (2014), no. 9 094007, arXiv:1408.5877.

[75] K.-W. Wei, B. Chen, and X.-H. Guo, *Masses of doubly and triply charmed baryons*, Phys. Rev. **D92** (2015), no. 7 076008, arXiv:1503.05184.

[76] Z.-F. Sun and M. J. V. Vacas, *Masses of doubly charmed baryons in the extended on-mass-shell renormalization scheme*, Phys. Rev. D **93** (2016) 094002.

[77] C. Alexandrou and C. Kallidonis, *Low-lying baryon masses using $N_f = 2$ twisted mass clover-improved fermions directly at the physical pion mass*, Phys. Rev. **D96** (2017), no. 3 034511, arXiv:1704.02647.

[78] C.-W. Hwang and C.-H. Chung, *Isospin mass splittings of heavy baryons in HQS*, Phys. Rev. **D78** (2008) 073013, arXiv:0804.4044.

[79] S. J. Brodsky, F.-K. Guo, C. Hanhart, and U.-G. Meissner, *Isospin splittings of doubly heavy baryons*, Phys. Lett. **B698** (2011) 251, arXiv:1101.1983.

[80] M. Karliner and J. L. Rosner, *Isospin splittings in baryons with two heavy quarks*, Phys. Rev. **D96** (2017), no. 3 033004, arXiv:1706.06961.

[81] V. V. Kiselev, A. K. Likhoded, and A. I. Onishchenko, *Lifetimes of doubly charmed baryons: Ξ_{cc}^+ and Ξ_{cc}^{++}*, Phys. Rev. **D60** (1999) 014007, arXiv:hep-ph/9807354.

[82] A. K. Likhoded and A. I. Onishchenko, *Lifetimes of doubly heavy baryons*, arXiv:hep-ph/9912425.

[83] B. Guberina, B. Melic, and H. Stefancic, *Inclusive decays and lifetimes of doubly charmed baryons*, Eur. Phys. J. **C9** (1999) 213, arXiv:hep-ph/9901323.

[84] A. I. Onishchenko, *Inclusive and exclusive decays of doubly heavy baryons*, in *5th International Workshop on Heavy Quark Physics Dubna, Russia, April 6-8, 2000*, 2000. arXiv:hep-ph/0006295.

[85] K. Anikeev *et al.*, *B physics at the Tevatron: Run II and beyond*, in *Workshop on B Physics at the Tevatron: Run II and Beyond Batavia, Illinois, September 23-25, 1999*, 2001. arXiv:hep-ph/0201071.

[86] C.-H. Chang, T. Li, X.-Q. Li, and Y.-M. Wang, *Lifetime of doubly charmed baryons*, Commun. Theor. Phys. **49** (2008) 993, arXiv:0704.0016.

[87] N. Bilic, B. Guberina, and J. Trampetic, *Pauli Interference Effect in D^+ Lifetime*, Nucl. Phys. **B248** (1984) 261.

[88] J.-M. Richard, *Double charm physics*, in *Workshop on Future Physics at COMPASS Geneva, Switzerland, September 26-27, 2002*, 2002. arXiv:hep-ph/0212224.

[89] A. V. Berezhnoy, V. V. Kiselev, A. K. Likhoded, and A. I. Onishchenko, *Doubly charmed baryon production in hadronic experiments*, Phys. Rev. **D57** (1998) 4385, arXiv:hep-ph/9710339.

[90] J.-W. Zhang *et al.*, *Hadronic production of the doubly heavy baryon Ξ_{bc} at LHC*, Phys. Rev. **D83** (2011) 034026, arXiv:1101.1130.

[91] V. V. Kiselev and A. K. Likhoded, *Baryons with two heavy quarks*, Phys. Usp. **45** (2002) 455, arXiv:hep-ph/0103169.

[92] J. P. Ma and Z. G. Si, *Factorization approach for inclusive production of doubly heavy baryon*, Phys. Lett. **B568** (2003) 135, arXiv:hep-ph/0305079.

[93] C.-H. Chang, C.-F. Qiao, J.-X. Wang, and X.-G. Wu, *The color-octet contributions to P-wave B_c meson hadroproduction*, Phys. Rev. **D71** (2005) 074012, arXiv:hep-ph/0502155.

[94] C.-H. Chang, J.-P. Ma, C.-F. Qiao, and X.-G. Wu, *Hadronic production of the doubly charmed baryon Ξ_{cc} with intrinsic charm*, J. Phys. **G34** (2007) 845, arXiv:hep-ph/0610205.

[95] H. He, Y. Liu, and P. Zhuang, *Ω_{ccc} production in high energy nuclear collisions*, Phys. Lett. **B746** (2015) 59, arXiv:1409.1009.

[96] J. Zhao, H. He, and P. Zhuang, *Searching for Ξ_{cc}^{+} in relativistic heavy ion collisions*, arXiv:1603.04524.

[97] J. Zhao and P. Zhuang, *Multicharmed Baryon Production in High Energy Nuclear Collisions*, Few Body Syst. **58** (2017), no. 2 100.

[98] LHCb, R. Aaij *et al.*, *Measurement of the J/ψ pair production cross-section in pp collisions at $\sqrt{s} = 13$ TeV*, JHEP **06** (2017) 047, arXiv:1612.07451, [Erratum: JHEP10,068(2017)].

[99] F.-S. Yu *et al.*, *Discovery Potentials of Doubly Charmed Baryons*, Chin. Phys. **C42** (2018), no. 5 051001, arXiv:1703.09086.

[100] A. K. Leibovich, Z. Ligeti, I. W. Stewart, and M. B. Wise, *Predictions for nonleptonic Lambda(b) and Theta(b) decays*, Phys. Lett. **B586** (2004) 337, arXiv:hep-ph/0312319.

[101] C.-D. Lu *et al.*, *Anatomy of the pQCD Approach to the Baryonic Decays $\Lambda_b^0 \to p\pi$, pK*, Phys. Rev. **D80** (2009) 034011, arXiv:0906.1479.

[102] SELEX (Segmented Large X baryon Spectrometer), https://www-selex.fnal.gov/. Accessed: June 2019.

[103] SELEX, M. Mattson *et al.*, *First Observation of the Doubly Charmed Baryon Ξ_{cc}^{+}*, Phys. Rev. Lett. **89** (2002) 112001, arXiv:hep-ex/0208014.

[104] SELEX, A. Ocherashvili *et al.*, *Confirmation of the double charm baryon Ξ_{cc}^{+} (3520) via its decay to $pD^{+}K^{-}$*, Phys. Lett. **B628** (2005) 18, arXiv:hep-ex/0406033.

[105] S. P. Ratti, *New results on c-baryons and a search for cc-baryons in FOCUS*, Nucl. Phys. Proc. Suppl. **115** (2003) 33.

[106] BaBar collaboration, B. Aubert *et al.*, *Search for doubly charmed baryons Ξ_{cc}^{+} and Ξ_{cc}^{++} in BaBar*, Phys. Rev. **D74** (2006) 011103, arXiv:hep-ex/0605075.

[107] Belle collaboration, R. Chistov *et al.*, *Observation of new states decaying into $\Lambda_c^{+}K^{-}\pi^{+}$ and $\Lambda_c^{+}K_S^{0}\pi^{-}$*, Phys. Rev. Lett. **97** (2006) 162001, arXiv:hep-ex/0606051.

[108] LHCb, R. Aaij *et al.*, *Search for the doubly charmed baryon Ξ_{cc}^{+}*, JHEP **12** (2013) 090, arXiv:1310.2538.

[109] O. S. Brüning *et al.*, *LHC Design Report*, CERN Yellow Reports: Monographs, CERN, Geneva, 2004.

[110] CERN: The European Organization for Nuclear Research, `https://home.cern`. Accessed: February 2019.

[111] LEP Design Report*: Vol.2. The LEP Main Ring*, Tech. Rep. CERN-LEP-84-01, 1984.

[112] L. Evans and P. Bryant, *LHC machine*, Journal of Instrumentation **3** (2008) S08001.

[113] F. Fayette, *Strategies for precision measurements of the charge asymmetry of the W boson mass at the LHC within the ATLAS experiment*, `arXiv:0906.4260`.

[114] CMS, S. Chatrchyan *et al.*, *The CMS Experiment at the CERN LHC*, JINST **3** (2008) S08004.

[115] ATLAS, G. Aad *et al.*, *The ATLAS Experiment at the CERN Large Hadron Collider*, JINST **3** (2008) S08003.

[116] ALICE, K. Aamodt *et al.*, *The ALICE experiment at the CERN LHC*, JINST **3** (2008) S08002.

[117] T. T. Collaboration *et al.*, *The TOTEM experiment at the CERN large hadron collider*, Journal of Instrumentation **3** (2008) S08007.

[118] T. L. Collaboration *et al.*, *The LHCf detector at the CERN large hadron collider*, Journal of Instrumentation **3** (2008) S08006.

[119] MoEDAL, V. A. Mitsou, *The MoEDAL experiment at the LHC: status and results*, J. Phys. Conf. Ser. **873** (2017), no. 1 012010, `arXiv:1703.07141`.

[120] LHCb collaboration, A. A. Alves Jr. *et al.*, *The LHCb detector at the LHC*, JINST **3** (2008) S08005.

[121] R. Aaij *et al.*, *Performance of the LHCb Vertex Locator*, JINST **9** (2014) P09007, `arXiv:1405.7808`.

[122] LHCb : Technical Proposal, Tech. Rep. CERN-LHCC-98-004, Geneva, 1998.

[123] LHCb, R. Aaij *et al.*, *Measurement of the b-quark production cross-section in 7 and 13 TeV pp collisions*, Phys. Rev. Lett. **118** (2017), no. 5 052002, `arXiv:1612.05140`, [Erratum: Phys. Rev. Lett.119,no.16,169901(2017)].

[124] LHCb, R. Aaij *et al.*, *LHCb Detector Performance*, Int. J. Mod. Phys. **A30** (2015), no. 07 1530022, `arXiv:1412.6352`.

[125] R. J. Federico Alessio, *LHCb Operations Plots Webpage*, `https://lbgroups.cern.ch/online/OperationsPlots/index.htm`. Accessed: February 2019.

[126] R. Frühwirth, *Application of kalman filtering to track and vertex fitting*, Nuclear Instruments and Methods in Physics Research Section A: Accelerators, Spectrometers, Detectors and Associated Equipment **262** (1987), no. 2 444 .

[127] P. d'Argent *et al.*, *Improved performance of the LHCb Outer Tracker in LHC Run 2*, JINST **9** (2017) P11016, `arXiv:1708.00819`.

[128] LHCb Silicon Tracker - Material for Publications, `https://lhcb.physik.uzh.ch/ST/public/material/index.php`. Accessed: February 2019.

[129] LHCb RICH Collaboration, N. Brook *et al.*, *LHCb RICH1 Engineering Design Review Report*, Tech. Rep. LHCb-2004-121. CERN-LHCb-2004-121, CERN, Geneva, Oct, 2005.

[130] LHCb RICH Collaboration, M. Adinolfi *et al.*, *LHCb RICH 2 engineering design review report*, Tech. Rep. LHCb-2002-009. CERN-LHCb-2002-009, CERN, 2002.

[131] C. Lippmann, *Particle identification*, Nucl. Instrum. Meth. **A666** (2012) 148, `arXiv:1101.3276`.

[132] R. Forty, *Rich pattern recognition for lhcb*, Nuclear Instruments and Methods in Physics Research Section A: Accelerators, Spectrometers, Detectors and Associated Equipment **433** (1999), no. 1 257 .

[133] M. Adinolfi *et al.*, *Performance of the LHCb RICH detector at the LHC*, Eur. Phys. J. **C73** (2013) 2431, `arXiv:1211.6759`.

[134] A. A. Alves Jr. *et al.*, *Performance of the LHCb muon system*, JINST **8** (2013) P02022, `arXiv:1211.1346`.

[135] F. Archilli *et al.*, *Performance of the Muon Identification at LHCb*, JINST **8** (2013) P10020, `arXiv:1306.0249`.

[136] LHCb Collaboration, R. Antunes-Nobrega *et al.*, *LHCb trigger system: Technical Design Report*, Technical Design Report LHCb, CERN, Geneva, 2003. revised version number 1 submitted on 2003-09-24 12:12:22.

[137] The MOORE Project, `http://lhcbdoc.web.cern.ch/lhcbdoc/moore/`. Accessed: February 2019.

[138] The DaVinci Project, http://lhcbdoc.web.cern.ch/lhcbdoc/davinci/. Accessed: February 2019.

[139] R. Aaij *et al.*, *Performance of the LHCb trigger and full real-time reconstruction in Run 2 of the LHC*, arXiv:1812.10790.

[140] R. Aaij *et al.*, *Tesla: an application for real-time data analysis in High Energy Physics*, Comput. Phys. Commun. **208** (2016) 35, arXiv:1604.05596.

[141] The Brunel Project, http://lhcbdoc.web.cern.ch/lhcbdoc/brunel/. Accessed: February 2019.

[142] The LHCb Starterkit github, https://lhcb.github.io/starterkit-lessons/first-analysis-steps/run-2-data-flow.html. Accessed: February 2019.

[143] A. Buckley *et al.*, *General-purpose event generators for LHC physics*, Phys. Rept. **504** (2011) 145, arXiv:1101.2599.

[144] T. Sjöstrand, S. Mrenna, and P. Skands, *PYTHIA 6.4 physics and manual*, JHEP **05** (2006) 026, arXiv:hep-ph/0603175.

[145] M. Clemencic *et al.*, *The LHCb simulation application, gauss: Design, evolution and experience*, Journal of Physics: Conference Series **331** (2011) 032023.

[146] C.-H. Chang, C. Driouichi, P. Eerola, and X. G. Wu, *BCVEGPY: An Event generator for hadronic production of the B_c meson*, Comput. Phys. Commun. **159** (2004) 192, arXiv:hep-ph/0309120.

[147] G. Corcella *et al.*, *HERWIG 6: An Event generator for hadron emission reactions with interfering gluons (including supersymmetric processes)*, JHEP **01** (2001) 010, arXiv:hep-ph/0011363.

[148] T. Gleisberg *et al.*, *Event generation with SHERPA 1.1*, JHEP **02** (2009) 007, arXiv:0811.4622.

[149] D. J. Lange, *The EvtGen particle decay simulation package*, Nucl. Instrum. Meth. **A462** (2001) 152.

[150] P. Golonka and Z. Was, *PHOTOS Monte Carlo: A precision tool for QED corrections in Z and W decays*, Eur. Phys. J. **C45** (2006) 97, arXiv:hep-ph/0506026.

[151] Geant4 collaboration, J. Allison *et al.*, *Geant4 developments and applications*, IEEE Trans. Nucl. Sci. **53** (2006) 270.

[152] The BOOLE Project, `http://lhcbdoc.web.cern.ch/lhcbdoc/boole/`. Accessed: February 2019.

[153] M. Alemia. *et al.*, *First operation of a hybrid photon detector prototype with electrostatic cross-focussing and integrated silicon pixel readout*, Nuclear Instruments & Methods in Physics Research Section A-accelerators Spectrometers Detectors and Associated Equipment **499** (2000).

[154] R. Cardinale *et al.*, *Analysis and correction of the magnetic field effects in the hybrid photo-detectors of the RICH2 ring imaging cherenkov detector of LHCb.*, Journal of Instrumentation **6** (2011) P06010.

[155] A. Borgia *et al.*, *The Magnetic Distortion Calibration System of the LHCb RICH1 Detector*, Nucl. Instrum. Meth. **A735** (2014) 44, `arXiv:1206.0253`.

[156] D. P. Sail, *Lifetime measurements of the $B_s \to KK$ system and RICH studies at LHCb.*, PhD thesis, University of Glasgow, 2013.

[157] LHCb collaboration, R. Aaij *et al.*, *Observation of the doubly charmed baryon Ξ_{cc}^{++}*, Phys. Rev. Lett. **119** (2017) 112001, `arXiv:1707.01621`.

[158] C.-H. Chang, J.-X. Wang, and X.-G. Wu, *GENXICC2.0: An upgraded version of the generator for hadronic production of double heavy baryons Ξ_{cc}, Ξ_{bc} and Ξ_{bb}*, Comput. Phys. Commun. **181** (2010) 1144, `arXiv:0910.4462`.

[159] I. Belyaev *et al.*, *Handling of the generation of primary events in Gauss, the LHCb simulation framework*, J. Phys. Conf. Ser. **331** (2011) 032047.

[160] M. De Cian, S. Farry, P. Seyfert, and S. Stahl, *Fast neural-net based fake track rejection in the LHCb reconstruction*, Tech. Rep. LHCb-PUB-2017-011. CERN-LHCb-PUB-2017-011, CERN, Geneva, Mar, 2017.

[161] L. Anderlini *et al.*, *The PIDCalib package*, Tech. Rep. LHCb-PUB-2016-021, CERN-LHCb-PUB-2016-021, CERN, Geneva, Jul, 2016.

[162] W. D. Hulsbergen, *Decay chain fitting with a Kalman filter*, Nucl. Instrum. Meth. **A552** (2005) 566, `arXiv:physics/0503191`.

[163] M. D. Needham, *Momentum scale calibration of the LHCb spectrometer*, Tech. Rep. LHCb-INT-2017-008. CERN-LHCb-INT-2017-008, CERN, Geneva, Apr, 2017.

[164] LHCb collaboration, R. Aaij *et al.*, *Measurement of* b*-hadron masses*, Phys. Lett. **B708** (2012) 241, `arXiv:1112.4896`.

[165] LHCb collaboration, R. Aaij *et al.*, *Precision measurement of D meson mass differences*, JHEP **06** (2013) 065, arXiv:1304.6865.

[166] H. Voss, A. Hoecker, J. Stelzer, and F. Tegenfeldt, *TMVA, the Toolkit for Multivariate Data Analysis*, PoS **ACAT** (2007) 040.

[167] R. Brun and F. Rademakers, *ROOT – An object oriented data analysis framework*, Nuclear Instruments and Methods in Physics Research Section A: Accelerators, Spectrometers, Detectors and Associated Equipment **389** (1997), no. 1 81, New Computing Techniques in Physics Research V.

[168] C. G. Broyden, *The convergence of a class of double-rank minimization algorithms 1. General considerations*, IMA Journal of Applied Mathematics **6** (1970), no. 1 76.

[169] G. Punzi, *Sensitivity of searches for new signals and its optimization*, eConf **C030908** (2003) MODT002, arXiv:physics/0308063.

[170] T. Skwarnicki, *A study of the radiative cascade transitions between the Upsilon-prime and Upsilon resonances*, PhD thesis, Institute of Nuclear Physics, Krakow, 1986, DESY-F31-86-02.

[171] S. S. Wilks, *The Large-Sample Distribution of the Likelihood Ratio for Testing Composite Hypotheses*, Annals Math. Statist. **9** (1938), no. 1 60.

[172] M. Pivk and F. R. Le Diberder, *SPlot: A Statistical tool to unfold data distributions*, Nucl. Instrum. Meth. **A555** (2005) 356, arXiv:physics/0402083.

[173] S. J. Brodsky, S. Groote, and S. Koshkarev, *Resolving the SELEX–LHCb double–charm baryon conflict: the impact of intrinsic heavy-quark hadroproduction and supersymmetric light-front holographic QCD*, Eur. Phys. J. **C78** (2018), no. 6 483, arXiv:1709.09903.

[174] LHCb collaboration, R. Aaij *et al.*, *Measurement of the lifetime of the doubly charmed baryon Ξ_{cc}^{++}*, Phys. Rev. Lett. **121** (2018) 052002, arXiv:1806.02744.

[175] LHCb, R. Aaij *et al.*, *A search for $\Xi_{cc}^{++} \to D^+ p K^- \pi^+$ decays*, JHEP **10** (2019) 124, arXiv:1905.02421.

[176] LHCb, R. Aaij *et al.*, *Precision measurement of D meson mass differences*, JHEP **06** (2013) 065, arXiv:1304.6865.

[177] G. A. Cowan, D. C. Craik, and M. D. Needham, *RapidSim: an application for the fast simulation of heavy-quark hadron decays*, Comput. Phys. Commun. **214** (2017) 239, arXiv:1612.07489.

[178] A. L. Read, *Presentation of search results: the CLs technique*, Journal of Physics G: Nuclear and Particle Physics **28** (2002) 2693.

[179] A. Piucci, *The LHCb upgrade*, Journal of Physics: Conference Series **878** (2017) 012012.

[180] LHCb, R. Aaij *et al.*, *First Observation of the Doubly Charmed Baryon Decay* $\Xi_{cc}^{++} \to \Xi_c^+ \pi^+$, Phys. Rev. Lett. **121** (2018), no. 16 162002, arXiv:1807.01919.

[181] S. Amerio *et al.*, *BDT based inclusive charm trigger*, Tech. Rep. LHCb-PUB-2017-004. CERN-LHCb-PUB-2017-004, CERN, Geneva, Feb, 2017.

[182] D. Derkach *et al.*, *LHCb trigger streams optimization*, Journal of Physics: Conference Series **898** (2017) 062026.

[183] L. Breiman, J. H. Friedman, R. A. Olshen, and C. J. Stone, *Classification and regression trees*, Wadsworth international group, Belmont, California, USA, 1984.

[184] V. V. Gligorov and M. Williams, *Efficient, reliable and fast high-level triggering using a bonsai boosted decision tree*, JINST **8** (2013) P02013, arXiv:1210.6861.

[185] LHCb, R. Aaij *et al.*, *Measurement of the* Ω_c^0 *baryon lifetime*, Phys. Rev. Lett. **121** (2018), no. 9 092003, arXiv:1807.02024.

[186] G. Apollinari, O. Brüning, T. Nakamoto, and L. Rossi, *High Luminosity Large Hadron Collider HL-LHC*, CERN Yellow Rep. (2015), no. 5 1, arXiv:1705.08830.

[187] J. Bennett, *Belle II physics prospects, status and schedule*, Journal of Physics: Conference Series **770** (2016) 012044.

[188] N. Meinert, *Measurement of the Masses and the Isospin Splitting of* Σ_c *Baryons*, tech. rep., Dec, 2016. LHCb-ANA-2016-079.

[189] A. Powell *et al.*, *Particle identification at LHCb*, vol. ICHEP2010, p. 020, 2010. LHCb-PROC-2011-008.